University of Alberta

Functionalized Macrocyclic Ligands: Synthesis, Self–Assembly, and Solid–State Characterization

by Katie Campbell ©

A thesis submitted to the Faculty of Graduate Studies and Research in partial fulfillment of the requirements of the degree of Doctor of Philosophy

Department of Chemistry

Edmonton, Alberta

Fall, 2004

Library and
Archives Canada

Published Heritage
Branch

395 Wellington Street
Ottawa ON K1A 0N4
Canada

Bibliothèque et
Archives Canada

Direction du
Patrimoine de l'édition

395, rue Wellington
Ottawa ON K1A 0N4
Canada

Your file Votre référence
ISBN: 0-612-95914-7
Our file Notre référence
ISBN: 0-612-95914-7

The author has granted a non-exclusive license allowing the Library and Archives Canada to reproduce, loan, distribute or sell copies of this thesis in microform, paper or electronic formats.

The author retains ownership of the copyright in this thesis. Neither the thesis nor substantial extracts from it may be printed or otherwise reproduced without the author's permission.

L'auteur a accordé une licence non exclusive permettant à la Bibliothèque et Archives Canada de reproduire, prêter, distribuer ou vendre des copies de cette thèse sous la forme de microfiche/film, de reproduction sur papier ou sur format électronique.

L'auteur conserve la propriété du droit d'auteur qui protège cette thèse. Ni la thèse ni des extraits substantiels de celle-ci ne doivent être imprimés ou aturement reproduits sans son autorisation.

In compliance with the Canadian Privacy Act some supporting forms may have been removed from this thesis.

While these forms may be included in the document page count, their removal does not represent any loss of content from the thesis.

Conformément à la loi canadienne sur la protection de la vie privée, quelques formulaires secondaires ont été enlevés de cette thèse.

Bien que ces formulaires aient inclus dans la pagination, il n'y aura aucun contenu manquant.

Canada

Acknowledgement

I would first like to thank my supervisor, Rik, for his constant support and encouragement throughout the last five years. He has shared with us his infectious enthusiasm for chemistry and has taught me countless important lessons. During a particularly frustrating stage of one of my projects, he said to me: "Don't worry, just the fact that you care about your project this much is all I can ask for – I know you're doing your best". This is a perfect example of what it is like to work for Rik, and I am extremely grateful that I had the opportunity to work for someone who cares as much about inspiring his students as he does about achieving a good result. Thanks.

I would also like to thank all past and present group members for their friendship and support: Yuming, Sorin, Joon, Sara, Darren, Annabelle, Clement, Trent, Erin, Chad, Mojtaba, Paul, Thanh, Jamie, Andreea, and Nina. I would especially like to thank Yuming for his humour and patience with me when I was starting out, and Sara for her friendship during the last five years. Thanks also to all of the summer students that I have had the opportunity to work with: Natasha Tiemstra, Natasha Prepas–Strobeck, Monika Pawlowska, and David Ruan.

I have also benefited from several collaborations over the last five years and would like to thank Aaron Slepkov (Frank Hegmann), Chris Kuehl (Peter Stang), Charles Johnson (Michael Haley), and Kris Ooms (Rod Wasylishen) for their assistance and hard work. I would especially like to thank Kris whose contagious enthusiasm has made the last year a huge amount of fun.

There are numerous people in the Chemistry Department whose hard work has helped me achieve a lot of the results presented in this thesis. Thanks to Bob and Mike for all of the crystallography and your patience with my endless questions! Thanks also to everyone in the mass spec lab, especially Angie, who never *ever* gives up. I would like to acknowledge everyone, past and present, who helped me with all of the NMR spectroscopy: Tom, Glen, Gerdy, Lai, Albin, and Mark. Thanks for all of your time and assistance. Thanks to Diane for her constant cheerfulness and support.

Finally, I would like to thank my family for supporting me for the last five years. First I would like say a special thank you to my husband, Ron, for his endless support and encouragement. Thanks for putting up with all of the crazy times, and for cooking supper so much! I love you. Thanks also to my friend Percy for all of the great walks. I would also like to thank Dad and Benita, Mom and Jack, and Pete and Evelyn for their encouragement during the last five years, and for never asking when I'm going to get a real job!

I would also like to acknowledge the University of Alberta and NSERC for financial support during my doctoral studies.

Table of Contents

Chapter 1 Introduction to Functionalized, Shape–Persistent Macrocycles..........1

1.1 Why Macrocycles?..........1

1.2 Synthesis and Properties of Shape–Persistent Macrocycles Containing Heteroatom Functionality..........6

1.2.1 Oxaarenecyclynes and Macrocycles Containing Hydroxylic/Carboxylic Functionality..........7

1.2.2 Shape–Persistent Macrocycles Based on Thiophenes..........13

1.2.3 Shape–Persistent Macrocycles Containing Nitrogen–Based Heterocycles..........17

1.3 Conclusions..........28

1.4 References and Notes..........29

Chapter 2 Synthesis and Characterization of Cross–Conjugated Oligomers and Macrocycles..........34

2.1 Introduction..........34

2.2 Results and Discussion..........36

2.2.1 Synthesis of Cross–Conjugated Oligomers and Macrocycles..........36

2.2.2 Synthesis of Cyclic and Acyclic Oligomers Containing Heteroaromatic Functionality..........46

2.2.3 Solid–State Properties of Acyclic and Cyclic Pyridine–Containing Oligomers..........52

2.3 Conclusions.......57

2.4 References and Notes.......57

Chapter 3 Expanded Pyridines and Bipyridines – Supramolecular Building Blocks.......60

3.1 Introduction.......60

3.2 Results and Discussion.......62

3.2.1 Synthesis of Pyridine–Containing Oligomers and Macrocycles.......62

3.2.2 Solid–State Properties of Pyridine–Containing Oligomers.......69

3.2.3 Synthesis of Porphyrinic Supramolecular Assemblies.......72

3.2.4 Solid–State Characterization of Supramolecular Assemblies.......80

3.2.5 Electronic Properties of Cyclic and Acyclic Pyridine–Containing Oligomers and Supramolecular Assemblies.......85

3.2.6 Efforts Toward Building Blocks With Different Coordination Motifs.......91

3.3 Conclusions and Future Work.......98

3.4 References and Notes.......99

Chapter 4 Synthesis and Solid–State Characterization of Platinum–Containing Macrocycles.......103

4.1 Introduction.......103

4.2 Results and Discussion.......105

4.2.1 Synthesis and Characterization of Platinacycles.......105

4.2.2 Synthesis and Characterization of Coordination Compounds.......109

4.2.3 Solid–State Characterization of Platinum–Containing Macrocycles and Their Assembly Products......113

4.2.4 Electronic Properties of Platinum Complexes......122

4.2.5 Nonlinear Optical Properties as a Function of Platinum......126

4.3 Conclusions and Outlook......128

4.4 References and Notes......129

Chapter 5 Application of Pyridine–Containing Macrocycles Toward the Formation of Porous Solids......133

5.1 Introduction......133

5.2 Results and Discussion......140

5.2.1 Synthesis and Characterization of Bidirectionally Porous Assembly......140

5.2.2 Crystallographic Analysis of Porous Assembly......146

5.2.3 ^{129}Xe NMR Studies on Porous Organic Solids......152

5.3 Conclusions and Future Work......174

5.4 References and Notes......174

Chapter 6 Application of Ligand Exchange Reactions to Platinum–Containing Macrocycles......179

6.1 Introduction......179

6.2 Results and Discussion......183

6.2.1 Synthesis and Characterization of Trans– and Cis–Platinum Acetylide Complexes......183

6.2.2 Solid-State Properties of Trans– and Cis–Platinum Acetylide Complexes......190
6.2.3 Synthesis of Chiral Platinum Acetylide Complexes......196
6.2.4 Solid–State Properties of Chiral Platinum Acetylide Complexes......204
6.2.5 Electronic Properties of Chiral Platinum Acetylide Complexes......208
6.3 Conclusions and Future Work......211
6.4 References and Notes......213

Chapter 7 Conclusions and Future Work......216

Chapter 8 Experimental Section......222
8.1 General Details......222
8.2 Experimental Details for Chapter 2......227
8.3 Experimental Details for Chapter 3......241
8.4 Experimental Details for Chapter 4......264
8.5 Experimental Details for Chapter 5......272
8.6 Experimental Details for Chapter 6......275
8.7 References and Notes......294

Appendix A – Selected Spectra......295

List of Equations and Tables

Equation 2.1..36

Equation 2.2..37

Table 4.1 Summary of results for the macrocyclic series shown. γ_S and γ_{THF} are the molecular second hyperpolarizabilities of the samples and the THF reference, respectively..127

Table 6.1 Synthetic details for the formation of *trans*– and *cis*–platinum acetylide complexes **402**, **608**, **602a–c**, and **610a–c**..186

Table 6.2 A comparison of selected bond lengths [Å] and angles [°] for **602a**, **602b**, **602c**, **610a** (crystallographically independent molecule A), **610a*** (crystallographically independent molecule B), and **610b**..194

List of Figures

Figure 1.1 Schematic representations of synthetic approaches toward shape–persistent macrocycles....2

Figure 1.2 Schematic representation of the assembly of a shape–persistent macrocycle with a functionalized cavity....4

Figure 1.3 Schematic representation of the aggregation of a shape–persistent macrocycle with a functionalized periphery....5

Figure 2.1 ORTEP drawing of **209a**....43

Figure 2.2 ORTEP drawing of **217a** highlighting the non–bonded interactions between adjacent molecules....53

Figure 2.3 ORTEP drawing of oligomer **215a**....54

Figure 2.4 ORTEP drawing of **216c**....55

Figure 2.5 Crystal packing diagram of **216c** viewed down the crystallographic *a*–axis....56

Figure 3.1 Schematic representation of porous pyridine and 4,4′–bipyridine analogues....61

Figure 3.2 (Top) ORTEP drawing of adamantylidene–functionalized oligomer **302b**. (Bottom) ORTEP drawing of diphenylalkylidene–functionalized oligomer **302c**....70

Figure 3.3 ORTEP drawing of diphenylalkylidene–functionalized oligomer **303c**....72

Figure 3.4 (Top) ^{1}H NMR spectrum (300 MHz, CD_2Cl_2) of **305c** highlighting the *ortho*– and *para*–pyridyl protons. (Bottom) ^{1}H NMR spectrum (300 MHz, CD_2Cl_2) of **309c**....77

Figure 3.5 gHMQC NMR spectrum (500 MHz, CH_2Cl_2) of assembly **309c** showing correlations for *ortho*– and *para*–pyridyl protons....78

Figure 3.6 (Top) ORTEP drawing of supramolecular assembly **309a**. (Bottom) Crystal packing diagram viewed down the *b*–axis showing co–crystallized porphyrin....81

Figure 3.7 (Top) ORTEP drawing of supramolecular assembly **309c**. (Bottom) Alternate view emphasizing the chair conformation of the macrocyclic core....83

Figure 3.8 UV–vis absorption curves (CH_2Cl_2) for oligomers **302a–c**....86

Figure 3.9 UV–vis absorption curves (CH_2Cl_2) for extended oligomers **303b** and **303c**....87

Figure 3.10 UV–vis absorption curves (CH_2Cl_2) for macrocycles **304b** and **304c** and their porphyrinic assemblies **308b** and **308c**....88

Figure 3.11 UV–vis absorption curves (CH_2Cl_2) for supramolecular assemblies **309a** and **309c**....89

Figure 3.12 UV–vis absorption (solid line) and emission spectra (dashed line) for macrocycle **305c** and its oligomeric precursor **302c**. All spectra were recorded in CH_2Cl_2....90

Figure 3.13 UV–vis absorption (solid line) and emission (dashed line) spectra for supramolecular assembly **309c**. All spectra were recorded in CH_2Cl_2....91

Figure 3.14 (Left) ORTEP drawing of dimer **313**. (Right) Alternate view....94

Figure 4.1 Schematic representation of a bidentate macrocyclic ligand featuring metal σ–acetylide moieties....104

Figure 4.2 (Top) ^{1}H NMR (300 MHz, CD_2Cl_2) spectrum of macrocyclic ligand **304c**. (Bottom) ^{1}H NMR (400 MHz, CD_2Cl_2) spectrum of coordination complex **404**.........112

Figure 4.3 (Top) ORTEP drawing of **403a**. (Bottom) Alternate view of **403a** highlighting the planar, cyclic core; only the *ipso* carbons of the triphenylphosphine ligands and pendant diphenyl groups are shown, for clarity..........115

Figure 4.4 ORTEP drawing of **403b**..........116

Figure 4.5 (Top) ORTEP drawing of **304c** showing pseudo–envelope conformation; co–crystallized CH_2Cl_2 not shown. (Bottom) ORTEP drawing of **402**; co–crystallized CH_2Cl_2 and acetone not shown; only the *ipso* carbons of the triphenylphosphine ligands are shown, for clarity..........118

Figure 4.6 (Top) ORTEP drawing of **404**; co–crystallized $CHCl_3$ not shown. (Bottom) ORTEP drawing of **405**; co–crystallized CH_2Cl_2 not shown; only the *ipso* carbons of the triphenylphosphine ligands are shown, for clarity..........121

Figure 4.7 UV–vis absorption spectra (CH_2Cl_2) for ligands **304c**, **402** and their platinum complexes **404** and **405**..........123

Figure 4.8 UV–vis absorption spectra (CH_2Cl_2) for compounds **305c**, **403b**, and **406**..........124

Figure 4.9 Emission spectra (CH_2Cl_2) for compounds **304c** (exc. at 370 nm), **402** (exc. at 290 nm), **404** (exc. at 265 nm) and **405** (exc. at 290 nm)..........126

Figure 5.1 Porous structures via the aggregation of shape–persistent macrocycles....134

Figure 5.2 Porous structures via coordination to metal ions..........135

Figure 5.3 Porous metal–organic frameworks..........136

Figure 5.4 Porous solids via a “molecular tectonics” approach..........137

Figure 5.5 Porous structures through the use of macrocyclic ligands.......................... 137

Figure 5.6 (Top) ORTEP drawing of porous assembly **508**. (Bottom) Alternate view... 147

Figure 5.7 (Top) Crystal packing diagram of assembly **508** as viewed down the *a*–axis. (Bottom) Alternate view down the *c*–axis. Thermal ellipsoids are drawn at the 20% probability level; solvent and associated triflate anions have been omitted, for clarity... 149

Figure 5.8 ORTEP drawing of assembly **508** showing six of the eight co–crystallized solvent molecules. (Top) View down the *a*–axis showing two molecules of solvent in channel. (Bottom) View down the *c*–axis showing six molecules of solvent in channel.. 151

Figure 5.9 Variable temperature hyperpolarized ^{129}Xe NMR spectra of porous assembly **508** at 55 MHz... 154

Figure 5.10 Variable temperature hyperpolarized ^{129}Xe NMR spectra of porous macrocycle **216c** at 55 MHz.. 159

Figure 5.11 Variable temperature hyperpolarized ^{129}Xe NMR spectra of porous macrocycles **206c**, **216c**, and **305c** at 55 MHz.. 161

Figure 5.12 Hyperpolarized ^{129}Xe EXSY spectra (55 MHz) of porous solid **305c** at 20 °C (left) and –58 °C (right), with mixing times as indicated... 162

Figure 5.13 (Left) Schematic representation of a 1 × 1 × 1 array of unit cells of **216c** viewed down the *a*–axis. (Right) Schematic diagram showing pathway of xenon gas within the pore structure of the organic macrocycle **216c**. View shown follows the *c*–axis of a 1 × 1 × 1 array of unit cells of **216c**......165

Figure 5.14 Variable temperature hyperpolarized ^{129}Xe NMR spectra of platinacycle **402** at 55 MHz......166

Figure 5.15 Schematic representation of the crystal packing diagram of **402**. Shown is a 1 × 2 × 1 array of unit cells of **402** viewed down a line between the *b*– and *c*–axes. The "zig–zag" channel traversed by the xenon gas is represented by circles and ellipses......168

Figure 5.16 Variable temperature hyperpolarized ^{129}Xe NMR spectra (55 Mz) of platinacycles **403a** and **403b**......170

Figure 5.17 Schematic representation of the crystal packing diagram of **403a**. Shown is a 2 × 2 × 2 array of unit cells as viewed down the *a*–axis. A representation of the void space (when co–crystallized solvent is removed) present within the crystal lattice is shown in light blue......171

Figure 5.18 Schematic representation of location of channel (shown by ellipse) in the solid–state structure of **403b**. Shown is a 1 × 1 × 1 array of unit cells of **403b** as viewed down the *b*–axis......173

Figure 6.1 Schematic illustration showing cross–linking of platinum acetylide macrocycles......179

Figure 6.2 Formation of *cis*–chelated platinum acetylide complexes......180

Figure 6.3 Schematic representation of the formation of strained macrocyclic butadiynes from *cis*–platinum acetylide complexes......181

Figure 6.4 Construction of *cis*–chiral platinum acetylide complexes......182

Figure 6.5 $^{31}P\{^1H\}$ NMR spectra (162 MHz, CD_2Cl_2) following the reaction of **402** with dppee to form **608**. (Top) NMR spectrum of *trans*–macrocycle **402**; (Middle) NMR spectrum of the reaction mixture after 4 hours. (Bottom) NMR spectrum of *cis*–complex **608**....................188

Figure 6.6 ORTEP drawing of *trans*–$(Ph_3P)_2Pt(C{\equiv}C–Si\textit{i}–Pr_3)_2$, **602a**. Thermal ellipsoids are drawn at the 20% probability level....................191

Figure 6.7 ORTEP drawing of *trans*–$(Ph_3P)_2Pt(C{\equiv}C–\textit{p}–CN–C_6H_4)_2{\bullet}(CH_2Cl_2)_2$, **602b**. Thermal ellipsoids are drawn at the 20% probability level. Solvent has been omitted, for clarity....................192

Figure 6.8 ORTEP drawing of *trans*–$(Ph_3P)_2Pt(C{\equiv}Cpyr–\textit{meta}–(C{\equiv}CSi\textit{i}–Pr_3))_2$, **602c**. Thermal ellipsoids are drawn at the 20% probability level....................192

Figure 6.9 ORTEP drawing of *cis*–(dppee)$Pt(C{\equiv}C–Si\textit{i}–Pr_3)_2$, **610a** (Molecule A). Thermal ellipsoids are drawn at the 20% probability level....................193

Figure 6.10 ORTEP drawing of *cis*–(dppee)$Pt(C{\equiv}C–\textit{p}–CN–C_6H_4)_2{\bullet}CH_2Cl_2$, **610b**. Thermal ellipsoids are drawn at the 20% probability level. Solvent has been omitted, for clarity....................193

Figure 6.11 ORTEP drawing of complex **608**. Two molecules of co–crystallized $ClCH_2CH_2Cl$ and one molecule of water, and all but the *ipso* carbon atoms of the phenyl groups were removed, for clarity....................195

Figure 6.12 (Top) ORTEP drawing of *trans*-platinacycle **616**. (Bottom) Alternate view....................200

Figure 6.13 $^{31}P\{^1H\}$ NMR spectra (162 MHz, CD_2Cl_2) following the reaction of **402** with (*S,S*)–Chiraphos to form **614**. (Top) NMR spectrum of *trans*–macrocycle **402**.

(Middle) NMR spectrum of the reaction mixture after 48 hours. (Bottom) NMR spectrum of *cis*–chiral complex **614**..203

Figure 6.14 Schematic representation of two chiral conformations adopted by (*S,S*)–Chiraphos...204

Figure 6.15 ORTEP drawing of **612**..205

Figure 6.16 ORTEP drawing of molecule A of **614**...207

Figure 6.17 UV-vis absorption spectra for *cis*–chiral complexes in CH_2Cl_2...............209

Figure 6.18 CD spectra for *cis*–chiral complexes in CH_2Cl_2..211

Figure 6.19 Proposed synthesis of cross–linked species **622**.....................................212

Figure 7.1 Installation of metal species in the channels of **216c**.................................218

Figure 7.2 Formation of helical secondary structure through treatment of polymer/oligomer **706** with an enantiopure chelating phosphine ligand......................220

Figure 7.3 Illustration of cross–linking at the platinum acetylide centre.....................220

List of Schemes

Scheme 1.1 Use of a dicarboxylate template to synthesize shape–persistent macrocycle **112**....12

Scheme 1.2. Metal–templated synthesis of oligothiophene macrocycle **115**....14

Scheme 1.3 Synthesis of thiophene–containing macrocycle **118**....15

Scheme 1.4 Synthesis of unsymmetrical, thiophene–containing cyclophane **121b**....16

Scheme 1.5 Synthesis of pyridine–containing macrocycle **124**....18

Scheme 1.6 Preparation of rhenium complexes **130a** and **130b**....21

Scheme 1.7 Synthesis of bipyridine–containing macrocycle **136** via zirconocene–coupling strategy....25

Scheme 1.8 Metal–templated synthesis of phenanthroline–containing helical macrocycle **142**....28

Scheme 2.1 Synthesis of acyclic oligomers **204b** and **205b**....38

Scheme 2.2 Attempted synthesis of macrocycles **206b** and **207b**....39

Scheme 2.3 Synthesis of macrocycle **206c** featuring a *meta*–diethynylbenzene subunit....40

Scheme 2.4 Synthesis of macrocycles **210a** and **210b** featuring *para*–diethynylbenzene subunit....42

Scheme 2.5 Synthesis of helically chiral macrocycle **213**, featuring 1,2–diethynylbenzene subunit....45

Scheme 2.6 Attempted synthesis of macrocycle **216a**....48

Scheme 2.7 Synthesis of pyridine–containing macrocycle **216c**....50

Scheme 3.1 Synthesis of pyridine–containing oligomers **302a–c**, **303b**, and **303c**.......63

Scheme 3.2 Synthesis of expanded pyridine macrocycles **304b**, and **304c**....................64

Scheme 3.3 Synthesis of bidentate macrocycle **305a**..66

Scheme 3.4 Synthetic efforts toward macrocyclic ligand **305b**....................................67

Scheme 3.5 Synthesis of diphenylalkylidene–substituted macrocycle **305c**..................69

Scheme 3.6 Synthesis of supramolecular assemblies **308b** and **308c**............................73

Scheme 3.7 Synthesis of supramolecular assemblies **309a** and **309c**............................75

Scheme 3.8 First synthetic efforts toward bidentate macrocycle **310**............................93

Scheme 3.9 Synthesis of oligomeric precursors **316**, **317**, and **318**...............................95

Scheme 3.10 Attempted synthesis of bidentate macrocycle **310**....................................96

Scheme 3.11 Synthesis of assembly **320**...97

Scheme 4.1 Synthesis of platinacycle **402**..106

Scheme 4.2 Synthesis of bidentate platinacycles **403a** and **403b**.................................108

Scheme 4.3 Synthesis of coordination compounds **404** and **405**.................................110

Scheme 4.4 Synthesis of coordination complex **406**..113

Scheme 5.1 Synthesis of porous assembly **508**..141

Scheme 5.2 Attempted synthesis of larger assemblies **509a** and **509b**.........................143

Scheme 5.3 Attempted synthesis of assembly **511**...144

Scheme 6.1 Treatment of macrocycle **402** with diphosphine ligands..........................183

Scheme 6.2 Synthesis of *cis*–macrocycle **608**..185

Scheme 6.3 Synthesis of *trans*– and *cis*–bis(alkynyl)platinum complexes..................186

Scheme 6.4 Synthesis of *cis*–platinacycle **611**..190

Scheme 6.5 Synthesis of *cis*–chiral complex **612**...196

Scheme 6.6 Synthesis of *cis*–chiral complex **613**..........197

Scheme 6.7 Synthesis of chiral pyridine–containing macrocycles **614** and **615**..........198

Scheme 6.8 Synthesis of chiral platinacycle **617**..........199

Scheme 6.9 Synthesis of chiral platinum-dehydrobenzannulene complex **619**..........201

Scheme 6.10 Synthesis of chiral platinacycle **620** featuring (*R*,*R*)–Chiraphos..........202

Scheme 7.1 Proposed synthesis of alkynyl iodides **702**..........217

Scheme 7.2 Preparation of *cis*–chiral acetylide complexes using alternate chiral diphosphines..........219

List of Abbreviations

Ac	acetate
Aq	aqueous
BET	Brunauer–Emmet–Teller
Bn	benzyl
bpy	bipyridine
Bu	*n*–butyl
CD	circular dichroism
Chiraphos	2,3–bis(diphenylphosphino)butane
cm	centimeter
Cp	cyclopentadiene
CP	cross–polarization
d	doublet
dec	decomposition
DMF	*N,N*–dimethylformamide
DOKE	differential optical Kerr effect
dppee	bis(diphenylphosphino)ethylene
dppm	bis(diphenylphosphino)methane
dppp	bis(diphenylphosphino)propane
dpppn	bis(diphenylphosphino)pentane
EI	electron ionization
Et	ethyl

ESI	electrospray ionization
exc	excitation
EXSY	exchange spectroscopy
g	gram(s)
h	hours
Hex	hexyl
Hfac	1,1,1,5,5,5–hexafluoro–2,4–pentanedione
HOMO	highest occupied molecular orbital
HOPG	highly oriented pyrolitic graphite
HRMS	high resolution mass spectrometry
Hz	hertz
i	iso
IR	infrared
LUMO	lowest unoccupied molecular orbital
m	multiplet
M	Molar
MALDI	matrix–assisted laser desorption ionization
MAS	magic angle spinning
Me	methyl
MHz	megahertz
mL	milliliter
MLCT	metal–to–ligand charge–transfer
mmol	millimole

MOF	metal–organic framework
MOM	methoxymethyl
Mp	melting point
MS	mass spectrometry
NLO	nonlinear optical
nm	nanometer
NMR	nuclear magnetic resonance
oct	octyl
ORTEP	Oak Ridge thermal ellipsoid plot
OTf	triflate ($–OSO_2CF_3$)
PDA	polydiacetylene
Ph	phenyl
ppm	parts per million
Pr	propyl
pyr	pyridine
q	quartet
rt	room temperature
STM	scanning tunneling microscopy
t	triplet
TBAF	tetrabutylammonium fluoride
t–Bu	tertiary–butyl
THF	tetrahydrofuran
THP	tetrahydropyran

TLC	thin layer chromatography
TMEDA	*N,N,N′,N′*–tetramethylethylenediamine
TOF	time of flight
TPP	tris(*o*–phenylenedioxy)cyclophosphazene
UV–vis	ultraviolet–visible

List of Symbols

Å	angstrom
δ	chemical shift
γ	molecular second hyperpolarizability
ε	molar absorptivity
λ_{max}	wavelength of maximal absorption

List of Name Reactions

Breslow Acetylenic Coupling

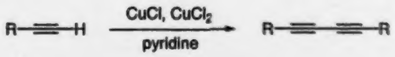

$$R{-}{\equiv}{-}H \xrightarrow[\text{pyridine}]{\text{CuCl, CuCl}_2} R{-}{\equiv}{-}{\equiv}{-}R$$

O'Krongly, D.; Denmeade, S. R.; Chiang, M. Y.; Breslow, R. *J. Am. Chem. Soc.* **1985**, *107*, 5544–5545.

Eglinton Acetylenic Coupling

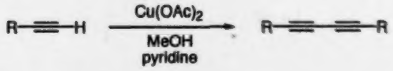

$$R{-}{\equiv}{-}H \xrightarrow[\substack{\text{MeOH}\\ \text{pyridine}}]{\text{Cu(OAc)}_2} R{-}{\equiv}{-}{\equiv}{-}R$$

Eglinton, G.; Galbraith, A. R. *Chem. Ind. (London)* **1956**, 737–738.

Glaser Acetylenic Coupling

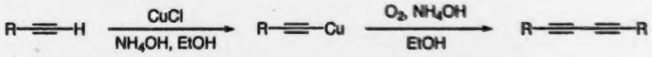

$$R{-}{\equiv}{-}H \xrightarrow[\text{NH}_4\text{OH, EtOH}]{\text{CuCl}} R{-}{\equiv}{-}Cu \xrightarrow[\text{EtOH}]{\text{O}_2\text{, NH}_4\text{OH}} R{-}{\equiv}{-}{\equiv}{-}R$$

(a) Glaser, C. *Ber. Dtsch. Chem. Ges.* **1869**, *2*, 422–424. (b) Glaser, C. *Ann. Chem. Pharm.* **1870**, *154*, 137–171.

Hay Acetylenic Coupling

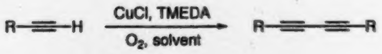

$$R{-}{\equiv}{-}H \xrightarrow[\text{O}_2\text{, solvent}]{\text{CuCl, TMEDA}} R{-}{\equiv}{-}{\equiv}{-}R$$

Hay, A. S. *J. Org. Chem.* **1962**, *27*, 3320–3321.

Sonogashira–Hagihara Cross–Coupling

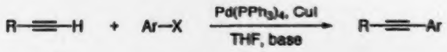

$$R{-}{\equiv}{-}H + Ar{-}X \xrightarrow[\text{THF, base}]{\text{Pd(PPh}_3)_4\text{, CuI}} R{-}{\equiv}{-}Ar$$

Sonogashira, K.; Tohda, Y. Hagihara, N. *Tetrahedron Lett.* **1975**, 4467–4470.

Stille Coupling

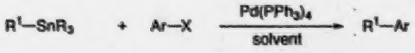

$$R^1\text{—}SnR_3 + Ar\text{—}X \xrightarrow[\text{solvent}]{Pd(PPh_3)_4} R^1\text{—}Ar$$

Stille, J. K. *Angew. Chem., Int. Ed. Engl.* **1986**, *25*, 508–523.

Suzuki Coupling

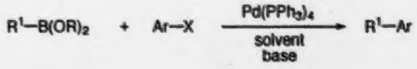

$$R^1\text{—}B(OR)_2 + Ar\text{—}X \xrightarrow[\substack{\text{solvent}\\ \text{base}}]{Pd(PPh_3)_4} R^1\text{—}Ar$$

Miyaura, N.; Suzuki, A. *Chem. Rev.* **1995**, *95*, 2457–2483.

Williamson Synthesis

$$RONa + R^1X \longrightarrow ROR^1 + NaX$$

Williamson, A. W. *J. Chem. Soc.* **1852**, *4*, 229.

Chapter 1 Introduction to Functionalized, Shape–Persistent Macrocycles

1.1 Why Macrocycles?

Unsaturated macrocyclic structures have been capturing the imagination of chemists since the late 1950's when Sondheimer reported the groundbreaking discovery of acetylenic homocoupling[1] for the formation of cyclic polyacetylenes **101** and **102**.[2] With the realization of buckminsterfullerene and related carbon–rich nanostructures,[3] the last two decades in particular have witnessed an explosion of interest in the synthesis and study of highly unsaturated, cyclic, nanoscale architectures.[4]

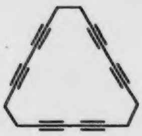

101

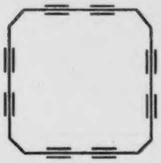

102

The realization of shape–persistent macrocycles has especially held a great deal of allure for synthetic chemists, due to the inherent challenges one faces when trying to access these elegant structures. In most cases, the synthesis of carbon–rich, macrocyclic structures relies on the judicious application of modern metal–mediated processes such as oxidative acetylenic homocoupling,[1] Sonogashira–Hagihara coupling,[5] Suzuki coupling,[6] Stille coupling,[7] and ring–closing metathesis.[8] These synthetic methods all favour a "building block" approach to the realization of unsaturated, cyclic structures. Some of the strategies that are applied to the synthesis of large cyclic structures are outlined in Figure 1.1. The first, so–called "shotgun" approach, uses a small readily available precursor to produce the targeted macrocycle in a single synthetic step where numerous coupling reactions, as well as the ring–closing event, occur within a single pot. Obviously, while this tactic has the attraction of a single step synthesis, it is also subject to a statistical mixture of products including various macrocyclic species as well as high molecular weight oligomers and polymers. An additional challenge is that these cyclic and acyclic byproducts often have similar properties (solubility, polarity) to that of the desired species, which may make purification onerous.

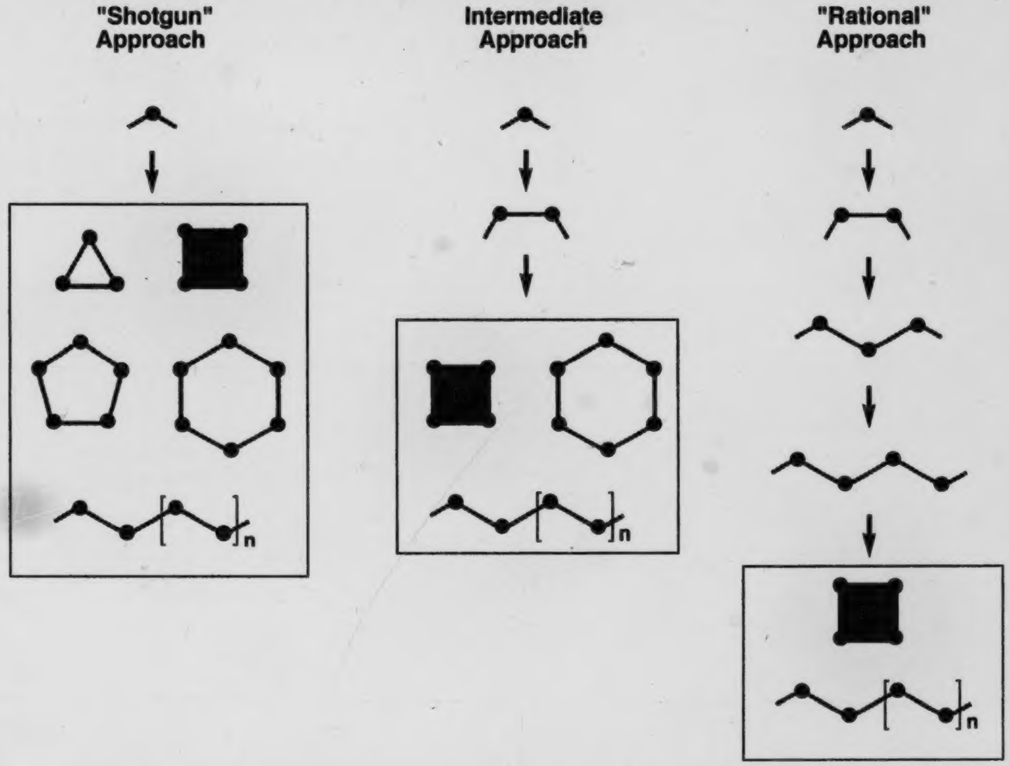

Figure 1.1 Schematic representations of synthetic approaches toward shape–persistent macrocycles.

An alternative, more rational approach can also be applied where the core structure is established through multiple chain elongation steps, followed by a single macrocyclization event. This approach often leads to much higher yields of the macrocyclization product in the final step but, due to entropic considerations, may also provide oligomeric/polymeric byproducts, an especially frustrating outcome in the final stage of a multi–step synthesis. Many chemists choose to adopt an intermediate approach to these syntheses, which may accomplish the two–fold task of minimizing the number of synthetic steps as well as the number of potential byproducts. It is important to note that the cyclization reaction can be further disfavoured when a strained macrocyclic product is targeted, biasing the statistical outcome, even under high dilution conditions. An additional consideration when outlining a synthetic approach is that of purification. In cases where a macrocyclic product is expected to possess limited solubility, it is even more desirable to reduce the number and/or quantity of byproducts formed, thus facilitating purification.

In addition to the synthetic challenges they represent, one of the simplest (and most honest) reasons why scientists target such structures is that they are aesthetically pleasing. For example, Haley and coworkers have realized the elegant "bow tie" and "pinwheel" dehydrobenzannulenes, **103** and **104**, in their quest for expanded graphdiyne substructures.[9]

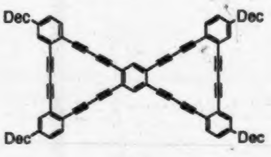

103

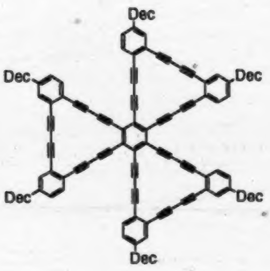

104

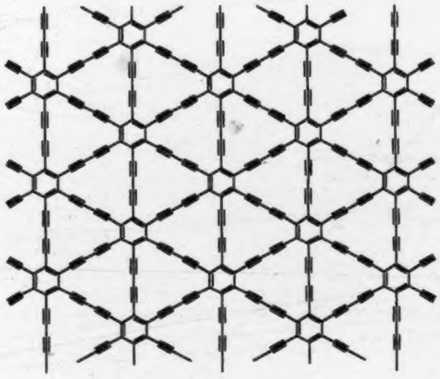

Graphdiyne

It is important to point out, however, that just because a macrocyclic structure is aesthetically pleasing does not mean that it is without function. In addition to the properties and functional groups present within the oligomeric precursor, upon macrocyclization two additional functionalities are introduced. First, the macrocyclic core that is established upon cyclization defines space as either inside the cavity or without. The size and shape of the cavity can be modified and, with appropriate derivatization, these two domains (interior and exterior) can possess dramatically different properties. The second consideration is that by definition, a shape–persistent macrocycle possesses a *non–collapsible* interior, such that functionality present within the cavity is held in a predefined arrangement. This is particularly intriguing as it allows for the selective *and* cooperative interaction of a host macrocycle with various guest species (Figure 1.2).

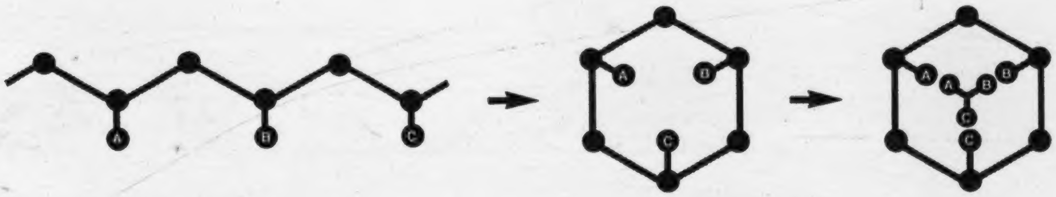

Figure 1.2 Schematic representation of the assembly of a shape–persistent macrocycle with a functionalized cavity.

The presence of rationally arranged functional groups on the periphery of a shape–persistent macrocycle also allows for the manipulation of intermolecular interactions. For example, suitable functionalization may promote the intermolecular aggregation of these species (Figure 1.3) and the subsequent formation of channel–containing solids. Porous solids are particularly desirable targets due to their potential as materials for gas capture and storage devices.[10]

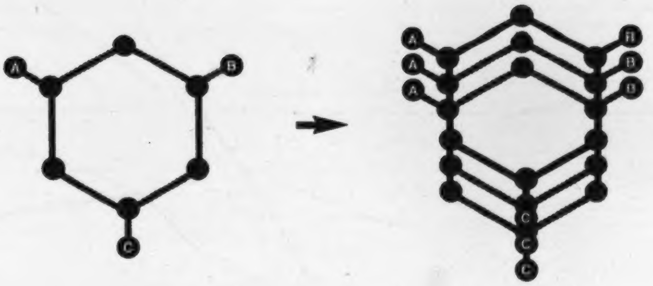

Figure 1.3 Schematic representation of the aggregation of a shape–persistent macrocycle with a functionalized periphery.

These desirable characteristics have inspired the development of numerous shape–persistent macrocycles that are tailored for specific applications. The work of Moore, Scott, Tobe, and Haley, among many others, has led to the realization of a vast array of carbon–rich macrocycles that are of interest due to their predictable functional properties. For example, the fascinating aggregation behaviour of phenylene–ethynylene macrocycles such as **105** has been intensely studied by Moore and coworkers.[11] These materials are potentially suitable for application as liquid–crystalline materials[12] and have been shown to form ordered monolayers.[13] Scott and coworkers have prepared and studied numerous pericyclynes such as **106**, to assess the importance of homoconjugation in these cyclic species.[14] The presence of a non–collapsible interior may also provide for the formation of extended tubular structures[15] and porous solids.[16] Carbon–rich macrocycles have also been realized as potential precursors for fullerenes and other carbon allotropes such as graphdiyne.[9a,17]

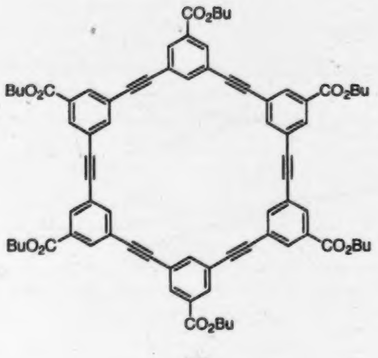

105

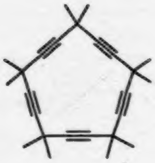

106

1.2 Synthesis and Properties of Shape–Persistent Macrocycles Containing Heteroatom Functionality

A recent and particularly active area of research has been the development of macrocyclic systems that contain heteroatom and heteroaromatic functionality.[18] Through the incorporation of heteroatoms or heteroaromatic groups it is possible to introduce or enhance the more desirable properties of a macrocyclic species. For example, the introduction of heteroatom or heteroaromatic functionality often leads to a macrocyclic product capable of selective host–guest interactions, either through coordination to a transition metal, or as a result of interaction between polar functional groups. This allows for more direct control of the aggregation properties of macrocyclic species, and thus, more robust channel–containing architectures may be achieved. Molecular wires constructed via the installation of metal centres within a macrocyclic cavity have also been envisioned. The presence of functionality within a shape–persistent cavity may also lead to the development of catalytic materials. Through the installation of appropriate coordinating groups, highly unsaturated cyclic chromophores may undergo conformational and/or electronic changes upon guest binding, which may lead to their application as sensory materials.

Described in this chapter are several significant and recent efforts toward the synthesis of shape–persistent macrocycles containing heteroatom and heteroaromatic functionality. The synthesis of cyclic compounds containing oxygen–based functionalities including phenols and carboxylates will be described, as well as several thiophene–containing derivatives. Numerous examples of pyridine–, bipyridine– and terpyridine–containing macrocyclic ligands are also available, and will be presented in the following discussion. The synthesis, binding ability, and interesting properties of this important class of cyclic molecules will be described, with an emphasis on cyclic structures which possess nanoscale dimensions. The discussion presented below is not intended to be a comprehensive review of the subject, and as such, only selected illustrative examples will be provided.

1.2.1 Oxaarenecyclynes and Macrocycles Containing Hydroxylic/Carboxylic Functionality

One of the simplest ways to visualize the placement of functionality into a macrocyclic structure is through the direct insertion of a heteroatom into the carbon–rich backbone of the macrocyclic core. Yoshida and coworkers have recently realized a series of oxaarenecyclynes, including **107** and **108**, based on diethynylbenzene subunits linked by ether moieties.[19] The synthesis of both macrocycles was achieved by multiple chain elongation steps followed by the application of a palladium–catalyzed cross–coupling reaction as the final, ring–closing step. This strategy was selected due to the relatively low yields of the Williamson reactions used to provide the ether linkages. Macrocycles **107** and **108** were thus achieved in 31 and 36% yield, respectively. X–ray crystallographic analysis of macrocycle **108** confirmed the planar, shape–persistent core and both macrocycles were shown through UV–vis analysis to form 1:1 "Saturn–type" complexes with C_{60} in solution.

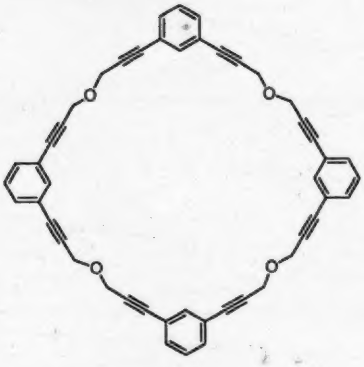

107

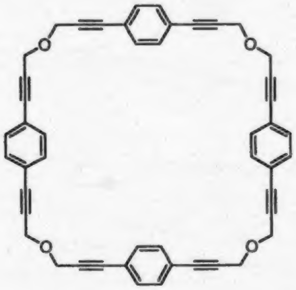

108

Rather than the direct installation of heteroatom functionality into the macrocyclic core, Höger and coworkers have instead adopted the approach of "decorating" the periphery of a macrocycle through the installation of alkyl, alkoxy, and phenolic hydroxy functionalities. In 1995, Höger reported the synthesis of macrocycle **109a**, which features both hydrophilic and hydrophobic domains.[20] Macrocycle **109a** was realized by protecting the phenolic hydroxyl groups of the aromatic building blocks as THP ethers, and removing them subsequent to the penultimate synthetic step. The cyclodimerization was achieved in greater than 60% yield, followed by quantitative removal of the hydroxyl–protecting groups. The macrocycle was readily soluble in pyridine, allowing for the growth of X–ray quality crystals of **109a** from this solvent. The solid–state structure of **109a** revealed that the phenol rings, which may freely rotate, had adopted a conformation such that they were all directed toward the exterior of the macrocycle. Furthermore, a total of eight pyridine molecules co–crystallized with each macrocyclic unit, and four of these solvent molecules had established hydrogen–bonding interactions with the phenolic hydroxy groups. The propyloxy side chains were present in the interior, hydrophobic region of the macrocycle.

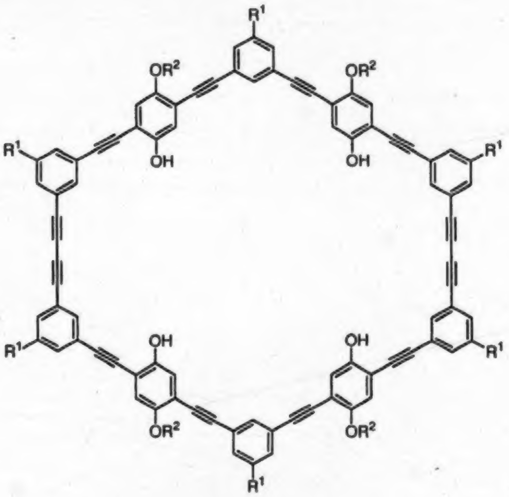

109a R^1 = Me, R^2 = Pr
109b R^1 = Me, R^2 = Hex
109c R^1 = *t*-Bu, R^2 = Hex

Höger and coworkers later established that in the presence of a suitable guest species, this macrocyclic conformation could be reversed, effectively 'switching' the hydrophilic and hydrophobic domains.[21] ^{1}H NMR binding studies showed that macrocycles **109b** or **109c** formed 1:1 complexes when treated with the rigid, tetraamine guest **110a** or **110b**. The binding constants were dependent on the size of the substituents on the amine guest, but the effects of larger substituents on the macrocyclic host were negligible, confirming that the host–guest event was occurring within the core of the macrocycle, rather than on the periphery.

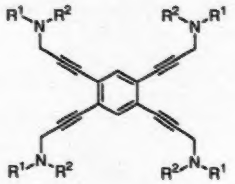

110a $R^1 = R^2 = Me$
110b $R^1 = Me, R^2 = Bn$

The ability of these amphiphilic macrocycles to switch conformational states based on the presence of external stimuli was confirmed by recent work by the same group.[22] When **109b** was crystallized from pyridine, the solid–state structure revealed that two of the phenolic hydroxy groups were directed toward the centre of the macrocyclic cavity, with the remaining two hydroxy groups directed toward the exterior. All four phenolic hydroxy groups had established hydrogen–bonds to four of the six co–crystallized pyridine solvent molecules. The authors suggest that this conformation of **109b** is the result of the incorporation of the more sterically–demanding hexyloxy side chains, versus the propyloxy side chains of **109a**, which all occupy space within the macrocyclic core. When the same macrocyclic species **109b** was crystallized in the presence of THF, a conformation was adopted in the solid–state where all four of the phenolic hydroxy groups were directed toward the interior of the conjugated macrocycle. The macrocycle **109b** co–crystallized with 12 molecules of THF, all of which occupy space within the macrocyclic cavity. Four of these solvent molecules are hydrogen–bonded to the hydroxyl groups. The use of the solvent to trigger this conformational change resulted in a large cavity at the centre of the macrocyclic species. This cavity is translated into large channels (ca. 8 by 10 Å) in the solid–state structure of **109b** upon aggregation and eclipsed packing of the macrocyclic species. These nanoscale channels may be suitable for specific host–guest interactions due to the presence of the four phenolic functionalities.

Höger and coworkers have taken advantage of the presence of polar functional groups and exploited them as sites for the attachment of templating groups, as shown in Scheme 1.1.[23] The branched oligomer **111** was synthesized by performing four simultaneous Sonogashira–Hagihara cross–coupling reactions at the bonds indicated in Scheme 1.1. The triisopropylsilyl–protected oligomer **111** was realized in a remarkable 90% yield and, subsequent to desilylation, was treated under acetylenic homocoupling conditions. This led to the formation of macrocycle **112** in an astounding 92% isolated yield. The templating biphenyl dicarboxylate was easily removed upon saponification. Moreover, in the same communication, the authors demonstrated that through the use of an unsymmetrical template, they could access macrocyclic species containing two *different* functional groups directed toward the core.

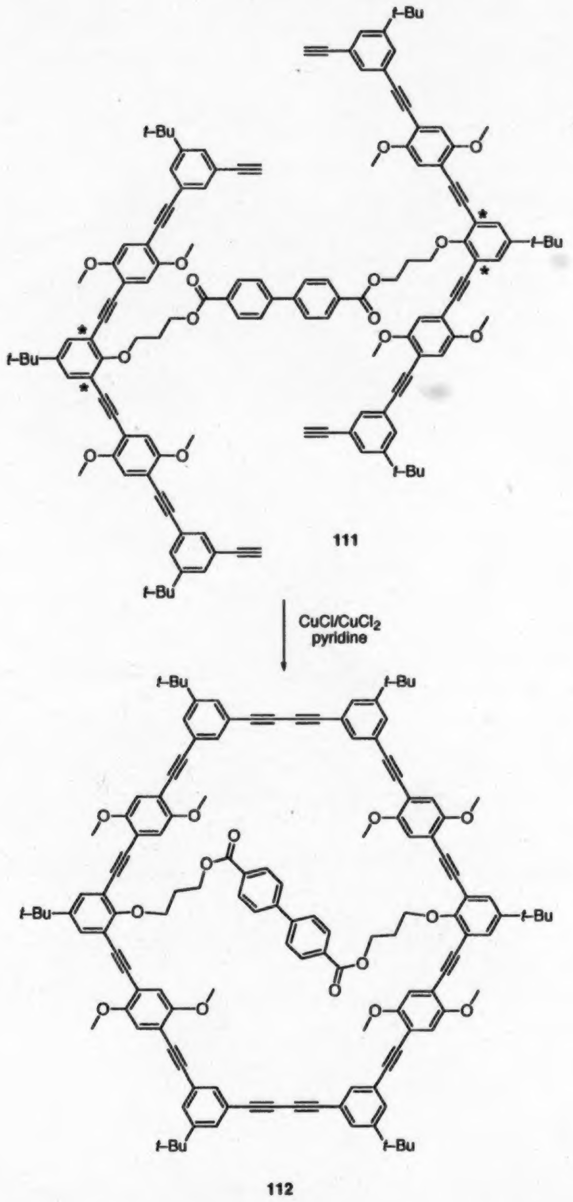
t-Bu
111
CuCl/CuCl$_2$
pyridine

112

Scheme 1.1 Use of a dicarboxylate template to synthesize shape–persistent macrocycle **112**.

1.2.2 Shape–Persistent Macrocycles Based on Thiophenes

Other authors have also exploited the presence of templating groups for the synthesis of shape–persistent macrocycles containing heteroaromatic groups. These strategies have been especially well adapted to the synthesis of cyclic oligothiophenes and thiophene–containing macrocycles. Bäuerle and co–workers have recently established that strained thiophene–containing macrocycles are accessible through the strategy outlined in Scheme 1.2.[24] The *cis*–platinum acetylide macrocycle **113** was prepared using established methods in 91% yield. Forcing reductive elimination at the metal centre by treatment with iodine led to the formation of the strained butadiyne macrocycle **114** in 54% yield. Previous attempts to synthesize this macrocycle using traditional acetylenic homocoupling strategies had been completely unsuccessful, likely due to the high degree of strain present within this macrocyclic product. X–ray crystallographic analysis confirmed the highly strained (yet planar) structure of **114** with the minimum alkyne bond angle measured to be 160.3°. The macrocyclic precursor **114** was then converted to the desired cyclo–oligothiophene **115** in 19% yield. The authors attribute the relatively modest yield to a combination of ring strain in the precursor and the need for extremely high temperatures to effect this transformation. These two factors likely contribute to the partial decomposition of macrocycle **114**.

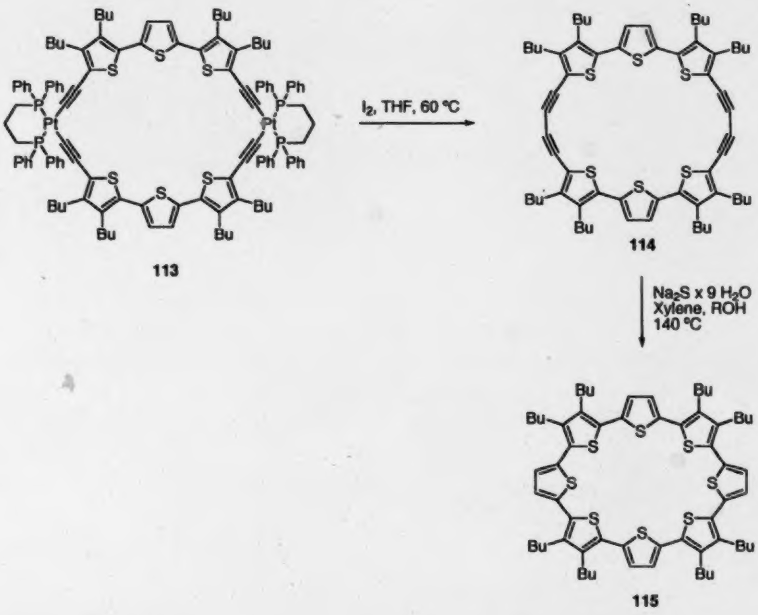

Scheme 1.2. Metal–templated synthesis of oligothiophene macrocycle **115**.

Macrocycle **115** represents the smallest member of the family of cyclo–oligothiophenes prepared to date. In previous work, Bäuerle and coworkers described the construction of several larger oligothiophenes **116a–c** using the more traditional approach of acetylenic homocoupling to access the butadiynyl precursors.[25] These macrocycles and their butadiyne–containing precursors have been intensely studied and these species have been shown to form ordered layers on a highly oriented pyrolitic graphite (HOPG) surface through extensive scanning tunneling microscopy (STM) measurements.[26] All of these macrocycles have central cavities in the nanometer regime that may be suitable for guest complexation.

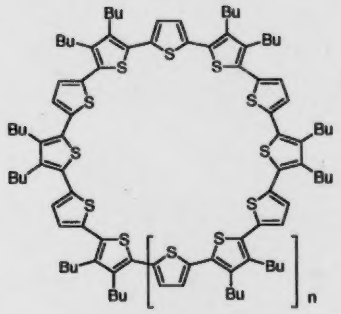

116a n = 1
116b n = 3
116c n = 4

In addition to the cyclic oligothiophenes, cyclophanes containing alternating thiophene moieties in combination with other aromatic rings have also been prepared. For example, Tobe and coworkers recently reported the synthesis of macrocycle **118** in 83% yield, achieved by treatment of the butadiyne–containing precursor **117** with sodium sulfide, in the presence of a crown ether (Scheme 1.3).[27] The interesting cyclic precursor, **117**, was realized in 73% yield via a single, ring–closing, acetylenic homocoupling reaction of the corresponding oligomeric octayne.

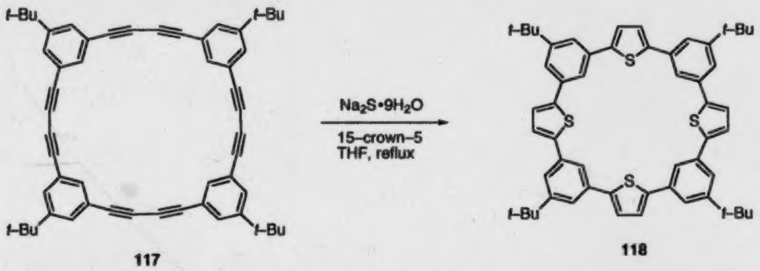

Scheme 1.3 Synthesis of thiophene–containing macrocycle **118**.

In an interesting communication, Marsella and coworkers exploited perfluorophenyl–phenyl quadrupole interactions to template the synthesis of a thiophene–containing cyclophane.[28] As shown in Scheme 1.4, the authors found that the mixed perfluorophenyl–phenyl cyclophane **121b** was reproducibly achieved in greater yield than either of the symmetrical analogues **121a** and **121c** when the oligomeric precursors were treated with Sonogashira cross–coupling conditions (**119a** + **120a** → **121a**, **119b** + **120b** → **121c**, **119a** + **120b** → **121b**). Other mixed macrocyclic derivatives were also prepared and their findings with these model systems support the argument that electrostatics are responsible for the self–assembly of the two coupling partners, leading to higher yields of the non–symmetrical product.

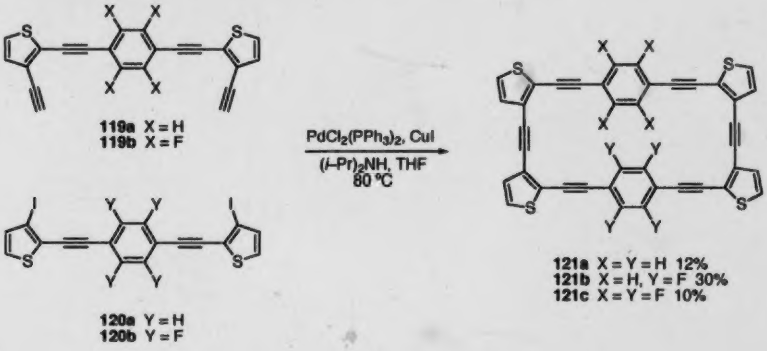

Scheme 1.4 Synthesis of unsymmetrical, thiophene–containing cyclophane **121b**.

A mixed heterocyclic macrocycle, **122**, was recently prepared by Baxter.[29] The helical macrocycle **122** was targeted due to the presence of both electron rich and electron poor heterocyclic rings. Compound **122** was achieved in relatively high yield (46%) via a copper–mediated acetylenic cyclo–dimerization. The author established, through extensive UV–vis absorption and fluorescence binding studies, that macrocycle **122** coordinates selectively to the following metals ions: silver (I), cobalt (II), nickel (II), and palladium (II). Significant differences in the absorption and emission spectra were observed for **122** in the presence of these metal ions, compared to that of the free ligand, demonstrating the potential utility of these species for sensory applications. Intriguingly, in the presence of high concentrations (4 equivalents) of silver (I), nickel

(II), and cobalt (II) ions, the precipitation of what were likely high molecular weight coordination polymers was also observed.

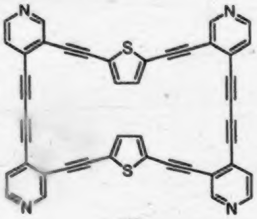

122

1.2.3 Shape–Persistent Macrocycles Containing Nitrogen–Based Heterocycles

Shape–persistent macrocycles featuring pyridine, bipyridine, and related nitrogen–based heterocycles are among the most prolific functionalized macrocycles of this class. This is due, for the most part, to the well–established ability of pyridine–based ligands to coordinate to transition metal centres.

Yoshida and coworkers have reported the synthesis of pyridinophane **124** based on the incorporation of four 2,6–diethynylpyridine units directed toward the centre of the macrocycle.[30] Macrocycle **124** was achieved in modest yield (35% over three steps) via a single, ring–closing cross–coupling reaction of the corresponding oligomeric precursor **123**. The coordinative ability of the endotopic pyridines was demonstrated by the preparation of a copper (II) coordination complex, achieved via the treatment of **124** with $[Cu(hfac)_2]^{2+}2(X^-)$ (hfac = 1,1,1,5,5,5–hexafluoro–2,4–pentanedione). X–ray crystallographic analysis of the complex showed that the planar macrocycle **124** had coordinated to two copper species, which occupy space in the central cavity of the macrocycle. This central cavity possesses a diameter of ~1 nm. Interestingly, the complex **124**•2(Cu(hfac)$_2$) was shown to be a remarkably strong fluorescence emitter despite the known propensity of copper (II) ions to quench fluorescence.

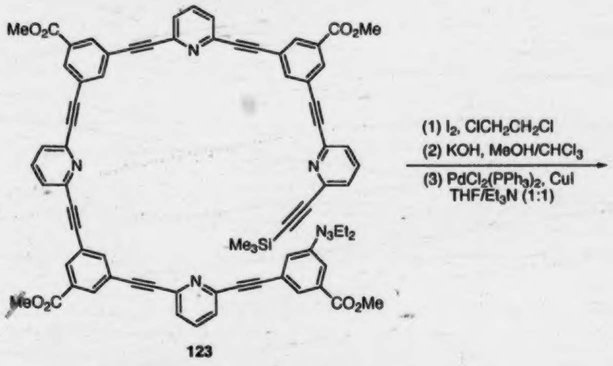
MeO2C
CO2Me
N
N
N
Me3Si
N3Et2
MeO2C
CO2Me
123
(1) I2, ClCH2CH2Cl
(2) KOH, MeOH/CHCl3
(3) PdCl2(PPh3)2, CuI
THF/Et3N (1:1)
MeO2C
CO2Me
N
N
N
N
MeO2C
CO2Me
124

Scheme 1.5 Synthesis of pyridine–containing macrocycle **124**.

Tobe and coworkers have prepared the analogous butadiyne–bridged pyridinophanes, **125** and **126**.[31] These macrocycles, **125** and **126**, were synthesized via a step–wise approach and were ultimately achieved in yields of 50 and 29% in the final, ring–closing step, respectively. The ability of these macrocycles, which feature endotopic binding sites, to associate with cationic guests was evaluated. When treated with the tropylium cation, the cyclic species **125** and **126** were shown to form 1:1 and 2:1 complexes with the organic guest, as established by ^{1}H NMR titration experiments.

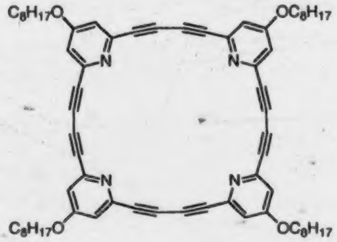
C8H17O
OC8H17
N
N
N
N
C8H17O
OC8H17

125

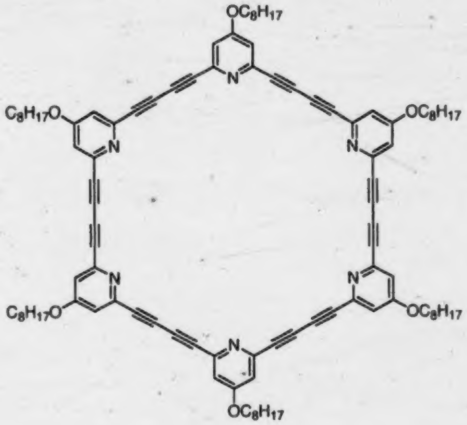
OC8H17
N
C8H17O
OC8H17
N
N
N
N
C8H17O
OC8H17
N
OC8H17

126

The unfunctionalized analogue of macrocycle **126**, the phenylacetylene macrocycle **127a**, as well as the cyano–functionalized derivative **127b** were also prepared by Tobe et al.[32] The aggregation properties of all three macrocyclic species **126**, **127a**, and **127b** were evaluated via concentration–dependent ^{1}H NMR spectroscopy. It was found that only the unfunctionalized derivative **127a** showed a tendency to self–aggregate in solution. The authors suggest that self–aggregation in the cases of **126** and **127b** is disfavoured due to electrostatic repulsion between nitrogen atoms of the pyridine and cyano groups, respectively. However, both the pyridine– and cyano–containing analogues **126** and **127b** form heterodimers with cyclophane **127a** and, in the case of **126**, higher aggregates are also observed. It is worth noting that **127b**, like the pyridine–containing derivative, was shown to bind cationic organic guests.

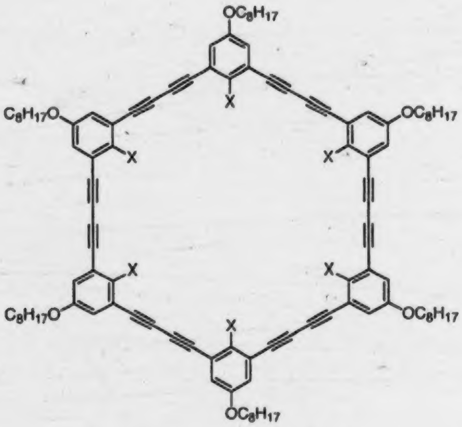

127a X = H
127b X = CN

Recently, the synthesis of a cyclo–oligopyrrole macrocycle, analogous to the oligothiophene derivatives described earlier, was reported by Sessler and coworkers.[33] The expanded porphyrin macrocycle **128** was realized in a remarkable 79% yield via the one–pot oxidative coupling of bipyrrole. Macrocycle **128** was formally isolated as the dihydrogen sulfate salt, and X–ray crystallographic confirms the near–planarity of the macrocyclic system. The sulfate ion is present in the centre of the cavity and is in hydrogen bond contact with all eight of the protonated pyrrole nitrogens via all four of the oxygen atoms. The authors suggest that this cationic host is potentially suitable for application as an anionic receptor. The UV–vis spectrum of macrocycle **128** was particularly interesting and showed an extremely strong and red–shifted Q–type absorption at ca. 1100 nm that is unusually greater in intensity than the Soret–like band.

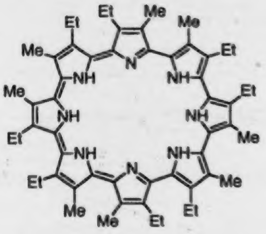

128

Macrocyclic derivatives featuring heteroaromatic groups directed away from the central cavity have also been realized. For example, Lees and coworkers have reported the synthesis of phenylacetylene macrocycles incorporating 3,5–diethynylpyridine subunits.[34] Macrocycles **129a** and **129b** were realized via intermolecular cross–coupling and oxidative homocoupling methodologies, respectively (Scheme 1.6). The macrocycles **129a** and **129b** were achieved in 54 and 32% yields, respectively, and their transition metal complexes **130a** and **130b** were prepared by treating with $(CH_3CN)Re(CO)_3(4,4'\text{–}t\text{–}Bu_2bpy)(PF_6)$ at elevated temperatures for a period of 1–3 days. The aggregation properties of ligands **129a** and **129b** were evaluated via variable concentration ^{1}H NMR spectroscopy and it was established that there is no aggregation of the cyclic species in the ground state. However, concentration–dependent fluorescence emission spectroscopy measurements indicated that the macrocycles **129a** and **129b** self–associate in the excited state, leading to excimer emission. The complexes **130a** and **130b** are also highly emissive but show no tendency to self–aggregate in either the ground or excited state.

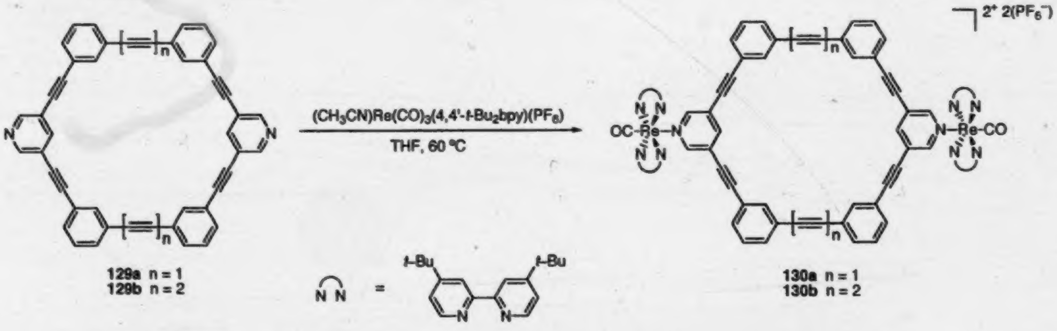

Scheme 1.6 Preparation of rhenium complexes **130a** and **130b**.

Baxter has also realized a pyridine–containing cyclophane **131**, featuring enforced exotopic binding sites.[35] Macrocycle **131** was achieved in a remarkable 71% yield via intermolecular oxidative cyclodimerization, using Hay conditions,[36] of the respective terminal diynes. Calculations showed that the energy–minimized structure of **131** is twisted such that a helically chiral conformation is realized. The ability of the fully conjugated macrocycle **131** to coordinate to transition metal ions was evaluated, and it was found that the fluorescence emission of the macrocycle is quenched upon coordination to palladium (II) or mercury (II) salts. The ability of macrocycle **131** to act as a sensor for metal ions was further established by the observation that the selective precipitation of coordination polymers occurs when **131** is treated with iron (II), cobalt (II), nickel (II), or silver (I) salts.

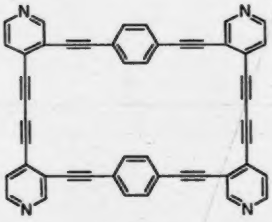

131

Baxter has also prepared a macrocyclic species **132**, based on the elaboration of a 2,2′–bipyridine subunit.[37] The cyclophane **132** was achieved in 34% yield, again through the use of Hay's oxidative homocoupling conditions. Variable temperature ^{1}H NMR studies allowed the author to suggest that the macrocycle **132** adopts a chirally twisted conformation where the two 2,2′–bipyridine moieties are in very close proximity. Upon heating, the possibility of interconversion between enantiomeric conformers exists, via an open, planar intermediate, leading to the variable temperature dependence observed. Furthermore, in the presence of an appropriate metal ion, the four nitrogens of the two bipyridine units may form a tetrahedral arrangement suitable for complexation. This would require conformational changes that could be sensed using UV–vis and/or fluorescence spectroscopies. Macrocycle **132** was found to bind specifically to copper (II), zinc (II), nickel (II), and cobalt (II) salts as observed through rigorous UV–vis absorption and fluorescence emission analysis. Baxter has also recently reported the synthesis and sensory properties of an analogous macrocycle **133** which features 2,2′–bipyridine integrated at the 6,6′ position.[38]

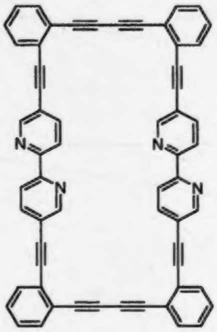

132

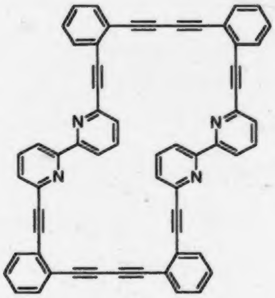

133

Several other research groups have also investigated the effects of incorporating 2,2′–bipyridine into the backbone of a shape–persistent macrocycle. This is due, in part, to the demonstrated ability of the bipyridine ligand to form robust transition metal complexes. An additional attraction is the fact that 2,2′–bipyridine can freely rotate, and thus coordinate to metal centres in an exo– or endo–topic fashion. The Schlüter group, in particular, has synthesized and intensely studied several bipyridine–containing phenylacetylene macrocycles.

Schlüter and coworkers have reported the syntheses of macrocycles **134a** and **134b,** which were achieved via Sonogashira cross–coupling at the indicated carbons.[39] The macrocycles **134a** and **134b** were isolated in 25 and 28% yield, respectively. X–ray crystallographic analysis confirmed the planar, shape–persistent core of **134b**. A total of four chloroform solvent molecules co–crystallized with **134b**, and two of these solvent molecules occupy space within the macrocyclic cavity, within hydrogen bonding distance (ca. 2.4 Å) of the pyridyl nitrogens. The macrocycles are stacked in the solid–state such that channels are realized, but the channels are significantly obscured by the presence of the alkoxy side chains. The hexyloxy side chains from one stacked column penetrate the channels of two adjacent columns.

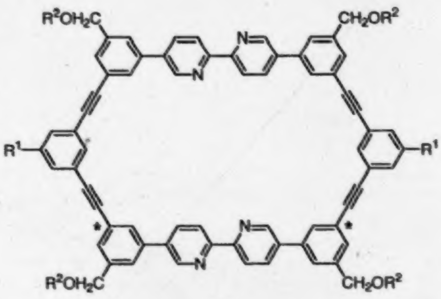

134a $R^1 = H$, $R^2 = Hex$
134b $R^1 = CH_2OHex$, $R^2 = MOM$
134c $R^1 = CH_2OHex$, $R^2 = THP$

Schlüter and coworkers later reported the synthesis of macrocycle **134c**, which features THP–protected alcohol functionalities potentially suitable for further elaboration.[40] Their attempts to remove the protecting group, however, resulted in the precipitation of what was presumably pyridinium salt(s) and, as a result, the authors were unable to confirm that the deprotection took place. They did, however, establish the ability of **134a** and **134c** to coordinate to transition metals through the preparation of two interesting ruthenium complexes. Treating the respective macrocycles with $Ru(bipy)_2Cl_2$, followed by anion exchange led to the formation of [**134a**$(Ru(bipy)_2)_2](PF_6)_4$ and [**134c**$(Ru(bipy)_2)_2](PF_6)_4$ in good isolated yields. Preliminary results suggested that removal of the THP ethers is possible when the 2,2′–bipyridine moieties are bound to ruthenium. The crystal structure of **134a** was also reported and like that of **134b**, the crystal packing diagram showed stacking such that channels were realized in the solid–state. Again, however, the resultant channels were obscured by the neighbouring hexyloxy side chains of adjacent columns.

2,2′–Bipyridine containing macrocycles have been reported by other groups, including that of Tilley, who used a zirconocene–coupling route for the formation of large, functionalized macrocycles such as **136**.[41] The zirconocene–containing precursor

135 was obtained in a remarkable 91% yield by treating the appropriate trimethylsilyl–protected diyne with $Cp_2Zr(pyr)(Me_3SiC{\equiv}CSiMe_3)$. Treatment of **135** with benzoic acid effects the protodemetalation, leading to the formation of macrocycle **136** in 88% yield. Single crystal X–ray crystallographic analysis of the zirconocene–containing precursor **135** confirmed the planar, cyclic structure.

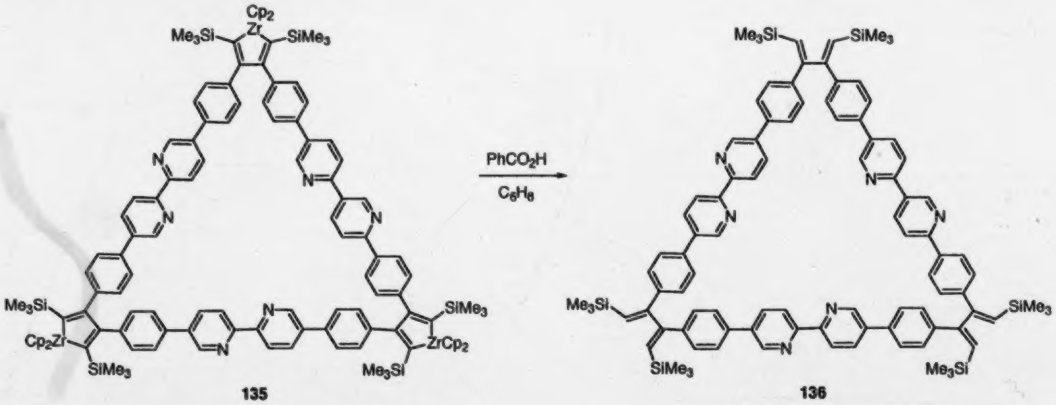

Scheme 1.7 Synthesis of bipyridine–containing macrocycle **136** via zirconocene–coupling strategy.

Macrocyclic systems featuring more complex pyridine–based ligands have also been achieved. For example, Schlüter and coworkers have reported the synthesis of an amazingly large collection of terpyridine–containing phenylethynylene macrocycles **137a–e** and **138a–e**.[42] While only two of these macrocycles was assembled in greater than 20% yield (macrocycles **137a** and **137b**), the authors note that many of the macrocyclic products possessed prohibitively low solubility in common organic solvents, which was likely a contributing factor to the low isolated yields of these species. X–ray crystallographic analysis was performed on three of the macrocycles containing a single terpyridine unit, **137a**, **137b**, and **137d**. The ORTEP drawing of **137a** shows that the macrocycle is in a near planar conformation with only one of the terpyridine rings tilted slightly out of the plane. Layers of the macrocycles are stacked atop one another in a slightly offset manner such that channels are realized, although the channels are not exactly perpendicular to the plane of the macrocyclic units. These channels are again obscured by the pendant hexyloxy side chains. Macrocycle **137b** has also adopted a planar conformation in the solid–state. Interestingly, the solid–state structure for **137d**, which features two hexyl side chains in the interior of the macrocycle, is remarkably different from those of **137a** and **137b**. The macrocycle is significantly distorted from planarity, but nevertheless provides columnar stacks in the solid–state. Again, however, these large cavities (>1 nm) are filled with the solubilizing side chains, as well as co–crystallized solvent molecules.

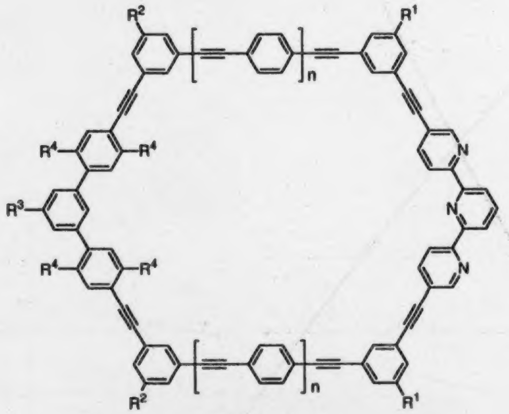

137a $n = 0$, $R^1 = R^2 = R^3 = OHex$, $R^4 = H$
137b $n = 0$, $R^1 = R^2 = CH_2OHex$, $R^3 = OHex$, $R^4 = H$
137c $n = 0$, $R^1 = CH_2OHex$, $R^2 = CH_2OTHP$, $R^3 = OHex$, $R^4 = H$
137d $n = 0$, $R^1 = R^2 = OHex$, $R^3 = H$, $R^4 = Hex$
137e $n = 1$, $R^1 = R^2 = CH_2OHex$, $R^3 = OHex$, $R^4 = H$

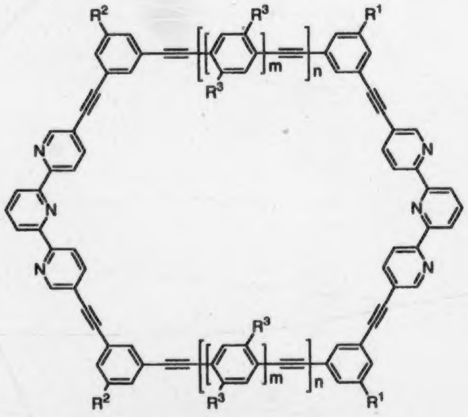

138a $n = m = 0$, $R^1 = R^2 = CH_2OHex$
138b $n = 1$, $m = 0$, $R^1 = R^2 = CH_2OHex$
138c $n = m = 1$, $R^1 = R^2 = CH_2OHex$, $R^3 = H$
138d $n = m = 1$, $R^1 = CH_2OHex$, $R^2 = CH_2OTHP$, $R^3 = H$
138e $n = m = 1$, $R^1 = R^2 = CH_2OHex$, $R^3 = Hex$

Baxter has also prepared a terpyridine–containing cyclophane **139**, which possesses pendant triisopropylsilyl–protected ethynes that fulfill a dual role of mediating solubility as well as providing a means for future elaboration.[43] Macrocycle **139** was achieved in 39% yield via an intermolecular oxidative homocoupling strategy. An examination of the electronic properties of **139** revealed that the macrocycle is strongly fluorescent, and shows no tendency to self–aggregate in either the ground or excited state.

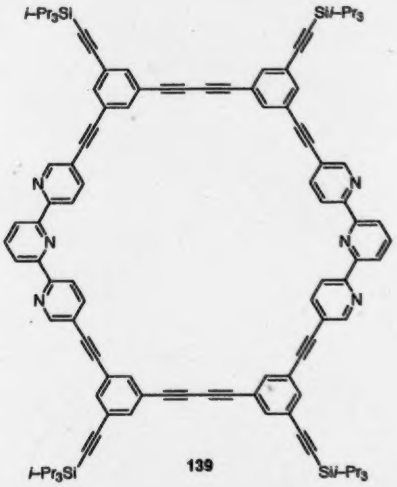

139

The phenanthroline subunit may also be applied to the synthesis of shape–persistent macrocycles, as recently demonstrated by the Fallis group.[44] $Cu(OAc)_2$ was used to template the formation, via oxidative homocoupling, of the helical cyclophane **142**. Compound **140** was treated with 0.5 equivalents of $Cu(OAc)_2$ in pyridine/diethyl ether for a period of 2 hours, followed by the addition of a further 5.5 equivalents of the copper salt. The synthesis of helical macrocycle **142** was achieved in a remarkable 70% yield upon treatment with potassium cyanide, which effects the release of the phenanthroline ligands. In addition to observed colour changes that suggested the presence of **141**, the authors provided confirmation of the formation of this intermediate by performing the analogous coupling reaction in a single step, by the direct addition of all 6 equivalents of the copper catalyst. These conditions provided **142** in only 15% yield, suggesting that the formation of the intermediate **141** is crucial in the step–wise synthesis.

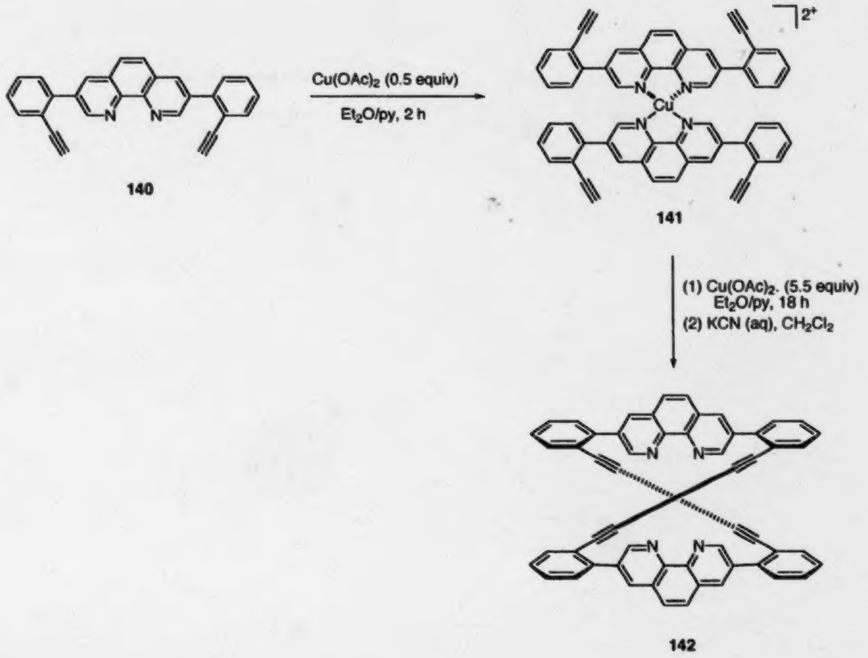

Scheme 1.8 Metal–templated synthesis of phenanthroline–containing helical macrocycle **142**.

1.3 Conclusions

The synthetic efforts of several research groups toward the realization of three major classes of heteroatom–containing shape–persistent macrocycles have been described. Many authors have adopted creative approaches to these syntheses, including a variety of templating strategies to combat the low yields that often accompany a macrocyclization reaction. In addition, several groups have demonstrated the potential of these derivatized carbon–rich macrocycles to serve as functional materials for several exciting applications. Many of the macrocyclic species described, due to the presence of polar functional groups, may function as materials for sensory applications, as porous solids and liquid crystalline materials.

Clearly, there is ample room for growth in this newly emerging area of research. There are still relatively few examples of shape–persistent macrocycles that were achieved in truly outstanding yields. This may be due to the fact that, as yet, no general templating strategies exist to aid in the exclusive formation of macrocyclic products. Additionally, in many cases, the functional groups that are installed to facilitate the synthesis, purification, and analytical characterization of these materials may also prove detrimental with respect to the functional properties that are intended. However, as we have seen, numerous research groups have been actively and creatively attempting to overcome these obstacles.

1.4 References and Notes

1. Siemsen, P.; Livingston, R. C.; Diederich, F. *Angew. Chem. Int. Ed.* **2000**, *39*, 2632–2657.
2. (a) Sondheimer, F.; Amiel, Y.; Wolovsky, F. *J. Am. Chem. Soc.* **1957**, *79*, 4247–4248. (b) Sondheimer, F.; Wolovsky, R. *J. Am. Chem. Soc.* **1959**, *81*, 4755–4756.
3. (a) *Top. Curr. Chem. Vol. 199: Fullerenes and Related Structures*; Hirsch, A., Ed.; Springer: Berlin, 1999. (b) *The Fullerenes*; Kroto, H. W.; Fischer, J. E.; Cox, D. E., Eds.; Pergamon Press: Exeter, 1993.
4. *Top. Curr. Chem. Vol. 201: Carbon Rich Compounds II, Macrocyclic Oligoacetylenes and Other Linearly Conjugated Systems*; de Meijere, A. Ed.; Springer: Berlin, 1999.
5. Sonogashira, K.; Tohda, Y. Hagihara, N. *Tetrahedron Lett.* **1975**, *50*, 4467–4470.
6. Miyaura, N.; Suzuki, A. *Chem. Rev.* **1995**, *95*, 2457–2483.

7. Stille, J. K. *Angew. Chem., Int. Ed. Engl.* **1986**, *25*, 508–523.

8. Trnka, T. M.; Grubbs, R. H. *Acc. Chem. Res.* **2001**, *34*, 18–29.

9. (a) Wan, W. B.; Brand, S. C.; Pak, J. J.; Haley, M. M. *Chem. Eur. J.* **2000**, *6*, 2044–2052. (b) Wan, W. B.; Haley, M. M. *J. Org. Chem.* **2001**, *66*, 3893–3901.

10. (a) Dybtsev, D. N.; Chun, H.; Yoon, S. H.; Kim, D.; Kim, K. *J. Am. Chem. Soc.* **2004**, *126*, 32–33. (b) Sharma, A. C.; Borovik, A. S. *J. Am. Chem. Soc.* **2000**, *122*, 8946–8955. (c) Eddaoudi, M.; Kim, J.; Rosi, N.; Vodak, D.; Wachter, J.; O'Keefe, M.; Yaghi, O. M. *Science* **2002**, *295*, 469–472. (e) Rudkevich, D. M. *Angew. Chem. Int. Ed.* **2004**, *43*, 558–571.

11. (a) Lahiri, S.; Thompson, J. L.; Moore, J. S. *J. Am. Chem. Soc.* **2000**, *122*, 11315–11319. (b) Moore, J. S. *Acc. Chem. Res.* **1997**, *30*, 402–413. (c) Zhang, J.; Moore, J. S. *J. Am. Chem. Soc.* **1992**, *114*, 9701–9702.

12. (a) Mindyuk, O. Y.; Stetzer, M. R.; Heiney, P. A.; Nelson, J. C.; Moore, J. S. *Adv. Mater.* **1998**, *10*, 1363–1366. (b) Collins, S. K.; Yap, G. P. A.; Fallis, A. G. *Org. Lett.* **2000**, 2, 3189–3192. (c) Höger, S.; Enkelmann, V.; Bonrad, K.; Tschierske, C. *Angew. Chem. Int. Ed.* **2000**, *39*, 2268–2270.

13. Höger, S.; Bonrad, K.; Mourran, A.; Beginn, U.; Möller, M. *J. Am. Chem. Soc.* **2001**, *123*, 5651–5659.

14. (a) Scott, L. T., DeCicco, G. J.; Hyun, J. L.; Reinhardt, G. *J. Am. Chem. Soc.* **1983**, *105*, 7760–7761. (b) *Modern Acetylene Chemistry;* Stang, P. J.; Diederich, F., Eds; VCH: Weinheim, 1995, 321–349.

15. (a) Lin, C.–H.; Tour, J. *J. Org. Chem.* **2002**, *67*, 7761–7768. (b)

16. (a) Ge, P.–H.; Fu, W.; Herrmann, W. A.; Herdtweck, E.; Campana, C.; Adams, R. D.; Bunz, U. H. F. *Angew. Chem. Int. Ed.* **2000**, *39*, 3607–3610. (b) Müller, P.; Usón, I.; Hensel, V.; Schlüter, A. D.; Sheldrick, G. M. *Helv. Chim. Acta* **2001**, *84*, 778–785.

17. (a) Tobe, Y.; Fujii, T.; Matsumoto, H.; Tsumuraya, K.; Noguchi, D.; Nakagawa, N.; Sonoda, M.; Naemura, K.; Achiba, Y.; Wakabayashi, T. *J. Am. Chem. Soc.* **2000**, *122*, 1762–1775. (b) Ohkita, M.; Ando, K.; Suzuki, T.; Tsuji, T. *J. Org. Chem.* **2000**, *65*, 4385–4390. (c) Heuft, M. A.; Collins, S. K.; Fallis, A. G. *Org. Lett.* **2003**, *5*, 1911–1914. (d) Bunz, U. H. F.; Rubin, Y.; Tobe, Y. *Chem. Soc. Rev.* **1999**, *28*, 107–119. (e) Dosa, P. I.; Erben, C.; Iyer, V. S.; Vollhardt, K. P. C.; Wasser, I. M. *J. Am. Chem. Soc.* **1999**, *121*, 10430–10431.

18. (a) Xhao, D.; Moore, J. S. *Chem. Commun.* **2003**, 807–818. (b) Grave, C.; Schlüter, A. D. *Eur. J. Org. Chem.* **2002**, 3075–3098. (c) Yamaguchi, Y.; Yoshida, Y. *Chem. Eur. J.* **2003**, *9*, 5430–5440.

19. (a) Yamaguchi, Y.; Kobayashi, S.; Amita, N.; Wakamiya, T.; Matsubara, Y.; Sugimoto, K.; Yoshida, Z. *Tetrahedron Lett.* **2002**, *43*, 3277–3280. (b) Yamaguchi, Y.; Yoshida, Y. *Chem. Eur. J.* **2003**, *9*, 5430–5440.

20. Höger, S.; Enkelmann, V. *Angew. Chem., Int. Ed. Engl.* **1995**, *34*, 2713–2716.

21. Morrison, D. L.; Höger, S. *Chem. Commun.* **1996**, 2313–2314.

22. Höger, S.; Morrison, D. L.; Enkelmann, V. *J. Am. Chem. Soc.* **2002**, *124*, 6734–6736.

23. Höger, S.; Meckenstock, A.–D. *Chem. Eur. J.* **1999**, *5*, 1686–1691.

24. Fuhrmann, G.; Debaerdemaeker, T.; Bäuerle, P. *Chem. Commun.* **2003**, 948–949.

25. (a) Krömer, J.; Rios–Carreras, I.; Fuhrmann, G.; Musch, C.; Wunderlin, M.; Debaerdemaeker, T.; Mena–Osteritz, E.; Bäuerle, P. *Angew. Chem. Int. Ed.* **2000**, *39*, 3481–3486.

26. (a) Mena–Osteritz, E.; Bäuerle, P. *Adv. Mater.* **2001**, *13*, 243–246. (b) Mena–Osteritz, E. *Adv. Mater.* **2002**, *14*, 609–616.

27. Tobe, Y.; Utsumi, N.; Nagano, A.; Sonoda, M.; Naemura, K. *Tetrahedron* **2001**, *57*, 8075–8083.

28. Marsella, M.; Wang, Z.–Q.; Reid, R. J.; Yoon, K. *Org. Lett.* **2001**, *3*, 885–887.

29. Baxter, P. N. W. *J. Org. Chem.* **2004**, *69*, 1813–1821.

30. Yamaguchi, Y.; Kobayashi, S.; Miyamura, S.; Okamoto, Y.; Wakamiya, T.; Matsubara, Y.; Yoshida, Z. *Angew. Chem. Int. Ed.* **2004**, *43*, 366–399.

31. Tobe, Y.; Nagano, A.; Kawabata, K.; Sonoda, M.; Naemura, K. *Org. Lett.* **2000**, *2*, 3265–3268.

32. Tobe, Y.; Utsumi, N.; Nagano, A.; Naemura, K. *Angew. Chem. Int. Ed.* **1998**, *37*, 1285–1287.

33. Seidel, D.; Lynch, V; Sessler, J. L. *Angew. Chem. Int. Ed.* **2002**, *41*, 1422–1425.

34. Sun, S.–S.; Lees, A. J. *Organometallics* **2001**, *20*, 2353–2358.

35. Baxter, P. N. W. *Chem. Eur. J.* **2003**, *9*, 2531–2541.

36. Hay, J. S. *J. Org. Chem.* **1962**, *27*, 3320–3321.

37. Baxter, P. N. W. *J. Org. Chem.* **2001**, *66*, 4170–4179.

38. Baxter, P. N. W. *Chem. Eur. J.* **2002**, *8*, 5250–5264.

39. Henze, O.; Lentz, D.; Schlüter, A. D. *Chem. Eur. J.* **2000**, *6*, 2362–2367.

40. Henze, O.; Lentz, D.; Schäfer, A. Franke, P.; Schlüter, A. D. *Chem. Eur. J.* **2002**, *8*, 357–365.

41. Nitschke, J. R.; Zürcher, S.; Tilley, T. D. *J. Am. Chem. Soc.* **2000**, *122*, 10345–10352.

42. Grave, C.; Lentz, D.; Schäfer, A.; Samorì, P.; Rabe, J. P.; Franke, P.; Schlüter, A. D. *J. Am. Chem. Soc.* **2003**, *125*, 6907–6918.

43. Baxter, P. N. W. *Chem. Eur. J.* **2003**, *9*, 5011–5022.

44. Heuft, M. A.; Fallis, A. G. *Angew. Chem. Int. Ed.* **2002**, *41*, 4520–4523.

Chapter 2 Synthesis and Characterization of Cross–Conjugated Oligomers and Macrocycles

2.1 Introduction

Over the past two decades, transition metal mediated carbon–carbon bond formation has become the dominant means for the assembly of conjugated structures.[1,2] While there are numerous protocols available to the synthetic chemist, there are two general transformations which are universally employed for the formation of alkyne–containing structures. First are the palladium–catalyzed sp–sp^2 bond forming reactions such as those developed by Sonogashira and Hagihara.[3] These cross–coupling methodologies provide efficient access to the enyne and aryl–yne moieties from readily available terminal acetylenes and aryl– or vinyl–halides (or triflates). A second, equally powerful transformation(s) are the sp–sp bond forming reactions such as those discovered by Glaser[4] and developed by Eglinton,[5] Hay,[6] and Breslow.[7] These copper–mediated processes provide symmetrically substituted butadiynes from terminal acetylenes under remarkably mild conditions. Using these various methods (as well as many others) an amazing diversity of conjugated organic compounds, both cyclic and acyclic, have been realized.

It has become increasingly obvious that organic compounds will play a vital role in many emerging areas of materials science and, as such, attention has recently turned toward the creation of conjugated molecules with a predefined function. It is possible, using the modern synthetic methods mentioned above, to tailor specific molecular properties via a building block approach. As described in the introduction to this thesis, a particularly exciting avenue of research has been the construction of shape–persistent, conjugated macrocycles.[8] Through the appropriate structural modifications, it is possible to tailor the size and shape, as well as the conformational properties and association behaviour of these systems. Shape–persistent macrocycles capable of serving as, for example, sensors,[9] supramolecular hosts,[10] liquid crystals,[11] and porous materials[12] have been achieved.

Described in this chapter are our efforts toward the realization of several shape–persistent macrocycles. Much of the work described was done by or in collaboration with three summer students that I was fortunate enough to work with during my first four years of graduate study. Our early work focused on the incorporation of *meta*–, *para*–, and *ortho*–diethynylbenzene (or alkoxybenzene) into a cross-conjugated enyne framework. All of the macrocyclic products were constructed from versatile and easily accessible alkynylbenzene and vinyl triflate building blocks using a combination of palladium–catalyzed cross–coupling and copper–catalyzed acetylenic homocoupling methods. In addition to their synthesis, our general observations regarding the effects of pendant substitution will also be described.

As detailed in the introduction to this thesis, the covalent modification of a macrocyclic framework to incorporate functionality such as heteroaromatic rings allows for the preparation of cyclic structures capable of interacting with guest species such as metals and/or metal ions. As such, we targeted the installation of diethynylpyridine within the cross–conjugated core of a macrocyclic species.[13] The resulting pyridinophane features a pre–organized cavity with opposing donor sites based on the incorporation of pyridine sub–units directed toward the centre of the macrocyclic cavity. The synthesis and characterization of several cyclic and acyclic pyridine–containing oligomers will be described in the following discussion. In addition, X–ray crystallographic analysis provides a description of the size and constitution of the cavity that results upon stacking of the pyridinophane in the solid–state.

2.2 Results and Discussion

2.2.1 Synthesis of Cross–Conjugated Oligomers and Macrocycles

Most of the cross–conjugated materials synthesized within our group including the *iso*–polydiacetylene (PDA) oligomers[14] and radialenes[15] made by Drs. Yuming Zhao and Sara Eisler, respectively, have been realized using a modular approach based on palladium–catalyzed cross–coupling reactions between vinyl triflate building blocks and various terminal alkynes. Vinyl triflates such as **202a–c** are accessible from readily available ethynyl ketones via the procedures described by Stang et al. (Equation 2.1).[16]

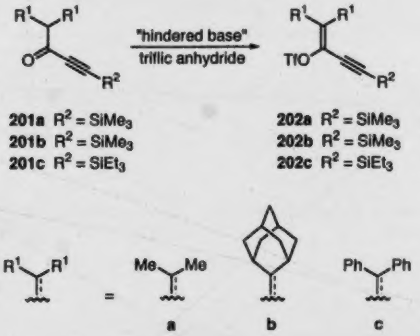

Eq. 2.1

It has been found within our group that the pendant alkylidene substitution can have a dramatic effect on both the solubility and stability of molecules created from these simple building blocks. Cyclic and acyclic oligomers based on the isopropylidene–derivatized triflate species **202a** are often susceptible to decomposition,[14,15] presumably via an oxygen ene reaction (Equation 2.2).[17] The incorporation of the adamantylidene group effectively shuts down this decomposition pathway by placing the methine protons (α to the alkylidene carbon) in an arrangement that is perpendicular to the π–system. However, materials constructed from this building block often suffer from extreme insolubility in common organic solvents.[14] More recent work in our group has focused on the incorporation of the diphenylalkylidene moiety, which has had the effect of improving *both* solubility and stability of resultant materials.[18]

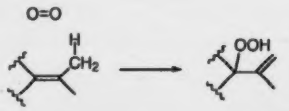

Eq. 2.2

Our earliest synthetic efforts focused on the realization of cross–conjugated macrocycles bearing pendant adamantylidene functionality (Scheme 2.1). 1,3–diethynylbenzene[19] (**203**) was cross–coupled with **202b** using $Pd(PPh_3)_4$ as catalyst and CuI as co–catalyst in the presence of Et_2NH in DMF. In general, all cross–coupling reactions were performed using 5% of the palladium catalyst, and 15% of the copper co–catalyst, per coupling event. The resultant oligomer, **204b**, was isolated as a colourless solid, subsequent to purification via silica gel chromatography. Oligomer **204b** was desilylated using TBAF in wet THF and the oligomer chain was extended through a second iteration of the cross–coupling step to yield oligomer **205b**.

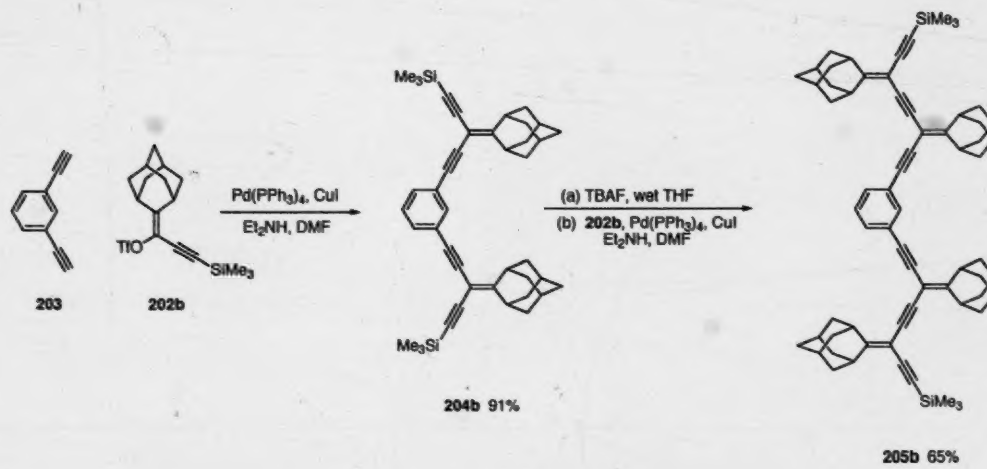

Scheme 2.1 Synthesis of acyclic oligomers **204b** and **205b**.

We then targeted the synthesis of cross–conjugated macrocycles **206b** and **207b** from these acyclic oligomers as outlined in Scheme 2.2. Compound **204b** was desilylated by treatment with TBAF in wet THF for a period of 30 minutes. Subsequent to an aqueous workup and with no further purification, the deprotected oligomer was treated to intermolecular oxidative homocoupling conditions. The deprotected polyyne was treated with CuI and TMEDA under high dilution conditions in dry CH_2Cl_2 in the presence of air for 36 hours. Subsequent to an aqueous workup, the solvent volume of the reaction mixture was reduced to yield an insoluble, off–white solid mass. ^{1}H NMR spectroscopic analysis of the crude mixture suggested that the solid was a mixture of products, presumably oligomeric in nature. There was no evidence for the presence of **206b** in the mixture and therefore, this synthetic sequence was abandoned.

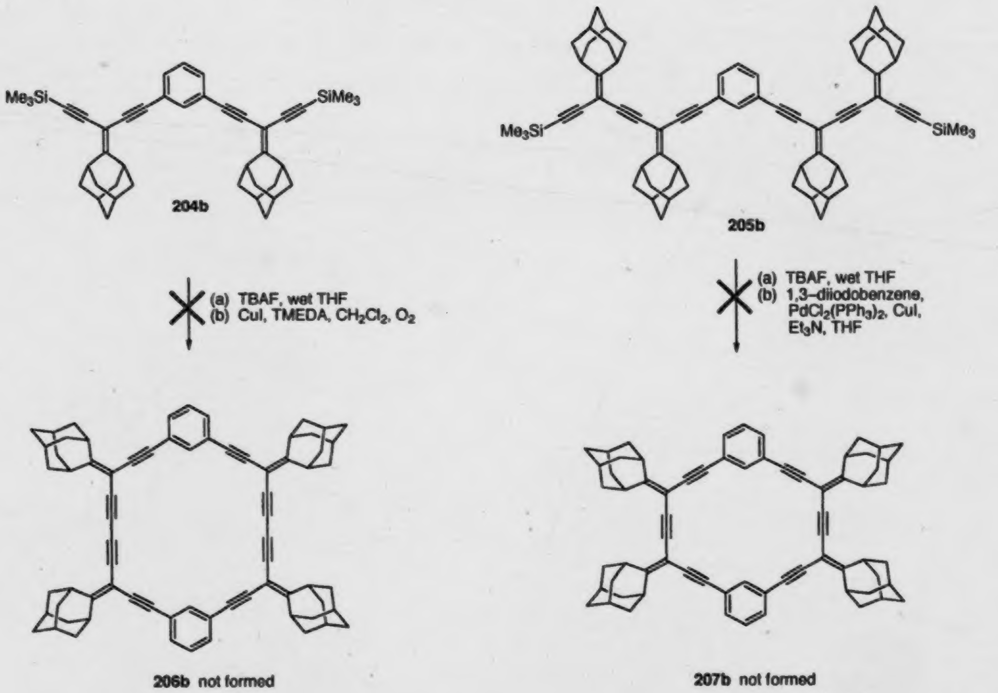
Me$_3$Si
SiMe$_3$
204b
Me$_3$Si
SiMe$_3$
205b
(a) TBAF, wet THF
(b) CuI, TMEDA, CH$_2$Cl$_2$, O$_2$
(a) TBAF, wet THF
(b) 1,3–diiodobenzene, PdCl$_2$(PPh$_3$)$_2$, CuI, Et$_3$N, THF
206b not formed
207b not formed

Scheme 2.2 Attempted synthesis of macrocycles **206b** and **207b**.

Macrocyclic oligomer **207b** was also targeted, from the acyclic oligomer **205b**. The silyl–protecting groups of **205b** were removed using TBAF in wet THF and the cross–coupling of the resulting terminal diacetylene with 1,3–diiodobenzene using $Pd_2Cl_2(PPh_3)_2$ as catalyst and CuI as cocatalyst was attempted. The reaction was carried out in dry, degassed Et_3N/THF in the absence of oxygen for a period of 4 days. Upon workup, the reaction mixture again yielded an insoluble, off–white mass. Preliminary ^{1}H NMR spectroscopic analysis suggested that the crude reaction product was a mixture. ESI MS analysis also indicated the presence of several species, but unfortunately, none of these was the desired product **207b**.

Rather than continuing to pursue these synthetic sequences, we chose to target macrocycle **206c**, featuring the diphenylalkylidene substitution. The incorporation of alternative substitution was expected to mediate the solubility of the macrocyclic species. Diethynyl benzene **203** was cross–coupled with diphenylalkylidene–substituted triflate **202c** using palladium catalysis, as shown in Scheme 2.3. Unlike the previous examples, heating to 50 °C for an extended period of time (14 hours) was required to effect this process. In general, all cross–coupling reactions with **202c** require gentle heating, presumably the result of the bulkier diphenyl substitution. Oligomer **204c** was achieved in 98% yield subsequent to purification on a silica gel column. Deprotection of **204c** was achieved by treating with TBAF in wet THF and the resulting desilylated tetrayne was treated with CuI/TMEDA at high dilution in dry CH_2Cl_2 in the presence of air for 14 hours. Aqueous workup and solvent removal led to the formation of a frustratingly insoluble yellow precipitate. It was found in subsequent experiments, however, that by reducing the solvent volume, subsequent to aqueous workup, by approximately 90% and then layering the resulting solution with acetone (1:1 v/v), the selective precipitation of **206c** could be achieved. Upon filtering and drying, pure **206c** was isolated in 39% yield as an orange–yellow solid.

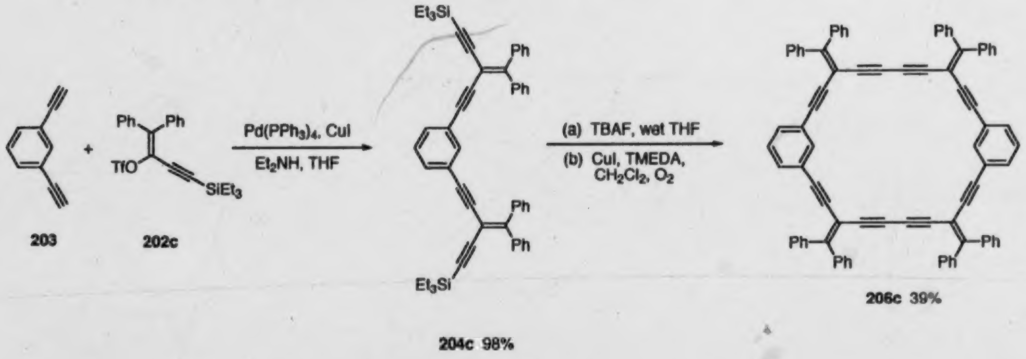

Scheme 2.3 Synthesis of macrocycle **206c** featuring a *meta*–diethynylbenzene subunit.

While **206c** was insufficiently soluble for meaningful ^{13}C NMR spectroscopic analysis, the ^{1}H NMR spectrum was consistent with the proposed structure. The isolated methine protons of the diethynylbenzene units appear as a triplet at δ 7.60. The remaining *ortho*– and *meta*–protons (with respect to the acetylene units) appear as a doublet of doublets and a triplet at 7.01 and 7.18 ppm, respectively. The protons of the diphenylalkylidene moieties appear as a multiplet in the range of δ 7.49 – 7.31. ESI mass spectral analysis (with added AgOTf) was also consistent with the proposed structure. The mass spectrum of **206c** showed signals at 1937 (19%), 1679 (53%), 1421 (66%) and 1165 (100%) assigned to the clusters $[M + Ag + 3AgOTf]^+$, $[M + Ag + 2AgOTf]^+$, $[M + Ag + AgOTf]^+$, and $[M + Ag]^+$, respectively.

We next turned out attention toward the synthesis of macrocycle **210a**, featuring *para*–diethynylbenzene substitution. Palladium–catalyzed cross–coupling between **208a** and triflate **202c** led to the formation of oligomer **209a** in 92% yield. Single crystals suitable for X–ray crystallographic analysis were grown by slow diffusion of a solution of **209a** in acetone layered with methanol at 4 °C. The ORTEP drawing (Figure 2.1) shows that the solid–state structure of **209a** is generally unremarkable with all alkylidene and alkynyl bond angles relatively close to the ideal values of 120 and 180°, respectively.

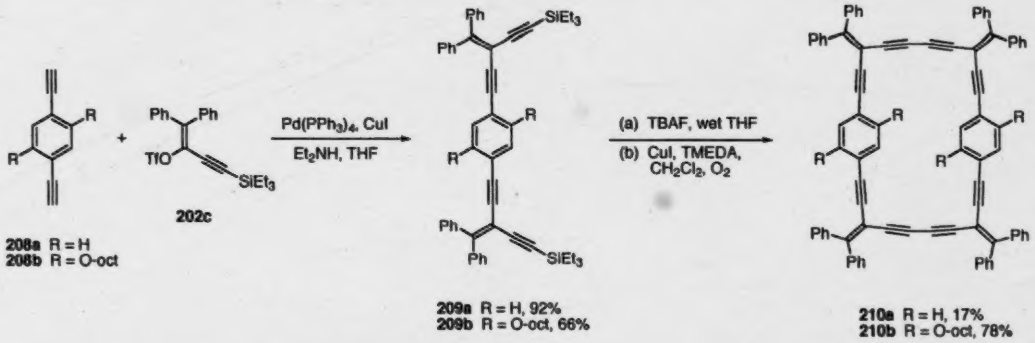
Ph
Ph
R
R
TfO
SiEt3
Pd(PPh3)4, CuI
Et2NH, THF
(a) TBAF, wet THF
(b) CuI, TMEDA, CH2Cl2, O2
208a R = H
208b R = O-oct
202c
209a R = H, 92%
209b R = O-oct, 66%
210a R = H, 17%
210b R = O-oct, 78%

Scheme 2.4 Synthesis of macrocycles **210a** and **210b** featuring *para*–diethynylbenzene subunit.

Subsequent to desilylation, the deprotected oligomer **209a** was treated with intermolecular oxidative homocoupling conditions, leading to the formation of **210a**. Macrocycle **210a** was isolated by reducing the solvent volume after workup by approximately 90% and then filtering and drying the resultant yellow precipitate. Disappointingly, **210a** was obtained in only 17% yield. This macrocyclic species was found to be even less soluble than **206c**, leading to difficulties with respect to both its isolation and characterization. The ^{1}H NMR spectrum of **210a** was consistent with the proposed structure, showing a multiplet in the range of 7.51 – 7.37 ppm, assigned to the aromatic protons of the pendant diphenylalkylidene groups. The methine protons of the diethynylbenzene subunit appear as a singlet at δ 7.35. Macrocycle **210a** was not sufficiently soluble for meaningful ^{13}C NMR spectroscopic analysis, but ESI mass spectral analysis was consistent with the proposed structure. The ESI mass spectrum (AgOTf added) of **210a** showed a prominent signal centred at *m/z* 1165 (98%), assigned to $[M + Ag]^+$.

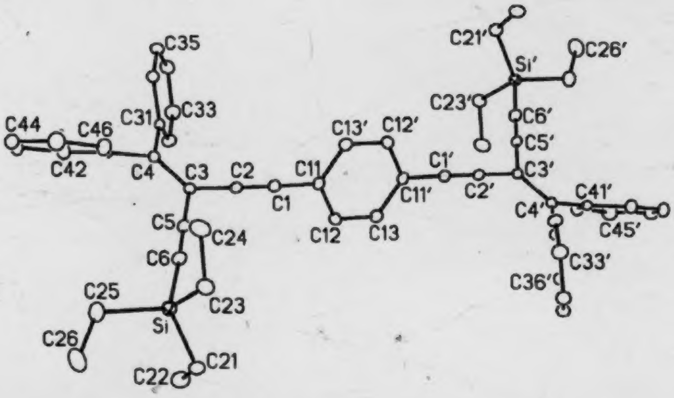

Figure 2.1 ORTEP drawing of **209a**. Selected bond angles [°]: C(2)–C(1)–C(11) 178.72(19), C(1)–C(2)–C(3) 176.55(16), C(3)–C(5)–C(6) 178.68(17), Si–C(6)–C(5) 175.44(15), C(2)–C(3)–C(5) 115.39(14). Thermal ellipsoids are drawn at the 20% probability level.

During my third and fourth years of graduate study, I was fortunate to work with an undergraduate student named Monika Pawlowska. Part of her summer research project was to explore the effect of incorporating solubilizing alkoxy side chains onto the periphery of these macrocyclic species. Palladium–catalyzed cross–coupling of the octyloxy–substituted diethynylbenzene[20] **208b** with vinyl triflate **202c** led to the formation of oligomer **209b** in 66% yield. Subsequent to desilylation, oligomer **209b** was treated with intermolecular oxidative homocoupling conditions, leading to the formation of **210b**. Macrocycle **210b** is a stable and highly soluble yellow solid, allowing for its purification via flash chromatography (alumina) and subsequent isolation in a remarkable 78% yield. The high isolated yield of this solubilized derivative provides some confirmation of our assumption that the relatively low yields of the macrocyclization reactions up to this point had been due to problems with respect to isolation of an insoluble product rather than due to low reactivity or the formation of excessive byproducts.

Gratifyingly, macrocycle **210b** was soluble enough for full spectroscopic characterization in solution. The ^{1}H NMR spectrum was consistent with the proposed structure and ^{13}C NMR analysis remarkably revealed all 25 of the expected non–equivalent carbon resonances. ESI mass spectral analysis also supported the presence of **210b** and revealed a cluster of signals centred at *m/z* 1593 assigned to $[M + Na]^+$ (42%). The isotopic distribution pattern of this signal closely resembles that calculated for $C_{116}H_{112}O_4Na$.

The final, and most interesting, macrocycle targeted in this series, also synthesized by Monika Pawlowska, was **213**, based on an *ortho*–substituted diethynylbenzene subunit (Scheme 2.5). Due to the strain imparted as a result of this substitution pattern, the macrocyclic core must twist, resulting in a helically chiral (albeit racemic) molecule. Octyloxy–substituted 1,2–diethynylbenzene,[21] **211**, was cross–coupled with vinyl triflate **202c**, resulting in the formation of oligomer **212**. Compound **212** was isolated, subsequent to purification on a silica column, as an unstable brown oil in a disappointing 35% yield. Numerous attempts were made to improve the yield of this step including varying reaction times and temperatures as well as the amount of added amine base. In general, we found that in the absence of heating, numerous byproducts were formed as the reaction proceeded, making the purification of **212** very difficult, resulting in low isolated yields. When the reaction mixture was heated, however, TLC analysis showed a greater amount of (baseline) decomposition, also to the detriment of the isolated yield, although the purification process was significantly less onerous.

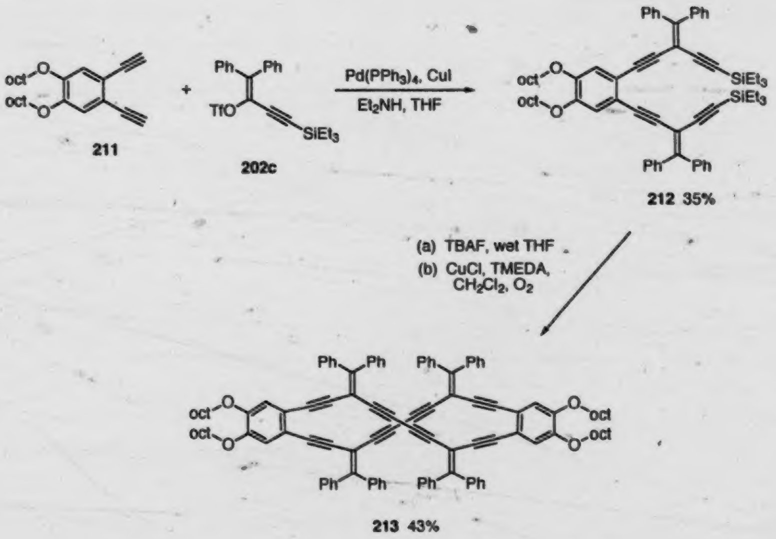
oct
oct
O
O
211
Ph
Ph
TfO
SiEt3
202c
Pd(PPh3)4, CuI
Et2NH, THF
Ph
Ph
SiEt3
SiEt3
Ph
Ph
212 35%
(a) TBAF, wet THF
(b) CuCl, TMEDA, CH2Cl2, O2
Ph
Ph
Ph
Ph
Ph
Ph
Ph
Ph
213 43%

Scheme 2.5 Synthesis of helically chiral macrocycle **213**, featuring 1,2–diethynylbenzene subunit.

Oligomer **212** was desilylated using TBAF in wet THF and the resulting deprotected oligomer was exposed to oxidative homocoupling conditions (at high dilution) leading to the formation of chiral macrocycle **213**. Macrocycle **213** was isolated as an amber semi–solid in 43% yield subsequent to chromatographic purification (alumina). Macrocycle **213** was subjected to full spectroscopic characterization. The ^{1}H NMR spectrum of **213** was consistent with the proposed structure and showed two multiplets in the ranges of 7.59 – 7.49 and 7.42 – 7.30 ppm, integrating to a total of 40H, attributable to the aromatic protons on the pendant diphenylalkylidene groups. The isolated methine protons of the diethynylbenzene rings appeared as a singlet at δ 6.60 and the remaining, all alkyl protons appeared upfield within expected chemical shift ranges. The ^{13}C NMR spectrum of macrocycle **213** also provided confirmation of the proposed structure, showing all 25 of the expected carbon resonances. The most convincing evidence for the formation of **213** came from MALDI–TOF mass spectral analysis, which clearly showed the molecular ion peak at *m/z* 1568.8 (13%).

It is worth noting that all of the alkynyl carbon resonances for **213** appeared significantly downfield relative to those of the presumably less–strained macrocycle **210b**. It has been shown previously in our group that acetylenic carbons are significantly deshielded as ring strain is introduced into enyne macrocycles.[22] The alkynyl carbon resonances for **210b** are observed in the range of 94.2–77.9 ppm and they appear at 103.8–88.5 ppm for **213**. The ^{13}C NMR chemical shift values for both the endo– and exocyclic alkylidene carbons are also affected by the degree of ring strain present. The endocyclic alkylidene carbons ($-C\equiv C-\mathit{C}(=C)-C\equiv C-$) for **210b** resonate at δ 101.9 and appear at δ 109.8 for **213**. The exocyclic alkylidene carbon resonance ($-C\equiv C-C(=\mathit{C})-C\equiv C-$) in the more strained macrocycle **213** appears at 149.3 ppm; these carbons resonate at δ 155.1 in the ^{13}C NMR spectrum of **210b**. These observations are consistent with previous studies performed by my colleague, Dr. Sara Eisler, who showed that the endocyclic carbons are deshielded with an increase ring strain, due to rehybridization at this carbon centre. The exocyclic carbons are, conversely, shielded as ring strain increases.

2.2.2 Synthesis of Cyclic and Acyclic Oligomers Containing Heteroaromatic Functionality

In addition to the realization of shape–persistent macrocycles based on an all carbon scaffold, we also targeted macrocycles bearing heteroaromatic functionality capable of interacting with metal ions. Through the covalent incorporation of 2,6–diethynyl pyridine sub–units, cross–conjugated macrocycles featuring a pre–organized cavity with opposing donor sites were achieved.[13] All of the syntheses presented below represent work done in collaboration with two talented summer research students, Natasha Tiemstra and Natasha Prepas–Strobeck, who were participants in the University of Alberta's WISEST (Women in Scholarship, Engineering, Science, and Technology) summer research program.

Our earliest efforts focused on the synthesis of conjugated macrocycle **216a**, featuring an isopropylidene–derivatized core, as outlined in Scheme 2.6. Beginning with 2,6-diethynyl pyridine,[23] a palladium–catalyzed cross–coupling reaction with 2 equivalents of vinyl triflate **202a** led to the formation of the pyridine–containing oligomer **215a** in 81% yield. Desilylation was achieved by treating with TBAF in wet THF, and the resulting deprotected tetrayne was treated with CuI and TMEDA under high dilution conditions in dry CH_2Cl_2 in the presence of air. Subsequent to workup and purification using flash chromatography (silica) a brownish solid was isolated.

The ^{1}H NMR spectrum of this solid was consistent with the desired structure **216a**, but the ESI mass spectrum showed no evidence of the expected molecular ion peak. Instead, a signal was observed at *m/z* 535.9 (100%), corresponding to the iodinated oligomer **217a**. This product is presumably the result of reductive elimination across a copper (II) species. Oligomer **217a** was the only product isolated from the reaction mixture in 33% yield. ^{13}C NMR spectroscopy provided additional confirmation of the structure of iodinated oligomer **217a**. Goroff and coworkers, among others, have extensively studied iodoalkynes and they have found that the alkynyl carbon adjacent to the iodine atom (–C≡*C*–I) in an alkynyl iodide characteristically resonates at least 60 ppm upfield relative to the analogous terminal acetylene carbon.[24] This is due, at least in part, to the "heavy atom effect" of iodine. The ^{13}C NMR spectrum of **217a** was consistent with these findings, showing a resonance at δ 8.6, assigned to the alkynyl carbons attached to iodine. All other expected non–equivalent carbon resonances were also observed in the ^{13}C NMR spectrum of **217a**.

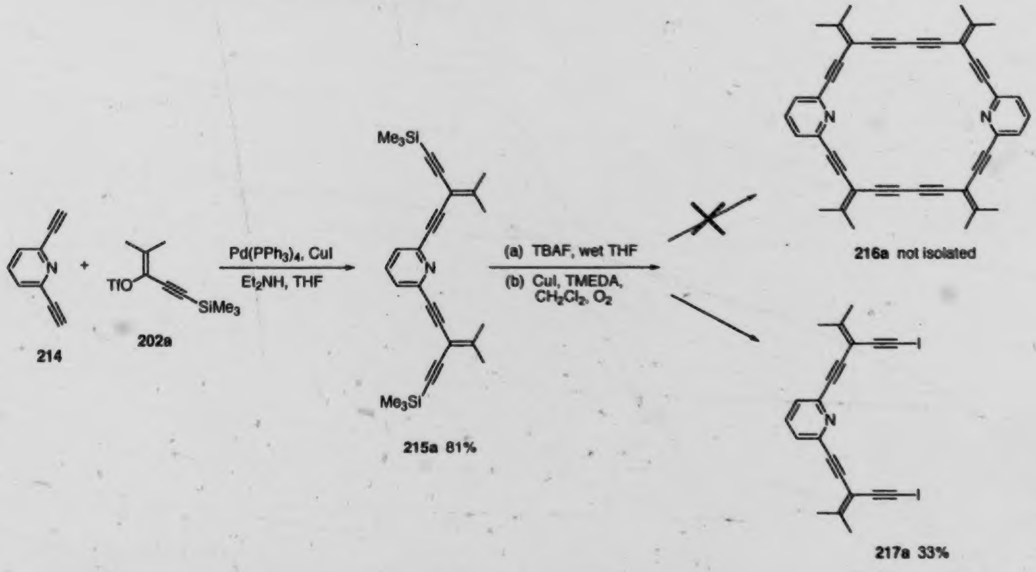

N
+
TfO
SiMe$_3$
214
202a
Pd(PPh$_3$)$_4$, CuI
Et$_2$NH, THF
Me$_3$Si
N
Me$_3$Si
215a 81%
(a) TBAF, wet THF
(b) CuI, TMEDA, CH$_2$Cl$_2$, O$_2$
N
N
216a not isolated
I
N
I
217a 33%

Scheme 2.6 Attempted synthesis of macrocycle **216a**.

We next targeted the synthesis of **216a** using an analogous homocoupling reaction, in the absence of CuI. While Breslow[7] or Eglinton[5] homocoupling conditions are often the method of choice to achieve this sort of transformation, we have found that in many cases the Hay conditions (CuCl and TMEDA in dry CH$_2$Cl$_2$ in the presence of air) lead to higher yields of the desired product. Treatment of the deprotected oligomer **215a** with Hay conditions for 2 days at room temperature, followed by aqueous workup and concentration led to the formation of an off–white precipitate, which was isolated upon filtering and drying.

While analysis of the ^{1}H NMR spectrum of this precipitate suggested the presence of pure **216a**, and gave no indication of the presence of a terminal alkyne, both ESI and MALDI-TOF mass spectral analysis indicated the presence of higher order oligomers, the not unexpected byproducts of a macrocyclization reaction. As with the previous examples described above, a problem that is frequently encountered in the synthesis of large, rigid, and highly conjugated macrocycles is that of severely reduced solubility, especially in the absence of peripheral alkyl groups or other derivatization, as is the case with **216a**. All of our attempts to purify macrocycle **216a** were hampered by its extreme insolubility as well as the instability of this compound, and as a result, this synthetic sequence was abandoned.

We next directed our attention to the synthesis of macrocycle **216c**, with pendant diphenyl functionality. We expected that the incorporation of the diphenylalkylidene moiety could, as we had observed previously, address the problems of instability and limited solubility that we had encountered in the synthesis of **216a**. Reaction of **214** with 2 equivalents of vinyl triflate **202c** using palladium catalysis led to the formation of oligomer **215c** in 49% yield. While we have found that cross–coupling reactions with **202c** generally proceed more rapidly and provide greater yields when heat is applied to the reaction mixture (ca. 50 °C), in this case even gentle heating resulted in the formation of numerous byproducts and lower isolated yields of **215c**. The highest yields (49%) were achieved when the reaction was performed at room temperature.

Subsequent to desilylation, the deprotected polyyne was exposed to intermolecular oxidative homocoupling conditions (CuCl/TMEDA in dry CH_2Cl_2 in the presence of air). After stirring at room temperature for 3 days, and performing an aqueous workup, the solution was concentrated to ca. 5 mL and 5mL of acetone was added. This led to the formation of a bright yellow precipitate, which upon filtering and drying gave pure **216c** in 62% yield. It is worth noting the importance of monitoring the solvent volume during this process. Evaporation to dryness of the reaction mixture in many cases leads to the precipitation of several byproducts (presumably oligomeric in nature) that will not go back into solution, leading to difficulties with respect to the purification of **216c**. Also noteworthy is the importance of rigorously washing the reaction mixture during aqueous workup with *both* saturated NH_4Cl and $NaHCO_3$. The copper salts produced in the reaction are extremely difficult to eliminate, requiring numerous washes with NH_4Cl. The macrocycle **216c** is easily protonated under these conditions, requiring numerous washes with $NaHCO_3$. Failure to conscientiously perform both of these washing steps consistently resulted only in the isolation of impure product, which, due to insufficient solubility, cannot be purified.

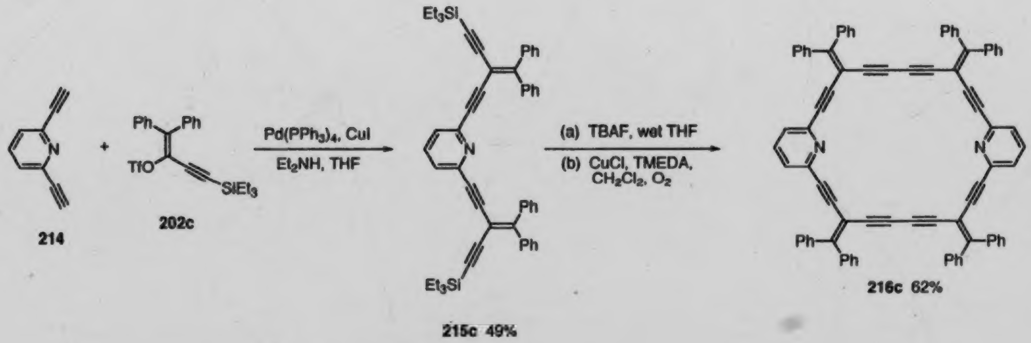

Scheme 2.7 Synthesis of pyridine–containing macrocycle **216c**.

While the incorporation of the diphenylvinylidene substitution had the desired effect with respect to stability (macrocycle **216c** can be stored indefinitely in the refrigerator and decomposes only at temperatures greater than 250 °C). it is still only sparingly soluble even in chlorinated solvents. Due to the problem of limited solubility, ^{13}C NMR analysis was not possible but the ^{1}H NMR spectrum of **216c** is consistent with the proposed structure. ESI MS analysis also supports the structure of **216c**, showing a peak at *m/z* 1059.4 (100%), assigned to the protonated macrocyclic species. The isotopic distribution of this peak is consistent with the calculated isotope pattern.

It is also worth mentioning that the first time that we attempted to access the homocoupled macrocycle **216c**, CuI was used to mediate this process. While ESI mass spectral analysis of the crude reaction mixture showed evidence of the desired macrocyclic species **216c** at *m/z* 1059.4 (7%), the spectrum was dominated by a large signal at *m/z* 784.5 (100%), which was unidentified at the time. As a result, we simply tried the reaction again using the Hay conditions, which were successful, as described above. In retrospect, we realized that the use of the iodide salt had again supplied an iodinated oligomer, **217c**, as evidenced by the signal observed in the ESI mass spectrum at *m/z* 784.5, which corresponds to [$C_{41}H_{24}NI_2^+$].

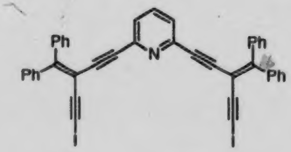

217c

2.2.3 Solid–State Properties of Acyclic and Cyclic Pyridine–Containing Oligomers

In addition to full spectroscopic characterization in solution, many of the pyridine–containing oligomers were highly crystalline solids, allowing for their characterization using X–ray analysis. Single crystals of the iodinated oligomer **217a** were grown by layering a CH_2Cl_2 solution of the oligomer with hexanes and allowing slow evaporation/diffusion at 4 °C. The ORTEP drawing of **217a** (Figure 2.2) shows that the oligomer has packed in the solid–state such that one iodine atom of each oligomer is in close contact with the pyridyl nitrogen of a neighbouring oligomer. This non–bonded distance is measured to be 2.93 Å (N–I(1′)), which is well within the combined van der Waals radii of nitrogen and iodine. It is well known that iodoalkynes are good Lewis acids, and these species have been shown to form acid–base complexes in the solid state. For example, Goroff and coworkers recently reported the solid–state structure of diiodohexatriyne co–crystallized with triphenylphosphine oxide.[25] They observed that these species packed such that there were close contacts between the iodine atoms of the iodoacetylene and the basic oxygen atoms of the adjacent triphenylphosphine oxide co–crystallite. The iodine–oxygen distance was measured to be ~ 2.8 Å, which is comparable to the distance measured in the case of **217a**. The carbon–iodine bonds lengths of **217a** were measured to be 2.013(4) (I(1)–C(18)) and 1.989(4) Å (I(2)–C(28)), which are also comparable to the bond lengths observed by Goroff and coworkers at 1.96 Å.

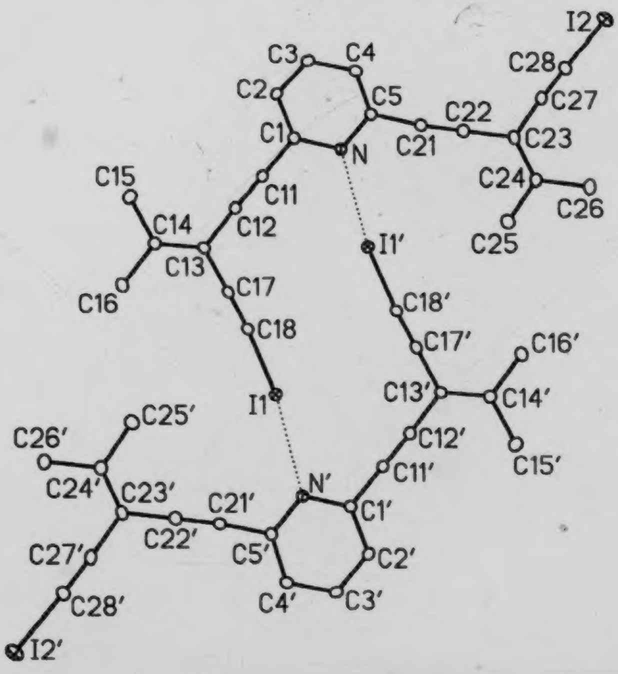
I2
C28
C27
C3
C4
C2
C5
C22
C23
C1
N
C21
C24
C15
C11
C26
C14
C12
I1′
C25
C13
C17
C18′
C16
C18
C17′
C16′
I1
C13′
C14′
C25′
C26′
C12′
N′
C11′
C15′
C24′
C23′
C21′
C1′
C22′
C27′
C5′
C2′
C28′
C4′
C3′
I2′

Figure 2.2 ORTEP drawing of **217a** highlighting the non–bonded interactions between adjacent molecules. Selected bond lengths [Å] and angles [°]: I(1)–C(18) 2.013(4), I(2)–C(28) 1.989(4), C(17)–C(18) 1.190(5), C(27)–C(28) 1.197(5), I(1)–N′ 2.927(3); I(1)–C(18)–C(17) 175.3(3), C(13)–C(17)–C(18) 179.9(5), C(11)–C(12)–C(13) 177.6(4), C(1)–C(11)–C(12) 178.6(4), C(5)–C(21)–C(22) 175.3(4), C(21)–C(22)–C(23) 179.5(5), C(23)–C(27)–C(28) 177.7(4), I(2)–C(28)–C(27) 176.9(3). Thermal ellipsoids are drawn at the 20% probability level.

Single crystals of **215a**, suitable for crystallographic analysis were grown by slow evaporation of a hexanes solution at 4 °C. The ORTEP drawing of **215a**, shown in Figure 2.3, shows that the oligomer has adopted a near planar conformation in the solid state. The degree of planarity can be established through analysis of the least–squares planes of the structure. For **215a**, the dihedral angle between plane 1 (defined by N–C(1)–C(2)–C(3)–C(4)–C(5)) and plane 2 (defined by C(11)–C(12)–C(13)–C(14)–C(15)–C(16)) is measured at 4.57(15)°. The dihedral angles between plane 1 and plane

3 (defined by C(21)–C(22)–C(23)–C(24)–C(25)–C(26)) and plane 2 and plane 3 are 3.80(15)° and 1.29(14)°, respectively. The structure is generally unremarkable with the mean alkyne and alkylidene bond angles determined to be 177.3° and 116.6°, respectively.

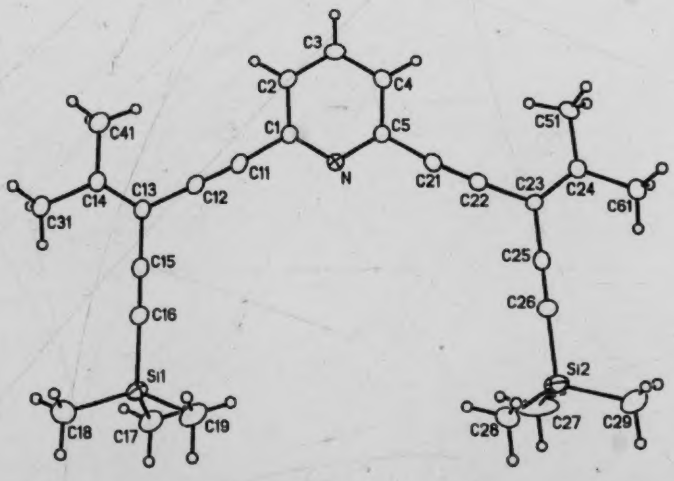

Figure 2.3 ORTEP drawing of oligomer **215a**. Selected bond angles [°]: Si(1)–C(16)–C(15) 179.2(3), C(13)–C(15)–C(16) 179.4(3), C(11)–C(12)–C(13) 179.2(3), C(1)–C(11)–C(12) 174.7(3), C(5)–C(21)–C(22) 173.4(3), C(21)–C(22)–C(23) 177.3(3), C(23)–C(25)–C(26) 179.6(3), Si(2)–C(26)–C(25) 175.6(3), C(12)–C(13)–C(15) 116.5(2), C(22)–C(23)–C(25) 116.7(2). Thermal ellipsoids are drawn at the 20% probability level.

Single crystals of **216c**, suitable for X–ray crystallographic analysis, were grown by dissolving the macrocycle in boiling $ClCH_2CH_2Cl/CH_2Cl_2$ (at 100 °C), and allowing slow evaporation from the resulting solution at room temperature. The ORTEP diagram (Figure 2.4) shows that the macrocycle has adopted a near planar conformation in the solid–state and as a result is relatively free from strain. A comparison of the alkynyl bond angles of **216c** with those of **215a** suggests that **216c** is only slightly more strained than the acyclic derivative. The mean alkyne bond angle of **216c** is 176.2° (with a maximum deviation from ideality of 6.3°), only slightly less than that of **215a** at 177.3°. In addition, the vinylidene bond angles of **216c**, C(12)–C(13)–C(15) and C(22)–C(23)–C(25) at 115.3 and 113.0° are similar to those of **215a**. The planar enyne core of macrocycle **216c** spans a diameter of 9.10 (N–N') by 9.00 (C(16)–C(26)) Å, enforcing a freespace cavity with dimensions of ca. 6.0 by 5.5 Å. In addition to the two molecules of **216c**, there are a total of 4 disordered solvent molecules present within the unit cell occupying 587.0 Å^3. As a result of the disorder, the solvent molecules could not be refined and it was not possible to crystallographically distinguish between CH_2Cl_2 and $ClCH_2CH_2Cl$. Removal of this solvent would generate approximately 18% free volume within the crystal lattice.

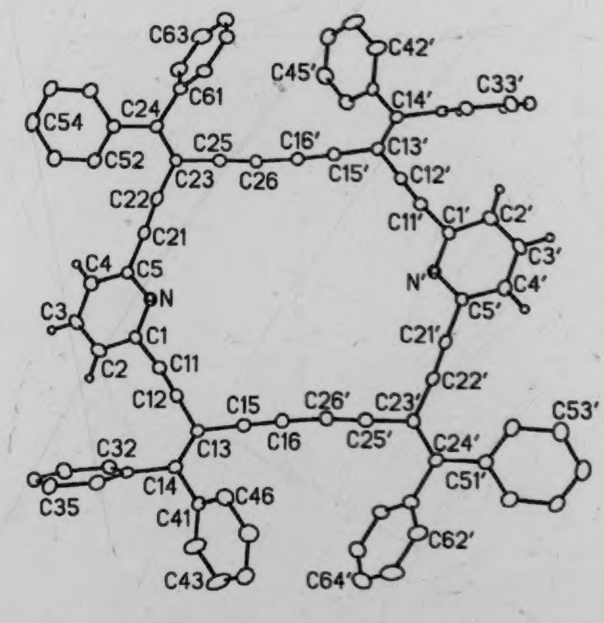
C63
C42'
C45'
C33'
C61
C14'
C24
C54
C25
C16'
C13'
C52
C23
C26
C15'
C12'
C22
C11'
C1'
C2'
C21
C3'
C4
C5
N'
C4'
N
C3
C5'
C1
C21'
C11
C2
C22'
C12
C15
C26'
C23'
C53'
C32
C13
C16
C25'
C24'
C51'
C14
C46
C35
C41
C62'
C43
C64'

Figure 2.4 ORTEP drawing of **216c**. Selected bond angles [°]: C(1)–C(11)–C(12) 174.0(4), C(11)–C(12)–C(13) 178.8(4), C(13)–C(15)–C(16) 179.0(4), C(15)–C(16)–C(26') 176.1(4), C(5)–C(21)–C(22) 174.7(3), C(21)–C(22)–C(23) 173.7(3), C(23)–C(25)–C(26) 178.5(4), C(25)–C(26)–C(16') 175.1(4), C(12)–C(13)–C(15) 115.3(3), C(22)–C(23)–C(25) 113.0(3). Thermal ellipsoids are drawn at the 20% probability level. Co-crystallized solvent not shown.

When viewed down the *a*–axis, the crystal packing diagram (Figure 2.5) of **216c** shows that the macrocycles have stacked such that channels are revealed in the solid state. The macrocycles are stacked at an approximate angle of 60° (relative to the *b*–axis), and there is ca. 4.5 Å between parallel, stacked, macrocyclic cores. The co–crystallized solvent molecules are occupying space within these channels (two per macrocyclic unit).

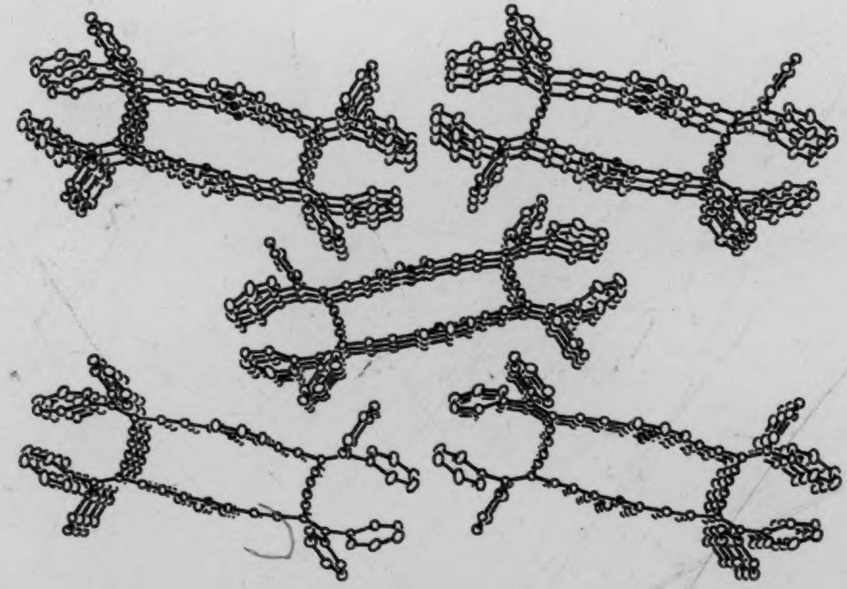

Figure 2.5 Crystal packing diagram of **216c** viewed down the crystallographic *a*–axis. Co–crystallized solvent has been omitted.

Several attempts were made to co–crystallize **216c** with small molecules suitable for inclusion in the pore structure including: metal salts such as AgOTf, short chain dicarboxylates such as succinic acid, and iodine. Unfortunately, to date, none of these attempts have been successful.

2.3 Conclusions

The successful synthesis of several shape–persistent cross–conjugated macrocycles has been described. Through the use of palladium–catalyzed cross–coupling and copper–catalyzed acetylenic homocoupling methodologies, macrocycles based on *meta*–, *para*–, and *ortho*–diethynylbenzene sub–units were realized including the interesting helically chiral derivative **213**. Elaboration of an enyne macrocyclic core to incorporate heteroaromatic functionality was also achieved. The resulting pyridinophane, which features endotopic binding sites, has been shown to stack in the solid–state such that large channels possibly suitable for the inclusion of guest molecules were realized.

2.4 References and Notes

1. *Metal–Catalyzed Cross–Coupling Reactions*; Diederich, F.; Stang, P. J., Eds.; Wiley–VCH: Weinheim, **1997**.
2. Siemsen, P.; Livingston, R. C.; Diederich, F. *Angew. Chem. Int. Ed.* **2000**, *39*, 2632–2657.
3. Sonogashira, K.; Tohda, Y. Hagihara, N. *Tetrahedron Lett.* **1975**, 4467–4470.
4. (a) Glaser, C. *Ber. Dtsch. Chem. Ges.* **1869**, *2*, 422–424. (b) Glaser, C. *Ann. Chem. Pharm.* **1870**, *154*, 137–171.
5. Eglinton, G.; Galbraith, A. R. *Chem. Ind. (London)* **1956**, 737–738.
6. Hay, A. S. *J. Org. Chem.* **1962**, *27*, 3320–3321.
7. O'Krongly, D.; Denmeade, S. R.; Chiang, M. Y.; Breslow, R. *J. Am. Chem. Soc.* **1985**, *107*, 5544–5545.

8. For a more comprehensive review of shape–persistent macrocycles and their applications, see Chapter 1, and references therein.

9. (a) Baxter, P. N. W. *J. Org. Chem.* **2004**, *69*, 1813–1821. (b) Baxter, P. N. W. *Chem. Eur. J.* **2003**, *9*, 2531–2541. (c) Lin, J.; Zhang, H.–C.; Pu, L. *Org. Lett.* **2002**, *4*, 3297–3300.

10. Zhao, D.; Moore, J. S. *Chem. Commun.* **2003**, 807–831.

11. (a) Collins, S. K.; Yap, G. P. A.; Fallis, A. G. *Org. Lett.* **2000**, *2*, 3189–3192. (b) Höger, S.; Enkelmann, V.; Bonrad, K.; Tschierske, C. *Angew. Chem. Int. Ed.* **2000**, *39*, 2268–2270. (c) Henze, O.; Lentz, D.; Schäfer, A.; Franke, P.; Schlüter, A. D. *Chem. Eur. J.* **2002**, *8*, 357–365.

12. (a) Campbell, K.; Kuehl, C. J.; Ferguson, M. J.; Stang, P. J.; Tykwinski, R. R. *J. Am. Chem. Soc.* **2002**, *124*, 7266–7267. (b) Grave, C.; Lentz, D.; Schäfer, A.; Samorì, P.; Rabe, J. P.; Franke, P.; Schlüter, A. D. *J. Am. Chem. Soc.* **2003**, *125*, 6907–6918.

13. Campbell, K.; Tiemstra, N. M.; Prepas–Strobeck, N. S.; McDonald, R.; Ferguson, M. J.; Tykwinski, R. R. *Synlett* **2004**, 182–186.

14. Zhao, Y.; Campbell, K.; Tykwinski, R. R. *J. Org. Chem.* **2002**, *67*, 336–344.

15. Eisler, S.; Tykwinski, R. R.; *Angew. Chem. Int. Ed.* **1999**, *38*, 1940–1943.

16. Stang, P. J.; Fisk, T. E. *Synthesis* **1979**, 438–440.

17. (a) Orfanopoulos, M.; Stratakis, M.; Elemes, Y. *Tetrahedron Lett.* **1989**, *30*, 4875–4878. (b) Orfanopoulos, M.; Stratakis, M.; Elemes, Y. *J. Am. Chem. Soc.* **1990**, *112*, 6417–6419. (c) Clennan, E. L.; Chen, X.; Koola, J. J. *J. Am. Chem. Soc.* **1990**, *112*, 5193–5199.

18. (a) Slepkov, A. D.; Hegmann, F. A.; Zhao, Y.; Tykwinski, R. R.; Kamada, K. *J. Chem. Phys.* **2002**, *116*, 3834–3840. (b) Zhao, Y.; Slepkov, A. D.; Akoto, C. O.; McDonald, R.; Hegmann, F. A.; Tykwinski, R. R. *Chem. Eur. J.*, in press.

19. Neenan, T. X.; Whitesides, G. M. *J. Org. Chem.* **1988**, *53*, 2489–2496.

20. Weder, C.; Wrighton, M. S. *Macromolecules* **1996**, *29*, 5157–5165.

21. Zhou, Q.; Carroll, P. J.; Swager, T. M. *J. Org. Chem.* **1994**, *59*, 1294–1301.

22. Eisler, S.; McDonald, R.; Loppnow, G. R.; Tykwinski, R. R. *J. Am. Chem. Soc.* **2000**, *122*, 6917–6928.

23. Bunten, K. A.; Kakkar, A. K. *Macromolecules* **1996**, *29*, 2885–2893.

24. Rege, P. D.; Malkina, O. L.; Goroff, N. S. *J. Am. Chem. Soc.* **2002**, *124*, 370–371.

25. Gao, K.; Goroff, N. S. *J. Am. Chem. Soc.* **2000**, *122*, 9320–9321.

Chapter 3 Expanded Pyridines and Bipyridines – Supramolecular Building Blocks

3.1 Introduction

As introduced in Chapter 2, carbon–rich, conjugated macrocycles are of considerable interest due to their potential as new materials with shape–persistent structures and desirable physical properties.[1] What is particularly appealing about this class of molecules is their high degree of tunability. The physical characteristics of these conjugated scaffolds can be easily modified through the application of appropriate design features. Through the covalent incorporation of functional groups, for example, their structures can be manipulated to provide desirable physical properties tailored for specific applications. In particular, coordinative functionality such as the nitrogen(s) of pyridine or bipyridine, directed toward the interior of macrocycles has been exploited in the design of artificial receptors[2] and ion sensors.[3]

We became intrigued by the idea of introducing functionality into a cross–conjugated, macrocyclic framework to provide a system capable of binding to metals and/or metal ions. Specifically, the incorporation of pyridine(s) such that the nitrogen(s) are directed away from the cyclic core could afford a ligand that, while still possessing all of the desirable attributes of a conjugated macrocycle, could also participate in self-assembly reactions.[4] Such a ligand could provide a variety of new hybrid architectures that feature metal atoms linked by a highly unsaturated, porous macrocycle.

Bipyridines and related pyridine–based ligands are among the most widely used constituents[5] of supramolecular assemblies, due in part to their rigidity and directed coordinative ability. This is particularly true of 4,4′-bipyridine,[6] which is frequently employed toward the realization of discrete, highly ordered nanostructures based on transition metal coordination. Macrocyclic ligands based on a 3,5–diethynylpyridine building block were therefore designed, with the expectation that they could function as pyridine and 4,4′–bipyridine analogues. The directed, exocyclic orientation of the pyridyl nitrogens ensures their predictable assembly into well-defined supramolecular scaffolds. Unlike bipyridines, however, the targeted macrocycles could potentially provide for the formation of porous solid–state structures through the presence of the rigid, shape–persistent core (Figure 3.1).

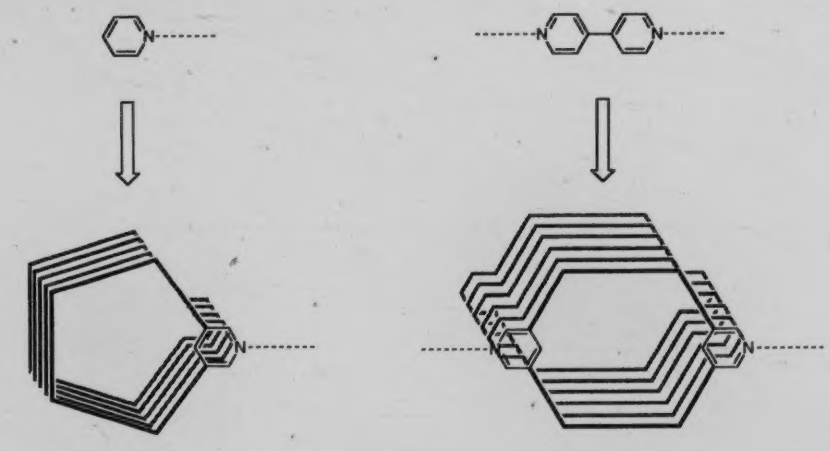

Figure 3.1 Schematic representation of porous pyridine and 4,4′–bipyridine analogues.

This chapter describes the synthesis of several oligomeric, pyridine–containing precursors and the resulting porous ligands that we have constructed using these building blocks. We have demonstrated the coordinative ability of these macrocyclic pyridine analogues via axial coordination to a ruthenium porphyrin to give the corresponding supramolecular assemblies. These structures were targeted due to the widespread interest in multiporphyrin architectures,[7] in addition to the well-established photophysical features of porphyrins.[8] X-ray crystallographic analysis of these assemblies has established the ability of these macrocycles to form highly ordered crystalline materials and has provided insight into the scope and limitations of these macrocyclic ligands as supramolecular building blocks.

3.2 Results and Discussion

3.2.1 Synthesis of Pyridine–Containing Oligomers and Macrocycles

Our initial synthetic efforts focused on the synthesis of a series of pyridine–containing oligomers that could be elaborated to provide the desired supramolecular building blocks. The synthesis of oligomers **302a–c**, **303b**, and **303c** is detailed in Scheme 3.1. Readily available 3,5–diethynylpyridine[9] **301** was cross–coupled[10] with the appropriate vinyl triflate[11] **202a–c** to provide oligomers **302a–c** using $Pd(PPh_3)_4$ as catalyst and CuI as cocatalyst. In general, all cross–coupling reactions were performed using 5% of the palladium catalyst, and 15% of the copper co–catalyst, per coupling event. All reactions were performed in dry, degassed THF in the presence of Et_2NH to facilitate formation of the copper–acetylide intermediate. The reactions to provide **302a** and **302b** proceeded rapidly at room temperature and were complete in less than one hour. By contrast, the coupling reaction to form **302c** required heating to 55 °C for a period of 24 hours. Compounds **302a–c** were isolated as stable, colourless solids in 79, 67, and 61% yields, respectively, following purification using chromatographic separation on alumina.

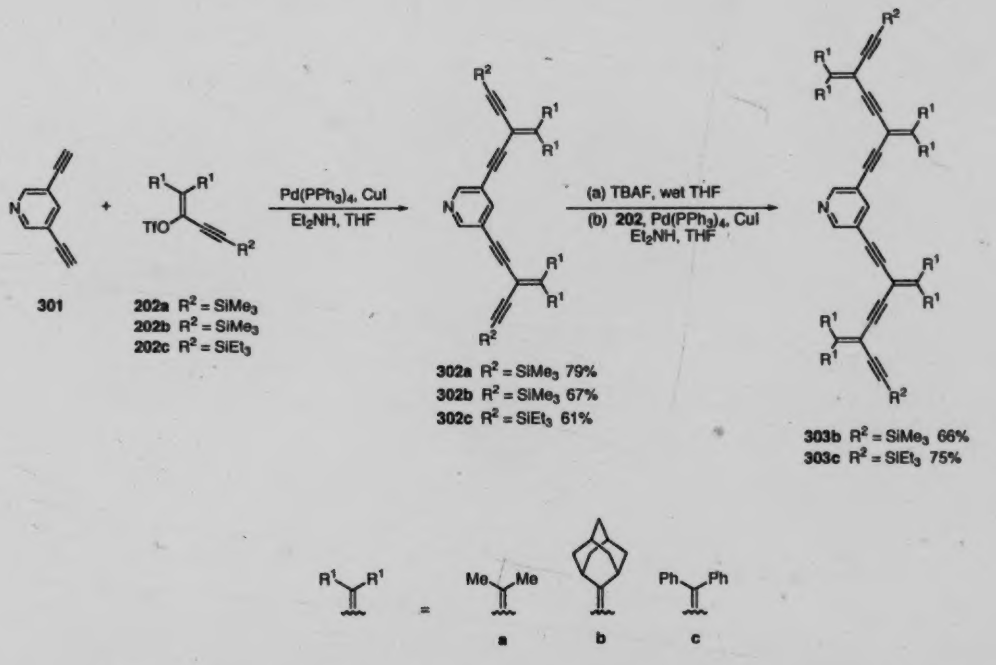
301
202a R^2 = SiMe$_3$
202b R^2 = SiMe$_3$
202c R^2 = SiEt$_3$
Pd(PPh$_3$)$_4$, CuI
Et$_2$NH, THF
302a R^2 = SiMe$_3$ 79%
302b R^2 = SiMe$_3$ 67%
302c R^2 = SiEt$_3$ 61%
(a) TBAF, wet THF
(b) 202, Pd(PPh$_3$)$_4$, CuI
Et$_2$NH, THF
303b R^2 = SiMe$_3$ 66%
303c R^2 = SiEt$_3$ 75%
a
b
c

Scheme 3.1 Synthesis of pyridine–containing oligomers **302a–c**, **303b**, and **303c**.

Tetraynes **302b** and **302c** were then elaborated via a second iteration of the cross–coupling step to form the expanded oligomers **303b** and **303c**. Treatment of **302b** and **302c** with TBAF in wet THF effected the removal of the silyl–protecting groups. The deprotected tetraynes were carried on subsequent to an aqueous workup, with no further purification, to a second palladium–catalyzed cross–coupling reaction with triflate **202b** or **202c**. The reaction to form the diphenylalkylidene substituted oligomer **303c** again required heating for an extended period to complete the transformation. By contrast, the reaction to form **303b** was complete after stirring at room temperature for 1 hour. Solids **303b** and **303c** were achieved in 66 and 75% yields, respectively, following chromatographic purification on alumina. All oligomeric species **302a–c**,

303b, and **303c** were fully characterized using IR, ^{1}H, and ^{13}C NMR spectroscopies, as well as high–resolution mass spectrometry.

Oligomers **303b** and **303c** were then elaborated to form the macrocyclic pyridine analogues **304b** and **304c** as outlined in Scheme 3.2. Treatment of the trialkylsilyl–protected acetylenic oligomers with TBAF in wet THF led to the formation of the terminal acetylenes which were carried on, subsequent to an aqueous workup, to an intramolecular oxidative homocoupling[12] reaction. CuI, in the presence of TMEDA and oxygen, was used to effect this process[13] leading to the formation of **304b** and **304c** in 75 and 53% yields, respectively. Macrocycles **304b** and **304c** are gratifyingly stable and soluble solids, allowing for their purification using chromatography on alumina.

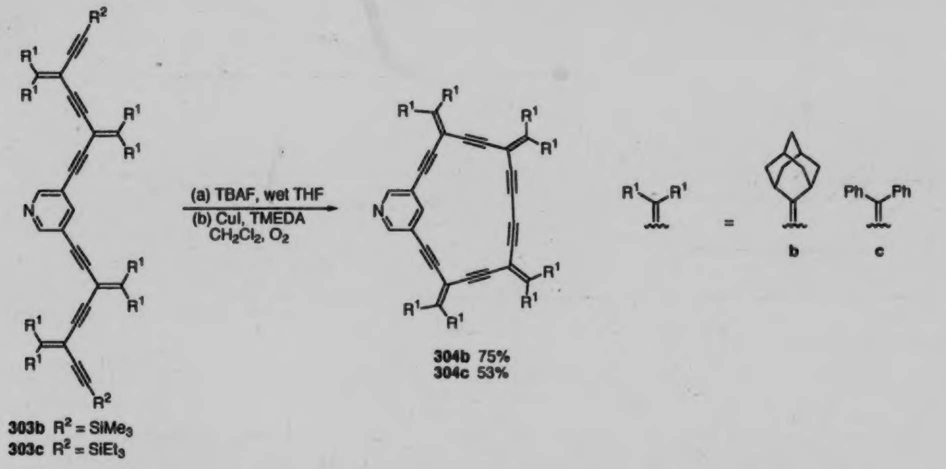

Scheme 3.2 Synthesis of expanded pyridine macrocycles **304b**, and **304c**.

Both macrocycles **304b** and **304c** were fully characterized using IR, ^{1}H, and ^{13}C NMR spectroscopy as well as mass spectral analysis. Analysis of the ^{1}H NMR (300 MHz, CD_2Cl_2) spectrum of **304b** shows resonances for the *ortho*– and *para*–pyridyl protons at 8.56 and 7.97 ppm, respectively. The adamantyl methine protons α to the alkylidene carbons appear as broad singlets at δ 3.36 (2H), 3.29 (2H), and 3.20 (4H). The remaining adamantyl protons appear as a broad multiplet at 2.09 – 1.86 ppm. The ^{13}C NMR spectrum (75 MHz, CD_2Cl_2) of **304b** shows all of the expected non–equivalent aromatic, alkynyl, and alkylidene carbon resonances. In the upfield region of the spectrum, only 10 of the expected 14 methine and methylene adamantyl carbon resonances are observed due to coincidental overlap. ESI mass spectral analysis supported the structure of **304b**, with a signal at *m/z* 806.5 (100%) corresponding to $[M + H]^+$.

The ^{1}H NMR spectrum of **304c** also showed resonances for the *ortho–* and *para–*pyridyl protons in the downfield region at δ 8.21 (d, 2H) and 7.90 (t, 1H), respectively. The remaining (all aromatic) protons appeared as a multiplet at 7.44 – 7.07 ppm. The ^{13}C NMR spectrum (125 MHz, CD_2Cl_2) remarkably shows 27 of the 29 expected non–equivalent resonances. The alkylidene carbons give signals at 159.2, 155.4, 101.5, and 101.0 ppm. The six alkynyl carbons resonate further upfield between 93.5 – 76.0 ppm. Only 17 of the expected 19 aromatic carbon resonances appear in the range of 149.8 – 120.2 ppm, due to coincidental overlap of three aromatic methine carbons. The structure of **304c** was also supported through high–resolution ESI mass spectral analysis which showed a peak for $[M + H]^+$ at *m/z* 934.3475 (100%) (calcd. for $C_{73}H_{44}N$ is 934.3474).

We next turned our attention to the synthesis of bidentate supramolecular building blocks, **305a–c**. Our first target was the isopropylidene–derivatized macrocycle **305a** (Scheme 3.3). Deprotection of the trimethylsilyl–protected acetylenes of **302a** was achieved by treating with methanolic K_2CO_3. The resulting tetrayne was then carried on, subsequent to an aqueous workup, to an intermolecular oxidative acetylenic homocoupling reaction, via treatment with CuI and TMEDA at high dilution in CH_2Cl_2 in the presence of air. The reaction was stirred at room temperature until TLC analysis indicated the absence of any of the starting tetrayne, about 1.5 hours. Following aqueous workup, the solvent volume was reduced to afford a solid mixture containing **305a** and what was presumed to be oligomeric byproducts. This mixture was extremely insoluble in organic solvents, making column chromatography impractical. As well, all attempts to selectively extract **305a** from this mixture were unsuccessful.

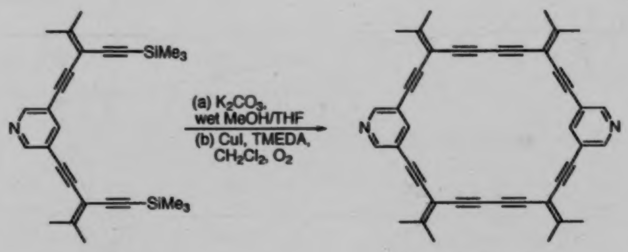

302a

305a not isolated

Scheme 3.3 Synthesis of bidentate macrocycle **305a**.

We then focused on adamantylidene–substituted macrocycle **305b**, expecting that both the solubility and stability of the macrocyclic ligand would be improved with the incorporation of this functionality. Following deprotection, the tetrayne **302b** was subjected to standard oxidative coupling conditions as shown in Scheme 3.4. Surprisingly, none of the anticipated macrocyclic product **305b** was observed. Instead, the only isolated product was the iodinated oligomer, **306**. This product is presumably formed via reductive elimination across a Cu(II) species to yield the alkynyl iodide, as previously discussed in Chapter 2. Attempts to perform the analogous homocoupling reaction of the deprotected oligomer using CuCl as the catalyst were then targeted. After monitoring the reaction for 5 days, however, TLC analysis still revealed the presence of a significant amount of the starting material, even after bubbling oxygen through the reaction mixture. As oxidative coupling reactions are often favored by strong base and rigidly anhydrous reaction conditions,[12] our strategy was again modified. Oxygen was vigorously bubbled through a solution of deprotected **302b**, CuCl, and DBU in pyridine over molecular sieves for 14 hours. Subsequent to aqueous work–up, ^{1}H NMR and mass spectral analysis of the crude product revealed the presence of the protonated macrocyclic product **305b**. Unfortunately, all attempts to isolate the pure, deprotonated macrocyclic species **305b** were unsuccessful.

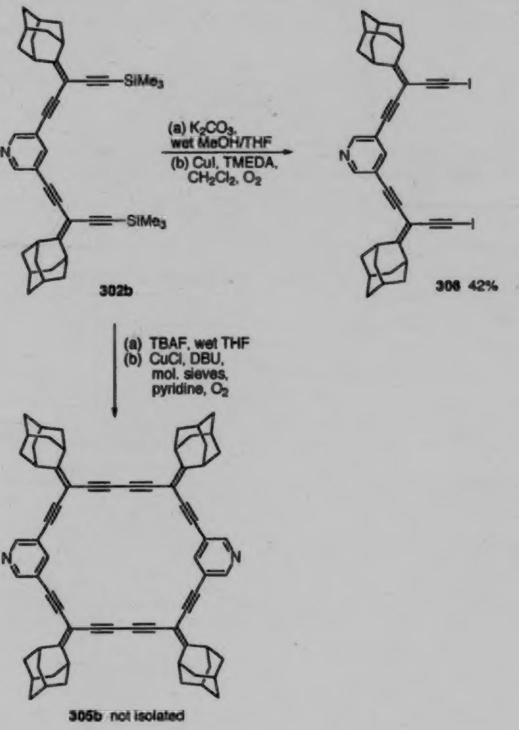
SiMe3
SiMe3
N
(a) K2CO3, wet MeOH/THF
(b) CuI, TMEDA, CH2Cl2, O2
I
I
N
302b
306 42%
(a) TBAF, wet THF
(b) CuCl, DBU, mol. sieves, pyridine, O2
N
N
305b not isolated

Scheme 3.4 Synthetic efforts toward macrocyclic ligand **305b**.

The next modification to the synthesis was to incorporate diphenylalkylidene functionality. It was anticipated that the greater solubility and stability imparted to the system via the incorporation of the diphenylalkylidene substitution would facilitate purification and characterization of the resultant macrocycle **305c**. Desilylation of **302c** was effected by treatment with TBAF in wet THF. This afforded the deprotected tetrayne, which was subjected to intermolecular homocoupling conditions (CuI/TMEDA in CH_2Cl_2, in the presence of air) as shown in Scheme 3.5. After the addition of ether to the reaction mixture, washing with sat'd NH_4Cl and drying, the solvent was reduced by about 80%, leading to the formation of a bright yellow precipitate. This solid was filtered and dried to give pure **305c** in 52% yield. It is worth noting that pure **305c** has been accessible by this method alone. All attempts to isolate **305c** from the crude reaction mixture subsequent to evaporation of the solvent have been unsuccessful. As with macrocycle **305a**, the crude reaction mixture is quite insoluble and, therefore, difficult to purify by column chromatography. Likewise, attempts to resolvate the crude reaction mixture and then recrystallize **305c** have been equally unsuccessful. While the ligand **305c** is marginally soluble (less than 2 mg/mL in CH_2Cl_2), it is quite stable to air, heat, and light, and it may be stored for months under refrigeration without observable degradation. It decomposes thermally only at temperatures exceeding 170 °C. As a result of the extremely limited solubility of **305c**, meaningful ^{13}C NMR spectroscopic analysis was not possible, but the ^1H NMR spectrum of **305c** was consistent with the proposed structure. The most convincing evidence for the formation of the macrocycle **305c** was provided by ESI high resolution mass spectral analysis which showed a signal at *m/z* 1059.3738 corresponding to [M + H]$^+$ (calcd for $C_{42}H_{47}N_2$ is *m/z* 1059.3734).

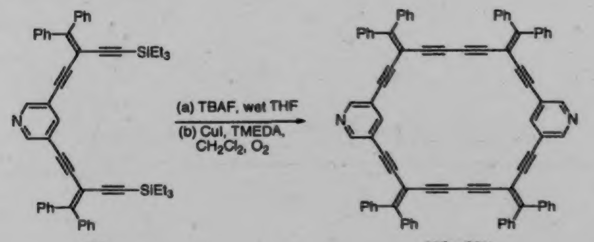

302c

305c 52%

Scheme 3.5 Synthesis of diphenylalkylidene–substituted macrocycle **305c**.

3.2.2 Solid–State Properties of Pyridine–Containing Oligomers

Single crystals of **302b** and **302c**, suitable for X–ray crystallographic analysis were grown by slow evaporation from CH_2Cl_2/acetone and acetone solutions, respectively, at 4 °C. The ORTEP drawings are shown in Figure 3.2. While **302b** has adopted a conformation where the silyl–protected acetylenes are directed away from the nitrogen of the pyridine ring, the acetylenes of **302c** have adopted the opposite conformation and appear on the same side of the molecule as the nitrogen of the pyridyl ring. Despite this obvious difference, both oligomers have adopted a nearly planar conformation in the solid–state. The degree of planarity can be established through analysis of the least–squares planes of the structures. For **302b**, the dihedral angle between plane 1 (defined by N–C(1)–C(2)–C(3)–C(4)–C(5)) and plane 2 (defined by C(11)–C(12)–C(13)–C(30)) is measured at 7.1(2)°. The dihedral angles between plane 1 and plane 3 (defined by C(16)–C(17)–C(18)–C(40)) and plane 2 and plane 3 are 10.32(19)° and 9.2(2)°, respectively.

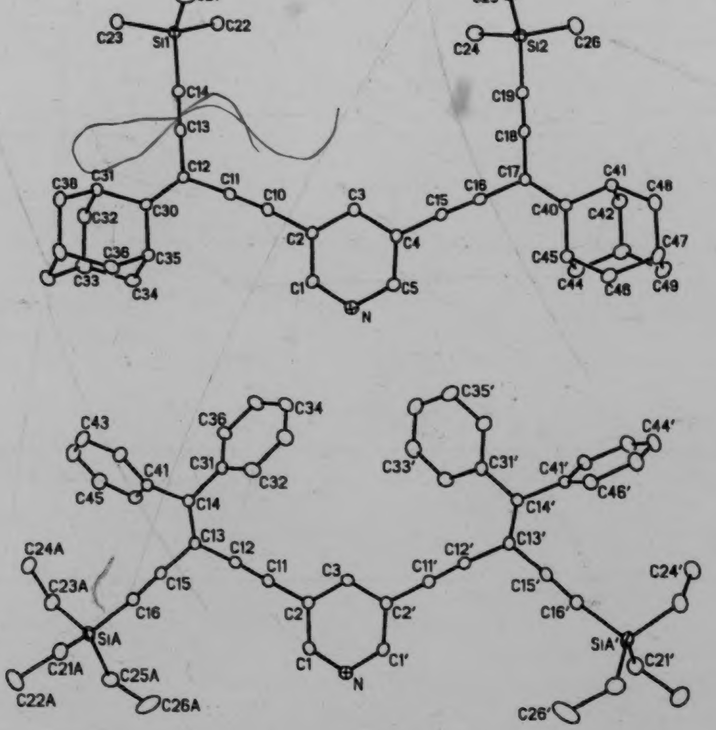
C21
C22
C23
Si1
C14
C13
C12
C11
C10
C3
C15
C16
C17
C18
C19
Si2
C24
C25
C26
C41
C48
C40
C42
C47
C45
C44
C46
C49
C4
C5
N
C1
C2
C38
C31
C32
C30
C36
C35
C33
C34
C43
C36
C34
C41
C31
C32
C45
C14
C13
C12
C11
C3
C24A
C23A
C15
C16
SiA
C21A
C22A
C25A
C26A
C2
C1
N
C2'
C1'
C11'
C12'
C13'
C14'
C15'
C16'
SiA'
C21'
C24'
C26'
C31'
C33'
C35'
C41'
C44'
C46'

Figure 3.2 (Top) ORTEP drawing of adamantylidene–functionalized oligomer **302b**. Selected bond lengths [Å] and angles [°]: C(10)–C(11) 1.193(3), C(13)–C(14) 1.208(3), C(15)–C(16) 1.192(3), C(18)–C(19) 1.206(3); Si(1)–C(14)–C(13) 178.3(2), C(12)–C(13)–C(14) 179.0(2), C(10)–C(11)–C(12) 177.9(3), C(2)–C(10)–C(11) 174.4(2), C(4)–C(15)–C(16) 175.5(2), C(15)–C(16)–C(17) 177.0(3), C(17)–C(18)–C(19) 175.9(3), Si(2)–C(19)–C(18) 176.3(2), C(16)–C(17)–C(18) 115.81(19), C(11)–C(12)–C(13) 116.29(19). (Bottom) ORTEP drawing of diphenylalkylidene–functionalized oligomer **302c**. Selected bond lengths [Å] and angles [°]: C(11)–C(12) 1.191(2), C(15)–C(16) 1.199(2); SiA–C(16)–C(15) 173.9(2), C(13)–C(15)–C(16) 177.2(2), C(11)–C(12)–C(13) 176.32(18), C(2)–C(11)–C(12) 178.4(2), C(12)–C(13)–C(15) 113.67(14). Thermal ellipsoids are drawn at the 20% probability level.

Oligomer **302c** has adopted a slightly more planar conformation as evidenced by measurement of the analogous dihedral angles. The angle between plane 1 (defined by

N–C(1)–C(2)–C(3)–C(1′)–C(2′)) and plane 2 (defined by C(12)–C(13)–C(14)–C(15)) is 3.80(13)°. The dihedral angle between plane 2 and plane 2′ (defined by C(12′)–C(13′)–C(14′)–C(15′)) is measured to be 7.58(13)°.

All of the alkylidene and alkynyl bond angles of **302b** are slightly distorted from ideality with mean values of 116.05 and 176.8°, respectively. By contrast, the mean alkyne bond angle for **302c** was determined to be 176.5° and the vinylidene angle was measured at 113.67(14)° for C(12)–C(13)–C(15). This small increase in strain is likely the result of crystal packing effects, rather than an effect of the pendant substitution.

Single crystals of extended oligomer **303c,** suitable for X–ray crystallographic analysis, were grown by slow diffusion of an Et_2O/MeOH solution at 4 °C. The ORTEP drawing is shown in Figure 3.3. This structure is slightly more distorted than those of the shorter oligomers **302b** and **302c** with a mean alkyne bond angle of 175.1°. The largest deviation from ideality appears in the alkynyl bond C(25)–C(26)–C(27) which is measured at 171.1(6)°. The alkylidene angles are similarly distorted with a mean value of 113.8° and a maximum deviation of 8.1° for C(26)–C(27)–C(29). The structure is otherwise unremarkable, other than noting that it is exceptional that the material formed a highly crystalline solid, given the lack of symmetry in the resultant structure and the high degree of flexibility inherent in **303c**.

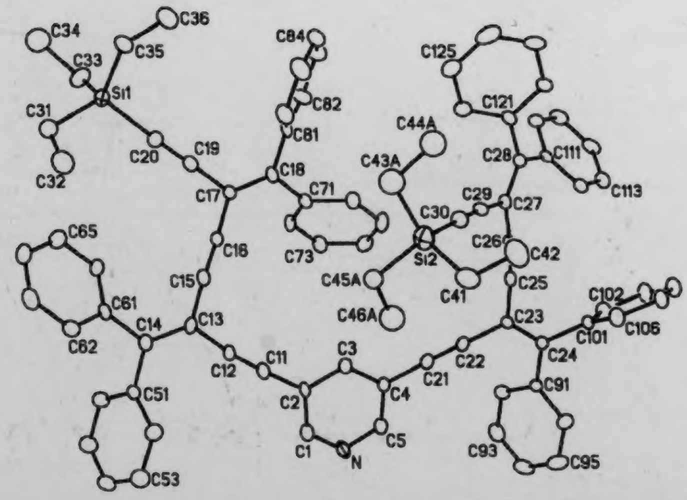
C34
C36
C33
C35
Si1
C31
C20
C19
C32
C84
C82
C81
C18
C17
C71
C125
C121
C44A
C43A
C28
C111
C113
C30
C29
C27
C26
C42
Si2
C65
C16
C73
C15
C45A
C25
C41
C102
C61
C14
C13
C46A
C23
C101
C106
C62
C11
C3
C22
C24
C12
C21
C4
C91
C51
C2
C1
N
C5
C93
C95
C53

Figure 3.3 ORTEP drawing of diphenylalkylidene–functionalized oligomer **303c**. Selected bond lengths [Å] and angles [°]: C(11)–C(12) 1.187(6), C(15)–C(16) 1.195(7), C(19)–C(20) 1.198(6), C(21)–C(22) 1.181(6), C(25)–C(26) 1.199(7), C(29)–C(30) 1.198(6); C(16)–C(17)–C(19) 114.4(4), C(12)–C(13)–C(15) 114.1(5), C(22)–C(23)–C(25) 114.6(4), C(26)–C(27)–C(29) 111.9(5). Thermal ellipsoids are drawn at the 20% probability level.

3.2.3 Synthesis of Porphyrinic Supramolecular Assemblies

Having successfully synthesized several pyridine–containing macrocycles, we chose to demonstrate the coordinative ability of these ligands by axially coordinating them to metalloporphyrin **307**. These structures were targeted due to a widespread interest in the preparation of porphyrin and multiporphyrin architectures.[7] This particular ruthenium–porphyrin was selected by our collaborator, Prof. Neil Branda as it was a common building block used by members of his research group at the outset of this project. Porphyrin **307** was easily synthesized[14] from readily available starting materials, and its ability to coordinate to pyridine and pyridine–containing ligands is well–established.[15]

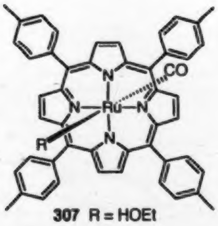

307 R = HOEt

In many cases throughout this thesis, the highly soluble and easily accessible ligand **304** is used as a model compound to establish the feasibility of reactions featuring the less–accessible bidentate ligand **305**. Thus, our initial synthetic efforts focused on the preparation of assemblies **308b** and **308c** as shown in Scheme 3.6. Addition of 1 equivalent of ruthenium porphyrin **307** to a solution of **304b** in CH_2Cl_2 led to the formation of a single product as indicated by TLC analysis. Purification of **308b** was achieved using column chromatography on alumina, leading to the isolation of the pure assembly in 80% yield.

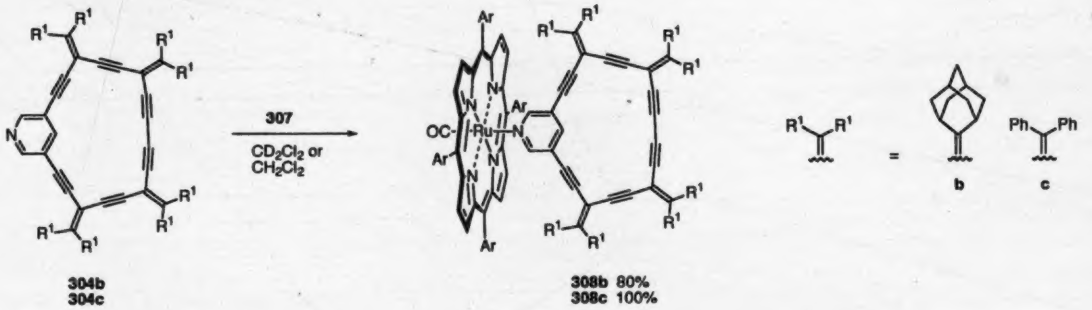

Scheme 3.6 Synthesis of supramolecular assemblies **308b** and **308c**.

By contrast, when the porphyrin **307** was added to a CH_2Cl_2 solution of **304c**, TLC analysis showed only the presence of the starting materials, **307** and **304c**. ^1H NMR spectroscopic analysis of the crude reaction mixture (*vide infra*), however, suggested that the desired supramolecular assembly *had* formed, which indicated that

308c was simply not stable to the chromatographic conditions. To achieve pure **308c**, a solution of **307** in CD_2Cl_2 was slowly titrated into an NMR tube containing ligand **304c** in CD_2Cl_2. This resulted in the quantitative isolation of the pure supramolecular assembly **308c**, upon solvent removal and drying. In general, the greatest success was achieved through careful control of stoichiometry via NMR titration experiments, allowing for the quantitative formation of the pure assemblies without the need for subsequent purification(s).

Following these successful experiments, we next turned our attention to the formation of assemblies **309**, featuring the expanded 4,4′–bipyridine ligands (Scheme 3.7). While macrocycle **305a** had not been realized in its pure form, to our surprise, treatment of the insoluble product mixture that contained **305a** with 2 equivalents of porphyrin **307** (based on **302a**) in CH_2Cl_2 resulted in a bright red solution, with only traces of the insoluble material remaining. TLC analysis (alumina) of this solution clearly indicated the formation of only one product. Not unexpectedly, coordination to the porphyrin resulted in a product with vastly increased solubility. This allowed for the isolation of assembly **309a** as a dark red solid, in 39% yield (overall from **302a**), via column chromatography on neutral alumina. Excess porphyrin remaining from the reaction could be easily recovered by flushing the column with $EtOH/CH_2Cl_2$ following the isolation of **309a**. While pure **309a** shows limited stability under ambient conditions, it can be stored indefinitely under refrigeration. Thermally, the assembly **309a** decomposes at 132 °C.

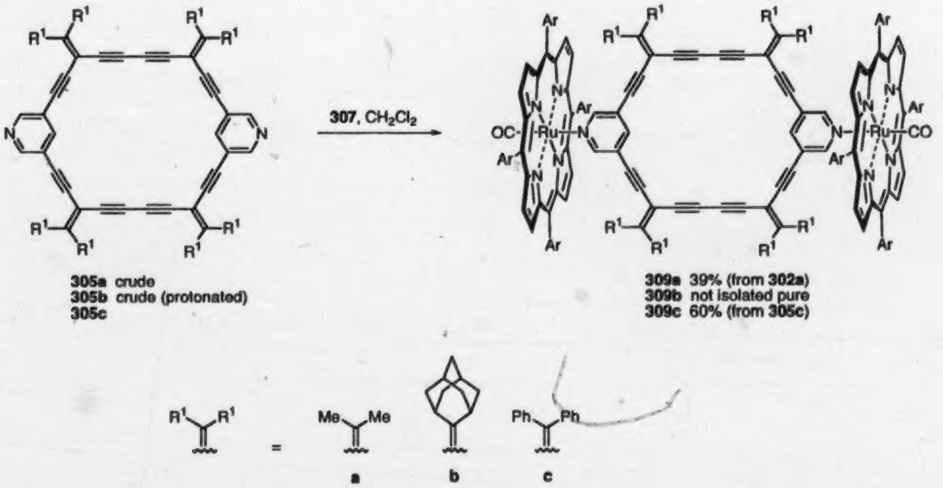

Scheme 3.7 Synthesis of supramolecular assemblies **309a** and **309c**.

Due to the success of this strategy, porphyrin **307** was then added to the crude reaction mixture containing the adamantylidene–functionalized macrocycle **305b**, (following treatment with base) in an attempt to mediate the purification of this species. ESI mass spectral analysis revealed the presence of the desired assembly product **309b**, but all efforts to purify **309b** via recrystallization and chromatography were unsuccessful. While further efforts would likely allow for the isolation **305b** and the corresponding assembly **309b**, this synthesis produced such low yields of the desired product that to do so was considered impractical, and this synthetic sequence was abandoned.

The self–assembly reaction of pure **305c** with porphyrin **307** was performed in CH_2Cl_2 via addition of 2 equivalents of porphyrin **307**. Crystallization from CH_2Cl_2 allowed for isolation of the desired assembly **309c** in 60% yield as a bright red solid. The progress of the assembly reaction, like the previous examples, can be monitored by ^1H NMR spectroscopy. Aliquots of **307** were slowly added to a dilute solution of **305c** in CD_2Cl_2, resulting in the formation of the assembly product **309c**. The reaction appears to proceed quantitatively based on NMR analysis. Despite the apparent high yield of the self-assembly reaction, the moderate isolated yield of **309c** is due to the less robust nature of **309c** in comparison to that of the isopropylidene functionalized analogue, **309a**. Unlike **309a**, the macrocyclic portion of **309c** dissociates from the ruthenium–porphyrin when subjected to chromatography, with either alumina or silica, regardless of solvent. Whereas the complex **309c** shows far greater solubility in CH_2Cl_2 in comparison to macrocycle **305c**, attempts to selectively crystallize the complex from a CH_2Cl_2 solution via the addition of other solvents (e.g., hexanes, ether, toluene) results in the dissociation of complex **309c** and the precipitation of macrocycle **305c**. This behavior is in stark contrast to complex **309a**, which precipitates intact from solution, despite the fact that macrocycle **305a** is considerably less soluble than **305c**. In the solid state, however, **309c** is thermally quite stable, decomposing at greater than 250 °C.

The most convincing evidence for the formation of the porphyrinic assemblies **308b**, **308c** and **309a**, **309c** in solution comes primarily from NMR spectroscopic analysis. In the ^{1}H NMR spectrum of **305c**, for example, the *ortho–* and *para–*pyridyl protons give rise to signals at 8.13 and 7.83 ppm, respectively (Figure 3.4). Upon assembly with the tetratolylporphyrin **307**, these protons are significantly shielded to δ 1.12 and 6.08, respectively, due to the diamagnetic anisotropy of the porphyrin ring (Figure 3.4, bottom). The *ortho–* and *para–*pyridyl protons of **308c** (which also features the diphenylalkylidene substitution) resonate at nearly identical chemical shifts of δ 1.19 and 6.37. As can be seen, the anisotropic effect of the porphyrin ring is especially dramatic for the *ortho*–protons, due to their proximity to the porphyrin. The *ortho*– and *para*–protons of **308b** appear at 1.26 and 6.30 ppm, respectively. Similarly, the ^1H NMR spectrum of assembly **309a** shows the *ortho*– and *para*–pyridyl proton signals at 1.30 and 6.04 ppm, respectively.

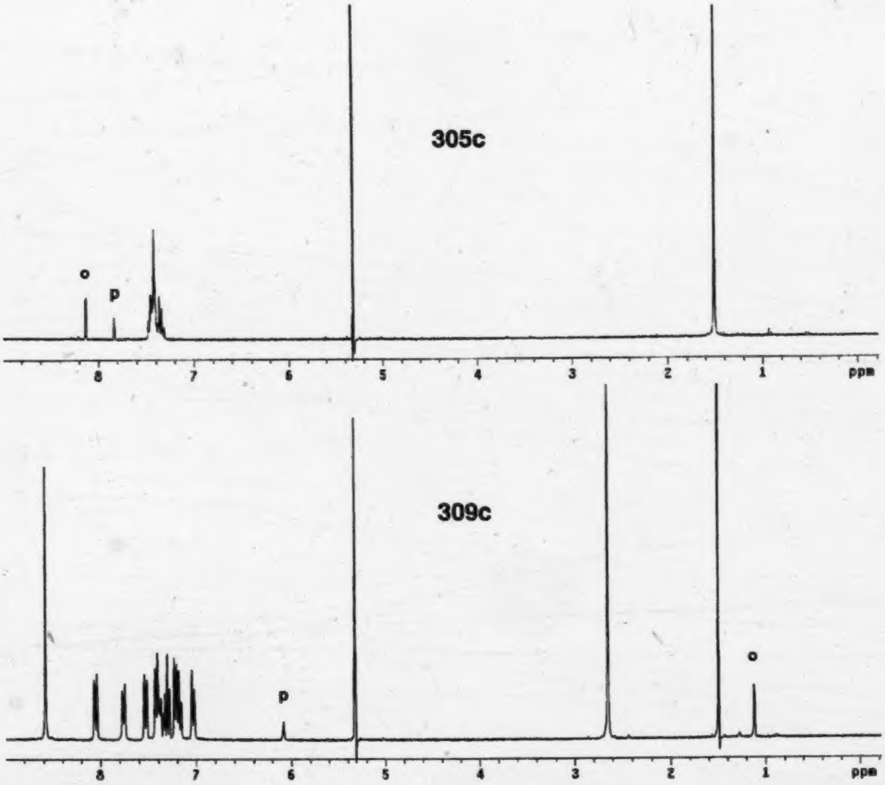

Figure 3.4 (Top) ^1H NMR spectrum (300 MHz, CD_2Cl_2) of **305c** highlighting the *ortho*– and *para*–pyridyl protons. (Bottom) ^1H NMR spectrum (300 MHz, CD_2Cl_2) of **309c**.

Two–dimensional gHMQC NMR analyses for **308b**, **308c** and **309a**, **309c** provided confirmation of these proton assignments. As shown in Figure 3.5, the signals ascribed to the *ortho*– and *para*–pyridyl protons of **309c** correlate to signals at ca. 145.2

and 139.6 ppm, respectively, on the F2 axis of the spectrum, consistent with the chemical shifts expected for these pyridyl carbons.

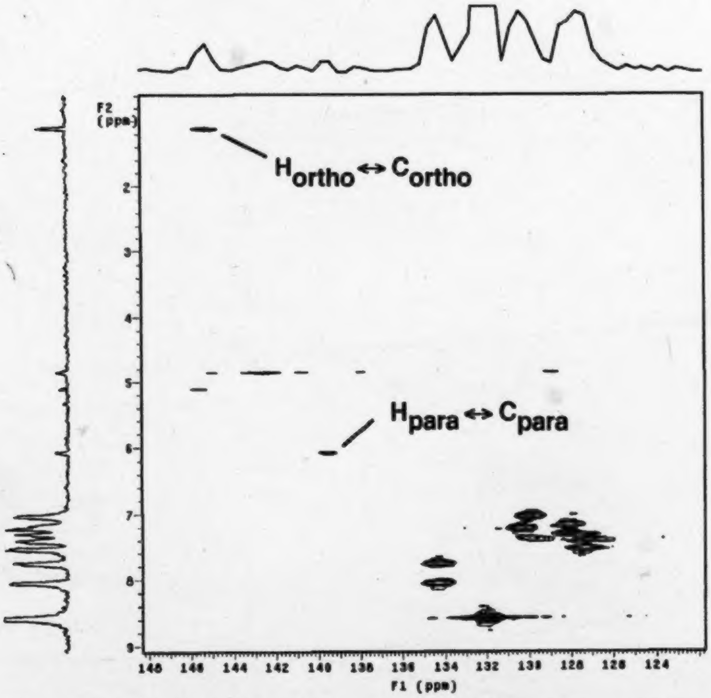

Figure 3.5 gHMQC NMR spectrum (500 MHz, CH_2Cl_2) of assembly **309c** showing correlations for *ortho*– and *para*–pyridyl protons.

The solution state presence of complexes **308b**, **308c** and **309a**, **309c** is also supported by MS analysis. The ESI mass spectra of **308b** and **308c** each show signals consistent with $[M + H]^+$ at *m/z* 1605 (47% intensity) and 1733.5 (16% intensity), respectively. In the ESI mass spectrum of **309a** (nitromethane), a cluster of signals centred at *m/z* 2160 (3% intensity) is observed. Comparison of the calculated and observed isotopic distribution patterns for **309a** suggests that these signals are consistent with a combination of protonated $[M + H]^+$ and radical cation species $[M]^{+\bullet}$. A fragment peak of greater intensity (21%) is observed at *m/z* 1361, resulting from the loss of one porphyrin unit. The isotopic distribution of this peak also suggests the presence of both the radical cationic and protonated species. Other significant fragments include peaks at *m/z* 798 (100% intensity, radical cation) corresponding to the porphyrin and at *m/z* 563 (92%) representing the protonated macrocyclic ligand [**305a** + H]$^+$. Numerous attempts were made to improve the intensity of the $[M + H]^+$ and/or $[M]^{+\bullet}$ peaks including: varying the applied voltage, using different combinations of solvents, and acquiring the spectra at lower temperatures. All strategies resulted in a loss of sensitivity with no significant gains in intensity.

For the less robust assembly, **309c**, an $[M + H]^+$ signal is not found in the ESI mass spectrum. A signal at *m/z* 1856 (3%) is observed, corresponding to the fragment resulting from the loss of one porphyrin moiety. MALDI-TOF analysis has also been employed for **309c**, with 1,8,9–trihydroxyanthracene as the matrix and irradiation at 337 nm. The most diagnostic signal is found at *m/z* 1829, corresponding to the assembly **309c** with the loss of one complete porphyrin moiety as well as the CO of the second porphyrin. As the photochemical dissociation of CO from ruthenium porphyrins is well known,[16] this fragmentation is not unexpected considering the irradiation wavelength. In addition to the protonated macrocycle at *m/z* 1059.9, signals corresponding to the porphyrin radical cation (*m/z* 770.4) and a porphyrin dimer (*m/z* 1535.2, where both species are decarbonylated) are also clearly present in the spectrum.

3.2.4 Solid–State Characterization of Supramolecular Assemblies

Single crystals of **309a** suitable for X–ray crystallographic analysis were obtained from a crude reaction mixture containing **309a** and excess porphyrin **307** in CH_2Cl_2. The complex **309a** co–crystallized with one equivalent of **307** such that the excess porphyrin is captured between the layers of the assembly product. An ORTEP drawing of **309a** is shown in Figure 3.6 (top), and the internal dimensions of the macrocycle circumscribed by the enyne scaffold provides a cavity of 6.4 by 10 Å. The framework of the macrocyclic core is virtually planar. It also appears to be nearly free from strain, as all alkyne angles are within 8.2° of the expected value of 180° with a mean deviation of 3.6°. Furthermore, the alkylidene bond angles C(77)–C(78)–C(82) and C(85)–C(86)–C(90) at 113.7 and 115.5° are quite similar to those found for the analogous acyclic systems, **302b**, **302c**, and **303c**, which were described earlier.

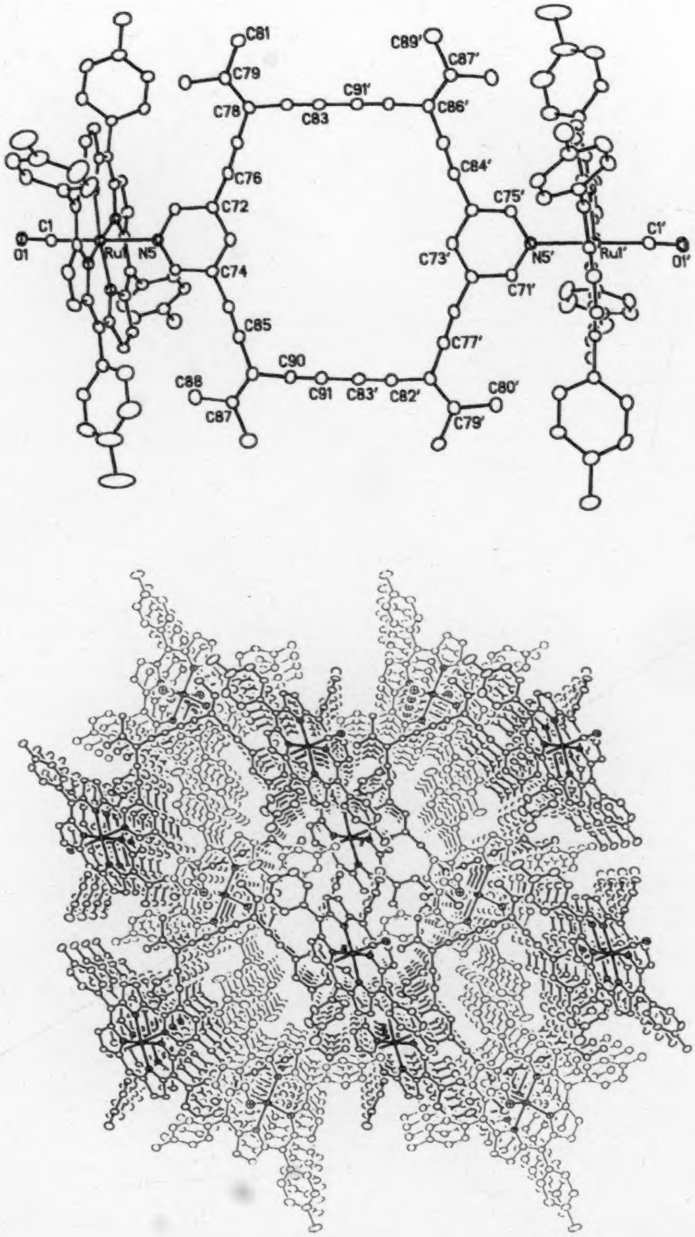
C81
C79
C78
C83
C91'
C89'
C87'
C86'
C84'
C76
C72
C75'
O1
C1
Ru1
N5
C73'
N5'
Ru1'
C1'
O1'
C74
C71'
C85
C77'
C90
C88
C87
C91
C83'
C82'
C80'
C79'

Figure 3.6 (Top) ORTEP drawing of supramolecular assembly **309a**. Selected bond lengths [Å] and angles [°]: Ru(1)–N(5) 2.218(5), Ru(1)–C(1) 1.841(6); N(5)–Ru(1)–C(1) 177.7(2), C(77)–C(78)–C(82) 115.5(6), C(85)–C(86)–C(90) 113.7(6). (Bottom) Crystal packing diagram viewed down the *b*–axis showing co–crystallized porphyrin. Thermal ellipsoids are drawn at the 20% probability level.

When the crystal packing for **309a** is viewed along the *b*–axis (Figure 3.6, bottom), stacking of the macrocyclic portion of the assembly in the solid state can be observed. The majority of the cavity created by organization of the macrocycles is occupied by the tolyl groups of two of the offset porphyrin co–crystallites. The layers of the macrocyclic assemblies are separated by approximately 9 Å, to accommodate the co–crystallized porphyrin molecules. While single crystals are also available from a CH_2Cl_2 solution of pure **309a**, to date, all attempts at X–ray crystallographic analysis have been hindered by the rapid desolvation of these crystals. Likewise, attempts to co–crystallize **309a** with small molecules (such as 1,4–bis(triisopropylsilyl)butadiyne, pyrene, and *n*–hexadecane) that might be suitable for inclusion in the pores of **309a** have also been unsuccessful.

Single crystals of **309c** suitable for X–ray analysis were formed from a CH_2Cl_2 solution of the pure assembly in the presence of *n*–hexadecane. The structure of **309c** incorporates one hexadecane molecule in the unit cell, the presence of which hampered data refinement. Figure 3.7 shows the ORTEP drawing of centrosymmetrical **309c** and confirms the coordination of **305c** to the porphyrin in the solid state. Analysis of this solid–state structure reveals that the enyne core of the macrocycle is no longer planar as found for **309a**, but rather, it adopts a chair–like conformation.

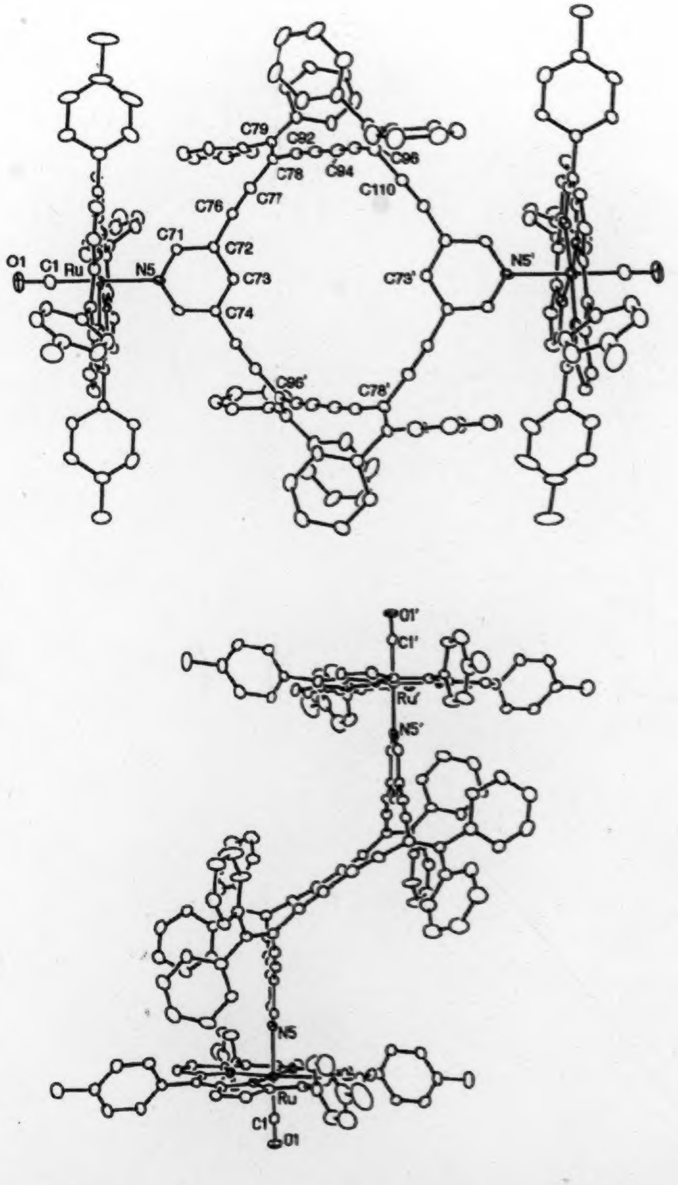
C79
C92
C78
C94
C96
C110
C77
C76
C71
C72
O1
C1
Ru
N5
C73
C74
N5'
C73'
C96'
C78'
O1'
C1'
Ru'
N5'
N5
Ru
C1
O1

Figure 3.7 (Top) ORTEP drawing of supramolecular assembly **309c**. Selected bond lengths [Å] and angles [°]: Ru(1)–N(5) 2.219(6), Ru(1)–C(1) 1.819(9),;N(5)–Ru(1)–C(1) 179.4(3), C(77)–C(78)–C(92) 113.6(7), C(95)–C(96)–C(110) 112.3(8). (Bottom) Alternate view emphasizing the chair conformation of the macrocyclic core. Thermal ellipsoids are drawn at the 20% probability level; hexadecane has been removed, for clarity.

The degree of distortion can be approximated by measuring the dihedral angles of the three chairs generated in this conformation. Using a dummy atom at the center of the pyridine ring as one vertex (centroid) of the hexagon, and the alkylidene carbons C(78) and C(96) as the others, the following dihedral angles are obtained: (1) 59.3° [(centroid)–C(78)–C(96)–(centroid)′], (2) 61.8° [C(78)–C(96)–(centroid)′–C(78)′] and (3) 64.5° [C(96)–(centroid)′–C(78)′–C(96)′]. This gives an average value of 61.9°, considerably larger than that of cyclohexane at 55.1°.[17] The distortion from planarity is also greater than that of a recently reported expanded radialene,[18] which has an average dihedral angle of 57.2°. The macrocyclic portion of assembly **309a**, by the same comparison, possesses a mean dihedral angle of only 3.2°.

The chair conformation of **309c** results in a reduction of the alkylidene bond angles C(77)–C(78)–C(92) and C(95)–C(96)–C(110), which at 113.6 and 112.3°, respectively, are smaller by 1.8° than those found for precursor **302c**. The remarkable puckering of the macrocyclic core likely results from increased steric interactions between the diphenylalkylidene substitution and the attached porphyrin ring(s). This observation also helps to account for the observed fragility of the assembly **309c** in solution. Somewhat surprisingly, the disparity in chemical stability between **309a** and **309c** is not reflected in N–Ru bond lengths, which are identical for both molecules (2.218 Å for **309a** and **309c**).

The apparent flexibility of the macrocyclic ligand of **309c** in the solid–state discussed above suggested that, in solution, the interconversion between two degenerate chair conformations (via a twisted or planar intermediate) or between a chair and planar conformation might be feasible. Attempts to explore this possibility have, however, been inconclusive due to the lack of a suitable spectroscopic signature that would indicate a planar or twisted conformation. Variable–temperature ^{1}H NMR spectra obtained over a temperature range of 30 to –80 °C for **309c** showed no significant chemical shift change for any resonance that would suggest that two conformations were in equilibrium in solution.

3.2.5 Electronic Properties of Cyclic and Acyclic Pyridine–Containing Oligomers and Supramolecular Assemblies

In addition to their full characterization in both the solution and solid state, the electronic absorption and emission properties of these porphyrinic supramolecular assemblies and their precursors were evaluated. Shown in Figure 3.8 are the electronic absorption curves for oligomers **302a–c**. Not surprisingly, the absorption bands for **302a** and **302b** are very similar. The maximal high energy absorption for **302a** appears at 300 nm (ε = 30,300) with a lower energy shoulder at ca. 310 nm. For the more electron–rich oligomer **302b**, this transition appears at slightly lower energy (305 nm, ε = 32,900) with a shoulder at ca. 318 nm. Oligomer **302c**, containing the pendant diphenylalkylidene groups, gives a far more intense and lower energy absorption at 348 nm (ε = 41,600) due to its extended conjugation length.

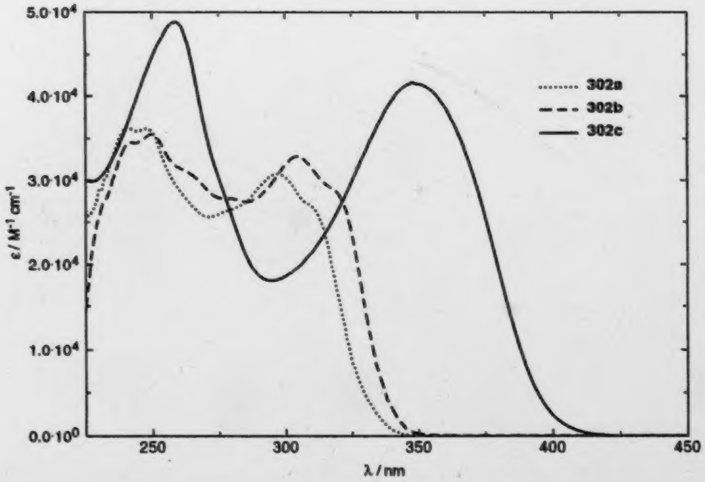

Figure 3.8 UV–vis absorption curves (CH_2Cl_2) for oligomers **302a–c**.

The absorption curves of the extended oligomers **303b** and **303c** (Figure 3.9) show a similar trend with the maximal high energy absorption for **303b** appearing at 292 nm (ε = 53,600), at higher intensity than the precursor **302b**. A lower energy shoulder is visible at ca. 312 nm. The lower energy HOMO–LUMO gap that results upon incorporation of the diphenylalkylidene moietie(s) is also reflected in the lower energy absorptions observed for oligomer **303c**. No increase in intensity is observed in the UV–vis spectrum of **303c** (relative to **302c**) but in addition to the absorption observed at 343 nm (ε = 53,400), a second band is observed at 373 nm (ε = 50,300). This band is presumably the result of the addition of the Ph–ene–yne–ene–Ph chromophore.

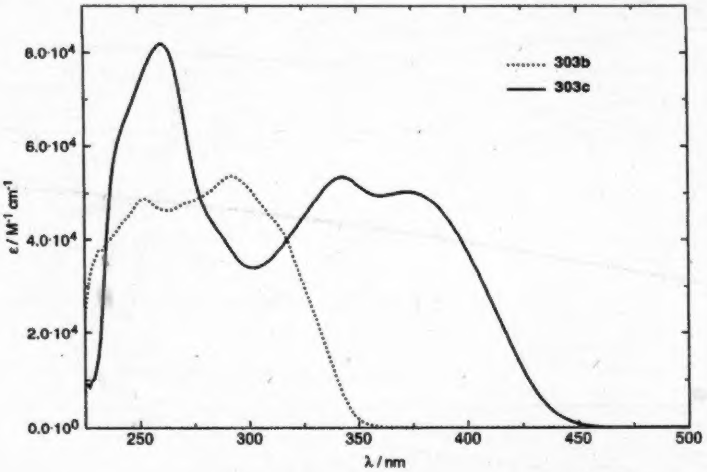

Figure 3.9 UV–vis absorption curves (CH_2Cl_2) for extended oligomers **303b** and **303c**.

Shown in Figure 3.10 are the UV–vis absorption curves for **304b** and **304c** and their porphyrinic assemblies **308b** and **308c**. The absorption spectrum for **308b** is, more or less, the sum of its components (i.e., **304b** + **307**). The spectrum is dominated by the intense Soret band, observed at 413 nm (ε = 222,800). The two Q–bands appear at 533 and 567 nm, which is at slightly lower energy than that observed for uncoordinated **307** which absorbs at 530 and 562 nm. As with **308b**, the absorption spectrum of **308c** is, for the most part, a sum of its component parts (i.e., **304c** + **307**). However, all of the absorptions are of slightly lower intensity than that expected if there were a strictly additive relationship. The Soret band and both Q–bands appear at identical energies to that observed in the spectrum of **308b**.

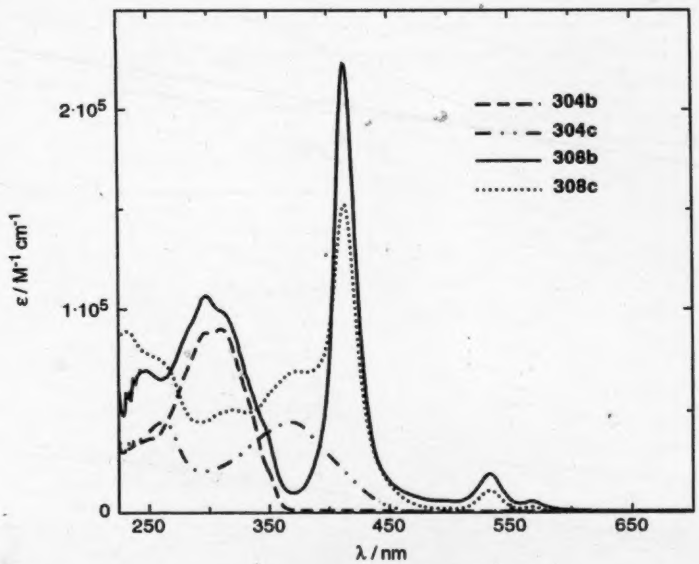

Figure 3.10 UV–vis absorption curves (CH_2Cl_2) for macrocycles **304b** and **304c** and their porphyrinic assemblies **308b** and **308c**.

Figure 3.11 shows the UV–vis absorption curves for **309a** and **309c**, featuring the bidentate macrocyclic ligand. The absorption curves are very similar and are both dominated by the absorptions of the porphyrinic chromophores.

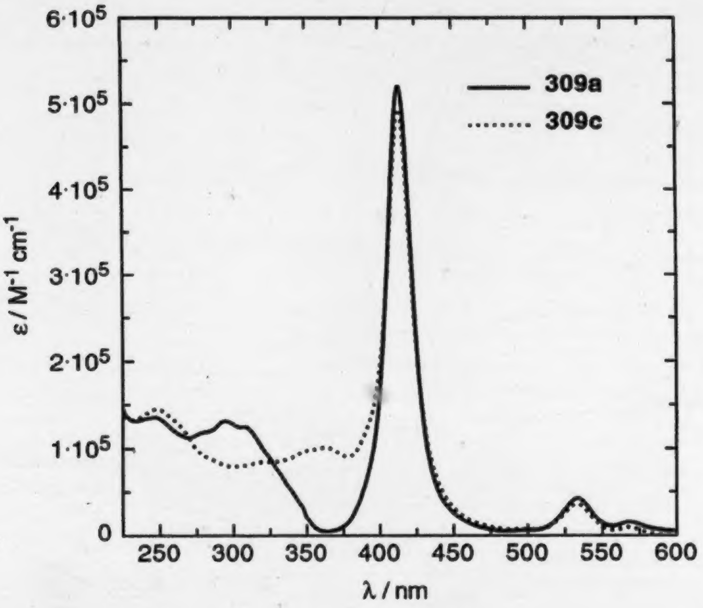

Figure 3.11 UV–vis absorption curves (CH_2Cl_2) for supramolecular assemblies **309a** and **309c**.

The electronic characteristics of assemblies **309a** and **309c**, as well as their components, were also analyzed by fluorescence spectroscopy. Whereas structures with dimethylalkylidene substitution do not show significant fluorescence, the diphenylalkylidene moiety greatly enhances emission. As seen in Figure 3.12, the absorption spectrum for **305c** shows a longer wavelength absorption band, the shoulder centered near 401 nm, as a result of the extended conjugated framework in comparison to precursor **302c** (λ_{max} = 348 nm). The lower energy HOMO–LUMO gap for **305c** is also reflected in the emission spectrum, where the emission maximum for **305c**, centered at 491 nm (excitation at 362 nm), is red-shifted by 45 nm from that of **302c** at 446 nm (excitation at 340 nm).

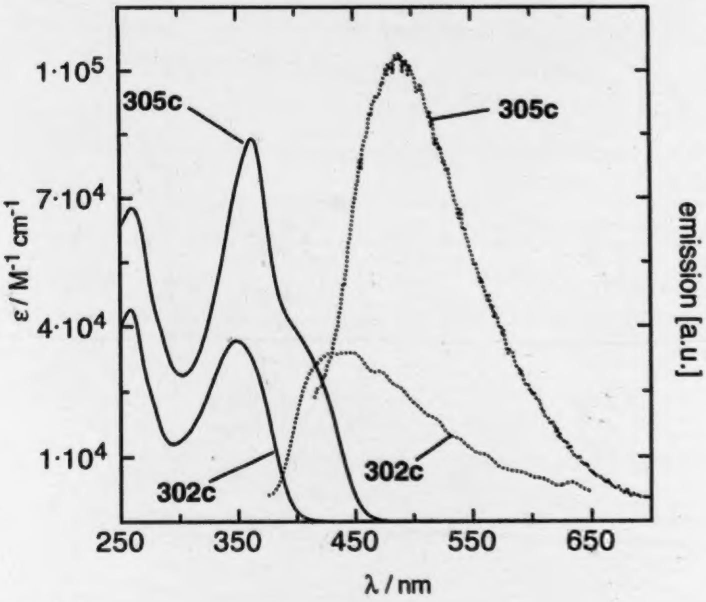

Figure 3.12 UV–vis absorption (solid line) and emission spectra (dashed line) for macrocycle **305c** and its oligomeric precursor **302c**. All spectra were recorded in CH_2Cl_2.

The absorption spectrum of **309c** is for the most part the sum of its component parts, i.e., **305c** + 2 equivalents of **307**. The Soret Band for both complexes **309a** and **309c** is found at 413 nm, the identical energy as **307**. The two Q–Band absorptions for complexes **309a** and **309c** found at 569 and 534 nm, however, are slightly red shifted versus **307** (562 and 530 nm). Assembly **309c** shows an emission at 489 nm (excitation at 364 nm), situated in the region of low molar absorptivity for the porphyrin (Figure 3.13). Although the emission energy for **309c** is nearly identical to that of the pure macrocycle **305c**, the relative intensity is greater for **309c**. This fact supports emission from the macrocyclic core of **309c** rather than emission from free **305c** generated from a dissociation equilibrium established in solution. A very weak emission from **309c** can also be observed at *ca.* 725 nm (not shown). This emission is characteristic of porphyrin **307** in solution.[15] It is unknown, therefore, whether this low energy emission results from the porphyrin complexed in **309c**, or from a small concentration of free porphyrin generated via dissociation of **309c** (or from both).

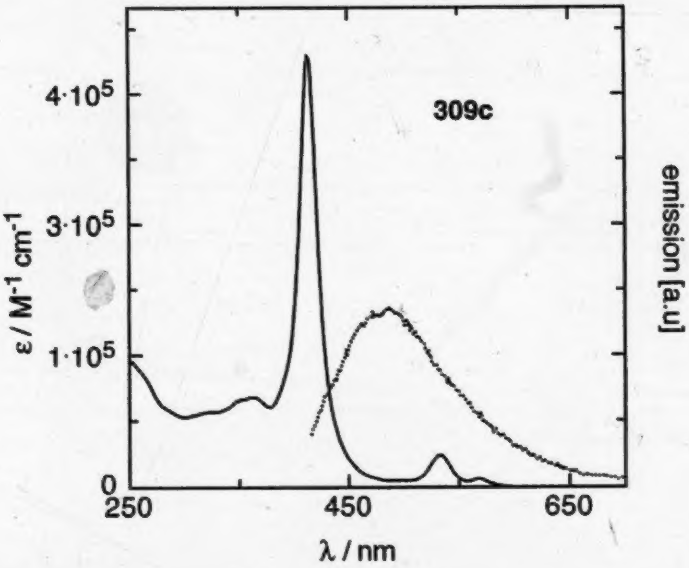

Figure 3.13 UV–vis absorption (solid line) and emission (dashed line) spectra for supramolecular assembly **309c**. All spectra were recorded in CH_2Cl_2.

3.2.6 Efforts Toward Building Blocks With Different Coordination Motifs

In addition to the synthesis of porous, 4,4′–bipyridine analogues, we have also targeted supramolecular building blocks featuring different coordination motifs. Described below are our preliminary efforts to realize a macrocyclic building block **310** featuring 3,5–diethynylpyridine subunits installed at the corners of a cross–conjugated macrocycle. It was expected that the installation of the pyridine sub–units at these locations would provide us with a bidentate building block with coordination sites at a

90° angle (with respect to one another). This would provide us with both linear and bent supramolecular building blocks and would permit us to access a variety of new supramolecular assemblies.

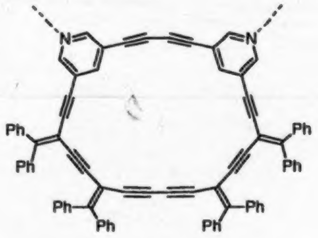

310

Our first synthetic efforts focused on the elaboration of the diethynylpyridine dimer **313**. Differentially–protected diethynylpyridine **312** was synthesized by cross–coupling compound **311**[19] with triisopropylsilylacetylene using palladium catalysis. Compound **312** was then mono–deprotected using methanolic K_2CO_3. Treatment of the terminal acetylene with oxidative homocoupling conditions led to the formation of dimer **313** in 75% isolated yield.

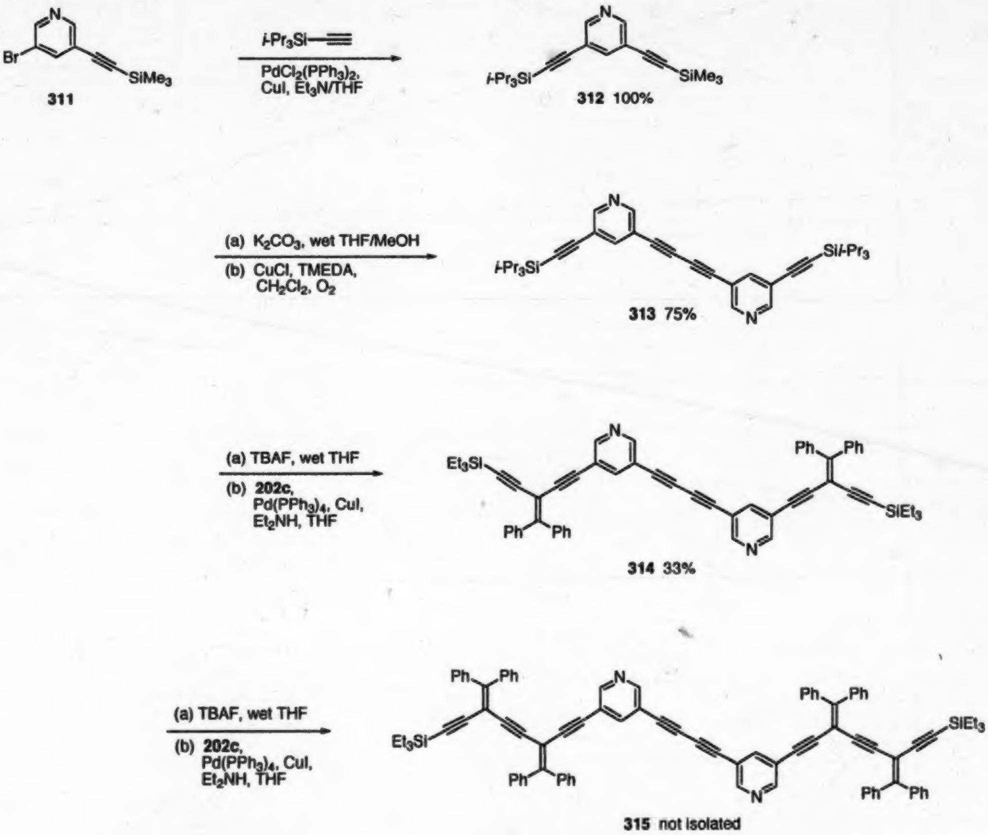
311
i-Pr3Si—≡
PdCl2(PPh3)2, CuI, Et3N/THF
312 100%
(a) K2CO3, wet THF/MeOH
(b) CuCl, TMEDA, CH2Cl2, O2
313 75%
(a) TBAF, wet THF
(b) 202c, Pd(PPh3)4, CuI, Et2NH, THF
314 33%
(a) TBAF, wet THF
(b) 202c, Pd(PPh3)4, CuI, Et2NH, THF
315 not isolated

Scheme 3.8 First synthetic efforts toward bidentate macrocycle **310**.

Single crystals of dimer **313**, suitable for X–ray crystallographic analysis, were grown by slow evaporation from a CH_2Cl_2/hexanes solution at 4 °C. The ORTEP drawing, shown in Figure 3.14, is generally unremarkable. The mean alkyne bond angle is determined to be 177.5°. The dihedral angle between planes defined by the atoms comprising the pyridine ring is 25.40°.

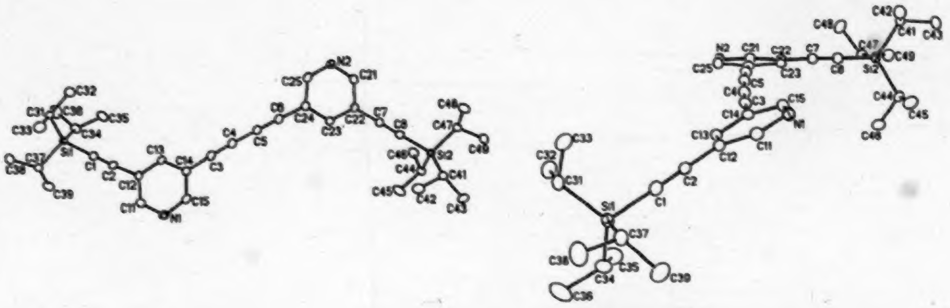

Figure 3.14 (Left) ORTEP drawing of dimer **313**. (Right) Alternate view. Selected bond angles [°]: C(14)–C(3)–C(4) 176.8(3), C(3)–C(4)–C(5) 178.0(3), C(4)–C(5)–C(6) 177.2(3), C(5)–C(6)–C(24) 174.2(2). Thermal ellipsoids are drawn at the 20% probability level.

The triisopropylsilyl–protecting groups of **313** were removed by treating with TBAF in THF and the resulting tetrayne was then cross–coupled with triflate **202c** using palladium catalysis to form the oligomer **314**. TLC analysis of the reaction mixture suggested the presence of several byproducts and **314** was isolated in only 33% yield following purification on an alumina column. Numerous attempts were made to improve the yield of this coupling reaction, including varying the temperature, reaction time, and amount of added base present, but none of these strategies were effective.

Oligomer **314** was carried on, subsequent to removal of the triethylsilyl protecting groups, to a second cross–coupling reaction with triflate **202c**. This reaction similarly resulted in a mixture of products and baseline material as indicated by TLC analysis. Chromatographic separation on alumina was attempted, but preliminary ^{1}H NMR spectroscopic analysis suggested that the oligomer **315** was only ~80% pure and was present in less than 40% yield. Rather than pursue this low–yielding and arduous synthetic route, we instead targeted an alternate route as shown in Scheme 3.9.

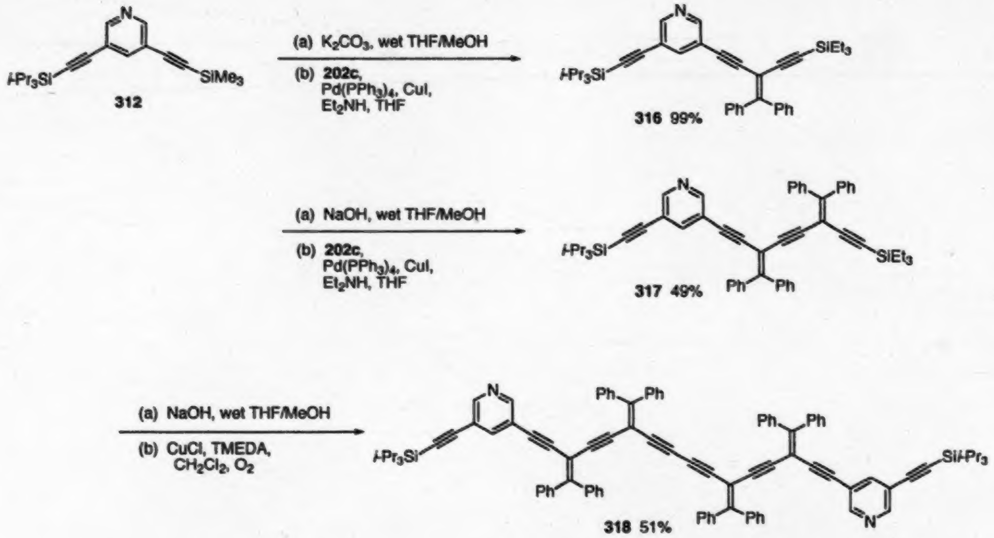
i-Pr3Si
SiMe3
312
(a) K2CO3, wet THF/MeOH
(b) 202c, Pd(PPh3)4, CuI, Et2NH, THF
SiEt3
316 99%
Ph
Ph
(a) NaOH, wet THF/MeOH
(b) 202c, Pd(PPh3)4, CuI, Et2NH, THF
317 49%
(a) NaOH, wet THF/MeOH
(b) CuCl, TMEDA, CH2Cl2, O2
Si-i-Pr3
318 51%
N

Scheme 3.9 Synthesis of oligomeric precursors **316**, **317**, and **318**.

In this approach, rather than pre–forming the diethynylpyridine dimer **313** and building on this core structure, we instead chose to form the pyridyl butadiynyl linkage as the *last* step in the synthesis. This strategy would allow us to avoid the ineffectual coupling reactions onto **313** and would also allow us to retain the solubilizing triisopropylsilyl groups until the last step of the synthesis. After the selective mono–desilylation of **312**, a cross–coupling reaction with triflate **202c** gratifyingly led to the formation of **316** in quantitative yield. This oligomer was elaborated via a second iteration of the coupling step to provide **317** in 49% yield, subsequent to chromatographic purification on alumina. The triethylsilyl–protecting group was selectively removed from oligomer **317** by treating with NaOH in wet THF/MeOH. The deprotected oligomer was then treated with CuCl in TMEDA in CH_2Cl_2 (in the presence of air) for a period of 14 hours at room temperature. After aqueous workup, and purification on an alumina column, oligomer **318** was isolated in 51% yield as a yellow solid.

Time allowed for only a single attempt at the synthesis of macrocycle **310** as shown in Scheme 3.10. After removal of the triisopropylsilyl groups using TBAF, the resulting deprotected oligomer was treated under oxidative homocoupling conditions at high dilution in CH_2Cl_2. After aqueous workup, solvent removal resulted in the formation of a yellow precipitate, which was filtered and dried. MALDI–TOF MS analysis suggested that this insoluble solid is a mixture containing the desired macrocycle **310** (*m/z* 1060.3, 100%) in addition to several higher molecular weight oligomers. It is reasonable to believe that, through a combination of finding the appropriate coupling conditions (catalyst and concentration) as well as exercising proper care during workup and solvent reduction, it should be possible to obtain macrocycle **310** in its pure form.

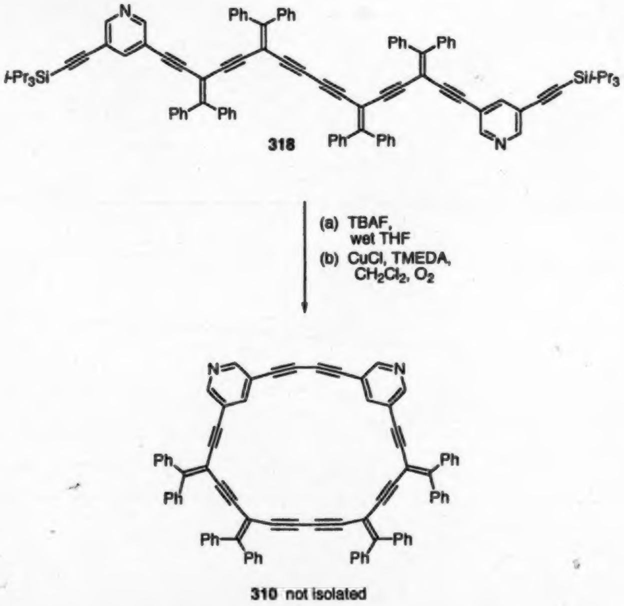

Scheme 3.10 Attempted synthesis of bidentate macrocycle **310**.

In addition to the synthesis of macrocycle **310**, we also explored the possibility of utilizing the oligomer **318** as a supramolecular building block. There has recently been a great deal of interest in the formation of helical assemblies,[20] and we wished to establish that the treatment of **318** with a metal fragment capable of accepting two pyridine ligands would result in a cyclic structure. As shown in Scheme 3.11, slow addition of *cis*–$Pt(OTf)_2(PEt_3)_2$[21] (**319**) to a CD_2Cl_2 solution of oligomer **318** resulted in the quantitative formation of assembly **320**.

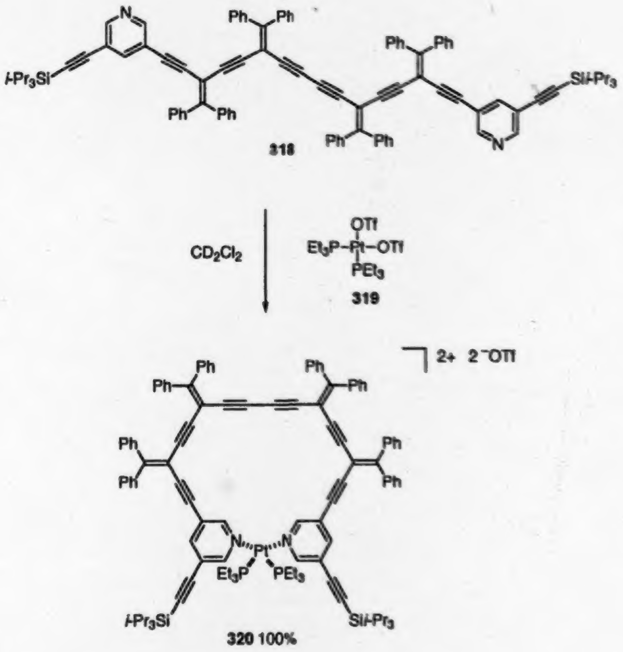
i-Pr3Si
Ph
Ph
Ph
Ph
Ph
Ph
Ph
Ph
SiI-Pr3
318
CD2Cl2
OTf
Et3P–Pt–OTf
PEt3
319
2+ 2⁻OTf
Et3P
PEt3
Pt
i-Pr3Si
SiI-Pr3
320 100%

Scheme 3.11 Synthesis of assembly **320**.

This self–assembly process is easily monitored using ^1H NMR spectroscopy. The two *ortho*–protons of the oligomeric precursor **318** appear as doublets at δ 8.54 and 8.28. The *para*–pyridyl proton appears as a triplet at 7.53 ppm. Upon coordination to the platinum centre, the two *ortho*–protons of **320** are deshielded and appear as broad singlets at 9.17 and 8.67 ppm. The broadness of the signals can be attributed to coupling with platinum. The *para*–pyridyl protons are no longer observed and are presumably shielded upon platinum coordination and are obscured by the multiplet of aromatic protons observed at δ 7.38 – 7.20. Convincing evidence for the formation of a discrete species is provided by the $^{31}P\{^{1}H\}$ NMR spectrum, which shows a single resonance at δ –3.94 ($^{1}J_{P-Pt} = 3206$ Hz). The most convincing evidence for the formation of assembly **320** comes from the ESI mass spectrum. Two significant peaks are observed at *m/z* 1954 (16%) and 902 (100%). These peaks are assigned to fragments $[M - (^{-}OTf)]^{+}$ and $[M - 2(^{-}OTf)]^{2+}$, respectively.

3.3 Conclusions and Future Work

In this chapter, the successful syntheses of several functionalized macrocycles based on a simple 3,5–diethynylpyridine building block have been described. Using a combination of straightforward palladium– and copper–catalyzed coupling methodologies, we have synthesized porous pyridine and 4,4′–bipyridine analogues bearing differing alkylidene substitution. We have demonstrated that these macrocycles can function as ligands and have established their ability to participate in self–assembly reactions through the preparation of nano–scale porphyrinic assemblies. In addition to characterizing these species in solution, the structures of these assemblies in the solid–state have also been evaluated. While X–ray crystallographic analysis has demonstrated the potential of these ligands and their assemblies to form highly ordered, channel–like materials, we have also recognized some of the limitations of these macrocycles as porous ligands. Pendant alkylidene substitution can play an important role in the coordinative ability of these "rigid" macrocyclic ligands.

The future of this work lies in the preparation of higher order, porous assemblies that will rely on the use of less sterically demanding metal fragments as the directing force for the assembly of our porous bipyridine analogues. As briefly mentioned in the last section of this chapter, we also plan to access macrocyclic ligands possessing different coordination motifs

3.4 References and Notes

1. (a) Mena–Osteritz, E.; Bäuerle, P. *Adv. Mater.* **2001**, *13*, 243–246. (b) Nakamura, K.; Okubo, H.; Yamaguchi, M. *Org. Lett.* **2001**, *3*, 1097–1099. (c) Höger, S.; Morrison, D. L.; Enkelmann, V. *J. Am. Chem. Soc.* **2002**, *124*, 6734–6736. (d) Tobe, Y.; Utsumi, N.; Kawabata, K.; Nagano, A.; Adachi, K.; Araki, S.; Sonoda, M.; Kirose, K.; Naemura, K. *J. Am. Chem. Soc.* **2002**, *124*, 5350–5364. (e) Collins, S. K.; Yap, G. P. A.; Fallis, A. G. *Org. Lett.* **2000**, *2*, 3189–3192. (f) Ge, P.–H.; Fu, W.; Herrmann, W. A.; Herdtweck, E.; Campana, C.; Adams, R. D.; Bunz, U. H. F. *Angew. Chem. Int. Ed.* **2000**, *39*, 3607–3610. (g) Eisler, S.; Tykwinski, R. R. *Angew. Chem. Int. Ed.* **1999**, *38*, 1940–1943. (h) Zhao, D.; Moore, J. S. *J. Org. Chem.* **2002**, *67*, 3548–3554. (i) Venturi, M.; Marchioni, F.; Balzani, V.; Opris, D. M.; Henze, O.; Schlüter, A. D. *Eur. J. Org. Chem.* **2003**, *21*, 4227–4233.
2. (a) Nitschke, J. R.; Tilley, T. D. *Angew. Chem. Int. Ed.* **2001** *40*, 2142–2145. (b) Henze, O.; Lentz, D.; Schlüter, A. D.; *Chem. Eur. J.* **2000**, *6*, 2362–2367. (c) Tobe,

Y.; Nagano, A.; Kawabata, K.; Sonoda, M.; Naemura, K. *Org. Lett.* **2000**, *2*, 3265–3268.

3. (a) Baxter, P. N. W. *J. Org. Chem.* **2001**, *66*, 4170–4179. (b) Baxter, P. N. W. *Chem. Eur. J.* **2003**, *9*, 2531–2541.

4. (a) Campbell, K.; McDonald, R.; Branda, N. R.; Tykwinski, R. R. *Org. Lett.* **2001**, *3*, 1045–1048. (b) Campbell, K.; McDonald, R.; Tykwinski, R. R. *J. Org. Chem.* **2002**, *67*, 1133–1140. (c) Sun, S.–S.; Lees, A. J. *Organometallics* **2001**, *20*, 2353–2358.

5. (a) Holliday, B. J.; Mirkin, C. A. *Angew. Chem. Int. Ed.* **2001**, *40*, 2022–2043. (b) Leininger, S.; Olenyuk, B.; Stang, P. J. *Chem. Rev.* **2000**, *100*, 853–908. (c) Fujita, M. *Chem. Soc. Rev.* **1998**, *27*, 417–425. (d) Philp, D.; Stoddart, J. F. *Angew. Chem., Int. Ed. Engl.* **1996**, *35*, 1154–1196. (e) Hof, F.; Craig, S. L.; Nuckolls, C.; Rebek Jr., J. *Angew. Chem. Int. Ed.* **2002**, *41*, 1488–1508. (f) Qin, Z.; Jennings, M. C.; Puddephatt, R. J. *Inorg. Chem.* **2003**, *42*, 1956–1965. (g) Bosch, E.; Barnes, C. L. *Inorg. Chem.* **2001**, *40*, 3097–3100. (h) Machado, V. G.; Baxter, P. N. W.; Lehn, J.–M. *J. Braz. Chem. Soc.* **2001**, *12*, 431–462.

6. (a) Han, W. S.; Lee, S. W. *Dalton Trans.* **2004**, *10*, 1656–1663. (b) Kuehl, C. J.; Mayne, C. L.; Arif, A. M.; Stang P. J. *Org. Lett.* **2000**, *2*, 3727–3729. (c) Zaworotko, M. J. *Angew. Chem. Int. Ed.* **2000**, *39*, 3052–3054.

7. (a) Stulz, E.; Scott, S. M.; Bond, A. D.; Teat, S. J.; Sanders, J. K. M. *Chem. Eur. J.* **2003**, *9*, 6039–6048. (b) Chichak, K.; Branda, N. R. *Chem. Commun.* **2000**, 1211–1212. (c) Haycock, R. A.; Hunter, C. A.; James, D. A.; Michelsen, U.; Sutton, L. R. *Org. Lett.* **2000**, *2*, 2435–2438. (d) Hartnell, R. D.; Arnold, D. P. *Organometallics* **2004**, *23*, 391–399. (e) Baldini, L.; Ballester, P.; Casnati, A.; Gomila, R. M.;

Hunter, C. A.; Sansone, F.; Ungaro, R. *J. Am. Chem. Soc.* **2003**, *125*, 14181–14189. (f) Ballester, P.; Gomila, R. M.; Hunter, C. A.; King, A. S. H.; Twyman, L. J. *Chem. Commun.* **2003**, 38–39. (g) Stulz, E.; Scott, S. M.; Ng, Y.–F.; Bond, A. D.; Teat, S. J.; Darling, S. L.; Feeder, N.; Sanders, J. K. M. *Inorg. Chem.* **2003**, *42*, 6564–6574. (h) Thamyongkit, P.; Speckbacher, M.; Diers, J. R.; Kee, H. L.; Kirmaier, C.; Holten, D.; Bocian, D. F.; Lindsey, J. S. *J. Org. Chem.* **2004**, *69*, 3700–3710.

8. (a) Karotki, A.; Drobizhev, M.; Dzenis, Y.; Taylor, P. N.; Anderson, H. L.; Rebane, A. *Phys. Chem. Chem. Phys.* **2004**, *6*, 7–10. (b) Mongin, O.; Hoyler, N.; Gossauer, A. *Eur. J. Org. Chem.* **2000**, 1193–1197. (c) Ogawa, K.; Kobuke, Y. *Angew. Chem. Int. Ed.* **2000**, *39*, 4070–4073. (d) Anderson, H. L. *Chem. Commun.* **1999**, 2323–2330. (e) Vicente, M. G. H.; Jaquinod, L.; Smith, K. M. *Chem. Commun.* **1999**, 1771–1782. (f) Fan, J.; Whiteford, J. A.; Olenyuk, B.; Levin, M. D.; Stang, P. J.; Fleischer, E. B. *J. Am. Chem. Soc.* **1999**, *121*, 2741–2752. (g) Drain, C. M.; Nifiatis, F.; Vasenko, A.; Batteas, J. D. *Angew. Chem. Int. Ed.* **1998**, *37*, 2344–2347. (h) Wagner, R. W.; Seth, J.; Yang, S. I.; Kim, D.; Bocian, D. F.; Holten, D.; Lindsey, J. S. *J. Org. Chem.* **1998**, *63*, 5042–5049.

9. Ng, S. C.; Novak, I.; You, X.; Huang, W. *J. Phys. Chem. A* **1998**, *102*, 904–908.

10. (a) Zhao, Y.; Tykwinski, R. R. *J. Am. Chem. Soc.* **1999**, *121*, 458–459. (b) Zhao, Y.; Campbell, K.; Tykwinski, R. R. *J. Org. Chem.* **2002**, *67*, 336–344.

11. (a) Stang, P. J.; Fisk, T. E. *Synthesis* **1979**, 438–440. (b) Stang, P. J.; White, M. R.; Maas, G. *Organometallics* **1983**, *2*, 720–725.

12. Siemsen, P.; Livingston, R. C.; Diederich, F. *Angew. Chem. Int. Ed.* **2000**, *39*, 2632–2657.

13. Hay, A. S. *J. Org. Chem.* **1962**, *27*, 3320–3321.

14. Collman, J. P.; Barnes, C. E.; Brothers, P. J.; Collins, T. J.; Ozawa, T.; Gallucci, J. C.; Ibers, J. A. *J. Am. Chem. Soc.* **1984**, *106*, 5151–5163.

15. Chichak, K.; Branda, N. R. *Chem. Commun.* **1999**, 523–524.

16. (a) Saito, M.; Endo, A.; Shimizu, K.; Satô, G. P. *Electrochim. Acta* **2000**, *45*, 3021–3028. (b) Funatsu, K.; Kimura, A.; Imamura, T.; Ichimura, A.; Sasaki, Y. *Inorg. Chem.* **1997**, *36*, 1625–1635.

17. Kahn, R.; Fourme, R.; André, D.; Renaud, M. *Acta Crystallogr. Sect. B* **1973**, *29*, 131–138.

18. Nielsen, M. B.; Schreiber, M.; Baek, Y. G.; Seiler, P.; Lecomte, S.; Boudon, C.; Tykwinski, R. R.; Gisselbrecht, J.–P.; Gramlich, V.; Skinner, P. J.; Bosshard, C.; Günter, P.; Gross, M.; Diederich, F. *Chem. Eur. J.* **2001**, *7*, 3263–3280.

19. Tominaga, M.; Kato, M.; Okano, T.; Sakamoto, S.; Yamaguchi, K.; Fujita, M. *Chem. Lett.* **2003**, *32*, 1012–1013.

20. (a) Huc, I. *Eur. J. Org. Chem.* **2004**, 17–29. (b) Yamada, K.; Yagishita, S.; Tanaka, H.; Tohyama, K.; Adachi, K.; Kaizaki, S.; Kumagai, H.; Inoue, K.; Kitaura, R.; Chang, H.–C.; Kitagawa, S.; Kawata, S. *Chem. Eur. J.* **2004**, *10*, 2647–2660. (c) Heemstra, J. M.; Moore, J. S. *Org. Lett.* **2004**, *6*, 659–662.

21. Stang, P. J.; Cao, D.H.; Saito, S.; Arif, A. M.; *J. Am. Chem. Soc.* **1995**, *117*, 6273–6283.

Chapter 4 Synthesis and Solid–State Characterization of Platinum–Containing Macrocycles

4.1 Introduction

As introduced in previous chapters, the predictable and directional bonding of organic ligands allows for the engineering of supramolecular coordination complexes with extraordinary structures and functional properties. The prolific use of pyridine–based ligands to access well–ordered architectures such as molecular squares,[1] cages[2] and tubular structures[3] inspired us to prepare porous, macrocyclic analogues of these ligands. We have established that cross–conjugated, pyridine–containing macrocycles are synthetically accessible and have demonstrated some degree of control over the physical properties of these species through the modification of pendant substitution. These macrocyclic ligands have proven to be excellent building blocks for supramolecular chemistry.

Described in this chapter are our efforts to further manipulate the properties of these compounds through the incorporation of additional functionality into the macrocyclic enyne core. We envisioned macrocycles (**401**) featuring metal σ–acetylide linkage(s) as shown schematically in Figure 4.1, and specifically, we targeted macrocycles featuring platinum–acetylide moieties. The installation of the metal–acetylide functionality was expected to accomplish several goals. First, the presence of solubilizing phosphine–based ligands on the square planar platinum centre was expected to facilitate the synthesis and purification of the resulting macrocyclic ligands.

In addition to this consideration, we also expected to access macrocyclic ligands with even larger pore sizes than those described in Chapter 3. Furthermore, the presence of platinum within the macrocyclic core would provide a site for additional elaboration via displacement of the phosphine ligands.[4]

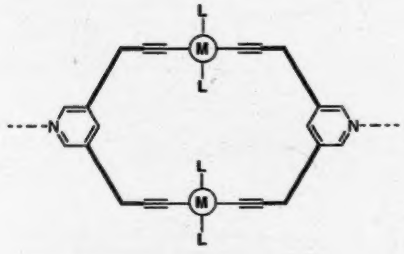

401

Figure 4.1 Schematic representation of a bidentate macrocyclic ligand featuring metal σ–acetylide moieties.

In addition to confronting these practical issues, we also planned to explore the structural and electronic effects of incorporating the metal acetylide moiety into the backbone of our cross–conjugated macrocyclic systems. The insertion of a metal centre into an unsaturated material can introduce or enhance a range of optical,[5] electronic,[6] or redox[7] properties that are not present within the core organic framework. This is due, in part, to the potential for the d–orbitals of the metal centre to interact with and across the pendant acetylenic π–system.[8] Numerous metal acetylide–based materials including polymers,[9] dendrimers,[10] and metallamacrocycles[11,12,8b] have been achieved and demonstrate unique physical properties. These materials, based on metal alkynyl scaffolds, have attracted a great deal of attention due to their potential to act as, for example, liquid crystals,[13] molecular wires,[14] as well as luminescent[15] and nonlinear optical materials.[16]

Described in this chapter are the successful syntheses of several pyridine-containing platinacycles.[17] To establish the coordinative ability of these platinum-containing ligands, coordination complexes were targeted and their synthesis is also discussed. The solid–state structural effects of incorporating the platinum–acetylide linkage were explored via X–ray crystallographic analysis of the ligands as well as their coordination complexes. UV–vis absorption and fluorescence emission spectroscopies were used to explore the electronic properties of these systems, and the third order nonlinear optical properties of four compounds were evaluated in collaboration with Aaron Slepkov and Prof. Frank Hegmann in our Physics Department.

4.2 Results and Discussion

4.2.1 Synthesis and Characterization of Platinacycles

As outlined in the introduction to this chapter, macrocycles featuring platinum–acetylide linkages were targeted due to our interest in preparing ligands with diverse structural and electronic properties from common precursors. In addition to these considerations, a more practical aspect involved the need to enhance the solubility of the macrocycles and expand their pore sizes. The installation of the platinum–acetylide moiety was expected to address these issues as well as provide us with the ability to further direct their assembly via ligand exchange at the platinum centre.

The synthesis of macrocycle **402** is outlined in Scheme 4.1. The acyclic oligomer **303c** was dissolved in THF and desilylated by treating with TBAF at room temperature for 30 minutes. Subsequent to an aqueous workup, the deprotected diyne was dissolved in Et_2NH and a stoichiometric quantity of $PtCl_2(PPh_3)_2$ was added. The resulting solution was degassed for ca. 1 hour and a catalytic amount of CuI was added.[18] The reaction mixture was then stirred at 40 °C for 14 hours. After cooling, an aqueous workup was performed and platinacycle **402** was isolated in 70% yield, subsequent to purification on a silica gel column.

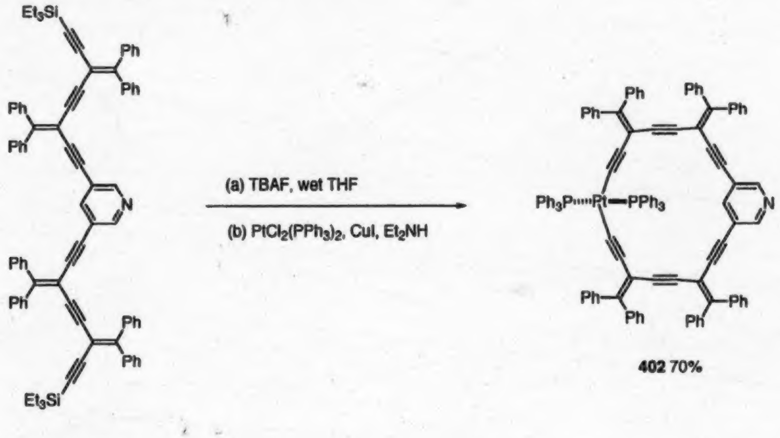

303c

402 70%

Scheme 4.1 Synthesis of platinacycle **402**.

Platinacycle **402** is a robust yellow solid that is stable indefinitely at ambient temperatures and melts only at temperatures greater that 248 °C. This ligand was fully characterized using ^{1}H–, ^{13}C–, and ^{31}P–NMR spectroscopy in addition to IR spectroscopy, ESI MS, and combustion analysis. The ^{13}C NMR spectrum of **402** remarkably showed 31 of the expected 33 unique carbon resonances. The ^{31}P NMR spectrum showed a single resonance at δ 20.0, which is a characteristic chemical shift value for triphenylphosphine bound to a platinum acetylide species. The *trans* stereochemistry about the platinum centre was confirmed by the one bond phosphorous–platinum coupling which was measured to be 2610 Hz, which is a typical value for *trans*–platinum acetylide complexes.[19] The most convincing evidence for the formation of **402** was provided by the ESI mass spectrum. MS analysis revealed two significant ion peaks at *m/z* 1676.4 (100%), 1654.4 (82%), assigned to $[M + Na]^+$ and $[M + H]^+$, respectively.

Bidentate platinacycles featuring two pyridine moieties (**403a** and **403b**) were also targeted and their synthesis is outlined in Scheme 4.2. The acyclic oligomer **302c** was desilylated by treating with NaOH in wet THF/MeOH for 4 hours. Subsequent to an aqueous workup, the deprotected oligomer could be divergently elaborated to provide either **403a** or **403b** via reaction of the deprotected polyyne with $PtCl_2(PPh_3)_2$ or $PtCl_2(PEt_3)_2$ in the presence of catalytic CuI under high dilution conditions in Et_2NH. Platinacycles **403a** and **403b** are both stable yellow solids and were isolated in yields of 45 and 71%, respectively, subsequent to purification by either silica gel chromatography or selective precipitation from CH_2Cl_2/acetone. The higher isolated yield of the triethylphosphine derivative **403b** is likely due to the fact that this analogue is significantly more soluble than **403a**. Compound **403a**, while considerably easier to handle than the unfunctionalized derivative **305c**, is still only marginally soluble, even in chlorinated solvents, leading to difficulties with respect to its isolation.

It is worth noting the importance of using *no* heat when removing the solvent, subsequent to workup, in all reactions to form *trans*–platinum acetylides. Despite the fact that heat is applied during the transmetallation reaction, and that *all* platinacycles (**402**, **403a** and **403b**) are thermally stable solids, heating during solvent removal leads to a darkening of the solution(s) accompanied by a bad odour. In all cases, this procedure results in lower overall yields, predominantly due to increased problems with respect to purification.

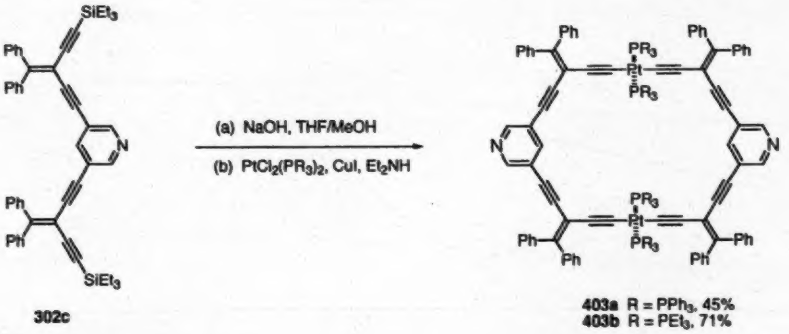

Scheme 4.2 Synthesis of bidentate platinacycles **403a** and **403b**.

Gratifyingly, both platinacycles were sufficiently soluble for full characterization. The ^{1}H NMR spectrum of **403a** was consistent with the proposed structure although, due to multiple overlapping aromatic proton resonances, it was not particularly diagnostic. The resonances for the *ortho*– and *para*–pyridyl protons were, however, observed as a doublet and triplet at δ 7.77 and 7.35, respectively. By contrast, the ^{13}C NMR spectrum of the platinacycle **403a** provided far more direct confirmation for the structure of this compound. All 21 of the expected non–equivalent carbon resonances are observed in the spectrum. While low signal to noise (the result of the limited solubility) did not permit the observation of phosphorous– or platinum–coupling to the alkynyl carbon coordinated to the platinum centre, all of the carbons of the pendant triphenylphosphine ligands showed the expected coupling to phosphorous. The ^{31}P NMR spectrum showed a single resonance at δ 18.0, confirming the presence of the metal–acetylide linkage. This chemical shift value is comparable to that observed in the spectrum of **402**. Again the observed signal to noise was insufficient to observe coupling to platinum. By far the most convincing evidence for the formation of **403a** came from mass spectral analysis. The ESI mass spectrum of **403a** showed a large signal at *m/z* 2498.7 (100% relative intensity) corresponding to $[M + H]^+$.

All of the spectroscopic data acquired for the more soluble derivative **403b** was similarly consistent with the proposed structure. The ^{1}H NMR spectrum of **403b** was significantly more diagnostic and confirmed the presence of the triethylphosphine ligands. Two multiplets were observed at 1.88 – 1.83 and 1.10 – 1.00 ppm, corresponding to the methylene and methyl protons of the ligand, respectively. The ^{31}P NMR spectrum of **403b** also provided evidence for the proposed cyclic structure and showed a single resonance at δ 13.9 ($^1J_{P\text{-}Pt}$ = 2344 Hz), slightly upfield relative to **403a** as a result of the shielding alkyl groups. The ^{13}C NMR spectrum of **403b** showed 18 of the 19 expected non–equivalent carbon resonances, and ESI mass spectral analysis also indicated the presence of **403b**.

4.2.2 Synthesis and Characterization of Coordination Compounds

As described in Chapter 3, macrocyclic ligands featuring diphenylalkylidene substitution (ligands **304c** and **305c**) could participate in self–assembly reactions with the ruthenium porphyrin **307** but the resulting assemblies were significantly less robust than those bearing isopropylidene or adamantylidene groups. We suspected that this was due to steric interactions between the pendant diphenyl moieties and the porphyrinic ring. This supposition was nicely supported by the solid–state structure of **309c** as demonstrated by the chair conformation adopted by ligand **305c**. We expected that the use of a metal or metal ion bearing smaller, less sterically–demanding ligands would facilitate self–assembly processes featuring these ligands. To establish the coordinative ability of ligand **304c** as well as its expanded platinacycle analogue **402**, coordination compounds **404** and the interesting bimetallic species, **405**, were targeted. The details of their synthesis are outlined in Scheme 4.3.

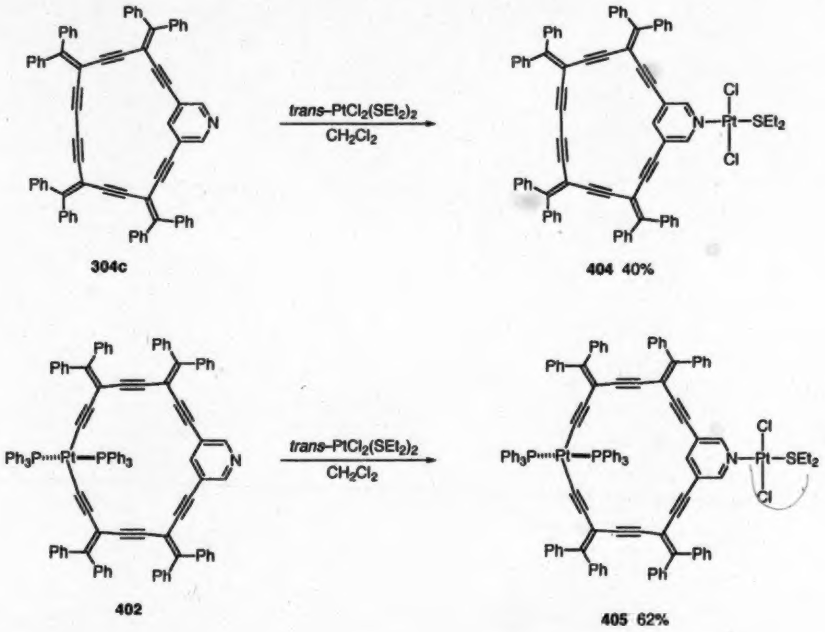

Scheme 4.3 Synthesis of coordination compounds **404** and **405**.

Treatment of CH_2Cl_2 solutions of macrocyclic ligands **304c** and **402**, with *trans*–$PtCl_2(SEt_2)_2$[20] for a period of 1–2 days under ambient conditions led to the formation of **404** and **405** in 40 and 62% yields, respectively. The pure complexes were isolated as robust, orange crystalline solids following purification on a silica gel column using CH_2Cl_2 as eluent. Interestingly, the thermal stability of **404** is substantially greater than that of the uncoordinated ligand **304c**, with **404** decomposing only at 238 °C (**304c** decomposes at 104 °C). Complex **405** is also surprisingly stable, decomposing only at 196 °C.

Both transition metal complexes **404** and **405** were fully characterized in solution using ESI MS in addition to IR and NMR spectroscopies. Remarkably, the ^{13}C NMR spectrum of **404** showed 30 of the expected 31 unique carbon resonances and the spectrum for **405** was similarly well–resolved showing all 35 of the expected carbon resonances. Convincing evidence for the formation of these species was provided by ^{1}H NMR spectroscopy. The progress of the self–assembly reactions could be easily monitored through analysis of their ^{1}H NMR spectra. As seen in Figure 4.2 (top), the *ortho*– and *para*–pyridyl protons of the uncoordinated ligand **304c** appear as a doublet and triplet at δ 8.21 and 7.90, respectively. Upon coordination to the platinum centre, these protons are deshielded and resonate at 8.46 and 7.99 ppm, respectively (see Figure 4.2, bottom). Long range coupling of the *ortho* protons to platinum is also apparent in the platinum satellite peaks, which flank the resonance at δ 8.46. In addition to these observations, upon coordination by the macrocyclic ligand to platinum, inversion at the sulfur centre of the pendant SEt_2 ligand becomes slow relative to the NMR time scale. The result of this slow inversion is that the two diastereotopic methylene protons adjacent to the sulfur centre appear at significantly different chemical shifts, as evidenced by the two broad resonances observed at ca. 3.0 and 2.6 ppm. This assignment was confirmed using variable–temperature ^{1}H NMR spectroscopy: At 70 °C the signals for the diastereotopic methylene protons coalesce into a featureless broad singlet centred at 2.85 ppm.

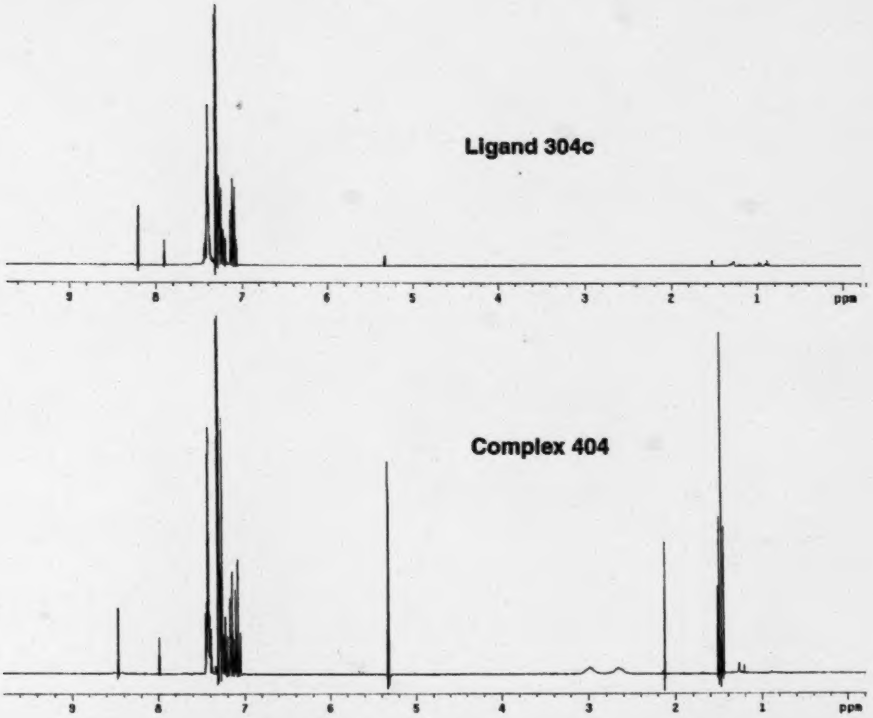

Figure 4.2 (Top) ^{1}H NMR (300 MHz, CD_2Cl_2) spectrum of macrocyclic ligand **304c**. (Bottom) ^{1}H NMR (400 MHz, CD_2Cl_2) spectrum of coordination complex **404**.

We had noted that the solubility of the macrocyclic ligands **304c** and **402** was greatly enhanced upon binding to the platinum complex and wished to establish that this reaction could be used to solubilize macrocycle **305c**. The insoluble bidentate ligand **305c** was treated with two equivalents of *trans*–$PtCl_2(SEt_2)_2$ in CH_2Cl_2 for a period of 4 days (see Scheme 4.4) leading to the formation of **406** in 49% yield. Complex **406** was isolated as a yellow solid following purification on a silica gel column using neat CH_2Cl_2.

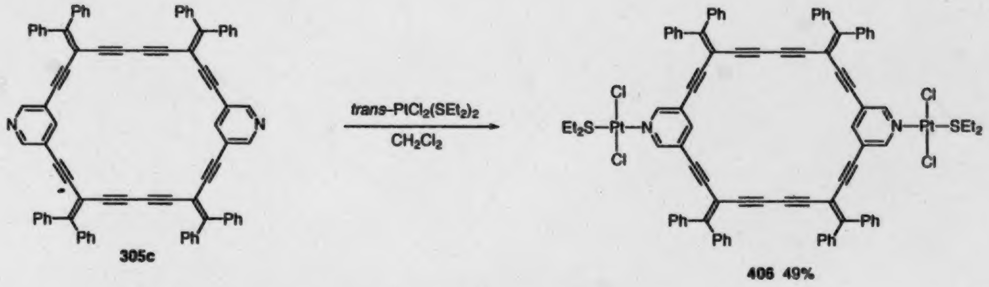

Scheme 4.4 Synthesis of coordination complex **406**.

Not surprisingly, complex **406** was significantly more soluble than the uncoordinated ligand **305c**, allowing for the full characterization of **406** including ^{13}C NMR analysis. As with the previous examples, upon coordination to the platinum centre, the *ortho–* and *para–*pyridyl protons are deshielded and give rise to a doublet and triplet at δ 8.43 and 7.90, respectively, in the ^{1}H NMR spectrum of **406**. The ^{13}C NMR spectrum of **406** shows all 19 of the expected non–equivalent carbon resonances. The ESI mass spectrum also provided convincing evidence for the formation of **406**. Two significant peaks were observed in the spectrum, which was acquired in the presence of added AgOTf, at *m/z* 1879 (100%) and 992 (77%), assigned as $[M + Ag]^+$ and $[M + 2Ag]^{2+}$, respectively.

4.2.3 Solid–State Characterization of Platinum–Containing Macrocycles and Their Assembly Products

Single crystals of bidentate platinacycles **403a** and **403b**, suitable for X–ray crystallographic analysis, were grown by slow evaporation from $CH_2Cl_2/ClCH_2CH_2Cl$/acetone and CH_2Cl_2/acetone solutions at 4 °C, respectively. The ORTEP drawing of **403a**, shown in Figure 4.3, confirms the assigned *trans–*

stereochemistry and square planar geometry about the platinum centre. The macrocyclic core is in a near planar conformation and, as such, is free from strain. The mean alkyne and alkylidene bond angles were measured at 174.5 and 114.4°, respectively. Interestingly, the triphenylphosphine ligands have not adopted a conformation where the platinum–phosphorous bonds are perpendicular to the macrocyclic enyne core. Rather, they are tilted such that the angle between the Pt–P(1) and Pt–P(2) bonds and a plane defined by Pt–Pt′–C(16)–C(26)–C(16′)–C(26′) are 147.1 and 36.0°, respectively. The cavity circumscribed by the enyne framework, which measures 9.0 by 9.6 (Pt–Pt) Å, is larger than that of **305c**, but has, in effect, been obscured through the incorporation of the platinum acetylide linkage and its associated ligands. While this may initially be seen as a drawback, it is worth noting that future experiments will focus on the displacement of the pendant phosphine ligands, resulting in the reconstruction of the macrocyclic pore structure.

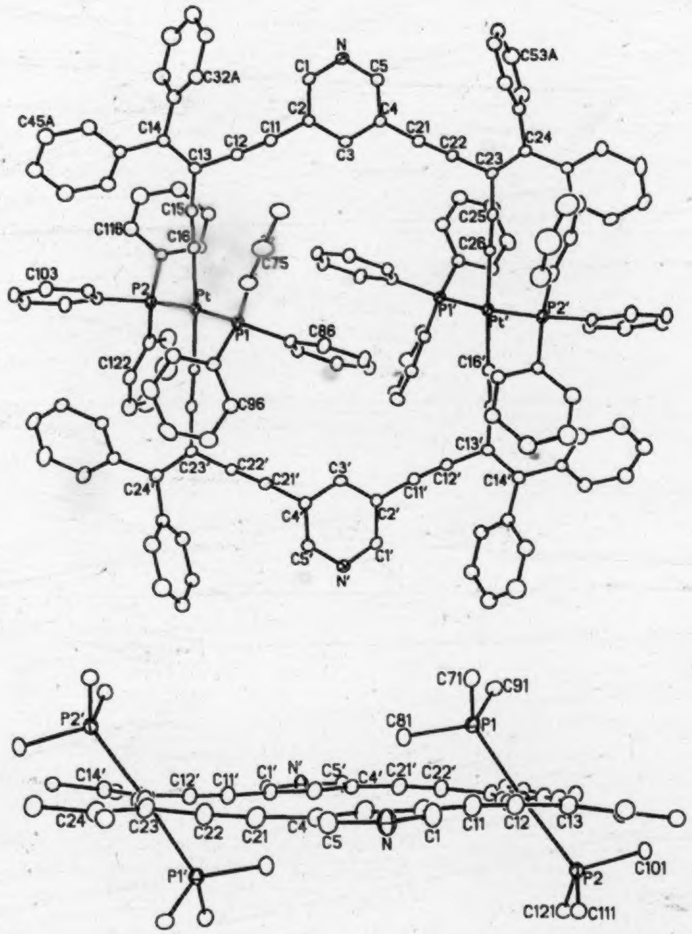
N
C1
C5
C2
C4
C3
C32A
C53A
C45A
C14
C13
C12
C11
C21
C22
C23
C24
C15
C16
C116
C75
C25
C26
C103
P2
Pt
P1
C86
P1'
Pt'
P2'
C122
C16'
C96
C13'
C12'
C11'
C14'
C23'
C22'
C21'
C3'
C24'
C4'
C2'
C5'
C1'
N'
C71
C91
P2'
C81
P1
C14'
C12'
C11'
C1'
N'
C5'
C4'
C21'
C22'
C24
C23
C22
C21
C4
C5
N
C1
C11
C12
C13
C101
P1'
P2
C121
C111

Figure 4.3 (Top) ORTEP drawing of **403a**. Selected bond lengths [Å] and angles [°]: Pt–P(1) 2.3084(15), Pt–P(2) 2.3028(15), Pt–C(16) 2.000(6), Pt–C(26′) 1.985(5), P(1)–Pt–P(2) 173.82(5), C(16)–Pt–C(26′) 177.7(2), C(12)–C(13)–C(15) 114.4(5), C(22)–C(23)–C(25) 114.3(5). (Bottom) Alternate view of **403a** highlighting the planar, cyclic core; only the *ipso* carbons of the triphenylphosphine ligands and pendant diphenyl groups are shown, for clarity. Thermal ellipsoids are drawn at the 20% probability level. Co–crystallized $ClCH_2CH_2Cl$ not shown.

A similar observation is made in the case of the triethylphosphine derivative **403b**. The ORTEP drawing of **403b** shown in Figure 4.4 shows that the phosphine ligands are again 'lying down' into the plane of the macrocycle. The angles between the Pt(1)–P(1), Pt(1)–P(2), Pt(2)–P(3), and Pt(2)–P(4) bonds and a plane defined by Pt(1)–Pt(2)–C(1)–C(17)–C(18)–C(34) were measured at 59.2, 125.0, 127.3, and 46.9°, respectively. Platinacycle **403b**, like its analogue, was similarly free from strain as reflected in the mean alkyne and alkylidene bond angles, which were measured at 174.7 and 114.2°, respectively.

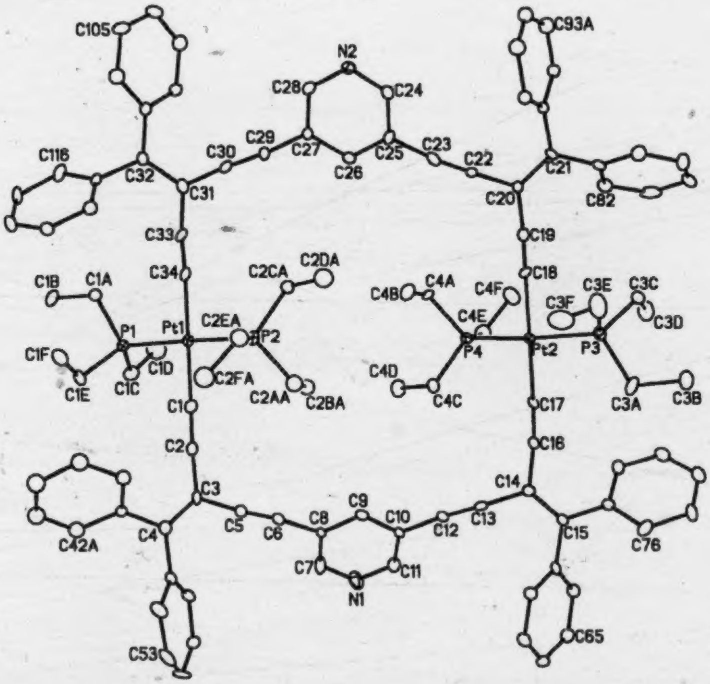
C105
C93A
N2
C28
C24
C29
C30
C27
C25
C23
C22
C116
C32
C31
C26
C21
C20
C82
C19
C33
C34
C2CA
C2DA
C18
C1B
C1A
C4A
C4F
C3E
C3C
C4B
C3F
C4E
C3D
P1
Pt1
C2EA
P2
P4
Pt2
P3
C1F
C1D
C2FA
C4D
C1E
C1C
C2AA
C2BA
C4C
C17
C3A
C3B
C1
C2
C16
C3
C14
C9
C5
C6
C8
C10
C12
C13
C4
C15
C42A
C76
C7
C11
N1
C65
C53

Figure 4.4 ORTEP drawing of **403b**. Selected bond lengths [Å] and angles [°]: Pt(1)–P(1) 2.282(3), Pt(1)–P(2) 2.311(3), Pt(2)–P(3) 2.300(3), Pt(2)–P(4) 2.286(3), Pt(1)–C(1) 1.967(11), Pt(1)–C(34) 2.009(11), Pt(2)–C(17) 1.975(10), Pt(2)–C(18) 2.030(11), P(1)–Pt(1)–P(2) 175.54(12), C(1)–Pt(1)–C(34) 179.0(5), P(3)–Pt(2)–P(4) 173.32(12), C(17)–Pt(2)–C(18) 177.1(5), C(2)–C(3)–C(5) 111.1(9), C(13)–C(14)–C(16) 113.8(9), C(19)–C(20)–C(22) 115.8(9), C(30)–C(31)–C(33) 115.9(10). Thermal ellipsoids are drawn at the 20% probability level. Co-crystallized CH_2Cl_2 not shown.

Single crystals of **304c** and **402**, suitable for X–ray crystallographic analysis, were grown via slow evaporation from CH_2Cl_2/acetone solutions of the respective ligands at 4 °C. The ORTEP diagram of **304c** (Figure 4.5, top) reveals the dimensions of this macrocyclic ligand, which spans 5.3 Å (C(3A) to C(20)) in the shortest dimension and 9.0 Å (C(13) to C(27)) in the other. The pentagon–shaped macrocycle has adopted a pseudo–envelope conformation in the solid state, one in which the alkylidene carbon C(13) rests 1.52 Å outside of a plane defined by the remaining four vertices of the pentagon that includes C(17), C(23), C(27) and the centroid of the pyridine ring (Py_{cent}). As a result of this puckering, the dihedral angle between the C(17)–C(23)–C(27)–Py_{cent} and C(17)–C(13)–Py_{cent} planes is 31°. The macrocycle is relatively free from strain as reflected in the mean alkyne bond angle of 175.3°, with a maximum deviation of 8.7° from ideality. Furthermore, the alkylidene bond angles C(12)–C(13)–C(15) 111.1(4)°, C(16)–C(17)–C(19) 113.3(3)°, C(22)–C(23)–C(25) 113.1(3)°, and C(26)–C(27)–C(29) 113.0(3)°, are only slightly less than those of the acyclic oligomer, **303c**.

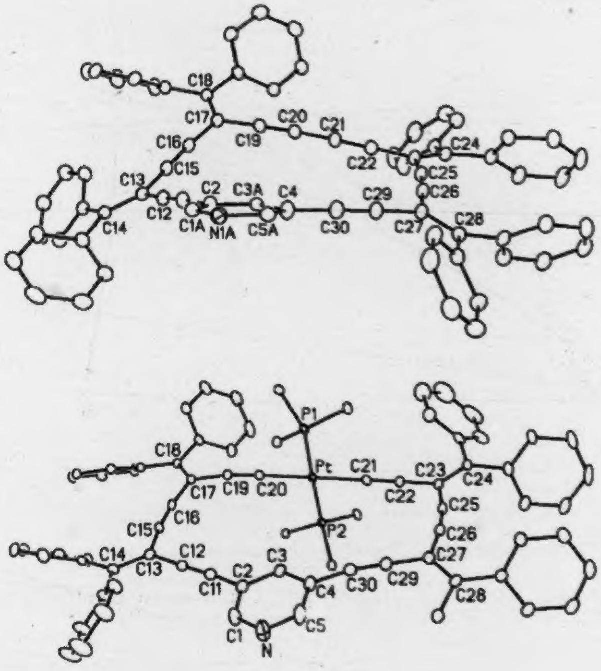
C18
C17
C20
C21
C16
C19
C22
C24
C13
C15
C25
C2
C3A
C4
C29
C26
C12
C28
C14
C1A
N1A
C5A
C30
C27
P1
C18
Pt
C21
C23
C24
C17
C19
C20
C22
C25
C16
C15
P2
C26
C12
C14
C3
C27
C13
C2
C11
C4
C30
C29
C28
C1
C5
N

Figure 4.5 (Top) ORTEP drawing of **304c** showing pseudo–envelope conformation; co–crystallized CH_2Cl_2 not shown. Alkylidene bond angles [°]: C(12)–C(13)–C(15) 111.1(4), C(16)–C(17)–C(19) 113.3(3), C(22)–C(23)–C(25) 113.1(3), C(26)–C(27)–C(29) 113.0(3). (Bottom) ORTEP drawing of **402**; co–crystallized CH_2Cl_2 and acetone not shown; only the *ipso* carbons of the triphenylphosphine ligands are shown, for clarity. Selected bond lengths [Å] and angles [°]: Pt–P(1) 2.3059(17), Pt–P(2) 2.2958(17), Pt–C(20) 1.994(6), Pt–C(21) 1.993(6), C(19)–C(20) 1.215(8), C(21)–C(22) 1.203(8); C(12)–C(13)–C(15) 112.7(6), C(16)–C(17)–C(19) 112.1(5), C(22)–C(23)–C(25) 111.4(6), C(26)–C(27)–C(29) 114.1(6), P(1)–Pt–P(2) 177.77(6), C(20)–Pt–C(21) 179.6(3). Thermal ellipsoids are drawn at the 20% probability level.

Crystallographic analysis of **402** shows that the macrocyclic core is slightly wider than that of **304c**, spanning 4.9 (C(3) to Pt) by 10.2 (C(15) to C(26)) Å (Figure 4.5, bottom). The conjugated skeleton is nearly planar with a maximum deviation from planarity of 0.07 Å, and the P(1)–Pt and Pt–P(2) bonds are nearly perpendicular to the plane of the macrocycle. Unexpectedly, the platinum–acetylide linkage and the increased planarity slightly add to the strain present in the conjugated framework of the ligand. The mean alkyne bond angle is 173.8° with a minimum angle of 169.4(8)° (C(4)–C(30)–C(29)). The alkylidene bond angles C(16)–C(17)–C(19) 112.1(5)°, C(12)–C(13)–C(15) 112.7(6)°, C(26)–C(27)–C(29) 114.1(6)°, and C(22)–C(23)–C(25) 111.4(6)°, are on average the same as found in **304c**. The P(1)–Pt–P(2) and C(20)–Pt–C(21) bond angles at 177.77(6) and 179.6(3)°, respectively, are consistent with those observed in unstrained platinum–acetylides. Thus, the strain that is imparted as a result of increasing planarity is accommodated primarily by a distortion of the acetylenic π–system, rather than in the metal acetylide linkage.

X–ray crystallographic analysis was performed on single crystals of **404** and **405** grown by slow evaporation of a $CHCl_3$ and CH_2Cl_2/acetone solution at 4 °C, respectively. The ORTEP diagram of **404** (Figure 4.6, top) confirms the coordination of macrocyclic ligand **304c** to the platinum centre, and shows that the coordinated macrocycle adopts a more planar conformation in comparison to the unbound ligand **304c**; C(23) is only 0.56 Å from the plane defined by the other four vertices of the pentagon C(17)–(C(13)–Py_{cent}–C(27)) and the dihedral angle between the C(17)–C(13)–Py_{cent}–C(27) and C(17)–C(23)–C(27) planes is 10.9°. Somewhat surprisingly, the increased planarity does not coincide with an increase in strain. The four alkylidene bond angles of **404** are comparable to those of the uncoordinated ligand, **304c**. The alkyne bond angles are similarly unaffected, with an average bond angle of 175.4° and a maximum deviation of 9.5° from the optimal value of 180°. The geometry about platinum is square planar, and the angle between the N–C(1)–C(2)–C(3)–C(4)–C(5) and N–Pt–Cl(1)–Cl(2)–S planes is 47.4°.

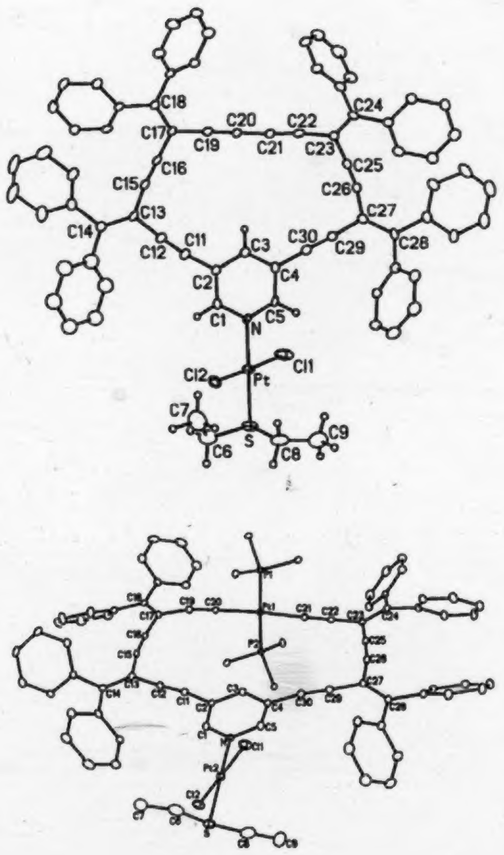
C18
C17
C20
C22
C24
C19
C21
C23
C25
C16
C15
C26
C13
C27
C14
C11
C3
C30
C29
C12
C28
C2
C4
C1
N
C5
Cl1
Cl2
Pt
C7
C6
S
C8
C9

Figure 4.6 (Top) ORTEP drawing of **404**; co–crystallized $CHCl_3$ not shown. Selected bond lengths [Å] and angles [°]: Pt–N 2.062(7), Pt–S 2.271(3), Pt–Cl(1) 2.285(3), Pt–Cl(2) 2.304(3); C(12)–C(13)–C(15) 112.2(8), C(16)–C(17)–C(19) 114.2(7), C(22)–C(23)–C(25) 112.4(8), C(26)–C(27)–C(29) 113.0(8), N–Pt–S 177.4(2), Cl(1)–Pt–Cl(2) 178.41(10). (Bottom) ORTEP drawing of **405**; co–crystallized CH_2Cl_2 not shown; only the *ipso* carbons of the triphenylphosphine ligands are shown, for clarity. Selected bond lengths [Å] and angles [°]: Pt(2)–N 2.051(4), Pt(2)–S 2.2665(14), Pt(2)–Cl(1) 2.3029(14), Pt(2)–Cl(2) 2.2909(14), Pt(1)–P(1) 2.3076(12), Pt(1)–P(2) 2.3037(12), Pt(1)–C(20) 2.004(4), Pt(1)–C(21) 1.998(4), C(19)–C(20) 1.201(6), C(21)–C(22) 1.209(6), C(12)–C(13)–C(15) 112.8(4), C(16)–C(17)–C(19) 111.1(4), C(22)–C(23)–C(25) 113.6(4), C(26)–C(27)–C(29) 112.6(4), P(1)–Pt(1)–P(2) 177.28(4), C(20)–Pt(1)–C(21) 176.36(19), N–Pt(2)–S 176.04(12), Cl(1)–Pt(2)–Cl(2) 178.87(5). Thermal ellipsoids are drawn at the 20% probability level.

In contrast, the ORTEP diagram of complex **405** (Figure 4.6, bottom) reveals that the macrocyclic portion of this complex is planar and almost completely unchanged upon coordination to the platinum centre. All alkyne and alkylidene bond angles are consistent with those observed in the unbound ligand **402**. All platinum–carbon, platinum–phosphorous, and platinum–nitrogen bond lengths and related bond angles are similarly unaffected.

4.2.4 Electronic Properties of Platinum Complexes

In addition to examining the solid–state properties of these systems, we also evaluated the effect of incorporating the platinum–acetylide moiety on the electronic properties of the macrocyclic ligands. Shown in Figure 4.7 are the UV–vis absorption spectra for macrocycles **304c** and **402** as well as their platinum complexes **404** and **405**. The absorption spectrum of the purely organic ligand **304c**, as described in Chapter 3, shows a broad, low energy absorption at 368 nm ($\varepsilon = 45{,}000$). Upon installation of the platinum acetylide linkage, two significant observations are made. First, the most intense absorption of **402** is blue–shifted relative to that of **304c** and appears at 357 nm ($\varepsilon = 79{,}900$). This absorption is nearly double in intensity relative to that of **304c**. A second, lower energy absorption is also observed in the spectrum of **402** and appears as a shoulder at ca. 417 nm. This low energy absorption is likely due to mixing of the platinum dπ–orbitals with the π^* orbitals of the acetylenic chromophore.[8]

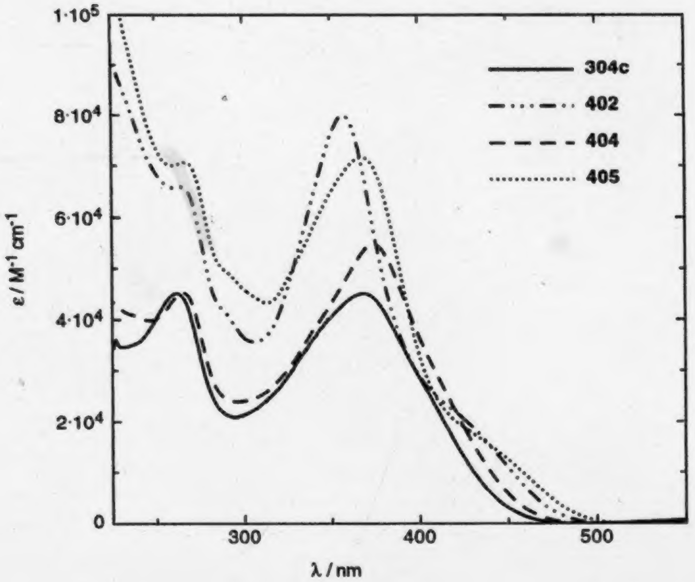

Figure 4.7 UV–vis absorption spectra (CH_2Cl_2) for ligands **304c**, **402** and their platinum complexes **404** and **405**.

The binding of ligand **304c** to a platinum centre, forming **404**, causes a red–shift in the lowest energy maximal absorption. The UV–vis absorption spectrum for complex **404** shows a broad absorption centred at 374 nm (ε = 54,700). This slight red shift is likely due to a loss of electron density at the pyridine upon coordination to the platinum centre, resulting in a lowering of the HOMO to LUMO gap. The absorption spectrum of complex **405**, featuring both platinum moieties, expresses both of these trends. A high intensity absorption is observed at 367 nm (ε = 71,700), which is at slightly higher energy than that observed for complex **404**, but is red–shifted when compared to that of the uncoordinated ligand, **402**. A low energy shoulder at ca. 428 nm is also observed in the spectrum of compound **405**, at very similar energy to that of **402**.

The UV–vis absorption spectra for the unfunctionalized macrocycle **305c**, as well as the two platinum containing species, **403b** and **406**, are shown in Figure 4.8.

The spectrum of ligand **305c** shows a maximal absorption at 362 nm (ε = 88,900) with a low–energy shoulder seen at ca. 397 nm. This lowest energy absorption is likely the result of the Ph–ene–yne–yne–ene–Ph chromophore. Upon coordination to platinum to form **406**, the high energy absorption is red–shifted, appearing at 371 (ε = 85,100), while the low energy shoulder absorption remains essentially unchanged at ca. 394 nm. The absorption spectrum of platinacycle **403b** shows a single, very broad absorption centred at 374 nm (ε = 81,600). We suspect that this peak is the result of two overlapping absorptions: The high energy maximal absorption as well as the lower energy metal–to–ligand charge–transfer (MLCT)[8] band, which appeared as a shoulder in the absorption spectra of the platinum–containing macrocycles previously described.

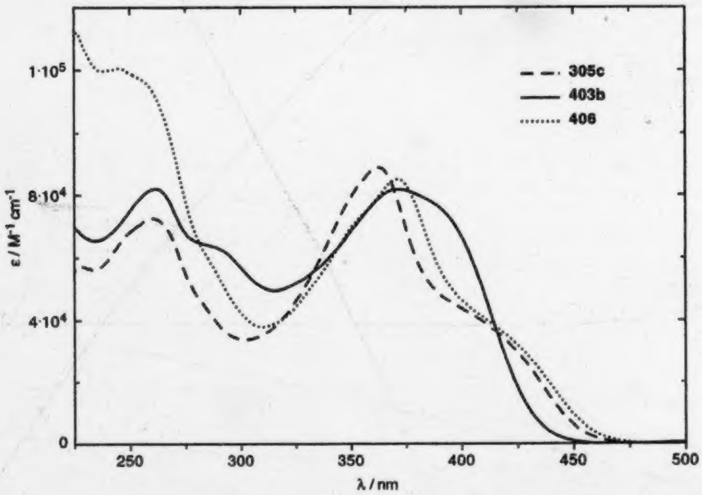

Figure 4.8 UV–vis absorption spectra (CH_2Cl_2) for compounds **305c**, **403b**, and **406**.

In addition to UV–vis analysis, the emission properties of these compounds were studied using fluorescence spectroscopy. The emission spectra of ligands **304c** and **402** as well as their coordination complexes **404** and **405** are shown in Figure 4.9. In all cases, the spectra were recorded in dry, oxygen–free CH_2Cl_2. The emissive properties of these compounds were studied by exciting at numerous wavelengths, depending on the respective absorptions observed in the UV–vis spectra. Shown in Figure 4.9 are, in all cases, the maximal emissions achieved with their respective excitation wavelengths.

The purely organic ligand **304c** shows the greatest fluorescence, providing a strong emission at 512 nm. Coordination to the platinum centre results in a complete loss of this emission when excited at 374 nm. When excited at high energy (265 nm), however, this compound (**404**) shows weak, high energy emissions. Platinacycle **402** is also emissive, showing maximal emissions at 335 and 347 nm, with a broad shoulder at ca. 430 nm, when excited at high energy. Interestingly, upon coordination to platinum, the emissive properties of this ligand are virtually unchanged, as seen in the spectrum of **405**. All three platinum–containing compounds **402**, **404**, and **405** also show extremely weak emissions at lower energy (ca. 670–690 nm) when irradiated at the indicated energies. Interestingly, however, none of these species show any low energy emission when excited at their absorption maxima.

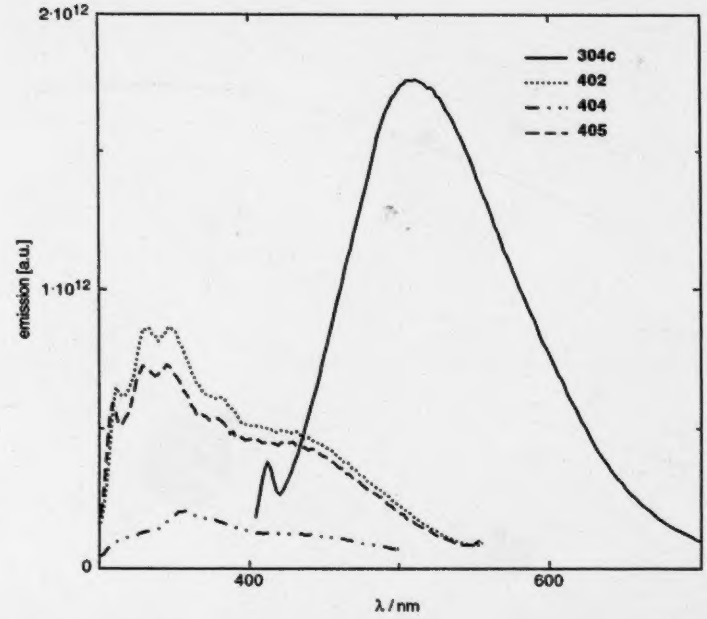

Figure 4.9 Emission spectra (CH_2Cl_2) for compounds **304c** (exc. at 370 nm), **402** (exc. at 290 nm), **404** (exc. at 265 nm) and **405** (exc. at 290 nm).

4.2.5 Nonlinear Optical Properties as a Function of Platinum

As described in the introduction to this chapter, platinum–acetylide complexes including cyclic and acyclic oligomers as well as polymers have been widely studied for their second and third order nonlinear optical properties. This is due to a number of factors including their ease of preparation, stability, and the presence of a delocalized π–electron system across the highly polarizable metal centre. We have collaborated with Aaron Slepkov, a graduate student in the University of Alberta's Physics Department and his supervisor, Prof. Frank Hegmann to measure the third order nonlinear optical second hyperpolarizabilities (γ) of compounds **304c**, **402**, **404** and **405**. All measurements were made using differential optical Kerr effect (DOKE) detection.[21]

Table 4.1 Summary of results for the macrocyclic series shown. γ_S and γ_{THF} are the molecular second hyperpolarizabilities of the samples and the THF reference, respectively.

Sample	Concentration (M)	$\gamma_S \times 10^{-34}$	γ_S/γ_{THF}
304c	0.0094	0.86	169
402	0.017	1.1	206
404	0.018	1.1	208
405	0.0087	1.4	272

The results of the measurements are summarized in Table 4.1. All of the measurements were made at extremely low concentrations (as indicated) in THF, primarily due to the limited solubility of the macrocyclic ligands. The molecular second hyperpolarizabilities γ_S were measured according to the methods previously described by Hegmann and coworkers.[22] These values were then normalized relative to γ_{THF} for the purpose of comparison. As anticipated, the introduction of the platinum acetylide linkage to form **402** results in an increase in the molecular hyperpolarizability relative to the purely organic ligand **304c**. However, the hyperpolarizability also increases from **304c** to **404**, upon coordination by the pyridine to the platinum centre. This implies that the third order nonlinear susceptibility is primarily a function of the presence of the platinum centre itself, regardless of its location and level of interaction with the pendant macrocyclic ligand. This trend continues upon the introduction of a second platinum centre as observed in the second hyperpolarizability of **405**. The implication of these results are that the second molecular hyperpolarizability for these macrocycles is not governed by the degree of linear conjugation present within the respective sample, but simply by the polarizability of the platinum centre(s) with a minimal contribution as a result of metal–to–ligand communication. To probe this interpretation, it would be of value to measure the third order nonlinear susceptibility of platinacycle **403b**, which showed a much higher degree of conjugation across the platinum centres than either **402** or **405**, but unfortunately, this compound simply does not possess the required solubility.

4.3 Conclusions and Outlook

Described in this chapter is the synthesis of a series of expanded pyridine and bipyridine analogues featuring platinum acetylide linkages. We have demonstrated that these soluble, metal–containing species are synthetically accessible in very good yields, especially relative to their unfunctionalized derivatives. We have also established that these porous ligands will participate in self–assembly processes. While X–ray crystallographic analysis demonstrates that we can achieve our goal of expanded pore sizes, it also highlights the potential pitfall of inaccessible pore structures due to the presence of other ligands on the metal centre. Further elaboration at the platinum centre(s) is intended via displacement of the pendant phosphine ligands, and, as such, this drawback will be addressed at a later time. The electronic properties of these species were also evaluated using UV–vis and emission spectroscopies, and these results suggest that communication across the metal centre(s) is effective. A collaboration allowed the measurement of the third order nonlinear optical susceptibilities of several compounds, and these preliminary results suggest that the second hyperpolarizability is primarily a function of the presence of platinum itself, regardless of its level of interaction with the pendant π–system.

4.4 References and Notes

1. (a) Mukherjee, P. S.; Das, N.; Kryschenko, Y. K.; Arif, A. M.; Stang, P. J. *J. Am. Chem. Soc.* **2004**, *126*, 2464–2473. (b) Yamamoto, T.; Arif, A. M.; Stang, P. J. *J. Am. Chem. Soc.* **2003**, *125*, 12309–12317. (c) Aoyagi, M.; Biradha, K.; Fujita, M. *Bull. Chem. Soc. Jpn.* **1999**, *72*, 2603–2606. (d) Sun, S.–S.; Lees, A. J. *J. Am. Chem. Soc.* **2000**, *122*, 8956–8967.

2. (a) Olenyuk, B.; Whiteford, J. A.; Fechtenkötter, A.; Stang, P. J. *Nature* **1999**, *398*, 796–799. (b) Chand, D. K.; Fujita, M.; Biradha, K.; Sakamoto, S.; Yamaguchi, K. *Dalton Trans.* **2003**, 2750–2756. (c) Kumazawa, K.; Biradha, K.; Kusukawa, T.; Okano, T.; Fujita, M. *Angew. Chem. Int. Ed.* **2003**, *42*, 3909–3913. (d) Sun, S.–S.; Lees, A. J. *Chem. Commun.* **2001**, 103–104. (e) Mukherjee, P. S.; Das, N.; Stang, P. J. *J. Org. Chem.* **2004**, *69*, 3526–3529.

3. (a) Aoyagi, M.; Biradha, K.; Fujita, M. *J. Am. Chem. Soc.* **1999**, *121*, 7457–7458. (b) Cotton, F. A.; Lin, C.; Murillo, C. A. *Chem. Commun.* **2001**, 11–12.

4. (a) Espinet, P.; Soulantica, K.; Charmant, J. P. H.; Orpen, A. G. *Chem. Commun.* **2000**, 915–916. (b) Campbell, K.; McDonald, R.; Ferguson, M. J.; Tykwinski, R. R. *J. Organomet. Chem.* **2003**, *683*, 379–387.

5. (a) Liu, Y.; Jiang, S.; Glusac, K.; Powell, D. H.; Anderson, D. F.; Schanze, K. S. *J. Am. Chem. Soc.* **2002**, *124*, 12412–12413. (b) Khan, M. S.; Al–Suti, M. K.; Al–Mandhary, M. R. A.; Ahrens, B.; Bjernemose, J. K.; Mahon, M. F.; Male, L.;

Raithby, P. R.; Friend, R. H.; Köhler, A.; Wilson, J. S. *Dalton Trans.* **2003**, 65–73. (c) McGarrah, J. E.; Kim, Y.–J.; Hissler, M.; Eisenberg, R. *Inorg. Chem.* **2001**, *40*, 4510–4511. (d) Kang, Y.; Lee, J.; Song, D.; Wang, S. *Dalton Trans.* **2003**, 3493–3499.

6. (a) Zhu, Y.; Millet, D. B.; Wolf, M. O.; Rettig, S. J. *Organometallics* **1999**, *18*, 1930–1938. (b) Younus, M.; Long, N. J.; Raithby, P. R.; Lewis, J. *J. Organomet. Chem.* **1998**, *570*, 55–62.
7. Adams, C. J.; Pope, S. J. A. *Inorg. Chem.* **2004**, *43*, 3492–3499.
8. (a) Yam, V. W.–W. *Acc. Chem. Res.* **2002**, *35*, 555–563. (b) Faust, R.; Diederich, F.; Gramlich, V.; Seiler, P. *Chem. Eur. J.* **1995**, *1*, 111–117.
9. (a) Bunten, K. A.; Kakkar, A. K. *Macromolecules* **1996**, *29*, 2885–2893. (b) Sun, Y.; Taylor, N. J.; Carty, A. J. *Organometallics* **1992**, *11*, 4293–4300. (c) Takahashi, S.; Kariya, M.; Yatake, T.; Sonogashira, K.; Hagihara, N. *Macromolecules* **1978**, *11*, 1063–1066. (d) Field, L. D.; Turnbull, A. J.; Turner, P. *J. Am. Chem. Soc.* **2002**, *124*, 3692–3702. (e) Adams, C. J.; James, S. L.; Raithby, P. R. *Chem. Commun.* **1997**, 2155–2156. (f) Long, N. J.; Williams, C. K. *Angew. Chem. Int. Ed,* **2003**, *42*, 2586–2617. (g) Iucci, G.; Infante, G.; Polzonetti, G. *Polymer*, **2002**, *43*, 655–663. (h) Sonogashira, K.; Ohga, K, Takahashi, S.; Hagihara, N. *J. Organomet. Chem.* **1980**, *188*, 237–243. (i) Siemsen, P.; Gubler, U.; Bosshard, C.; Günter, P.; Diederich, F. *Chem. Eur. J.* **2001**, *7*, 1333–1341.
10. (a) Onitsuka, K.; Fujimoto, M.; Ohshiro, N.; Takahashi, S. *Angew, Chem. Int. Ed.* **1999**, *38*, 689–692. (b) Takahashi, S.; Onitsuka, K.; Takei, F. *Macromol. Symp.* **2000**, *156*, 69–77. (c) Hurst, S. K.; Cifuentes, M. P.; Humphrey, M. G.

Organometallics **2002**, *21*, 2353–2355. (d) Onitsuka, K.; Iuchi, A.; Fujimoto, M.; Takahashi, S. *Chem. Commun.* **2001**, 741–742.

11. (a) Xu, D.; Hong, B. *Angew. Chem. Int. Ed.* **2000**, *39*, 1826–1829. (b) Yao, H.; Sabat, M.; Grimes, R. N.; Fabrizi de Biani, F.; Zanello, P. *Angew. Chem. Int. Ed.* **2003**, *42*, 1002–1001. (c) Onitsuka, K.; Yamamoto, S.; Takahashi, S. *Angew. Chem. Int. Ed.* **1999**, *38*, 174–176. (d) Whiteford, J. A.; Lu, C. V.; Stang, P. J. *J. Am. Chem. Soc.* **1997**, *119*, 2524–2533. (e) Pak, J. J.; Darwish, O. S.; Weakley, T. J. R.; Haley, M. M. *J. Organomet. Chem.* **2003**, *683*, 430–434.

12. Youngs, W. J.; Tessier, C. A.; Bradshaw, J. D. *Chem. Rev.* **1999**, *99*, 3153–3180.

13. Wang, S.; Mayr, A.; Cheung, K. K. *J. Mater. Chem.* **1998**, *8*, 1561–1565.

14. (a) Fernández, F. J.; Venkatesan, K.; Blacque, O.; Alfonso, M.; Schmalle, H. W.; Berke, H. *Chem. Eur. J.* **2003**, *9*, 6192–6206. (b) Xu, G.–L.; Zou, G.; Ni, Y.–H.; DeRosa, M. C.; Crutchley, R. J.; Ren, T. *J. Am. Chem. Soc.* **2003**, *125*, 10057–10065.

15. (a) Lo, W.–Y.; Lam, C.–H.; Yam, V. W.–W.; Zhu, N.; Cheung, K.–K.; Fathallah, S.; Messaoudi, S.; Le Guennic, B.; Kahlal, S.; Halet, J.–F. *J. Am. Chem. Soc.* **2004**, *126*, 7300–7310. (b) Lu, W.; Mi, B.–X.; Chan, M. C. W.; Hui, Z.; Che, C.–M.; Zhu, N.; Lee, S.–T. *J. Am. Chem. Soc.* **2004**, *126*, 4958–4971. (c) Wang, Y.–W.; Yang, Q.–Z.; Wu, L.–Z.; Li–Ping, Z.; Chen–Ho, T. *Chin. J. Chem.* **2004**, *22*, 114–116. (d) Yam, V. W.–W.; Lo, W.–Y.; Lam, C.–H.; Fung, W. K.–M.; Wong, K. M.–C.; Lau, V. C.–Y.; Zhu, N. *Coord. Chem. Rev.* **2003**, *24*, 539–547.

16. Marder, T. B.; Lesley, G.; Yuan, Z.; Fyfe, H. B.; Chow, P.; Stringer, G.; Jobe, I. R.; Taylor, N. J.; Williams, I. D.; Kurtz, S. K. In *Materials for Nonlinear Optics:*

Chemical Perspectives Marder, S. R.; Sohn, J. E.; Stucky, G. D. Eds. **1991**, ACS Symposium Series, 605–615.

17. Campbell, K.; McDonald, R.; Ferguson, M. J.; Tykwinski, R. R. *Organometallics* **2003**, *22*, 1353–1355.
18. Sonagashira, K.; Ohga, K.; Takahashi, S.; Hagihara, N. *J. Organomet. Chem.* **1980**, *188*, 237–243.
19. D'Amato, R.; Furlani, A.; Colapietro, M.; Portalone, G.; Casalboni, M.; Falconieri, M.; Russo, M. V. *J. Organomet. Chem.* **2001**, *627*, 13–22.
20. Cox, E. G.; Saenger, H.; Wardlaw, W. *J. Chem. Soc.* **1934**, 182–186.
21. Ho, P. P.; Alfano, R. R. *Phys. Rev. A* **1979**, *20*, 2170–2187.
22. Slepkov, A. D.; Hegmann, F. A.; Zhao, Y. M.; Tykwinski, R. R.; Kamada, K. *J. Chem. Phys.* **2002**, *116*, 3834–3840.

Chapter 5 Application of Pyridine–Containing Macrocycles Toward the Formation of Porous Solids

5.1 Introduction

Recently, there has been renewed interest in the rational design and construction of porous solids due to an increased demand for 'smart' materials with tailored functional properties. Solids possessing large and robust pores or cavities may find application as materials for molecular sensing and/or separations[1] as well as gas capture and storage devices.[2] The installation of appropriate chemical functionality within a pore may also lead to materials capable of more elaborate interactions with suitable guest molecules. For example, porous systems capable of acting as synthetic receptors[3] have been envisioned. Another exciting avenue focuses on the development of pores or channels that can function as sites for chemical reactions to occur. The incorporation of suitable functionality within these pores may lead to catalytic materials[4] capable of functioning as reusable synthetic analogues of enzymes.

While most synthetic and naturally–occurring porous solids are inorganic zeolites, recent focus has shifted toward the development of similar materials based on an organic or hybrid metal–organic scaffold. The high degree of tunability available through synthetic chemistry has made organic–based materials attractive targets. While numerous strategies have been applied toward the formation of porous organic or metal–organic solids, most of these approaches have been based upon one of two basic design principles. The first, and purely organic, strategy involves the construction of nanoscale, shape–persistent macrocycles[5] such as the example shown in Figure 5.1 by

Höger and coworkers.[6] Subsequent to their synthesis, these macrocyclic species are crystallized, and porous structures are realized when the macrocyclic building blocks eclipse one another in the solid–state. The intermolecular assembly of these species to form tubular structures, however, can be very difficult to control. In most cases, weak interactions such as π–π stacking, van der Waals forces, and hydrophobic effects are relied upon to support the aggregation. However, the aggregation of these species can be enhanced through the introduction of side chains such as alkyl or alkoxy groups onto the periphery of the macrocyclic core(s). The incorporation of side chains also helps to mediate the solubility problems associated with such rigid, symmetrical, and highly unsaturated structures. Unfortunately, in many cases,[7] the peripheral side chains can also obscure the channels that are created upon eclipsing in the solid–state, as described in Chapter 1.

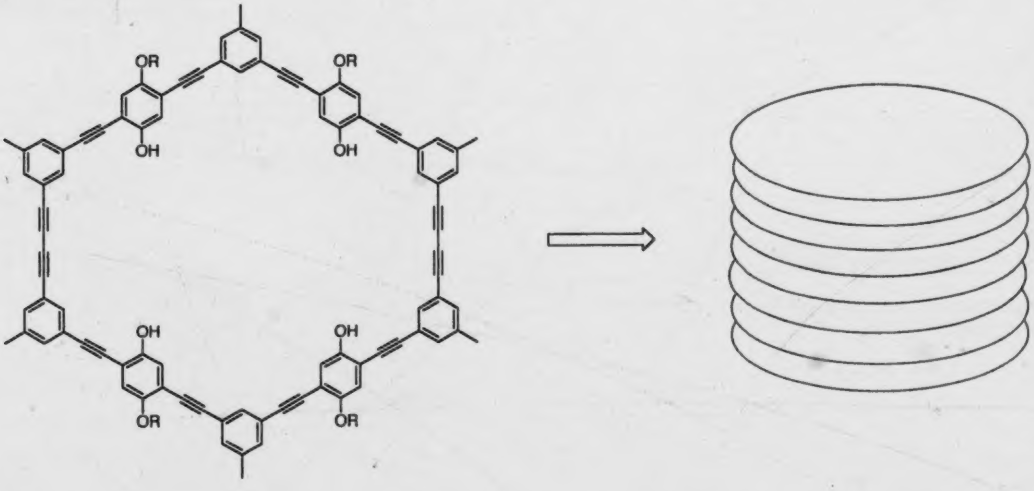

501

Figure 5.1 Porous structures via the aggregation of shape–persistent macrocycles.

A second strategy toward the formation of porous solids relies on the use of coordination chemistry to establish the pore size and shape. Rigid organic ligands such as 4,4'–bipyridine (Figure 5.2) will self–assemble, in the presence of an appropriate metal or metal ion, to provide supramolecular assemblies of predictable size and shape.[8] By controlling the coordination geometry about the metal centre as well as the binding geometry of the bi– or tri–dentate ligand, it is possible in most circumstances to reliably access architectures of predetermined morphology. While predictability has been achieved with respect to the intermolecular assembly of these components, controlled aggregation of the resultant assemblies is still extremely challenging. As with the previous approach described above, weak intermolecular interactions are often relied upon to realize pores or channels in the solid–state. An additional challenge is present in that many of these systems succumb to lattice interpenetration upon assembly, thwarting the potential utility of the channels that might be constructed.

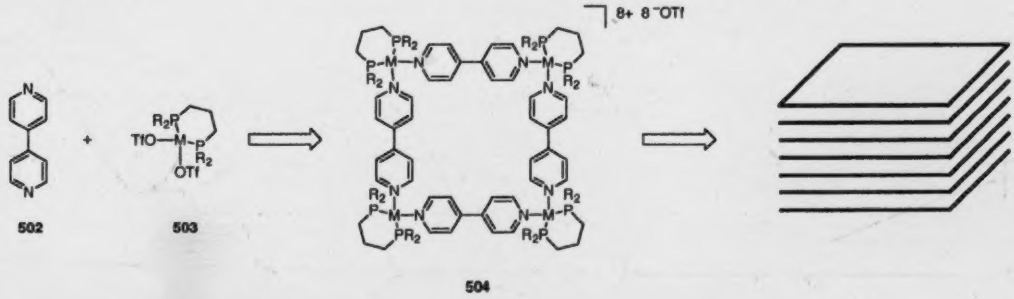

Figure 5.2 Porous structures via coordination to metal ions.

Some of these challenges have been addressed through the inception of metal–organic frameworks (MOFs) such as those developed by Yaghi and coworkers.[9] To circumvent the problem(s) of lattice interpenetration and unpredictability with respect to intermolecular association, metals capable of binding to the organic linkers outside of two dimensions have been introduced (Figure 5.3). This approach very closely mirrors the model of an inorganic zeolite. Rather than relying upon weak intermolecular interactions to direct the assembly of component parts, dative bonds in all three directions are established, leading to infinite porous assemblies. While this approach does lead to the predictable assembly of metal and ligand to form porous solids, such systems are still susceptible to lattice interpenetration and are, to date, limited to carboxylate–based organic ligands. Problems with respect to characterization may also occur because these assemblies are not discrete molecular entities, but rather infinite, polymeric networks.

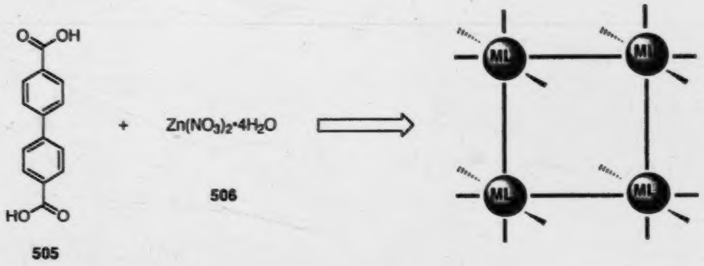

Figure 5.3 Porous metal–organic frameworks.

Infinite porous assemblies are also accessible via the use of "molecular tectonics" as developed by Wuest and coworkers.[10] This strategy relies on hydrogen–bonding interactions (Figure 5.4) rather than metal coordination to achieve the assembly of the porous framework. While these systems are also susceptible to interpenetration, they nevertheless retain very large void volumes suitable for the inclusion *and* exchange of guest molecules, highlighting the robust nature of these networks.

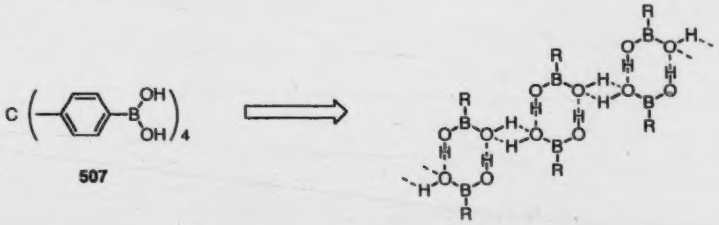

Figure 5.4 Porous solids via a "molecular tectonics" approach.

As described in previous chapters, much of my thesis research has focused on the synthesis of conjugated macrocycles bearing pyridine functionality due, in part, to their potential to act as porous ligands in self–assembly reactions. We envisioned that these porous ligands or "building blocks" could be directed, under appropriate conditions, to form porous structures in the solid–state (Figure 5.5). This strategy incorporates some of the design features described above. First, the pore size and shape are established through the construction of a shape–persistent macrocycle. In addition, functionality capable of binding to a metal atom or ion is covalently introduced into the backbone of the macrocyclic species by way of the diethynylpyridine moiety. This provides a means to rationally direct the assembly of these macrocyclic species via metal coordination, while avoiding such potential pitfalls as lattice interpenetration and chemical or thermal instability. The successful application of our strategy toward the realization of a bidirectionally porous solid,[11] and its characterization in both the solution and solid state will be described in the following discussion.

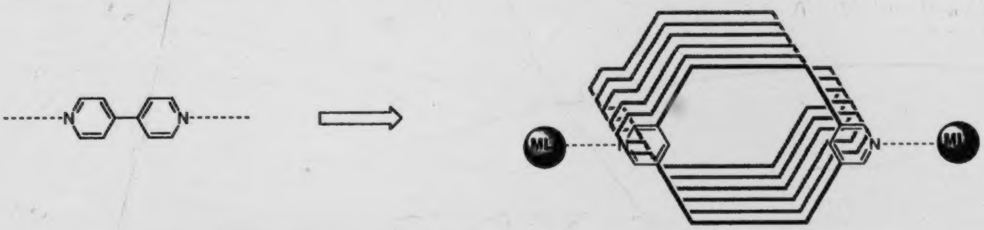

Figure 5.5 Porous structures through the use of macrocyclic ligands.

In addition to the synthetic challenges that are encountered when designing porous materials, researchers in this field are often faced with the even greater difficulty of characterizing the materials they have constructed, particularly in the solid–state. In the absence of high quality crystals suitable for X–ray crystallographic analysis, the study of many materials is routinely abandoned. An additional difficulty is encountered even in the rare cases where a porous organic solid is characterized by X–ray crystallography. In many cases solvent molecules occupy the void space, channel, or pore that is created upon packing. The full potential of porous organic solids relies on the ability of guest molecules to enter and exit the pore structure, and this can be prevented if the channels are obstructed with solvent molecules. In cases where the solvent can be removed from channels present in the solid, it is difficult to say with confidence whether the core solid–state structure remains intact. In many circumstances, when the solvent is removed from a solid, the desolvated crystal shatters or collapses and is no longer suitable for X–ray crystallographic analysis.

As described above, we have established that the use of macrocycles as ligands is an effective strategy for the formation of porous materials, as demonstrated by X–ray analysis of the resultant crystalline solid. Like others in this field, however, we encountered difficulties when we tried to remove the solvent present within the crystal lattice. We found that the crystal integrity was not sustainable in the absence of the associated solvent molecules. It was at this point that we began to look for alternatives to X–ray crystallography for the characterization of porous structures.

Many of the conventional techniques for studying porous solids such as porosimetry and BET (Brunauer–Emmet–Teller) analysis are based on nitrogen gas sorption.[12] However, in most cases, these techniques require a prohibitively large amount of sample. An additional concern is that many of these analyses are performed at very low temperatures (77 °K), which may cause significant structural changes in the host solid, relative to their properties at practical, elevated temperatures.

Hyperpolarized ^{129}Xe NMR spectroscopy is a well–established method for the study of porous systems and has been used extensively to provide insight into the porous nature of inorganic zeolites.[13] The extremely high polarizability of xenon gas and its resultant chemical shift sensitivity make this method ideal for investigating the porous nature of zeolitic materials. While this technique has only rarely been applied to the study of purely organic porous materials,[14] in collaboration with Kristopher Ooms, a graduate student in Prof. Rod Wasylishen's group, we decided to explore the possibility of applying this technique to the study of our porous organic and metal–organic systems. Variable temperature hyperpolarized ^{129}Xe NMR spectra of several of our porous solids were acquired and the trends observed have helped us to establish that it is possible to remove solvent molecules from the crystal lattice and that these solids retain their porosity in the absence of these associated solvent molecules. Trends observed primarily in the chemical shifts as well as additional exchange spectroscopy experiments have provided us with a great deal of insight into the porous nature of these materials and the dynamics of the guest gas molecules. These results will be described in detail in the discussion that follows.

5.2 Results and Discussion

5.2.1 Synthesis and Characterization of Bidirectionally Porous Assembly

As discussed in previous chapters, macrocycle **305c** was synthesized because we envisioned that it could function as a porous 4,4′–bipyridine analogue in self–assembly reactions. In collaboration with Prof. Peter Stang and his graduate student Christopher Kuehl, we targeted assemblies featuring our macrocyclic ligand(s) linked by *cis*–$(TfO)_2Pt(PEt_3)_2$ (**319**)[15] which they have shown to be an effective "corner piece" for supramolecular architectures derived from bipyridine ligands.

The synthesis of assembly **508** is outlined in Scheme 5.1.[11] One equivalent of macrocyclic ligand **305c** was suspended in dry CH_2Cl_2 and then slowly added (over 15 minutes) to a solution of two equivalents of *cis*–$(TfO)_2Pt(PEt_3)_2$ (**319**) in dry CH_2Cl_2. The reaction mixture was then stirred at room temperature for 18 hours under a positive pressure of N_2. A second portion of the macrocycle was then suspended in dry CH_2Cl_2 and slowly added to the reaction mixture. After stirring at room temperature for a further 18 hours, 80% of the solvent was allowed to evaporate in air, yielding assembly **508** as bright orange crystals in 84% yield.

It is worth noting that the synthesis and subsequent isolation of **508** is only successful if several variables are carefully controlled. First, it is important that all starting materials are rigorously dried. In particular, the *cis*–platinum species **319** must be freshly crystallized from dry CH_2Cl_2/diethyl ether. This prevents the formation of what is presumably hydrated platinum species,[16] the presence of which inhibits both the binding of the pyridine-containing macrocycle to platinum as well as the isolation of supramolecular assembly. In addition, it is also very important to control both the dilution of all reactants as well as their order and rate of addition to the reaction mixture. Assembly **508** can only be isolated in pure form via recrystallization from the reaction mixture and the presence of excessive numbers and/or quantities of byproducts seriously inhibits the success of this purification step.

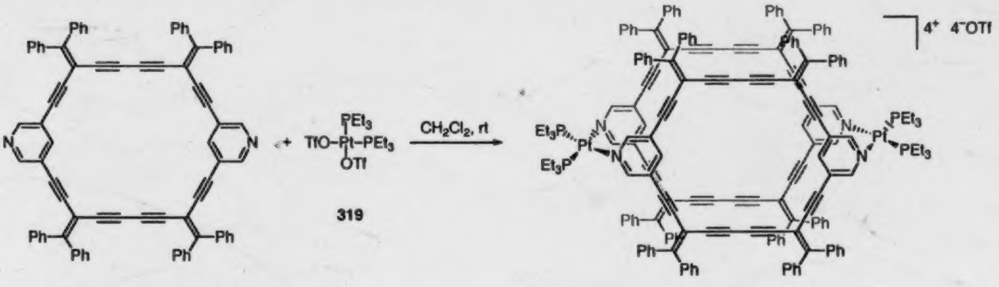

305c **319** **508**

Scheme 5.1 Synthesis of porous assembly **508**.

Assembly **508** was fully characterized in the solution state, using several NMR spectroscopic techniques in combination with IR spectroscopy and ESI mass spectral analysis. The ^{1}H NMR spectrum confirms the binding of macrocycles **305c** to the platinum centre(s). The ^{1}H NMR spectrum of free macrocyclic ligand **305c** shows resonances for the *ortho–* and *para–*pyridyl protons as a doublet and a triplet at δ 8.13 and 7.83, respectively. By contrast, these same resonances appear as a second–order multiplet at δ 8.42 and a triplet at δ 7.95, respectively, in the ^{1}H NMR spectrum of the complex **508**. The observed splitting pattern of the *ortho* protons is the result of long–range coupling to the magnetically inequivalent phosphorous nuclei. This observation was confirmed through analysis of the $^1H_{ortho}$ $\{^1H_{para}\}$ and ^{1}H $\{^{31}P\}$ NMR spectra. Decoupling of the *ortho* protons from either the *para–*pyridyl protons or the adjacent phosphine ligands led to the collapse of the broad, second–order signal into a simple, although barely resolved, doublet. The ^{13}C $\{^1$H$\}$ NMR spectrum also provided convincing evidence for the formation of **508** in solution. Resonances for 19 of the 20 unique carbons of **508** were observed. In addition, the $^{31}P\ \{^1H\}$ and $^{19}F\ \{^1H\}$ NMR spectra each showed only a single resonance at –1.3 and –78.2 ppm, respectively, confirming the presence of a discrete, symmetrical species in solution.

The most convincing evidence for the formation of the *dimeric* assembly **508** in solution came from the ESI mass spectral analysis. The ESI mass spectrum was acquired by slow infusion of a solution of **508** in $CH_2Cl_2/MeNO_2$. Significantly, a prominent signal is observed at *m/z* 745 (24%) and is assigned to $[$**508** $- 4(^{-}OTf)]^{4+}$. In addition, several peaks consistent with the fragmentation of **508** are observed at *m/z* 1059 (9%), 492 (78%), and 429 (100%), assigned to $[$**305c** $+ H]^+$, $[$**319** $- 2(^{-}OTf) + NO_2Me]^+$, and $[$**319** $- 2(^{-}OTf)]^+$, respectively.

Larger supramolecular assemblies were also targeted featuring our 'expanded' bipyridine analogues **403a** and **403b** (Scheme 5.2). Platinacycles **403a** and **403b** were treated with identical reaction conditions to that described above but, frustratingly, in neither case was the desired assembly isolated. In both cases, ^1H and ^{31}P NMR spectroscopy indicated the formation of a mixture of products, rather than a single, discrete species. In an attempt to restrict the formation of byproducts, numerous NMR titration experiments were performed where the respective macrocyclic ligand (**403a** or **403b**) was dissolved in CD_2Cl_2 and slowly added to an NMR tube containing one equivalent of **319** dissolved in CD_2Cl_2. This synthetic approach also resulted in the formation of a mixture of products, as evidenced by ^1H and ^{31}P NMR spectroscopy. This was especially frustrating as spectroscopic analysis clearly indicated that all of the starting materials were being consumed upon addition and ESI mass spectral analysis clearly showed signals that were attributable to fragments of the desired assemblies. Clearly the platinacycles **403a** and **403b** were able to coordinate to the platinum species **319**, but no single product could be isolated, despite numerous attempts at crystallization.

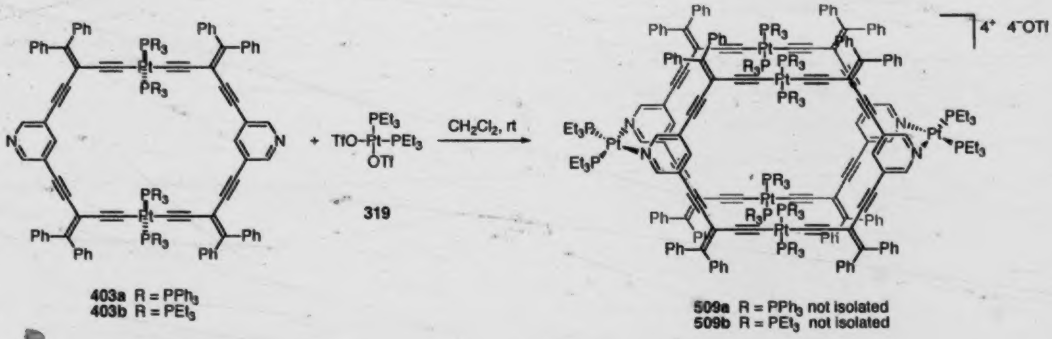
Ph
PR3
Pt
N
PEt3
TfO–Pt–PEt3
OTf
CH2Cl2, rt
319
Et3P
R3P
4+ 4⁻OTf
403a R = PPh3
403b R = PEt3
509a R = PPh3 not isolated
509b R = PEt3 not isolated

Scheme 5.2 Attempted synthesis of larger assemblies **509a** and **509b**.

We next turned our attention to the synthesis of assembly **511** (Scheme 5.3). It was thought that steric interactions between the pendant triphenylphosphine ligands of stacking platinacycles could be preventing the desired ring–closing reaction to form **509a** (or **509b**). The incorporation of the extended bimetallic "spacer" **510**[17] was expected to eliminate any steric interactions between reacting macrocyclic units.

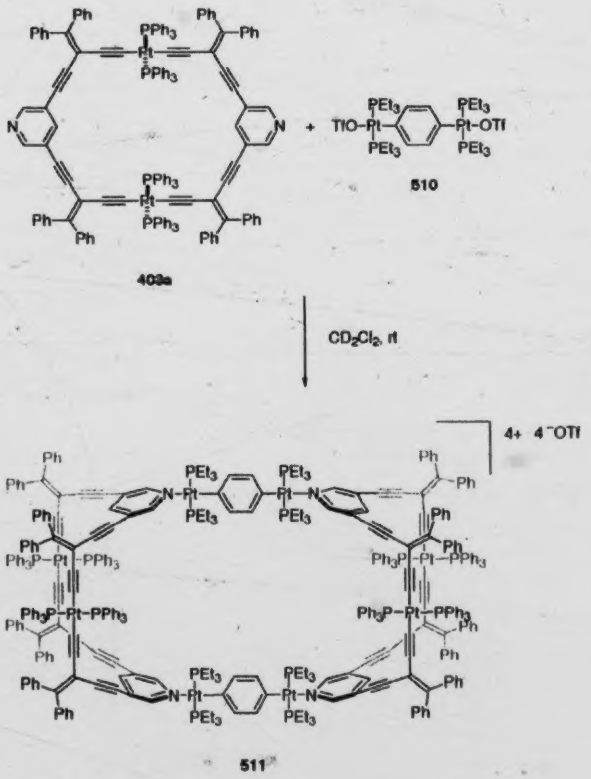

Scheme 5.3 Attempted synthesis of assembly **511**.

Platinacycle **403a** was dissolved in CD$_2$Cl$_2$ and, over a period of two days, was titrated into a CD$_2$Cl$_2$ solution of **510**. Spectroscopic analysis confirmed the formation of a single, discrete product. ^{1}H NMR analysis of the reaction mixture was not especially diagnostic, showing several broad multiplets in the low field region of the spectrum. The ^{31}P NMR spectrum, however, showed only two resonances at 18.0 ($^1J_{P-Pt}$ = 2611 Hz) and 14.4 ($^1J_{P-Pt}$ = 2703 Hz) ppm, assigned to the triphenylphosphine and triethylphosphine groups, respectively. Preliminary ^{13}C NMR analysis was also performed and, although the signal to noise was poor, 20 out of the 26 expected non–equivalent carbon resonances were observed. The ESI mass spectrum of the reaction mixture showed signals at *m/z* 2968 and 1719 corresponding to [(2(**403a**) + **510** – 2($^{-}$OTf))$^{2+}$] and [(**403a** + **510** – 2($^{-}$OTf))$^{2+}$], respectively. Frustratingly, however, ESI MS analysis did not provide any evidence of a molecular ion peak. Several different ionization conditions were applied including MALDI (using both anthracene and dithranol as matrices), but all attempts led only to the observation of fragments in the mass spectra. In the absence of mass spectral confirmation of the proposed structure or X–ray crystallographic analysis, we cannot say with confidence that assembly **511** was the product formed under these reaction conditions.

This example highlights a difficulty that is often faced by researchers in this field: In the absence of X–ray quality crystals, it can be impossible to confidently identify the product of a self–assembly reaction. Mass spectral analysis of large assemblies that are established using weak, non–covalent interactions is often just not possible. Without mass spectral confirmation of a proposed structure, it is not reasonable to rule out, for example, the formation of a tetrameric rather than a dimeric structure.

5.2.2 Crystallographic Analysis of Porous Assembly

In addition to full characterization in solution, the solid–state properties of assembly **508** were also examined. Single crystals suitable for X–ray crystallographic analysis were grown by slow evaporation from a solution of **508** in $CH_2Cl_2/ClCH_2CH_2Cl$ at room temperature. The representation of assembly **508** in Figure 5.6 shows how the remarkably flexible building block **305c** has adopted a boat–like conformation, presumably to reduce steric interactions between the pendant diphenylvinylidene groups and adjacent ligands. The macrocycle is relatively free from strain as reflected in the alkyne bond angles, which depart from the ideal value of 180° by a maximum of 7.7°, with a mean deviation of 4.8°. Furthermore, the vinylidene bond angles are comparable to those of similar acyclic systems.[18] The N–Pt–N bond angle of 83.3° is also consistent with that observed in unstrained molecular squares constructed from bipyridine and related *cis*–platinum complexes.[19]

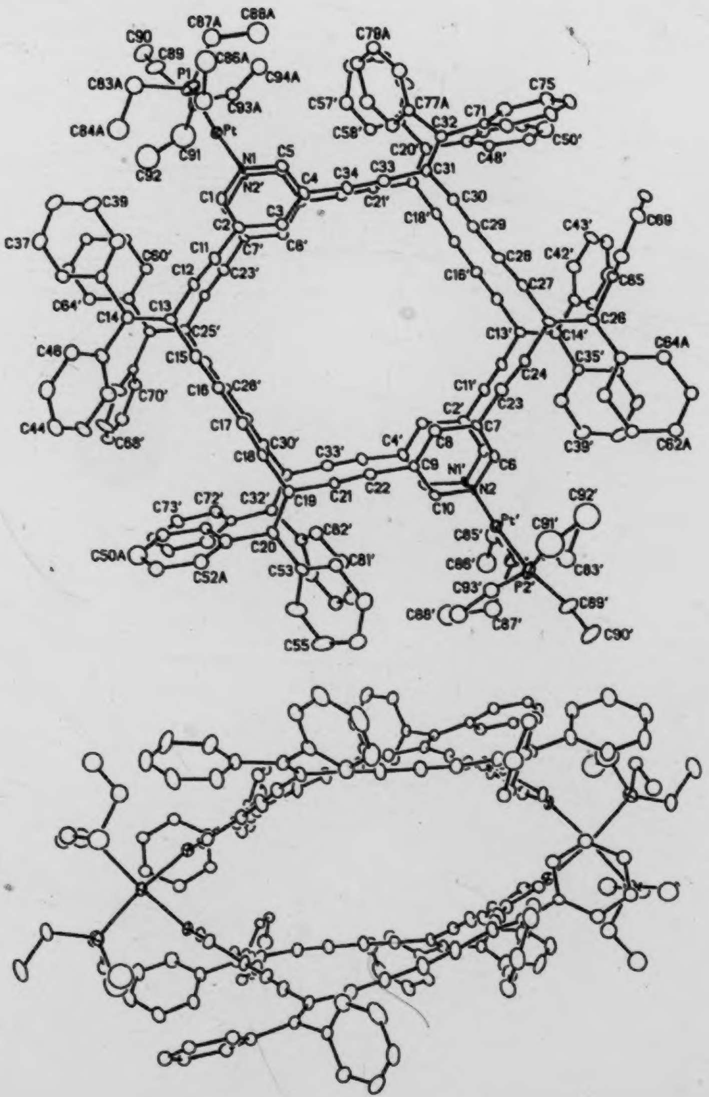
C90
C87A
C88A
C89
P1
C86A
C79A
C83A
C94A
C93A
C57'
C77A
C75
C84A
Pt
C91
C58'
C32
C71
C92
N1
C5
C20'
C50'
C48'
C4
C34
C33
C31
N2'
C1
C21'
C30
C3
C18'
C29
C39
C2
C69
C43'
C37
C11
C7'
C8'
C28
C42'
C60'
C12
C23'
C16'
C27
C85
C13
C64'
C14
C25'
C13'
C14'
C26
C15
C64A
C46
C35'
C16
C26'
C11'
C24
C70'
C2'
C23
C44
C17
C7
C39'
C62A
C88'
C4'
C8
C30'
C18
C33'
C9
N1'
C6
C22
C21
N2
C73'
C72'
C32'
C19
C10
C92'
C82'
Pt'
C91'
C50A
C20
C85'
C81'
C86'
C83'
C52A
C53
C93'
P2'
C88'
C87'
C89'
C90'
C55

Figure 5.6 (Top) ORTEP drawing of porous assembly **508**. (Bottom) Alternate view. Selected bond lengths [Å] and angles [°]: Pt–P(1) 2.273(4), Pt–P(2) 2.282(4), Pt–N(1) 2.120(9), Pt–N(2) 2.141(8); P(1)–Pt–P(2) 97.16(13), P(1)–Pt–N(2′) 173.5(2), P(2)–Pt–N(1) 172.3(2), N(1)–Pt–N(2′), C(12)–C(13)–C(15) 114.5(10), C(18)–C(19)–C(21) 113.7(10), C(24)–C(25)–C(27) 113.0(10), C(30)–C(31)–C(33) 113.9(11). Thermal ellipsoids are drawn at the 20% probability level; $ClCH_2CH_2Cl$ and associated triflate anions have been omitted, for clarity.

The six dihedral angles of the boat–like conformation of the macrocycle approximate the degree of distortion of the macrocyclic core. Using dummy atoms generated at the center of the pyridine rings as two centroids (cen) of the hexagon and the alkylidene carbons C(31), C(25), C(19), and C(13), the following dihedral angles are obtained: (1) 23.7° [(cen1)–C(31)–C(25)–(cen2)], (2) 49.5° [C(31)–C(25)–(cen2)–C(19)], (3) 34.9° [C(25)–(cen2)–C(19)–C(13)], (4) 8.8° [(cen2)–C(19)–C(13)–(cen1)], (5) 30.3° [C(19)–C(13)–(cen1)–C(31)], and (6) 14.2° [C(13)–(cen1)–C(31)–C(25)].[20]

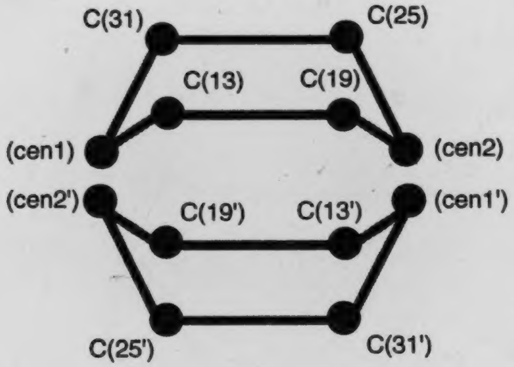

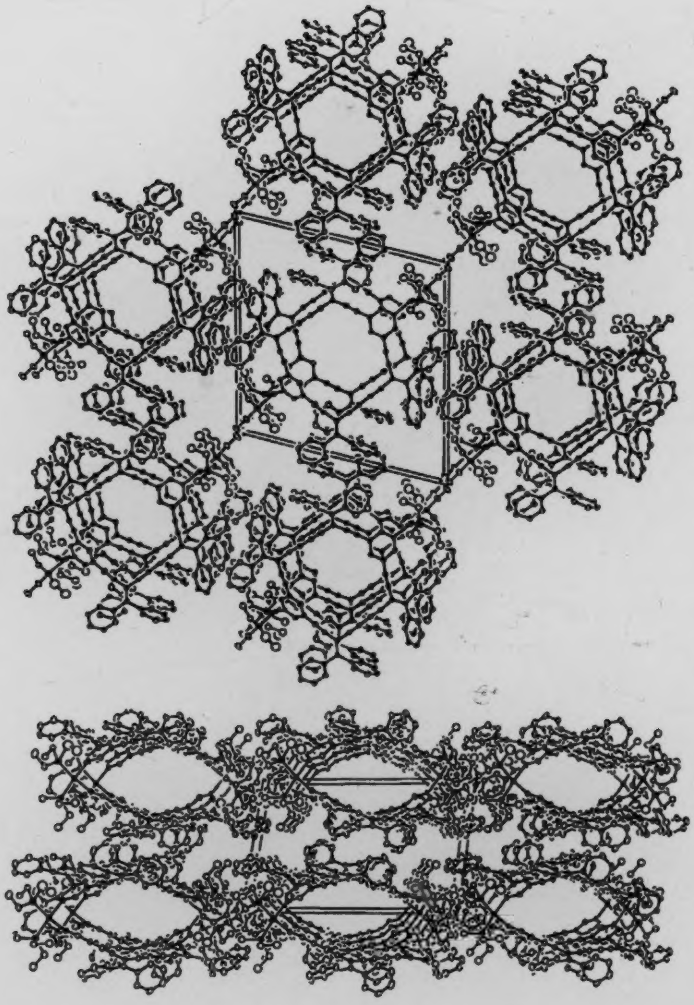

Figure 5.7 (Top) Crystal packing diagram of assembly **508** as viewed down the *a*–axis. (Bottom) Alternate view down the *c*–axis. Thermal ellipsoids are drawn at the 20% probability level; solvent and associated triflate anions have been omitted, for clarity.

The solid-state structure of **508** possesses two sets of perpendicular channels that result from the combined attributes of the macrocyclic building block and the supramolecular assembly. When viewed along the *c*–axis (Figure 5.7, bottom), the channels resulting from the boat–like conformation of the macrocycle are clearly evident. This cavity is 7.5 Å across by 16.3 Å (Pt–Pt). When viewed along the *a*–axis (Figure 5.7, top), stacking of the macrocyclic portion of the assembly provides a second set of perpendicular channels, with smaller internal dimensions as circumscribed by the enyne scaffold of the macrocycle at 6.6 (H–H) by 9.7 (C(16)–C(29)) Å. Noteworthy is the selective uptake of $ClCH_2CH_2Cl$ from the solvent mixture into the crystal lattice; the unit cell of **508** incorporates a total of eight solvent molecules. Two molecules are located within the channel defined by the conjugated macrocyclic core, as viewed down the *a*–axis (Figure 5.8, top). These two molecules also occupy space in the perpendicular channel circumscribed by the supramolecular assembly. Four additional solvent molecules are also present in this channel, for a total of six when viewed along the *c*–axis (four of which are shown in Figure 5.8, bottom). Two of the associated triflate ions are also present in this channel (not shown). The remaining two solvent molecules and two triflate ions occupy positions peripheral to the assembly. Overall, there is a significant proportion of void space in the structure, calculated at 13%, when the co–crystallized solvent is excluded. Including the space occupied by the solvent molecules, the void space is a remarkable 28% of the unit cell volume.

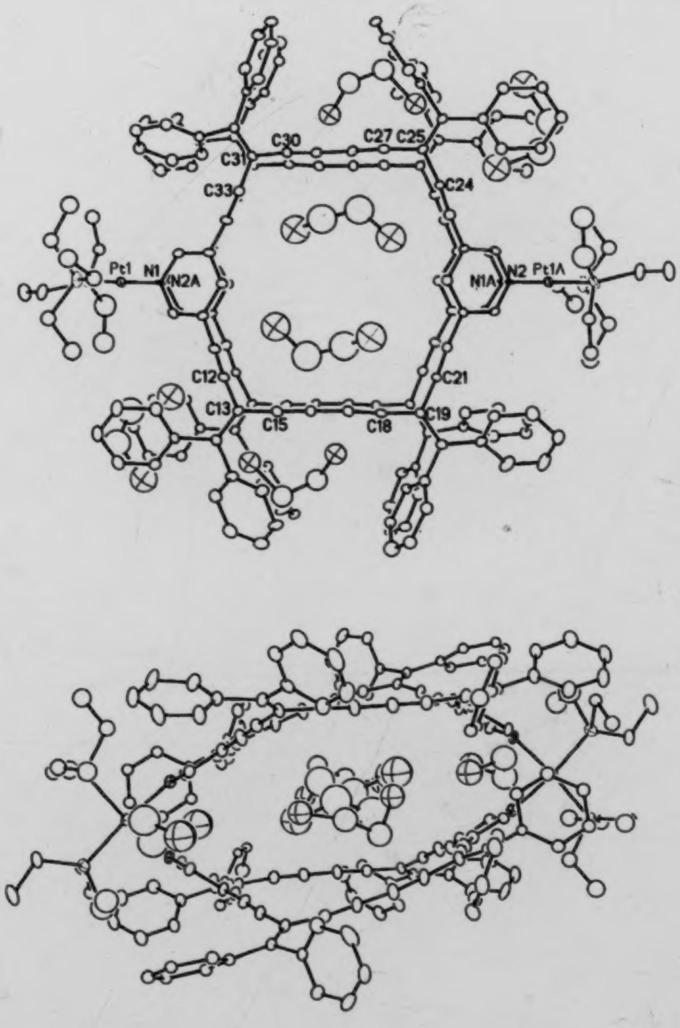
C30
C27
C25
C31
C33
C24
Pt1
N1
N2A
N1A
N2
Pt1A
C12
C21
C13
C15
C18
C19

Figure 5.8 ORTEP drawing of assembly **508** showing six of the eight co-crystallized solvent molecules. (Top) View down the *a*–axis showing two molecules of solvent in channel. (Bottom) View down the *c*–axis showing six molecules of solvent in channel. Thermal ellipsoids are drawn at the 20% probability level.

5.2.3 ^{129}Xe NMR Studies on Porous Organic Solids

As described in the introduction to this chapter, the utility of a porous solid resides in its ability to accept and release guest molecules while retaining porosity in the solid state. While we were thrilled to discover that the porous assembly **508** had selectively included guest molecules into the bidirectional channel system, we also needed to determine whether the solid retained its porosity in the absence of the co–crystallized solvent.

Our initial attempts to address this question focused on the acquisition of X–ray quality crystals in the absence of the guest dichloroethane molecules. To our frustration, all of our efforts to grow crystals using alternative solvents were unsuccessful. With many solvent mixtures and crystallization conditions we achieved only non–crystalline precipitates and in the rare cases where crystals were achieved, the crystals desolvated rapidly and shattered before X–ray analysis could be performed. We also attempted to remove the solvent from crystals grown from a $CH_2Cl_2/ClCH_2CH_2Cl$ mixture. Again, we found that the crystals shattered upon removal of the solvent molecules and were no longer suitable for crystallographic analysis.

Inorganic–based porous materials have been studied extensively using a variety of solid–state NMR techniques. In particular, hyperpolarized ^{129}Xe NMR spectroscopy[13,21] has been used to provide information about pore size and shape as well as the dynamics of guest molecules present within porous structures. In collaboration with Kristopher Ooms in Prof. Rod Wasylishen's group we have used ^{129}Xe NMR spectroscopy to provide us with important solid–state structural information about our porous systems that was not available using conventional methods.

The strength of this technique for studying porous solids lies in the high degree of polarizability of the xenon gas. Xenon has a van der Waals radius of 2.16 Å (approximately the same size as methane) and is very sensitive to changes in its environment. The polarizability of the xenon gas results in a broad chemical shift range of at least 230 ppm,[13] making this technique extremely sensitive. The bulk gas is set as the reference (at 0 ppm) and all resonances appear downfield of the gas peak. In general, the greater the interaction between ^{129}Xe and the host solid, the higher the observed chemical shift value. This means that small pores or channels will result in a low field chemical shift value, with large pores affording resonances upfield as the xenon gas has limited interactions with the pore walls. In inorganic zeolites, sufficient study has occurred such that trends have been established and quantitative information can be extracted with respect to pore size.[22] While this is not the case with organic materials, we have acquired variable temperature ^{129}Xe NMR spectra for several of our organic and metal–organic materials and comparison of these spectra in combination with data acquired from X–ray crystallographic analysis allows us to draw some conclusions with respect to the porous nature of these materials in the absence of guest solvent molecules.

The variable temperature ^{129}Xe NMR spectra of porous solid **508** are shown in Figure 5.9. Each spectrum was remarkably acquired using less than 15 mg of sample. It is immediately apparent that there are two sites or pores present within the solid. First, at high temperatures, a broad, low field resonance is barely discernable in the range of 210–180 ppm. Upon cooling to room temperature, a second resonance begins to separate from the gas peak as the low field resonance diminishes in intensity. This resonance stabilizes at approximately –70 °C at a chemical shift of 112 ppm.

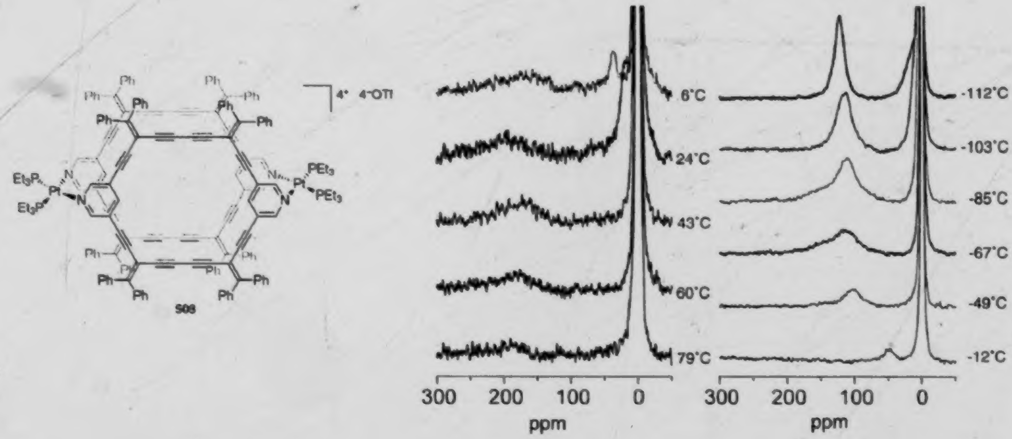

Figure 5.9 Variable temperature hyperpolarized ^{129}Xe NMR spectra of porous assembly **508** at 55 MHz.

The broadness and chemical shift value observed for the low field resonance suggests that there are several chemically similar small "dissolved" sites present within the crystal lattice and that the xenon gas is sampling several of these dissolved pockets at higher temperatures. These smaller sites are most likely peripheral to the main channel structure observed in the solid–state structure of **508**. It is well–established that xenon prefers to occupy pores where it has close contacts with the host system.[21] This assignment is supported by the fact that the observed chemical shift range is comparable to the chemical shift value of xenon dissolved in an organic solvent such as benzene or toluene.[xxiii]

As the temperature is lowered, the xenon gas begins to occupy space within the true pore or channel structure of our assembly, as evidenced by the growth of the upfield resonance. There are two possible explanations for this observation: First, at lower temperatures, reduced mobility of both the host solid as well as the guest xenon atoms may result in filling of (or condensation within) the dissolved sites, effectively denying access to any new gas molecules.[24] Condensed xenon gas molecules are not spectroscopically detectable due to the loss of polarization that results after performing a single NMR experiment. In the presence of condensed xenon, all of the new xenon gas molecules that are being continuously flowed through the host solid would be required to occupy space within the channels or pores for a longer period of time, as detectable on the NMR timescale. A second explanation is that with lower temperatures there is simply not enough mobility within the solid host to allow the xenon gas to enter the dissolved sites at all. For example, any restriction of slight motion of the pendant phenyl groups at the alkylidene may result in restricted access to the dissolved sites. With a reduction in temperature, the xenon in the gas phase can no longer enter the dissolved site and begins to sample the pore environment for a larger fraction of the experimental time. The amount of time that the xenon gas spends in the pore system increases with lower temperatures, resulting in a downfield shift of the resonance, which stabilizes at approximately –70 °C. The relatively downfield chemical shift value of this resonance suggests that the pore that the xenon is occupying is quite small.

Pines and coworkers[25] have studied the porous solid tris(*o*–phenylenedioxy)cyclophosphazene (TPP) using continuous flow laser–polarized ^{129}Xe NMR spectroscopy. Crystalline TPP provides a channel structure with pore walls that are composed primarily of benzene rings, allowing us to compare their results to our system, solid **508**. They assigned a ^{129}Xe resonance observed at δ 110 to xenon occupying space within a channel of a diameter of 5 Å. Based on this, we can suggest that the observed chemical shift value for solid **508** (112 ppm) indicates that the xenon gas is occupying space in the smaller of the two channels (parallel to the *a*–axis) present within the solid. This compares well with the results of X–ray crystallographic analysis, which suggested that the minimum free space diameter of this channel was 4.9 Å. Furthermore, a slight broadening to the low field side of the gas peak at extremely low temperatures (–112 °C) may be the result of the gas beginning to occupy space in the larger channel that follows the *c*–axis in the solid–state. While lower temperatures can not be achieved with the current system, and due to the fact that we are approaching the boiling point of xenon, we nevertheless expect that a second higher field resonance would appear at lower temperatures.

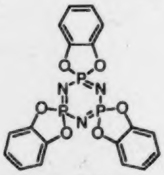

TPP

As a final test, solution state ^{1}H NMR was used to confirm that all of the solvent had been removed from the host solid **508** subsequent to the variable temperature NMR experiments. We have established that while the solid may be undergoing some structural changes upon removal of the guest, clearly these changes are not as dramatic as we had imagined. While we cannot, at this time, make any absolute assignments with respect to pore size, we have acquired the variable temperature ^{129}Xe NMR spectra of several other porous solids, which has allowed us to establish the relative pore size. These results have clearly shown that assembly **508** retains its porosity in the absence of guest solvent molecules.

The variable temperature hyperpolarized ^{129}Xe NMR spectra of porous macrocycle **216c** are shown in Figure 5.10. The crystal packing diagram of **216c**, as described in Chapter 2, clearly shows that the macrocycles are stacked atop one another such that pores with free space dimensions of approximately 5.0 × 5.5 × 6.1 Å are realized in the solid–state. Compound **216c**, as with **508**, crystallized such that there were solvent molecules present within the channel. As with the previous example, it is immediately apparent that there are two sites present within the solid **216c**, as evidenced by the two resonances observed in the variable temperature ^{129}Xe NMR spectra. At higher temperatures, a broad downfield resonance is observed at 200–180 ppm. Upon cooling to –49 °C, a second, upfield resonance appears at ~130 ppm and grows in intensity as the downfield resonance diminishes. This resonance is shifted to slightly lower field as the sample is cooled, and stabilizes at a chemical shift value of 141 ppm at –112 °C. The broad downfield resonance, as explained above, is suggestive of xenon dissolved in several small binding pockets within the crystal lattice. The broad nature of the resonance further indicates that the xenon gas is in rapid exchange between these different sites. As the temperature is lowered, xenon begins to occupy space within the cavity circumscribed by the macrocyclic enyne core.

Although there are very few examples of porous organic solids that have been studied using ^{129}Xe NMR, Ripmeester and coworkers have studied Dianin's compound (4–*p*–hydroxyphenyl–2,2,4–trimethylchroman) using ^{129}Xe CP/MAS NMR.[26] The crystal packing diagram of Dianin's compound reveals a purely organic pore system that is composed of an hourglass–type structure in each unit cell. The large cavities have a diameter of 6.3 Å and are separated by a "neck" with a diameter of 4.1 Å, which is comparable to that observed in the solid–state structure of **216c**.

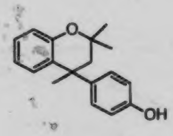

Dianin's compound

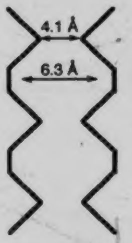

"Hourglass" channel

It was found that the ^{129}Xe chemical shift was dependent on the number of neighbouring pores that were filled with xenon. The observed xenon chemical shift was 134 ppm when there was one xenon atom per unit cell, and 152 ppm when there were two xenon atoms per unit cell. The similarity of the observed chemical shift values as well as the comparable pore structures allow us to tentatively assign the resonance observed at 141 ppm in the ^{129}Xe spectrum of **216c** to xenon occupying space within an hourglass–shaped channel that is slightly less than 6 Å in diameter. This correlates very well to the pore size that was observed in the solid–state structure of **216c**.

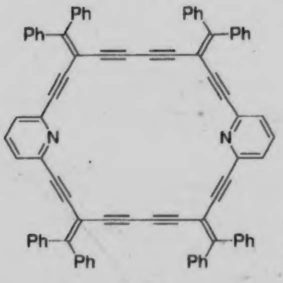

216c

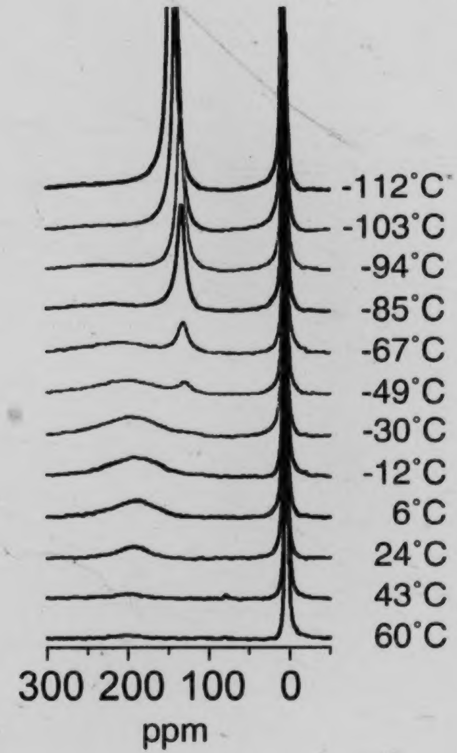

Figure 5.10 Variable temperature hyperpolarized ^{129}Xe NMR spectra of porous macrocycle **216c** at 55 MHz.

As described in the introduction to this chapter, one of the greatest challenges that researchers in this field face is an absolute reliance on X–ray crystallography as a means of determining whether a solid is porous or not. In addition to our goal of gaining insight into the solid–state structure of our porous solids in the absence of solvent molecules, we also intended to determine whether this technique could provide real insight into those systems for which X–ray crystallographic analysis was not possible. As described in earlier chapters, macrocycles **206c** and **305c** showed extremely limited solubility in organic solvents, and, as such, single crystals of these species suitable for X–ray crystallographic analysis could not be achieved. Shown in

Figure 5.11 are the variable temperature ^{129}Xe NMR spectra of compounds **206c**, **216c**, and **305c**. Gratifyingly, it is immediately apparent that all three macrocyclic samples show similar trends in their solid–state spectra. Given the structural similarity between the three cyclic species, it is not unreasonable to propose that they would share solid–state structural features. All three solids show a broad, low field resonance at higher temperatures, which diminishes in intensity as the temperature is lowered. An intense high field resonance also appears in the NMR spectra of all three solids at low temperatures. The high field resonance observed in the NMR spectra of compounds **216c** and **206c** begins to appear at –49 °C. This high field resonance observed in the spectrum of **206c** appears at 108 ppm and upon cooling to –112 °C is shifted to lower field at 141 ppm, which is identical to the chemical shift observed in the spectrum of **216c**. The relatively low chemical shift value observed for this resonance at elevated temperatures (–49 to –94 °C) implies that the rate of exchange between xenon in the channel and xenon in the bulk gas is faster than that of **216c**, leading to a higher field average in the observed resonance.

By contrast, the high field peak observed in the spectra of **305c** is discernable at 6 °C at a chemical shift value of 95 ppm. Upon cooling to –85 °C, the chemical shift of this resonance stabilizes and is consistently observed at 137 ppm. While there are slight differences in the temperatures at which these events are observed, and small differences in observed chemical shift value, it is clear that the pore structure for all three solids is similar in nature. It is worth noting that the temperature differences noted for the gain in intensity of the high field peak correspond to a loss in intensity of the low field resonance. This clearly supports the argument that there is an exchange process at work and that the xenon atoms only spend an observable amount of time in the pore or channel system when the dissolved pocket sites are inaccessible.

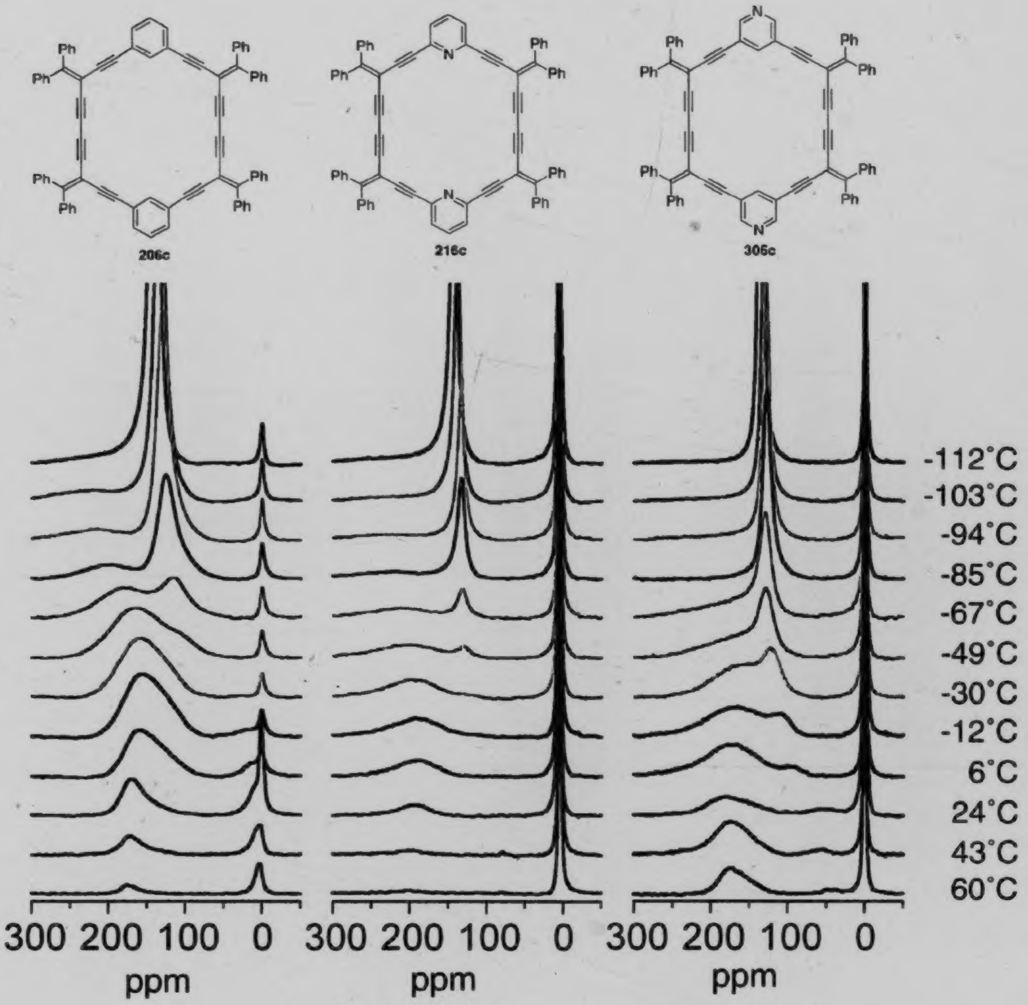

Figure 5.11 Variable temperature hyperpolarized ^{129}Xe NMR spectra of porous macrocycles **206c**, **216c**, and **305c** at 55 MHz.

To gain insight into the dynamics of the guest xenon molecules within the porous solids at both low and high temperatures, 2D exchange spectroscopy experiments were performed on macrocycle **305c**. The two sets of spectra acquired at 20 °C (left) and –58 °C (right) are shown in Figure 5.12. These experiments clearly support our earlier assumptions.

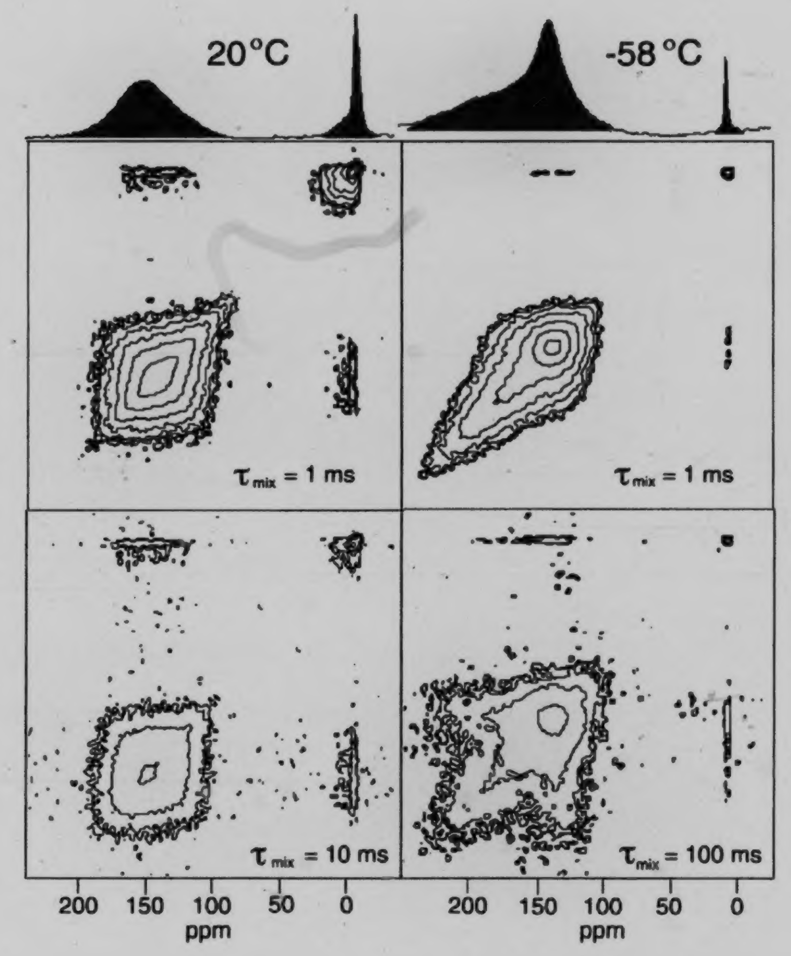

Figure 5.12 Hyperpolarized ^{129}Xe EXSY spectra (55 MHz) of porous solid **305c** at 20 °C (left) and –58 °C (right), with mixing times as indicated.

At room temperature, two exchange processes are clearly observed at mixing times of both 1 and 10 ms. First, the bulk xenon gas is clearly exchanging with the xenon atoms present within the dissolved sites observed downfield at ~180–200 ppm (shown in red) as evidenced by the cross peaks present off the diagonal showing a correlation between the downfield resonances and the zero peak (shown in green). More significant is the second exchange process that is observed. Our assignment of the downfield resonance as being the result of xenon gas "sampling" several dissolved sites that are similar in size and functionality is supported by the diamondoid peak that extends past the diagonal at 180–200 ppm. The shape of this peak clearly indicates that the xenon gas in the dissolved sites is exchanging and sampling several different sites on the time–scale of the NMR experiment. If there were no exchange process occurring, this peak would be a simple ellipse concurrent with the diagonal.

As the temperature is lowered to –58 °C, we begin to observe the growth of the high field resonance (shown in blue) that we have assigned to the channel structure existing within the macrocyclic core. With the appearance of this additional resonance, we also see evidence of a third exchange process. While this cross peak is barely discernable at a mixing time of 1 ms, at 100 ms there is clearly a correlation between the upfield channel resonance and the dissolved sites. This observation indicates that the xenon gas must enter the channel system in order to access the smaller, dissolved sites. This is further supported by the observation that at lower temperatures there is no longer a cross peak and, therefore, any exchange occurring directly between the bulk xenon gas and the dissolved sites. Instead we see exchange between the bulk xenon gas and the xenon occupying space within the pore or channel structure, as evidenced by the cross peak observed at ~135 ppm. Furthermore, the cross peak observed at 180–200 ppm is no longer diamondoid in shape, implying that the "dissolved" xenon gas must enter the channel system in order to exchange with another dissolved site.

Figure 5.13 shows a schematic representation of what we believe to be the pathway followed by the xenon gas. First, at higher temperatures, the xenon gas enters the pore system and travels rapidly (such that it is not observed on the NMR time–scale) through the pore where it can access numerous, chemically similar "dissolved" binding pockets. As the temperature lowers, these dissolved sites become less accessible as a result of restricted mobility of the solid. This causes the xenon gas to spend a greater amount of time within the actual channel structure. The significance of this experiment is that we have established that there is mobility within the channel structure. This means that the xenon gas is not simply "dissolving" into the solid matrix, but is actually traversing the pore structure that was chemically established through the construction and aggregation of our conjugated macrocycles.

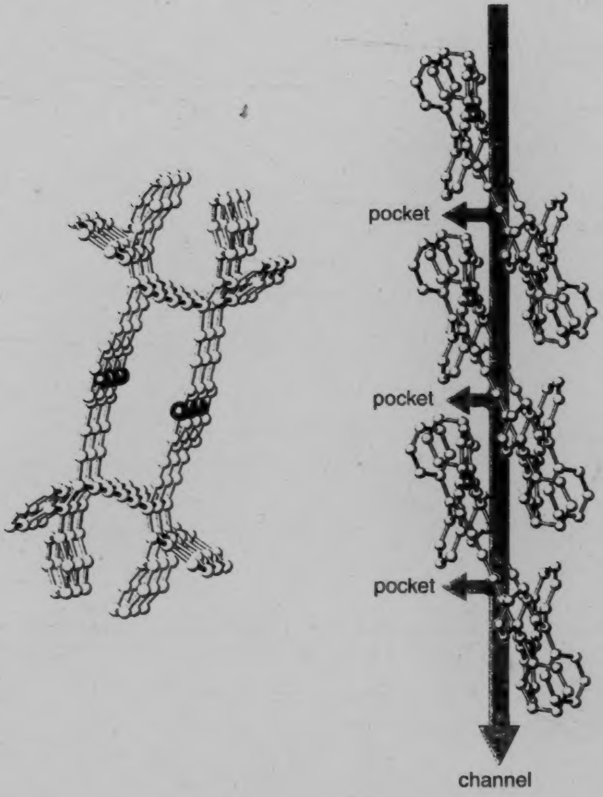

Figure 5.13 (Left) Schematic representation of a 1 × 1 × 1 array of unit cells of **216c** viewed down the *a*–axis. (Right) Schematic diagram showing pathway of xenon gas within the pore structure of the organic macrocycle **216c**. View shown follows the *c*–axis of a 1 × 1 × 1 array of unit cells of **216c**.

In addition to studying several purely organic porous solids using this technique, we also targeted the analysis of several metal–organic hybrids for comparison. Shown in Figure 5.14 are the variable temperature ^{129}Xe NMR spectra for platinacycle **402**. At higher temperatures, this solid provides the same low field resonance that we have seen in previous examples. This broad downfield resonance is observed at 200–175 ppm and is assigned to xenon gas occupying space within small, dissolved sites peripheral to the channel structure of the solid. Upon cooling, however, we begin to see some dramatic differences between this example and the largely organic samples that were previously described. At lower temperatures, *two* high field resonances are observed. First, a high field resonance begins to separate from the gas peak at –85 °C. This peak shifts to lower field upon cooling and is observed at ca. 71 ppm at –112 °C. This is concurrent with the growth of a second high field resonance at 125 ppm which appears at –94 °C and grows in intensity as the temperature is lowered. There are two possible explanations for this observation. First, it is possible that there are two chemically inequivalent channel structures present within the solid. A second possibility is that there are two chemically inequivalent sites within a single pore or channel and the xenon gas can occupy space in both of these sites under the experimental conditions.

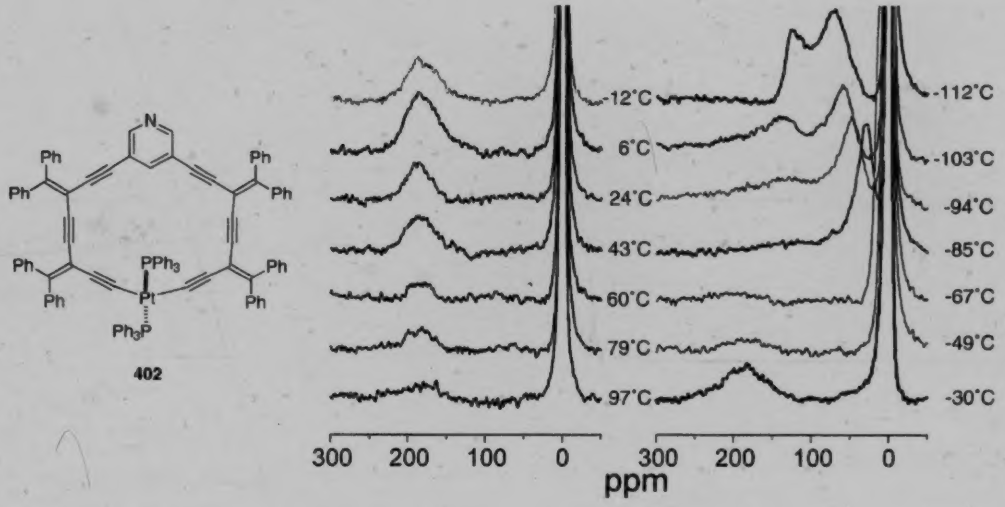

Figure 5.14 Variable temperature hyperpolarized ^{129}Xe NMR spectra of platinacycle **402** at 55 MHz.

Based on analysis of the solid–state structure of **402**, we believe the latter possibility to be the case. The solid–state packing of **402**, part of which is shown in Figure 5.15, reveals that there is only one channel present within the solid that is large enough to accommodate the xenon gas. In fact, it was this interstitial space where the co–crystallized CH_2Cl_2 and acetone molecules were shown to occupy space via crystallographic analysis. Unlike the previous examples, the xenon gas is not occupying space within the macrocyclic core of **402**. Access to the cavity at the centre of the macrocyclic enyne core is blocked entirely by the pendant triphenylphosphine ligands. Instead, the xenon gas is traversing a pathway on the periphery of the macrocyclic species, in between columns of the stacked macrocyclic ligands. It is easy to see that there are two chemically inequivalent sites present within this channel, as highlighted by the circles and ellipses shown in Figure 5.15. This observation forces us to rethink our definition of what makes a solid "porous". In many cases we look at crystal packing diagrams hoping to see space or a transparent path through the solid lattice. However, if much of the potential of porous organic solids relies on their ability to *interact* with potential guest molecules, including gases, perhaps we should be targeting solids with channel structures analogous to a small footpath through the woods rather than a superhighway. In addition, providing a clear path for associated solvent molecules to evaporate rapidly (and therefore energetically) can potentially destabilize the porous structure.

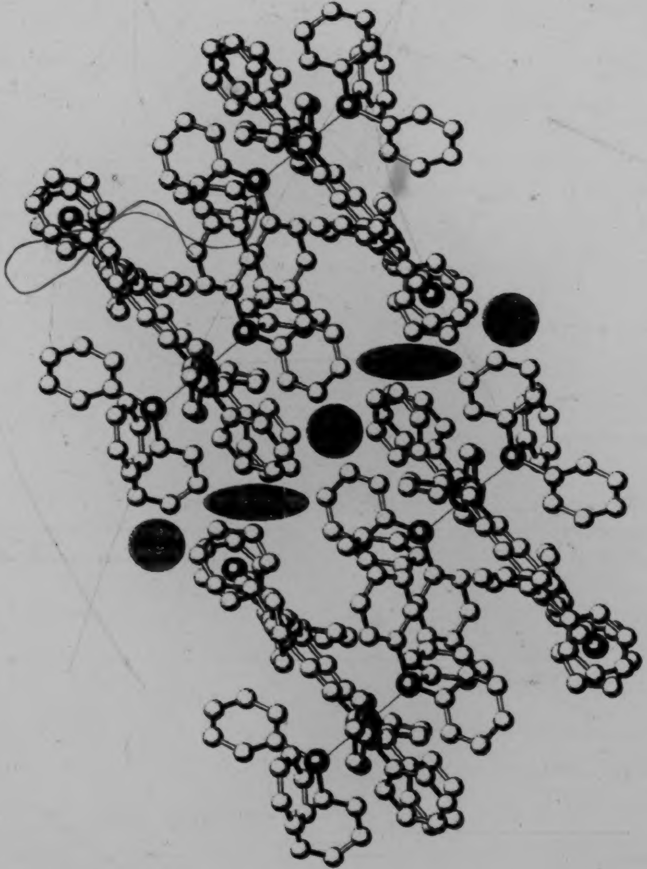

Figure 5.15 Schematic representation of the crystal packing diagram of **402**. Shown is a 1 × 2 × 1 array of unit cells of **402** viewed down a line between the *b*– and *c*–axes. The "zig–zag" channel traversed by the xenon gas is represented by circles and ellipses.

The variable temperature ^{129}Xe NMR spectra for platinacycles **403a** and **403b** were also acquired and are shown in Figure 5.16. These spectra again show marked differences relative to the purely organic species described above. The ^{129}Xe NMR spectra for **403a** show a very weak downfield resonance at ca. 210–190 ppm, which is only visible at relatively high temperatures (≥ 40 °C). This indicates that the xenon gas can only access the smaller sites within the crystal lattice under energetically favourable conditions. This is consistent with the crystal packing diagram for **403a** which shows a significant amount of void space (18%) when the solvent molecules are removed from the structure, but in the presence of co–crystallized solvent the void space was calculated to be zero. At lower temperatures, two upfield resonances emerge: First, a peak at δ 128 appears at –85 °C and grows in intensity as the temperature is lowered. The chemical shift of this resonance suggests that xenon is occupying space within a pore of the approximate dimensions of 5.5 Å. A second, broad, upfield resonance also begins to emerge from the gas peak at –67 °C. This resonance clearly indicates the presence of a larger pore that is still in rapid exchange with the gas peak, even at temperatures as low as –112 °C, where it appears at a chemical shift value of ca. 69 ppm.

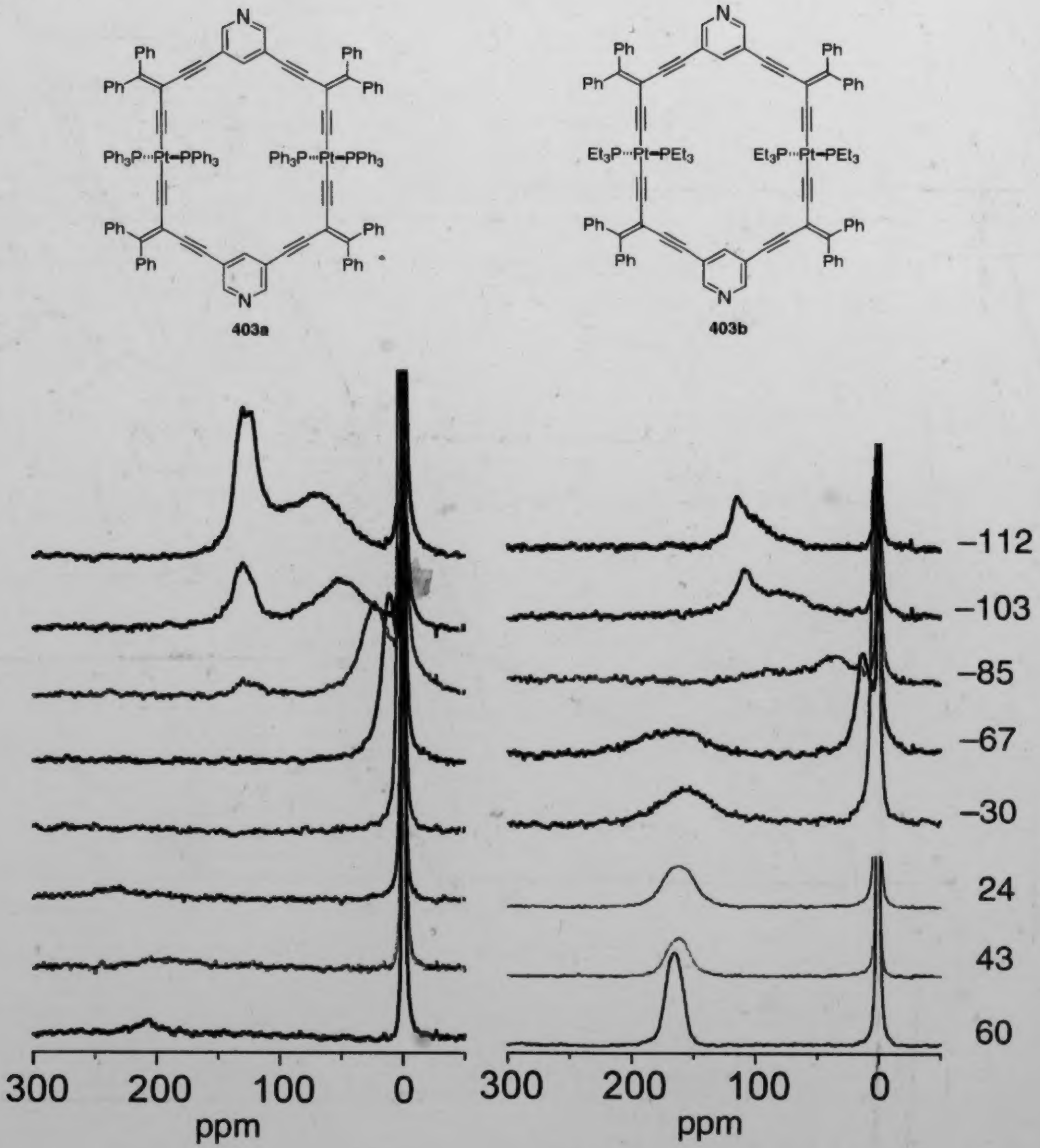

Figure 5.16 Variable temperature hyperpolarized ^{129}Xe NMR spectra (55 Mz) of platinacycles **403a** and **403b**.

It is far more difficult to visualize the channel structure in the case of **403a** when compared to the examples previously discussed, due to the complexity of the crystal packing diagram. Shown in Figure 5.17 is a portion of the crystal packing diagram of

403a and overlaid across this is a representation of the interstitial void space present within the crystal lattice, when the solvent molecules are removed.[xxvii] Clearly there are two chemically inequivalent void spaces present within the crystal lattice, consistent with our observations in the ^{129}Xe NMR spectra. Less obvious, however, is the route used by the xenon gas to access and move between these sites.

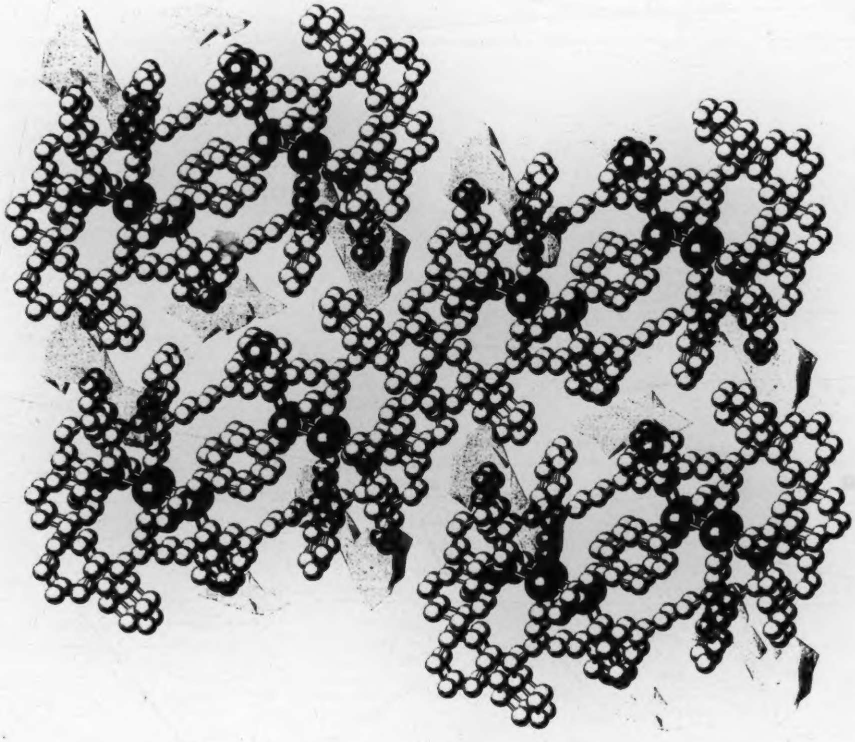

Figure 5.17 Schematic representation of the crystal packing diagram of **403a**. Shown is a 2 × 2 × 2 array of unit cells as viewed down the *a*–axis. A representation of the void space (when co–crystallized solvent is removed) present within the crystal lattice is shown in light blue.[27]

The variable temperature ^{129}Xe NMR spectra for platinacycle **403b** also show some noteworthy differences. First, at higher temperatures, rather than a broad resonance suggestive of an exchange process, such as that observed for every other compound included in this study, we instead observe a single, intense resonance at 167 ppm. The intensity of this narrow resonance suggests that, rather than sampling several similar small binding pockets, there is a single confined pore that is housing the xenon gas at elevated temperatures. It is tempting to speculate that this is due to the presence of the triethylphosphine ligands, and that the xenon is being held more tightly due to the flexible nature of the pendant alkyl groups. As the temperature is lowered, the growth of two upfield resonances is observed. First, at –67 °C, a resonance begins to separate from the gas peak, shifting to lower fields with a reduction in temperature until at –112 °C this resonance appears at δ 113. It would appear that this peak is also in exchange with a second resonance, which appears at –85 °C and shifts to 113 ppm when the temperature is lowered to –112 °C. Shown in Figure 5.18 is a schematic representation of the crystal packing diagram of **403b**, highlighting the solvent channel which is occupied by the xenon gas at low temperatures. We believe that the xenon gas is experiencing two chemically inequivalent environments within this single channel structure, as was the case for platinacycle **402**.

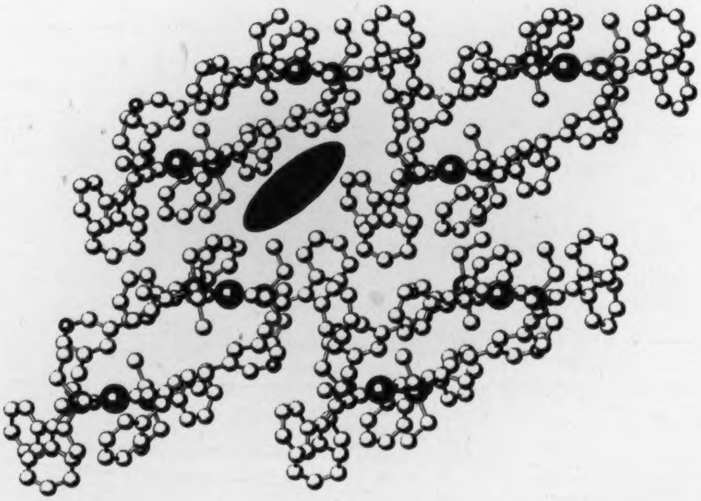

Figure 5.18 Schematic representation of location of channel (shown by ellipse) in the solid–state structure of **403b**. Shown is a 1 × 1 × 1 array of unit cells of **403b** as viewed down the *b*–axis.

Clearly, hyperpolarized ^{129}Xe NMR spectroscopy is a technique which can be successfully applied to the study of porous organic solids, even in the absence of X–ray crystallographic analysis. Trends observed in the ^{129}Xe chemical shift, as well as the dynamic behaviour of the guest xenon gas, have provided us with real insight into the porous nature of these systems. We have also established that, for the most part, X–ray crystallographic data acquired in the presence of guest solvent molecules can still provide a good model for the pore structures of these solids in the absence of co–crystallized solvent.

5.3 Conclusions and Future Work

In the discussion provided above, we have demonstrated the effectiveness of our strategy toward the formation of porous solids. Porous organic solid **508** was realized and fully characterized in solution, and our preliminary efforts to synthesize even larger assemblies were also described. X–ray crystallographic analysis confirms the presence of two large, perpendicular channels in the solid–state structure of **508** and also demonstrate the selective uptake of guest solvent molecules. We have established, through the use of hyperpolarized ^{129}Xe NMR spectroscopy, that this solid retains its porosity even in the absence of co–crystallized solvent molecules. We have also applied this technique to the study of several porous organic macrocycles and hybrid metal–organic species. These studies have shown that hyperpolarized ^{129}Xe NMR spectroscopy can be an effective technique for the study of porous organic solids, and can provide real insight into the porous nature of these species, even in the absence of X–ray crystallographic analysis.

5.4 References and Notes

1. (a) Stepanow, S.; Lingenfelder, M.; Dmitriev, A.; Spillmann, H.; Delvigne, E.; Lin, N.; Deng, X.; Cai, C.; Barth, J. V., Kern, K. *Nat. Mat.* **2004**, *3*, 229–233. (b) Ishii, Y.; Takenaka, Y.; Konishi, K. *Angew. Chem. Int. Ed.* **2004**, *43*, 2702–2705. (c) Baxter, P. N. W. *Chem. Eur. J.* **2003**, *9*, 2531–2541. (d) Lin, J.; Zhang, H.–C.; Pu, L. *Org. Lett.* **2002**, *4*, 3297–3300. (e) Barea, E.; Navarro, J. A. R., Salas, J. M.;

Quirós, M.; Willermann, M.; Lippert, B. *Chem. Eur. J.* **2003**, *9*, 4414–4421. (f) Cui, Y.; Ngo, H. L.; Lin, W. *Inorg. Chem.* **2002**, *41*, 5940–5942.

2. (a) Dybtsev, D. N.; Chun, H.; Yoon, S. H.; Kim, D.; Kim, K. *J. Am. Chem. Soc.* **2004**, *126*, 32–33. (b) Sharma, A. C.; Borovik, A. S. *J. Am. Chem. Soc.* **2000**, *122*, 8946–8955. (c) Eddaoudi, M.; Kim, J.; Rosi, N.; Vodak, D.; Wachter, J.; O'Keefe, M.; Yaghi, O. M. *Science* **2002**, *295*, 469–472. (e) Rudkevich, D. M. *Angew. Chem. Int. Ed.* **2004**, *43*, 558–571.
3. (a) Lee, K. H.; Lee, D. H.; Hwang, S.; Lee, O. S.; Chung, D. S.; Hong, J.–I. *Org. Lett.* **2003**, *5*, 1431–1433. (b) Trembleau, L.; Rebek Jr., J. *Science* **2003**, *301*, 1219–1220. (c) Enander, K.; Dolphin, G. T.; Baltzer, L. *J. Am. Chem. Soc.* **2004**, *126*, 4464–4465. (d) Zhong, Z.; Anslyn, E. V. *Angew. Chem. Int. Ed.* **2003**, *42*, 3005–3008.
4. (a) Hu, A.; Ngo, H. L.; Lin, W. *J. Am. Chem. Soc.* **2003**, *125*, 11490–11491. (b) Hu, A.; Ngo, H. L.; Lin, W. *Angew. Chem. Int. Ed.* **2003**, *42*, 6000–6003. (c) Walsh, D.; Arcelli, L.; Ikoma, T.; Tanaka, J.; Mann, S. *Nat. Mat.* **2003**, *2*, 386–390. (d) Brunet, P.; Demers, E.; Maris, T.; Enright, G. D.; Wuest, J. D. *Angew. Chem. Int. Ed.* **2003**, *42*, 5303–5306.
5. For a comprehensive review of shape–persistent macrocycles, please see Chapter 1, and references therein.
6. Höger, S.; Morrison, D. L.; Enkelmann, V. *J. Am. Chem. Soc.* **2002**, *124*, 6734–6736.
7. (a) Henze, O.; Lentz, D.; Schlüter, A. D. *Chem. Eur. J.* **2000**, *6*, 2362–2367. (b) Grave, C.; Lentz, D.; Schäfer, A.; Samorì, P.; Rabe, J. P.; Franke, P.; Schlüter, A. D. *J. Am. Chem. Soc.* **2003**, *125*, 6907–6918.

8. Leininger, S.; Olenyuk, B.; Stang, P. J. *Chem. Rev.* **2000**, *100*, 853–908. For examples of other supramolecular architectures featuring pyridine–based ligands, please see Chapters 3 and 4, and references therein.

9. (a) Yaghi, O. M.; O'Keefe, M.; Ockwig, N. W.; Chae, H. K.; Eddaoudi, M.; Kim, J. *Nature* **2003**, *423*, 705–714. (b) Chae, H. K.; Siberio–Pérez, D. Y.; Kim, J.; Go, Y.; Eddaoudi, M.; Matzger, A. J.; O'Keefe, M.; Yaghi, O. M. *Nature* **2004**, *427*, 523–527. (c) James, S. L. *Chem. Soc. Rev.* **2003**, *32*, 276–288. (d) Eddaoudi, M.; Moler, D. B.; Li, H.; Chen, B.; Reineke, T. M.; O'Keefe, M.; Yaghi, O. M. *Acc. Chem. Res.* **2001**, *34*, 319–330.

10. Fournier, J.–H.; Maris, T.; Wuest, J. D.; Guo, W.; Galoppini, E. *J. Am. Chem. Soc.* **2003**, *125*, 1002–1006.

11. Campbell, K.; Kuehl, C. J.; Ferguson, M. J.; Stang, P. J.; Tykwinski, R. R. *J. Am. Chem. Soc.* **2002**, *124*, 7266–7267.

12. For an overview of nitrogen adsorption techniques please see: *Adsorption by Powders and Porous Solids*; Rouquerol, F.; Rouquerol, J; Sing, K., Eds.; Academic Press: London, 1999.

13. Ratcliffe, C. I. in: *Annual Reports on NMR Spectroscopy, Volume 36*. Webb, G. A., Ed.; Academic Press: London, 1998, 123–221.

14. (a) Urban, C.; McCord, E. F.; Webster, O. W.; Abrams, L.; Long, H. W.; Gaede, H.; Tang, P.; Pines, A. *Chem. Mater.* **1995**, *7*, 1325–1332. (b) Moudrakovski, I. L.; Wang, L.–Q.; Baumann, T.; Satcher, Jr., J. H.; Exarhos, G. J.; Ratcliffe, C. I.; Ripmeester, J. A. *J. Am. Chem. Soc.* **2004**, *126*, 5052–5053. (c) Dubes, A.;

Moudrakovski, I. L.; Shahgaldian, P.; Coleman, A. W.; Ratcliffe, C. I.; Ripmeester, J. A. *J. Am. Chem. Soc.* **2004**, *126*, 6236–6237.

15. Stang, P. J.; Cao, D. H.; Saito, S.; Arif, A. M. *J. Am. Chem. Soc.* **1995**, *117*, 6273–6283.

16. This species has been isolated and characterized crystallographically: Campbell, K.; Ferguson, M. J.; Tykwinski, R. R. Unpublished results.

17. Manna, J.; Kuehl, C. J.; Whiteford, J. A.; Stang, P. J.; Muddiman, D. C.; Hofstadler, S. A.; Smith, R. D. *J. Am. Chem. Soc.* **1997**, *119*, 11611–11619.

18. Please see discussion of the solid–state structures of oligomers **302c** and **303c** provided in Chapter 3.

19. Whiteford, J. A.; Lu, C. V.; Stang, P. J. *J. Am. Chem. Soc.* **1997**, *119*, 2524–2533.

20. For an example of another distorted macrocycle see: Nielsen, M. B.; Schrieber, M.; Baek, Y. G.; Seiler, P.; Lecomte, S.; Boudon, C.; Tykwinski, R. R.; Gisselbrecht, J.–P.; Gramlich, V.; Skinner, P. J.; Bosshard, C.; Günter, P.; Gross, M.; Diederich, F. *Chem. Eur. J.* **2001**, *7*, 3263–3280.

21. Moudrakovski, I. L.; Nossov, A.; Lang, S.; Breeze, S. R.; Ratcliffe, C. I.; Simard, B.; Santyr, G.; Ripmeester, J. A. *Chem. Mater.* **2000**, *12*, 1181–1183

22. (a) Ito, T.; Fraissard, J. *J. Chem. Phys.* **1982**, *76*, 5225–5229. (b) Koskela, T.; Jokisaari, J.; Satyanarayana, C. *Micropor. Mater.* **2004**, *67*, 113–122. (c) Demarquay, J.; Fraissard, J. *Chem. Phys. Lett.* **1987**, *136*, 314–318. (d) Terskikh, V. V.; Moudrakovski, I. L.; Breeze, S. R.; Lang, S.; Ratcliffe, C. I.; Ripmeester, J. A.; Sayari, A. *Langmuir* **2002**, *18*, 5653–5656.

23. Stengle, T. R.; Reo, N. V.; Williamson, K. L. *J. Phys. Chem.* **1981**, *85*, 3772–3775.

24. For a previous example of xenon condensation at reduced temperatures, please see reference 21.

25. (a) Sozzani, P.; Comotti, A.; Simonutti, R.; Meersmann, T.; Logan, J. W.; Pines, A. *Angew. Chem. Int. Ed.* **2000**, *39*, 2695–2698. (b) Meersmann, T.; Logan, J. W.; Simonutti, R.; Caldarelli, S.; Comotti, A.; Sozzani, P.; Kaiser, L. G.; Pines, A. *J. Phys. Chem. A* **2000**, *104*, 11665–11670.

26. Lee, F.; Gabe, E.; Tse, J. S.; Ripmeester, J. A. *J. Am. Chem. Soc.* **1988**, *110*, 6014–6019.

27. Representation of pores was generated by the Cavities option in the ATOMS program (ATOMS, Version 5.1). The surface of the pores is defined by the possible loci of a sphere of 3 Å in diameter as it rolls over the surface of the porous solid. For an example of another channel representation generated using ATOMS see Reference 10.

Chapter 6 Application of Ligand Exchange Reactions to Platinum–Containing Macrocycles

6.1 Introduction

As described in Chapter 4, the synthesis of platinum–containing macrocycles was targeted to provide supramolecular building blocks featuring expanded pore sizes and enhanced solubility. In addition to these considerations, it was also predicted that the incorporation of a platinum acetylide linkage could provide the means to further control the assembly of these building blocks in the solid–state. While the coordinative potential of the pyridines could still be exploited in one dimension, cross–linking at the platinum centre via ligand exchange[1] (Figure 6.1) could provide access to more robust and highly ordered porous solids (**601**).

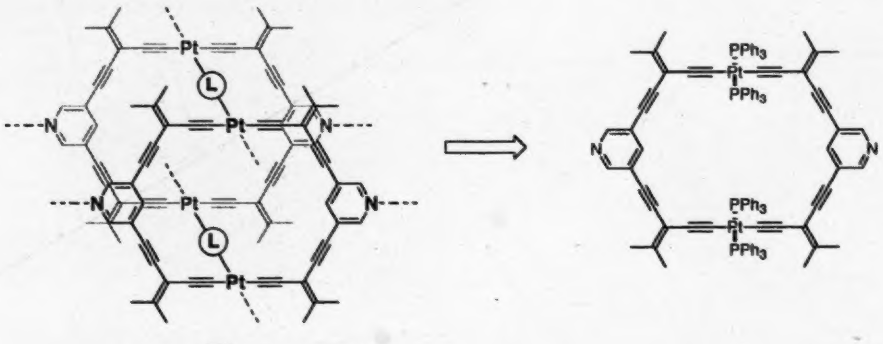

Figure 6.1 Schematic illustration showing cross–linking of platinum acetylide macrocycles.

Our early attempts to perform this cross–linking experiment involved the use of diphosphine ligands as bridges and the results of these experiments will be described in this Chapter. Disappointingly, we found that in all cases, treatment of a *trans*–platinum acetylide complex **602** with a diphosphine ligand did not lead to the desired bridging species **604** (Figure 6.2). However, in some cases, we observed that chelation of the diphosphine ligand had occurred (**603**), resulting in a change in coordination geometry about the metal centre. While we were initially disappointed with this result, we also recognized that as a consequence of changing the geometry about the metal centre, the shape of the pendant supramolecular building block(s) could also be manipulated.

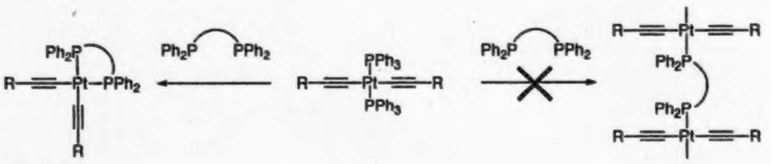

603

602

604

Figure 6.2 Formation of *cis*–chelated platinum acetylide complexes.

This observation led us to the realization that this methodology could be applied to the generation of new supramolecular building blocks possessing different coordination motifs. These new building blocks could be accessed, in a single step, from readily available precursors that had already been synthesized within our group. In addition to this, we also recognized that *cis*–platinum acetylide complexes are attractive synthetic targets in their own right. Bäuerle and coworkers have recently established that reductive elimination by *cis*–platinum acetylide complexes can be an effective strategy applied to the generation of strained butadiynes.[2] Their strategy is particularly effective for macrocyclic systems that resist oxidative homocoupling conditions to generate butadiynes as the ring–closing step. Transmetallation of the acetylenes to a *cis*–platinum complex followed by forcing reductive elimination at the metal centre can lead to a butadiyne macrocyclic product that is unavailable using conventional coupling conditions (Figure 6.3). The formation of butadiynes, however, can be limited by the often low–yielding reactions to generate the thermodynamically disfavored *cis*–platinum acetylide complexes.[3] The conversion of a more readily accessible *trans*–platinum acetylide complex to its *cis*–counterpart in a single, high–yielding step would be a useful addition to this synthetic methodology.

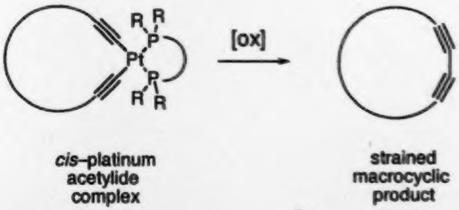
R R
P
Pt
P
R R
[ox]
cis–platinum acetylide complex
strained macrocyclic product

Figure 6.3 Schematic representation of the formation of strained macrocyclic butadiynes from *cis*–platinum acetylide complexes.

In addition to the facile preparation of *cis*–platinum acetylide complexes from their *trans*–counterparts, we also envisioned the preparation of *chiral* acetylide complexes by simply using a chiral, chelating diphosphine ligand. As described in earlier chapters, metal–directed self–assembly reactions[4] have become a powerful method used for the construction of supramolecular architectures including molecular squares,[5] cages,[6] and numerous polymeric and dendrimeric species.[7] In the last decade, scientists have become particularly intrigued with the effect of incorporating chiral ligands/groups into supramolecular and metallosupramolecular systems.[8] These materials have demonstrated potential in numerous enantioselective processes including asymmetric catalysis[9], chemical sensing[10], and selective guest inclusion[11].

In many cases,[8–10] the synthesis of metal–containing chiral supramolecules involves the elaboration[12] of an enantiopure building block, such as the numerous, readily–available chiral binaphthyl–based ligands, to incorporate functionality such as pyridine moieties or acetylene units capable of binding to a metal or metal ion. These building blocks are then assembled, by exploiting their ability to coordinate to metals, to provide metal–containing architectures with predictable sizes, shapes, and functional properties.

Our efforts in this area have focused on the development of a method that allows us to introduce a source of chirality *after* the construction of the desired supramolecular assembly. This approach allows us to minimize the use of expensive enantiopure ligands and also facilitates the divergent preparation of both enantiomers of a given assembly product from a single, common precursor. Using ligand exchange methodology, it is possible to convert *trans*–platinum acetylide complexes to their *cis*–counterparts in good to excellent yields by simply treating the *trans*–acetylide with a chelating diphosphine ligand.[1b] By extension, treatment of a readily accessible *trans*–acetylide complex with a chiral chelating ligand such as (*S*,*S*)-Chiraphos (Figure 6.4) provides ready access to chiral architectures and supramolecular building blocks in a single step. The results of these strategies will be described in the following discussion.

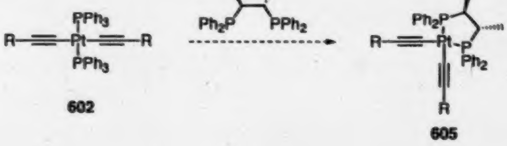

Figure 6.4 Construction of *cis*–chiral platinum acetylide complexes.

6.2 Results and Discussion

6.2.1 Synthesis and Characterization of Trans– and Cis–Platinum Acetylide Complexes

As described in the introduction to this chapter, we envisioned that the incorporation of a platinum acetylide linkage into the backbone(s) of a macrocyclic enyne core would provide an additional means to direct the assembly of these macrocyclic species in the solid state. This could occur by cross–linking two (or multiple) platinum acetylide centres through a bridging ligand such as a diphosphine (Scheme 6.1).

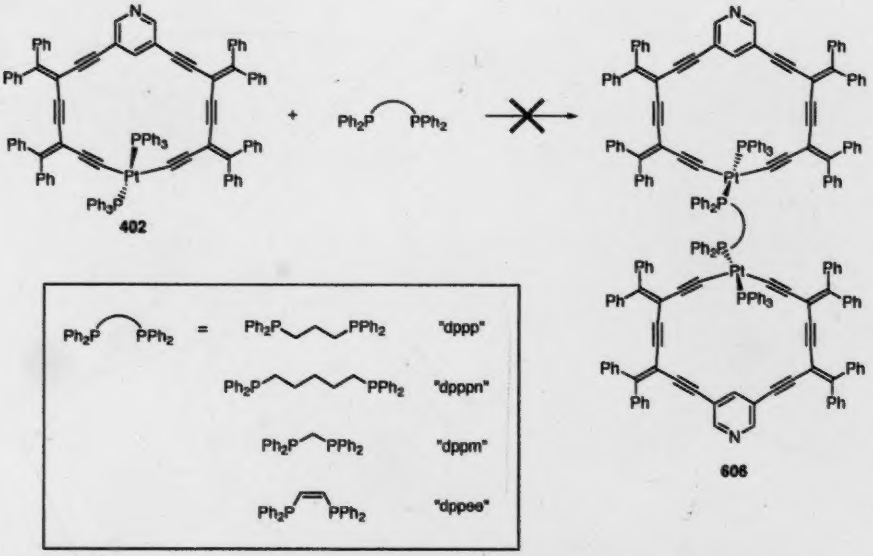

Scheme 6.1 Treatment of macrocycle **402** with diphosphine ligands.

To explore this concept, our efforts centred on the more readily accessible macrocycle **402**. Treatment of **402** with bis(diphenylphosphino)propane (dppp) in CD_2Cl_2 for 48 hours at room temperature led not to the formation of the desired bridging system **606**, but rather to the formation of a six–membered ring chelate **607** as revealed by ESI mass spectral analysis (*m/z* 1649, $[M + H]^+$, 100%). A small peak at higher mass (m/z 3191, 5%) was also observed in the mass spectrum corresponding to [2(**402**) – 4(PPh_3) + 2(dppp) + Ag]$^+$. While it is possible to interpret this signal as resulting from the desired bis(bridging) species, we have observed (vide infra) that many of our platinum acetylide complexes form high mass clusters under electrospray conditions. Thus, the product of this reaction is most likely the chelated species **607**.

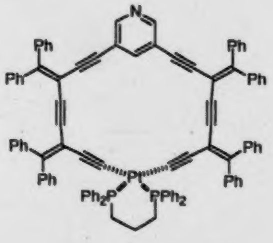

607

An increased chain length was expected to disfavor the formation of a chelate ring, and macrocycle **402** was thus treated with bis(diphenylphosphino)pentane (dpppn) using identical reaction conditions. While slow consumption of the ligand **402** was observed by ^{1}H NMR spectroscopy, ESI mass spectral analysis showed no evidence of either a chelate or a bridging species. We then turned our attention to a diphosphine ligand featuring a shorter chain length, reasoning that the formation of a ring chelate might also be discouraged in this fashion. Treatment of macrocycle **402** with bis(diphenylphosphino)methane (dppm), however, resulted only in an unidentified mixture of products. All signals observed in the ESI mass spectrum were of lower mass than the targeted bridging species **606** and they all inexplicably corresponded to fragments containing three phosphorous atoms. As such, no product was isolated from this reaction.

By this point, it was not at all unexpected that treatment of macrocycle **402** with *cis*–1,2–bis(diphenylphosphino)ethylene (dppee) also resulted in the formation of the chelate complex **608**. However, we also recognized the potential significance of this mode of reactivity. In addition to the possibility of accessing a new family of supramolecular building blocks, we also realized that a high–yielding method for the synthesis of *cis*–platinum acetylide complexes would be useful, as these complexes could be important synthetic intermediates.

With this in mind, we targeted the synthesis of *cis*–platinum acetylide complexes and the optimization of this methodology. Thus, it was determined that treatment of macrocycle **402** with one equivalent of dppee in CH_2Cl_2, followed by stirring at room temperature for 14 hours led to nearly complete conversion to **608**, and the strained *cis*–macrocycle was isolated in 87% yield following chromatographic purification (alumina). This stable, bright yellow solid was fully characterized including single crystal X–ray crystallographic analysis (vide infra).

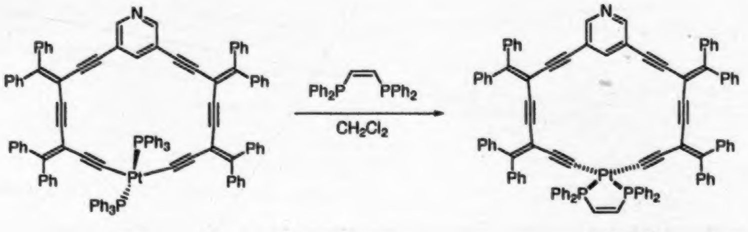

402

608 87%

Scheme 6.2 Synthesis of *cis*–macrocycle **608**.

To explore the scope of this reaction, a series of acyclic *trans*–platinum acetylide complexes were prepared as described in Scheme 6.3.[3,13] The appropriate terminal acetylene **609a–c** was added to a degassed solution of $(PPh_3)_2PtCl_2$ in Et_2NH. A catalytic amount of CuI was then added and the mixture was stirred at 50 °C for a period of 14 hours. After workup, the *trans*–$(PPh_3)_2Pt(C{\equiv}CR)_2$ complexes, **602a–c**, were all isolated as stable, colourless solids in good yield (see Table 6.1 for details).

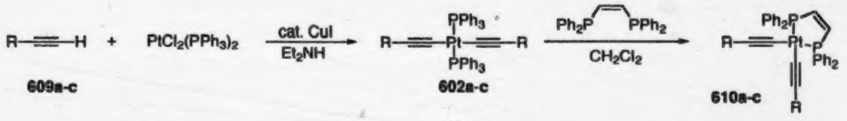

Scheme 6.3 Synthesis of *trans*– and *cis*–bis(alkynyl)platinum complexes.

The *trans*–bis(alkynyl) complexes were then easily converted to the *cis*–derivatives **610a–c** by treating a CH_2Cl_2 (or CD_2Cl_2) solution of the respective *trans*–complex (**602a–c**) with one equivalent of *cis*–1,2–bis(diphenylphosphino)ethylene (dppee) (Table 6.1). In all cases, the displacement of the triphenylphosphine appeared to be greater than 90% complete in less than two hours, but the mixtures were left overnight to ensure complete reaction. Solvent removal and purification by column chromatography (alumina) gave the *cis*–bis(alkynyl) complexes **608**, **610a–c** as stable solids in good to excellent yields. It is interesting to note that the *cis*–bis(alkynyl) complexes were consistently more soluble than their *trans*–analogues, significantly aiding their isolation and characterization.

Table 6.1 Synthetic details for the formation of *trans*– and *cis*–platinum acetylide complexes **402**, **608**, **602a–c**, and **610a–c**.

Compound		Yield (%)	Yield (%)	δ ^{31}P NMR ($^1J_{P-Pt}$, Hz)	δ ^{31}P NMR ($^1J_{P-Pt}$, Hz)
		402	**608**	**402**	**608**
Platinacycle **608**		70	87	20.0 (2610)	51.7 (2267)
Compound	**R**	**602**	**610**	**602**	**610**
a	–Si*i*–Pr$_3$	78	95	21.1 (2719)	52.0 (2208)
b	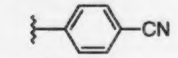	62	91	19.8 (2601)	53.9 (2276)
c	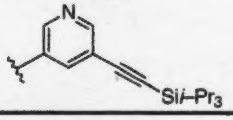	76	64	19.9 (2277)	53.9 (2277)

The progress of these ligand exchange reactions can be easily monitored using ^{31}P NMR spectroscopy as demonstrated by the representative example shown in Figure 6.5. Analysis of the ^{31}P NMR spectra of the *trans*–complexes **402** and **602** shows a virtual triplet at ca. 20 ppm. Upon addition of the dppee (δ –22), a loss in intensity of the virtual triplet corresponding to **402** and **602** is observed, coinciding with the growth of a new pseudo–triplet further downfield at ca. 54 ppm, attributed to the *cis*–complexes (**608**, **610**). The expulsion of triphenylphosphine is also observed at –4 ppm as dppee is consumed. In addition to the deshielding of the phosphorus as the *trans*–bis(phosphino)–species is converted to a *cis*–derivative, a decrease in the phosphorus–platinum coupling is also observed, consistent with *cis*–bis(phosphino)–platinum derivatives.[14] The $^{1}J_{P\text{–}Pt}$ value is ca. 2600–2700 Hz for the *trans*–bis(alkynyl) derivatives **402** and **602**, whereas upon chelation of the dppee to form **608** or **610**, the $^{1}J_{P\text{–}Pt}$ value is ca. 2200–2300 Hz.

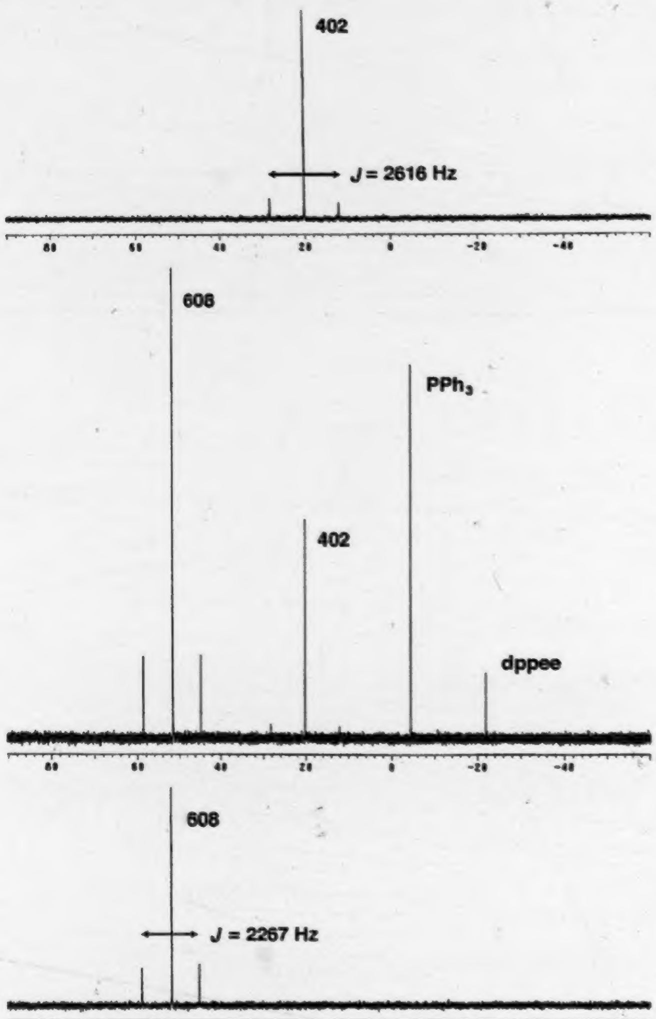

Figure 6.5 $^{31}P\{^1H\}$ NMR spectra (162 MHz, CD_2Cl_2) following the reaction of **402** with dppee to form **608**. (Top) NMR spectrum of *trans*–macrocycle **402**; (Middle) NMR spectrum of the reaction mixture after 4 hours. (Bottom) NMR spectrum of *cis*–complex **608**.

All of the bis(alkynyl) complexes were fully characterized using ^{1}H and ^{13}C NMR, and IR spectroscopies, electrospray mass spectral analysis, and microanalysis, where possible. In addition to ^{31}P NMR spectroscopy, convincing evidence for the conversion from *trans*– to *cis*–stereochemistry came from analysis of the ^{13}C NMR spectra. For example, in the *trans*–compounds **602a–c**, the σ–acetylide carbon ($L_2Pt(C{\equiv}CR)_2$) appears as a triplet (δ 128.9, 119.3 and 117.1, respectively) with a two–bond *cis*–coupling $^2J_{C-P}$ = 15 Hz. Upon chelation of the dppee ligand, the two phosphorus nuclei are no longer magnetically equivalent, leading to a more complex splitting pattern. This carbon resonance appears as an apparent doublet of doublets at δ 125.0, and 112.3 for **610a** and **610b**, respectively. The *cis*–coupling $^2J_{C-P}$ is still measured at 15 Hz in both cases, and the *trans*–$^2J_{C-P}$ coupling is significantly larger, ranging from 137 Hz for **610a** to 146 Hz for **610b**. For all six bis(alkynyl) complexes, the one–bond carbon–platinum coupling is not clearly observed due to insufficient signal/noise. The ^{13}C NMR spectrum of **608** was consistent with that of the other *cis*–bis(alkynyl) complexes and remarkably showed all 34 of the expected non–equivalent carbon resonances.

As previously stated, our interest in this ligand exchange reaction had been stimulated by a need to form varied supramolecular building blocks from common precursors. As such, this methodology has also been applied to the formation of the larger, bidentate macrocyclic ligand **611** (Scheme 6.4). Treatment of *trans*–platinacycle **403a** with dppee in CH_2Cl_2 led to the formation of the *cis*–derivative **611** after stirring at room temperature for 14 hours. After solvent removal, the crude solid was washed repeatedly with diethyl ether to remove the triphenylphosphine that had been released by the reaction. After washing, the solid was dried to leave pure **611**, isolated in 71% yield, as a pale yellow solid.

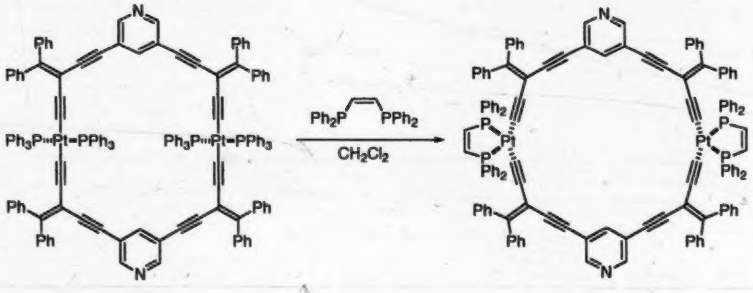

Scheme 6.4 Synthesis of *cis*–platinacycle **611**.

The ^{31}P NMR spectrum of the solid product again provided convincing evidence for the formation of **611**. The spectrum showed a single resonance at δ 53.6 with $^1J_{P\text{-}Pt}$ = 2292 Hz, which is consistent with all of the other bis(alkynyl) complexes. Further support for the structure of **611** comes from ESI mass spectral analysis, which shows three significant signals at *m/z* 2281 (25%), 2265 (75%) and 2243 (100%) corresponding to [M + K]$^+$, [M + Na]$^+$, and [M + H]$^+$, respectively. Molecular modeling for platinacycle **611** suggest that the *syn*– and *anti*–conformations about platinum (*syn*–conformation is shown in Scheme 6.4) should be easily interconverted in solution via bond rotation. Thus, it is unknown at present which conformation is preferred. As expected, the *syn*–conformation requires that the planes of the two pyridine rings are perpendicular to one another, providing us with a supramolecular building block featuring a new coordination motif.

6.2.2 Solid-State Properties of Trans– and Cis–Platinum Acetylide Complexes

In addition to full spectroscopic characterization in solution, the solid–state structural features of complexes **602a–c** and **610a,b** were also evaluated. Single crystals suitable for X–ray crystallographic analysis of **602a** were grown by slow evaporation from a CD_2Cl_2 solution of the complex at room temperature. Crystals of **602b**, **602c**, **610a**, and **610b** were grown by layering CH_2Cl_2 solutions of the respective complexes with hexanes and allowing slow diffusion at 4 °C. The ORTEP drawings are shown in Figures 6.6–6.10 and selected bond lengths and angles for **602a**, **602b**, **602c**, **610a** (two crystallographically independent molecules), and **610b** are summarized in Table 6.2. The only significant deviation in bond lengths between *cis*– and *trans*–derivatives is observed in the platinum–phosphorous bonds, which are consistently shorter for **610a** and **610b** than for **602a** and **602b**. The Pt–C≡C bond angles are typically linear, with the notable exception of **610b**, where a significant distortion occurs in the solid state and reduces these angles to 168.8(3) and 174.2(3)°. The ≡C–Pt–C≡ and P–Pt–P bond angles for **602a** and **602b** are all 180°. *Trans*–complex **602c** deviates slightly from this trend with ≡C–Pt–C≡ and P–Pt–P bond angles of 177.99(18) and 179.46(5) °, respectively. For complexes **610a** and **610b**, the P–Pt–P angles are quite consistent at ca. 86°, whereas the ≡C–Pt–C≡ bond angles vary from 89–95°, with complex **610b** showing the most significant distortion of this angle.

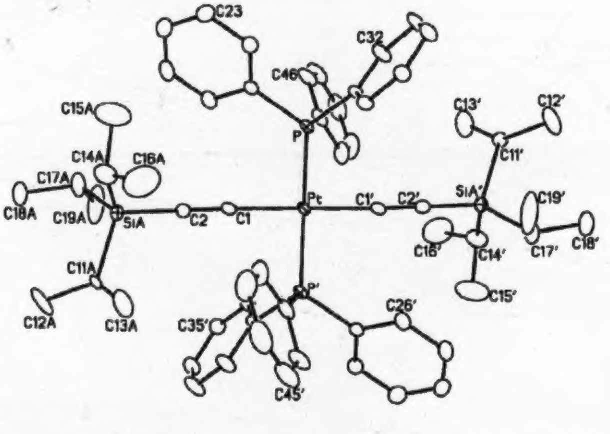

Figure 6.6 ORTEP drawing of *trans*–$(Ph_3P)_2Pt(C{\equiv}C{-}Si\textit{i}{-}Pr_3)_2$, **602a**. Thermal ellipsoids are drawn at the 20% probability level.

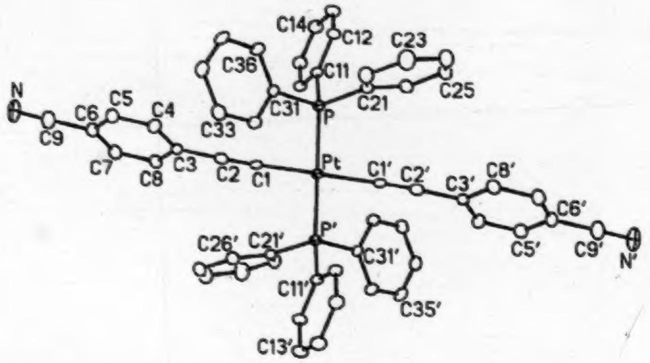
C14
C12
C23
C36
C11
C25
N
C5
C4
C6
C31
P
C21
C9
C33
Pt
C7
C8
C3
C2
C1
C1'
C2'
C3'
C8'
C6'
P'
C26'
C21'
C31'
C5'
C9'
N'
C11'
C35'
C13'

Figure 6.7 ORTEP drawing of *trans*–$(Ph_3P)_2Pt(C\equiv C\text{–}p\text{–}CN\text{–}C_6H_4)_2\bullet(CH_2Cl_2)_2$, **602b**. Thermal ellipsoids are drawn at the 20% probability level. Solvent has been omitted, for clarity.

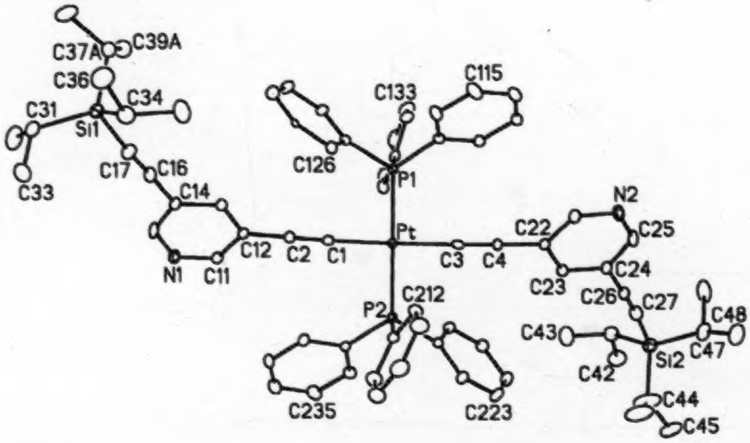
C37A
C39A
C36
C115
C34
C133
C31
Si1
C126
P1
C17
C16
C33
C14
N2
Pt
C22
C25
C12
C2
C1
C3
C4
N1
C11
C24
C23
C26
C27
C212
P2
C48
C43
C47
C42
Si2
C44
C235
C223
C45

Figure 6.8 ORTEP drawing of *trans*–$(Ph_3P)_2Pt(C\equiv C\text{pyr–}\textit{meta}\text{–}(C\equiv CSi\textit{i}\text{–}Pr_3))_2$, **602c**. Thermal ellipsoids are drawn at the 20% probability level.

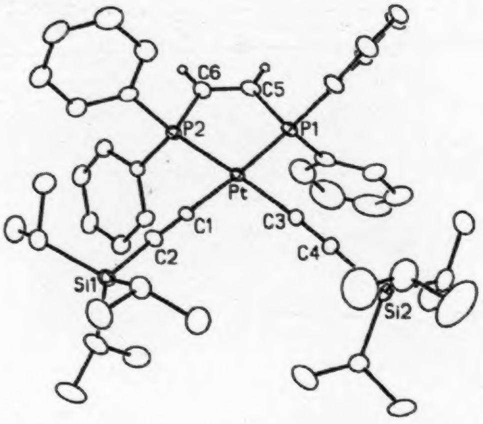
C6
C5
P2
P1
Pt
C1
C3
C2
C4
Si1
Si2

Figure 6.9 ORTEP drawing of *cis*–(dppee)Pt(C≡C–Si*i*–Pr$_3$)$_2$, **610a** (Molecule A). Thermal ellipsoids are drawn at the 20% probability level.

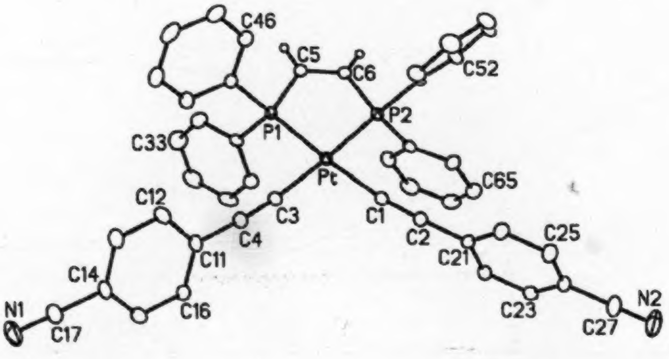
C46
C5
C6
C52
P1
P2
C33
Pt
C65
C12
C3
C1
C25
C4
C2
C11
C21
C14
N1
C16
C23
N2
C17
C27

Figure 6.10 ORTEP drawing of *cis*–(dppee)Pt(C≡C–*p*–CN–C$_6$H$_4$)$_2$•CH$_2$Cl$_2$, **610b**. Thermal ellipsoids are drawn at the 20% probability level. Solvent has been omitted, for clarity.

Table 6.2 A comparison of selected bond lengths [Å] and angles [°] for **602a**, **602b**, **602c**, **610a** (crystallographically independent molecule A), **610a*** (crystallographically independent molecule B), and **610b**.

	602a	**602b**	**602c**	**610a**	**610a***	**610b**
Bond lengths						
Pt–C(1)	2.005(4)	2.024(4)	1.999(4)	1.994(4)	2.014(5)	2.006(4)
Pt–C(3)	—	—	2.004(4)	2.004(5)	2.011(5)	2.009(3)
C(1)–C(2)	1.207(6)	1.152(6)	1.200(6)	1.219(6)	1.203(7)	1.212(5)
C(3)–C(4)	—	—	1.197(6)	1.207(7)	1.213(7)	1.205(5)
Pt–P(1)	2.2973(8)	2.3161(10)	2.3007(12)	2.2622(12)	2.2587(13)	2.2583(9)
Pt–P(2)	—	—	2.3099(12)	2.2600(13)	2.2599(13)	2.2545(9)
Bond angles						
Pt–C(1)–C(2)	176.2(4)	176.2(4)	177.3(4)	177.8(5)	177.7(5)	168.8(3)
Pt–C(3)–C(4)	—	—	175.7(4)	176.2(5)	177.1(5)	174.2(3)
C(1)–C(2)–X	—a	173.8(5)	172.0(5)	176.6(5)	178.5(5)	175.6(4)
C(3)–C(4)–X	—	—	172.9(5)	178.4(5)	174.6(5)	176.0(4)
P–Pt–P	180.0	180.0	179.46(5)	86.44(5)	86.18(5)	86.29(3)
■C–Pt–C■	180.0	180.0	177.99(18)	88.77(18)	89.24(18)	95.32(14)
P–Pt–C(1) [or P(1)–Pt–C(1)]	93.75(10)	87.26(11)	87.22(13)	176.48(14)	177.04(13)	174.36(10)
P–Pt–C(1') [or P(2)–Pt–C(3)]	86.25(10)	92.74(11)	88.95(12)	177.06(15)	177.42(14)	176.40(10)

[a] Positional disorder at Si precludes accurate determination

Single crystals of **608** were grown from a boiling 1,2–dichloroethane solution upon cooling and form a co–crystallite with two molecules of solvent and one molecule of water. The solid–state structure (Figure 6.11) confirms the heavily distorted and non–planar enyne framework, which would be expected due to the *cis*–platinum linkage. Overall, the main core of the macrocycle remains nearly planar, but then pivots dramatically at alkylidene carbons C(17) and C(23) to accommodate bonding to platinum. The bonding about platinum is quite similar to that observed for compounds

610a and **610b**. The majority of the distortion and strain is therefore borne by the alkylidene and acetylene framework. Somewhat surprisingly, the mean alkyne bond angle of **608** was determined to be 172.6°, which is comparable to that found for complex **402**, measured at 173.8°. Very little bond angle distortion occurs at the alkylidene carbons C(16)–C(17)–C(19) and C(22)–C(23)–C(25), which at 110.7(3)° and 112.8(3)° are remarkably similar to those of **402**, which average about 112.5°.

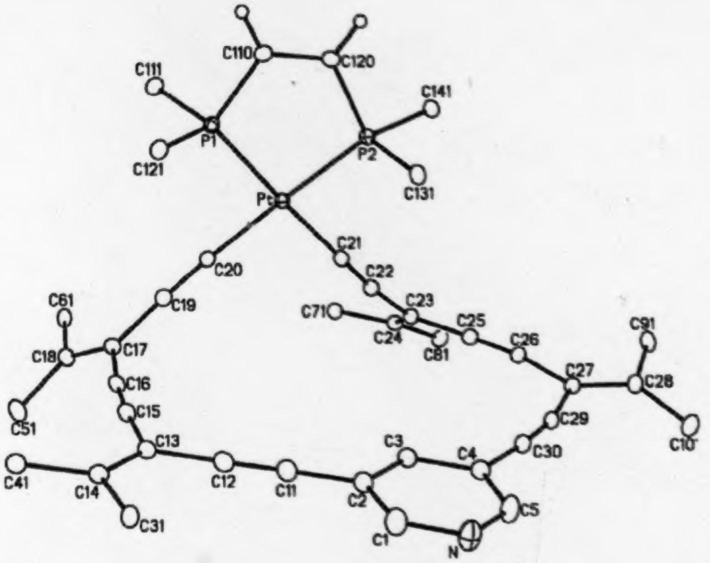
C110
C120
C111
C141
P1
P2
C121
C131
Pt
C21
C20
C22
C23
C71
C25
C91
C24
C81
C26
C61
C19
C17
C18
C27
C28
C16
C15
C29
C51
C13
C3
C4
C30
C10
C41
C14
C12
C11
C2
C5
C31
C1
N

Figure 6.11 ORTEP drawing of complex **608**. Selected bond lengths [Å] and angles [°]: Pt–P(1) 2.2686(8), Pt–P(2) 2.2711(8); P(1)–Pt–P(2) 85.61(3), P(1)–Pt–C(20) 92.30(9), P(1)–Pt–C(21) 174.62(9), P(2)–Pt–C(20) 172.76(9), P(2)–Pt–C(21) 93.65(9), C(20)–Pt–C(21) 89.07(13), C(2)–C(11)–C(12) 177.0(4), C(11)–C(12)–C(13) 178.9(4), C(13)–C(15)–C(16) 174.2(4), C(15)–C(16)–C(17) 172.3(3) C(17)–C(19)–C(20) 166.8(4), Pt–C(20)–C(19) 169.9(3), Pt–C(21)–C(22) 171.5(3), C(21)–C(22)–C(23) 173.8(4), C(23)–C(25)–C(26) 172.9(4), C(25)–C(26)–C(27) 171.1(4), C(27)–C(29)–C(30) 168.5(4), C(4)–C(30)–C(29) 174.5(4). Thermal ellipsoids are drawn at the 20% probability level. Two molecules of co–crystallized $ClCH_2CH_2Cl$ and one molecule of water, and all but the *ipso* carbon atoms of the phenyl groups were removed, for clarity.

6.2.3 Synthesis of Chiral Platinum Acetylide Complexes

It has been shown that *trans*–platinum acetylide complexes are readily accessible through the methodology described by Sonogashira and coworkers.[3] We have also established that these *trans*–complexes can be converted to their *cis*–counterparts in high isolable yields by simple treatment with a chelating diphosphine ligand. A natural extension of this research is the development of a route toward the formation of *chiral* macrocycles. We targeted a synthesis of chiral supramolecular building blocks that allowed for the divergent preparation of both enantiomers of a given product from a single precursor, necessitating the installation of the chiral group or ligand as part of the final step. Our ligand exchange methodology was ideal for such a strategy.

Our efforts began with the simple *trans*–bis(alkynyl) complex **602a**. We found that **602a** could easily be converted to its *cis*–chiral counterpart **612** (Scheme 6.5) by treating with one equivalent of (*S*,*S*)–Chiraphos in CH_2Cl_2 at room temperature for a period of 14 hours. Complex **612** was isolated as a colourless solid in 89% yield, subsequent to purification on a silica gel column.

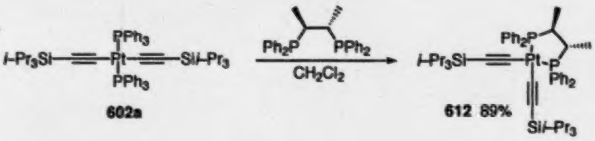

Scheme 6.5 Synthesis of *cis*–chiral complex **612**.

In a similar fashion, treatment of complex **602c** with two equivalents of (*S*,*S*)–Chiraphos in CD_2Cl_2 led to the quantitative formation of the chiral complex **613**. Remarkably, this reaction was complete in less than 15 minutes, perhaps as a result of the more electron–rich diphosphine ligand.

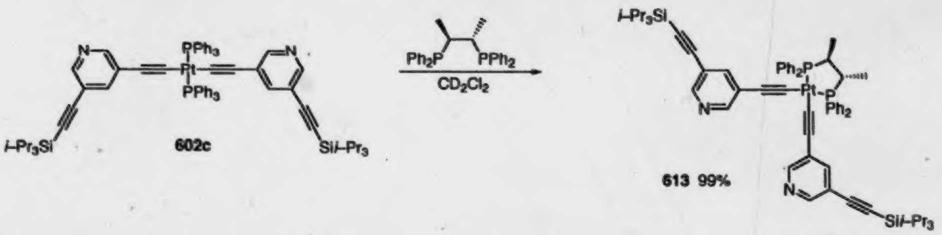

Scheme 6.6 Synthesis of *cis*–chiral complex **613**.

Having established that the ligand exchange methodology was effective using the chiral chelating ligand, (*S,S*)–Chiraphos, we next targeted the synthesis of larger, chiral macrocyclic systems, **614** and **615** (Scheme 6.7). Treatment of macrocycle **402** with 1 equivalent of (*S,S*)–Chiraphos in CD_2Cl_2 followed by stirring at room temperature for 4 days led to the formation of the chiral platinacycle **614**. The extended reaction time was presumably a reflection of the degree of strain present in the product **614** as well as the fact that the diphosphine ligand (unlike dppee) is free to rotate about the carbon–carbon bond of the ligand backbone. The reaction to form **615** took a similarly long time (ca. 5 days at room temperature). The *trans*-complex **403a** is extremely insoluble, even in chlorinated solvents, and, as a result, the reaction had to be carried out in a much higher volume of solvent (CH_2Cl_2). This may have been a contributing factor to the extended reaction time. Both complexes **614** and **615** were isolated in good yields, as stable yellow solids, following purification on a gradient silica gel column.

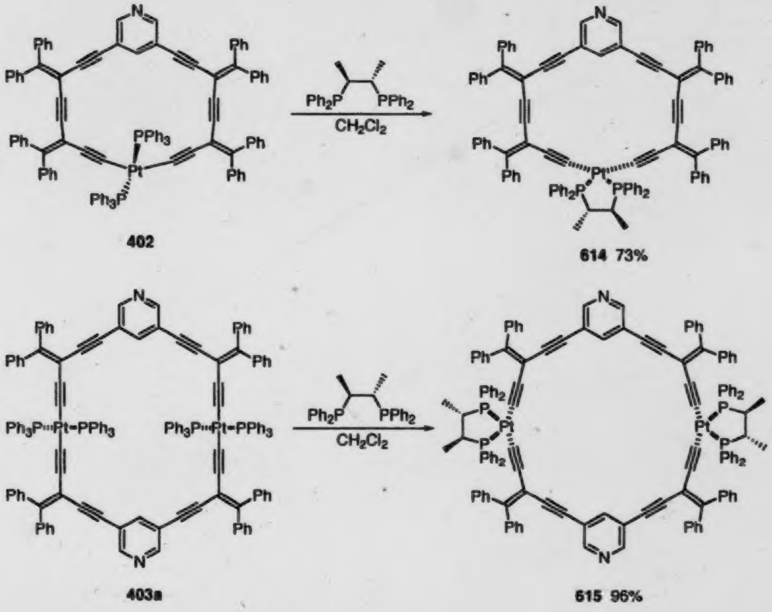

Scheme 6.7 Synthesis of chiral pyridine–containing macrocycles **614** and **615**.

In addition to our interest in the preparation of diverse supramolecular building blocks, we also targeted the extension of this methodology to the formation of chiral shape–persistent macrocycles. As such, our attention was next directed to the synthesis of chiral platinacycle **617**. The oligomeric species **209a** was desilylated by treatment with NaOH in THF/MeOH at room temperature until TLC analysis indicated full conversion to the deprotected tetrayne (about 4 hours). Subsequent to workup, the oligomer was intermolecularly coupled across platinum, using standard conditions (Scheme 6.8), to form the *trans*–platinacycle **616**. Macrocycle **616** was isolated in 64% yield, following purification on a gradient silica gel column.

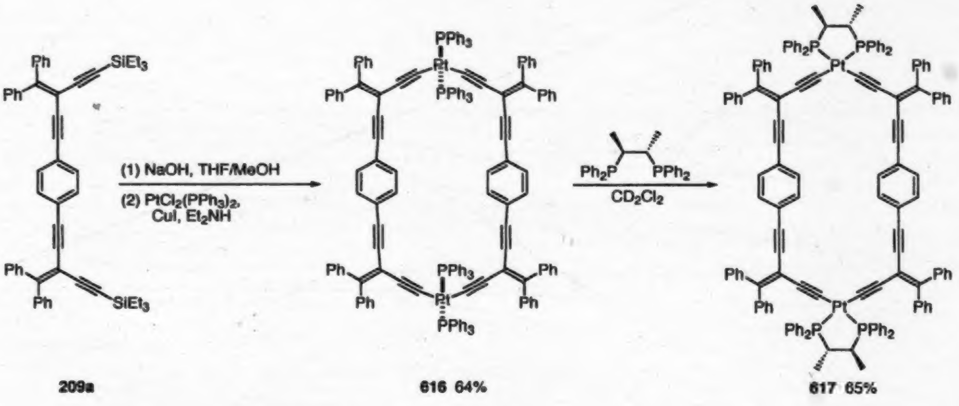

Scheme 6.8 Synthesis of chiral platinacycle **617**.

Platinacycle **616** was fully characterized using ^{1}H–, ^{13}C–NMR, and IR spectroscopies, as well as electrospray mass spectral analysis. The most convincing evidence for the formation of **616** came from the ^{31}P NMR spectrum, which showed a single apparent triplet at δ 18.6. The chemical shift of this resonance, in addition to the observed phosphorous–platinum coupling $^1J_{\text{P-Pt}} = 2626$ Hz, confirmed the presence of the *trans*–platinum acetylide linkage. Despite extremely limited solubility, the complex **616** was dissolved in boiling $CH_2Cl_2/ClCH_2CH_2Cl$ and, after slow evaporation at room temperature, single crystals suitable for X–ray crystallographic analysis were achieved. The ORTEP drawing (Figure 6.12) confirms the rigid, planar structure of **616**, as well as the presence of the metal acetylide linkage. It is interesting to note that, unlike platinacycles **403a** and **403b** (Figures 4.3 and 4.4, respectively), the pendant triphenylphosphine ligands of **616** have adopted a perpendicular arrangement with respect to the plane of the macrocyclic enyne core.

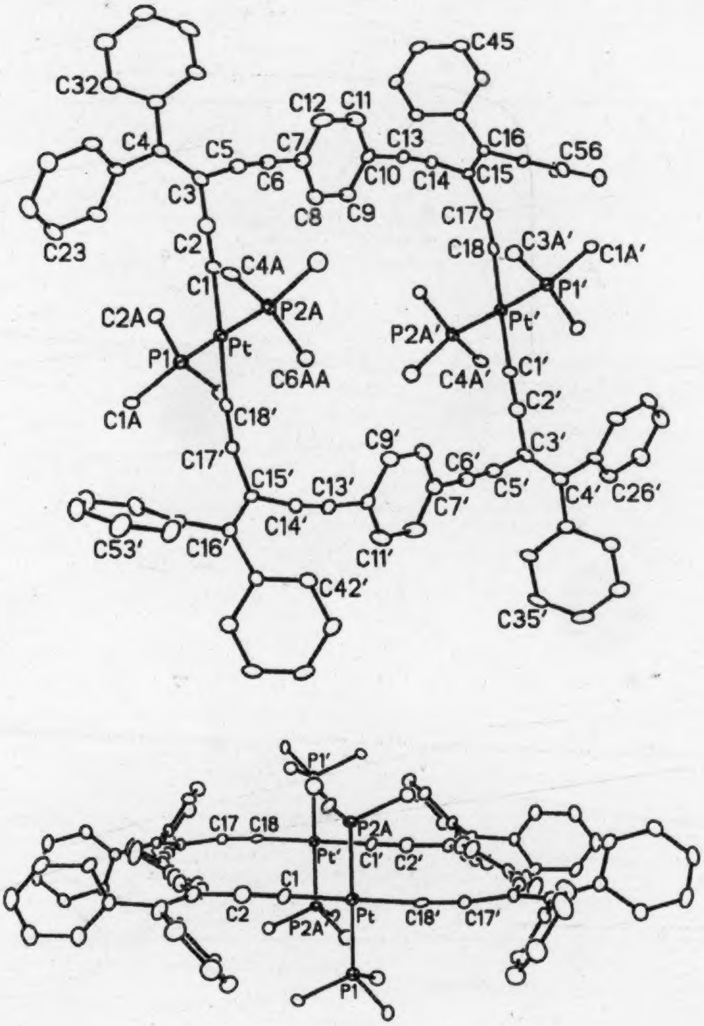
C45
C32
C12
C11
C4
C5
C7
C13
C16
C56
C6
C10
C14
C15
C3
C8
C9
C17
C2
C18
C3A'
C1A'
C23
C4A
C1
P1'
P2A
C2A
Pt'
P2A'
Pt
P1
C6AA
C4A'
C1'
C2'
C1A
C18'
C9'
C3'
C17'
C15'
C13'
C6'
C5'
C7'
C4'
C26'
C14'
C53'
C16'
C11'
C42'
C35'
P1'
P2A
C17
C18
Pt'
C1'
C2'
C1
C2
P2A'
Pt
C18'
C17'
P1

Figure 6.12 (Top) ORTEP drawing of *trans*-platinacycle **616**. (Bottom) Alternate view. Selected bond lengths [Å] and angles [°]: Pt–P(1) 2.3026(19), Pt–P(2A) 2.270(5), Pt–C(1) 1.965(7), Pt–C(18′) 1.997(7); P(1)–Pt–P(2A) 173.99(15), C(1) –Pt–C(18′) 178.1(3), Pt–C(1)–C(2) 176.3(7), C(1)–C(2)–C(3) 175.2(8), C(3) –C(5)–C(6) 172.3(9), C(5)–C(6)–C(7) 175.8(9), C(10)–C(13)–C(14) 172.8(8), C(13)–C(14)–C(15) 169.2(8), C(15)–C(17)–C(18) 166.8(7), C(17)–C(18)–Pt′ 176.5(6). Thermal ellipsoids are drawn at the 20% probability level. Co-crystallized $ClCH_2CH_2Cl$ and all but the *ipso* carbons of the triphenylphosphine rings have been omitted, for clarity.

Platinacycle **616** was converted to its chiral derivative **617** by treating with two equivalents of (*S,S*)–Chiraphos in CD_2Cl_2 and stirring at room temperature for 3 days. **617** was isolated as a pale yellow, relatively insoluble solid after purification on a gradient silica gel column. The insolubility of the solid **617** may have contributed to the lower isolated yield of this complex (65%).

The final example prepared in this series is the interesting dehydrobenzannulene complex **619**.[15] The *trans*–platinacycle **618** was provided by our colleagues Prof. Michael Haley and Charles Johnson II at the University of Oregon who collaborated with us on this project due to a shared interest in the preparation of chiral macrocycles. The *trans*–complex **618** was converted to its *cis*–chiral analogue **619** using the same general procedure that was successful for all of the other macrocycles (Scheme 6.9). The ligand exchange reaction was complete after a period of 3 days, and the chiral platinacycle **619** was isolated as a colourless solid in 83% yield, following purification on a gradient silica gel column.

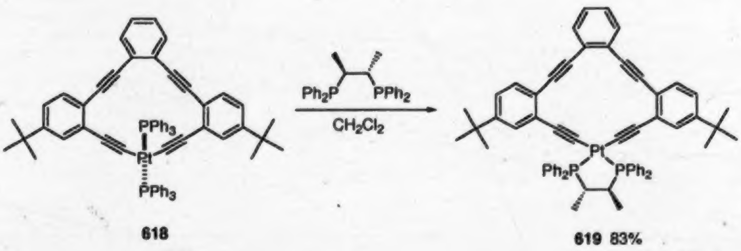

Scheme 6.9 Synthesis of chiral platinum-dehydrobenzannulene complex **619**.

To highlight the economy of our methodology, chiral complex **620** (Scheme 6.10) was prepared by treating macrocycle **403a** with two equivalents of (*R,R*)–Chiraphos for a period of 4 days. The divergent preparation of *both* enantiomers of a macrocyclic product from a common precursor demonstrates the success of our strategy which allows for the installation of chirality through ligand exchange at the final step of the synthesis.

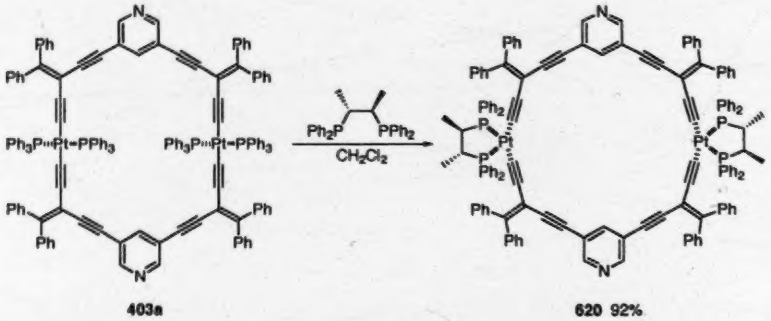

Scheme 6.10 Synthesis of chiral platinacycle **620** featuring (*R*,*R*)–Chiraphos.

The progress of these ligand exchange reactions to form chiral metallamacrocycles, like the achiral analogues, can be easily monitored by ^{1}H– and ^{31}P–NMR spectroscopy. The alkyl protons of the free ligand, (*S*,*S*)–Chiraphos, appear as a multiplet (methine) and quartet (methyl) at 2.50 – 2.43 and 1.17 ppm, respectively. Upon binding to the metal centre, these protons are shifted upfield and appear as broad multiplets centred at 2.49 – 2.16 and 0.95 – 0.84 ppm, respectively. Even more diagnostic are the ^{31}P NMR spectra of the reactions (for a representative example see Figure 6.13). As the reactions proceed, the free Chiraphos ligand, which appears as a singlet at –8.7 ppm, binds to the metal centre releasing triphenylphosphine, which is observed at –4.4 ppm. The *trans*–acetylide complex (**602a**, **602c**, **402**, **403a**, **616** and **618**), which shows a signal in the range of 18–21 ppm, is also consumed as the reaction proceeds, giving rise to a new resonance for the respective *cis*-chiral complex observed downfield at ca. 42–47 ppm. As the coordination geometry about the platinum centre changes from *trans* to *cis*, a change in the phosphorous–platinum coupling constant is also observed with the $J_{P\text{–}Pt}$ values measured to be ca. 2600–2720 Hz for the *trans*–

bis(alkynyl) derivatives (as previously described) and 2190–2250 Hz for the *cis*–chiral derivatives.

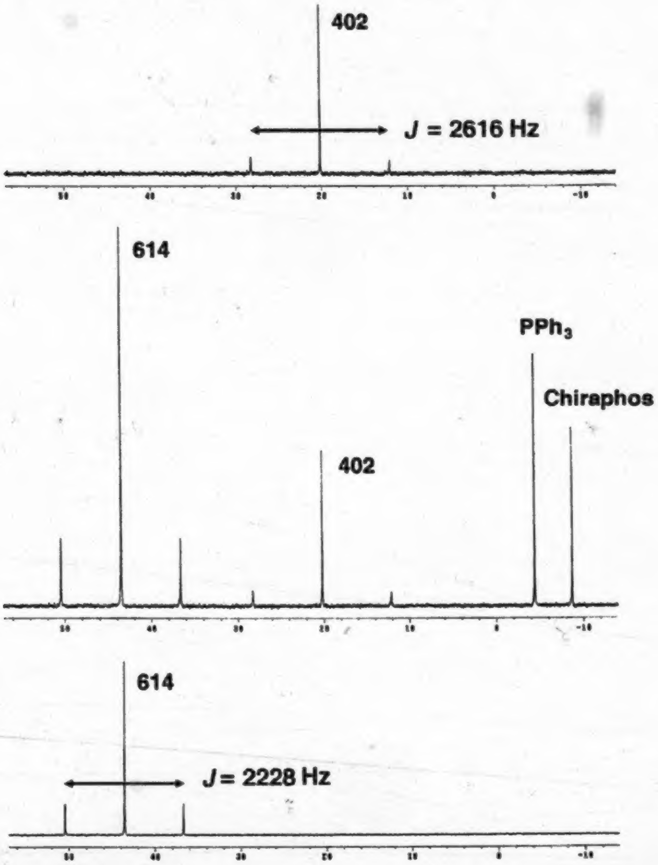

Figure 6.13 $^{31}P\{^1H\}$ NMR spectra (162 MHz, CD_2Cl_2) following the reaction of **402** with (*S,S*)–Chiraphos to form **614**. (Top) NMR spectrum of *trans*–macrocycle **402**. (Middle) NMR spectrum of the reaction mixture after 48 hours. (Bottom) NMR spectrum of *cis*–chiral complex **614**.

It is worth noting that all of the *cis*–chiral macrocyclic complexes were purified in a similar manner. The reactions proceed very cleanly and, as a result, the only impurities that need to be removed are triphenylphosphine as well as trace amounts of the starting materials (the *trans*–macrocycle and Chiraphos). Following application of the reaction mixture to a silica gel column, flushing with a relatively non–polar solvent system such as CH_2Cl_2 or CH_2Cl_2/hexanes removes the less polar excess phosphine ligand(s). A slight increase in polarity (10–30% acetone) is sufficient for removal of any remaining non–chelated macrocyclic complexes. This is followed by flushing with a far more polar solvent system (30–50% acetone) to isolate the pure *cis*–macrocycle.

6.2.4 Solid–State Properties of Chiral Platinum Acetylide Complexes

It is well known that 5–membered chelate rings can adopt two puckered, chiral conformations (Figure 6.14) about a square planar metal centre.[16] In the presence of stereogenic centres (as is the case with (*S,S*)–Chiraphos) these two conformations become diastereomeric. As a result, one of the chiral conformations is energetically more favorable. In the case of (*S,S*)–Chiraphos, the most stable conformation is the one in which the substituents on the chelate ring are equatorially disposed (the *δ–skew*).

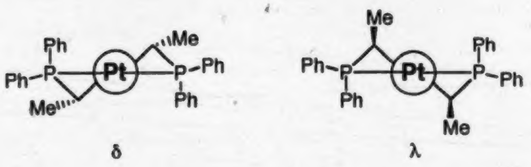

Figure 6.14 Schematic representation of two chiral conformations adopted by (*S,S*)–Chiraphos.

Single crystals of **612** and **614** suitable for X–ray crystallographic analysis were grown by slow evaporation/diffusion from CH_2Cl_2/hexanes and $CH_2Cl_2/ClCH_2CH_2Cl/Et_2O$ solutions of the complexes at 4 °C, respectively. The ORTEP drawing of **612** (Figure 6.15) shows that the complex is in the expected *δ–skew* conformation where the two methyl groups of Chiraphos are pseudoequatorial.

The torsional angle between the two pseudo–equatorial methyl groups of **612** is measured at –53.2(3)° for C(10)–C(1)–C(2)–C(20). The coordination geometry of complex **612** is square planar with angles about the platinum centre of 86.29(2)° [P(1)–Pt–P(2)] and 87.93(9)° [C(3)–Pt–C(5)] which are comparable to other platinum(II)–Chiraphos complexes.[17] All platinum–carbon and platinum–phosphorous bond lengths are nearly identical to those of the achiral analogue **610a**. Likewise, all of the bond angles about platinum for **612** are very similar to those of the achiral complex. The only notable difference is in the degree of bend observed in one of the acetylene bonds: Pt–C(3)–C(4) is measured at 172.0(3)°. This distortion, while significant, is likely the result of crystal packing forces in the solid–state. A greater degree of distortion was observed in the acetylene bonds of the achiral complex **610b** (ca. 169°).

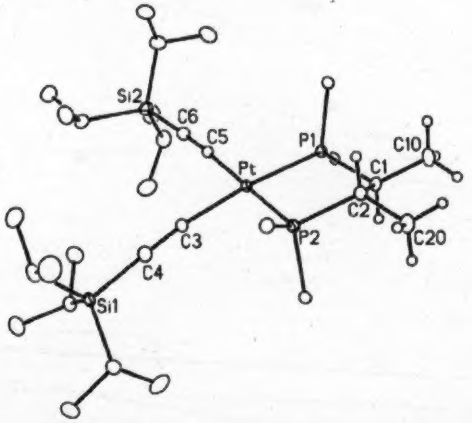

Figure 6.15 ORTEP drawing of **612**. Selected bond lengths [Å] and angles [°]: Pt–P(1) 2.2777(6), Pt–P(2) 2.2679(7), Pt–C(3) 2.008(2), Pt–C(5) 2.006(2), C(3)–C(4) 1.203(4), C(5)–C(6) 1.202(4); Pt–C(3)–C(4) 172.0(3), Pt–C(5)–C(6) 176.1(2), C(3)–C(4)–Si(1) 175.4(3), C(5)–C(6)–Si(2) 177.0(3), P(1)–Pt–P(2) 86.29(2), C(3)–Pt–C(5) 87.93(9), P(1)–Pt–C(5) 93.83(7), P(2)–Pt–C(3) 92.15(6). Thermal ellipsoids are drawn at the 20% probability level. Co–crystallized CH_2Cl_2 and all but the *ipso* carbon atoms of the phenyl groups were removed, for clarity.

The solid state structure of **614**, by contrast, shows some unexpected features. Complex **614** crystallized such that there are two independent molecules in the unit cell (only Molecule A is shown in Figure 6.16). The enyne core of the macrocycle is distorted in a fashion similar to that of its achiral analogue. While much of the macrocyclic core is near planar, the structure bends drastically at the vinylidene carbons C(17) and C(23) to accommodate for the *cis*–acetylide linkage to the platinum centre. The strain induced as a result of this conformational necessity is borne almost exclusively by the enyne core of the macrocycle. The coordination geometry about the platinum centre remains unchanged with bond angles about the metal of 87.5(6)° [C(20)–Pt(1)–C(21)] and 86.04(16)° [P(1)–Pt(1)–P(2)]. The effects of the strain are instead observed in the alkylidene and alkyne bond angles, which have observed mean values of 112.2° and 172.3°, respectively. These values are nearly identical to those observed in the achiral analogue **608**, and thus, the incorporation of a chiral chelating ligand imparts no additional strain. Interestingly, these bond angles are also comparable to the mean alkyne and alkylidene bond angles observed in the solid–state structure of *trans*-platinacycle **402** (175.3 and 112.6°, respectively).

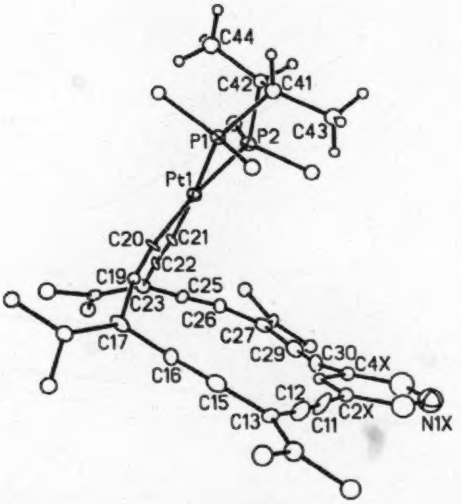

Figure 6.16 ORTEP drawing of molecule A of **614**. Selected bond lengths [Å] and angles [°]: Pt–P(1) 2.304(4), Pt–P(2) 2.303(5), Pt–C(20) 2.008(15), Pt–C(21) 2.041(15); P(1)–Pt–P(2) 86.04(16), P(1)–Pt–C(20) 92.1(5), P(1)–Pt–C(21) 177.5(5), P(2)–Pt–C(20) 172.8(5), P(2)–Pt–C(21) 94.6(5). Thermal ellipsoids are drawn at the 20% probability level. Co-crystallized solvent ($ClCH_2CH_2Cl$ and H_2O) and all but the *ipso* carbons of all phenyl rings have been removed, for clarity.

The most remarkable feature of the solid–state structure of **614** is that the Chiraphos ligand has adopted a *λ–skew* chiral conformation where the two methyl groups pendant to the five–membered chelate are pseudoaxial. The dihedral angle between these two methyl groups (C(43) and C(44)) is measured to be 167.4°. To the best of our knowledge, there is only one other example of Chiraphos adopting this conformation (in the solid–state) in the literature.[18]

It is generally accepted that the source of chiral induction in chelating phosphines of this type is the chiral array of phenyl groups on the phosphorous atoms.[16] As a result of the *skew* conformation of the 5–membered chelate ring, the two phenyl groups on each phosphorous are held in a rigid, chiral array, the result of chirality transfer from the proximal stereogenic centres. It is this chiral array of phenyl groups that interacts with other ligands associated with the metal centre. It is possible that **614** has adopted the normally disfavored *λ–skew* conformation to reduce steric interactions between the phenyl groups on the diphosphine ligand and the pendant diphenylalkylidene groups of the macrocyclic core. It is also possible that this conformation is the result of crystal packing effects, although this seems unlikely in view of the fact that there is only a single example of this conformation in the literature, despite the numerous crystal structures of Chiraphos complexes that have been published.

6.2.5 Electronic Properties of Chiral Platinum Acetylide Complexes

To gain insight into the electronic properties of these chiral conjugated complexes, the UV-vis absorption spectra were acquired and are shown in Figure 6.17. It can be seen that the absorption curves of all of the complexes are dominated by large, low–energy absorptions resulting from metal-to-ligand charge-transfer (MLCT), which is well-documented for σ-acetylide complexes.[19] These absorptions result from the mixing of the platinum dπ–orbitals with the π^* orbitals of the acetylenic chromophore(s).

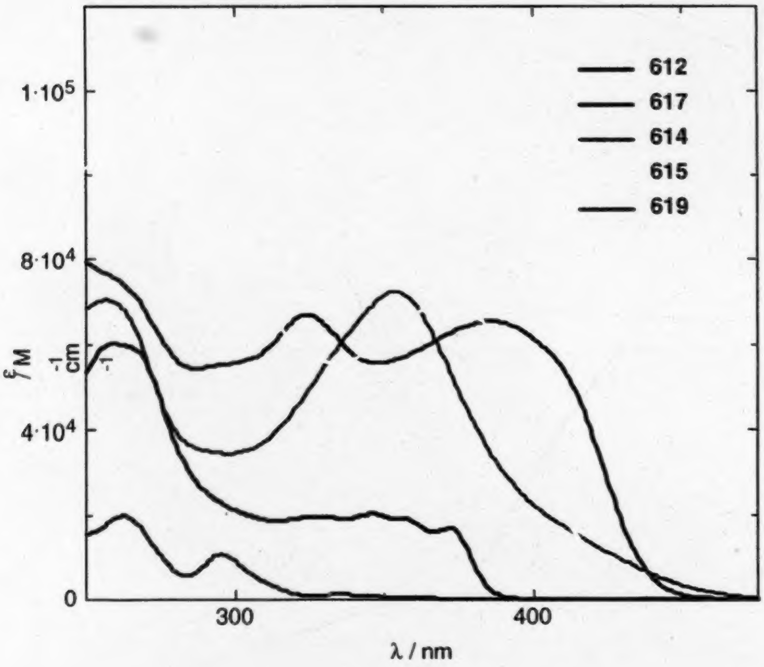

Figure 6.17 UV-vis absorption spectra for *cis*–chiral complexes in CH_2Cl_2.

The lowest energy absorption maxima occurs at λ_{max} = 386 nm (ε = 65,400) in the spectrum of complex **617**, which is not suprising as it is linearly conjugated across the *para*–diethynylbenzene segment and thus would be expected to have a smaller HOMO to LUMO gap than its cross–conjugated analogues. Complex **615**, on the other hand, is cross–conjugated due to the presence of the 3,5–diethynyl pyridine moiety and, as such, gives a higher energy absorption maxima at λ_{max} = 369 nm (ε = 69,300). The energy of this absorption may provide further evidence for electron delocalization across the platinum centres. In the absence of communication across the platinum centre, complex **615** would be expected to have a higher energy absorption maxima than that of complex **614** which is observed at λ_{max} = 354 nm (ε = 72,400). This is because, while both complexes possess an ene–yne segment in conjugation with the pyridine, complex **614** possesses the longest conjugated sub–unit (the ene–yne–ene chromophore). An alternative explanation for this observation is that **614** is bent (as we observed in the solid state) such that conjugation across the ene–yne segment is not possible. A rigid conformation such as this may also account for the relatively high molar absorptivity that is observed in the spectrum for **614**. Not suprisingly, the highly strained (and therefore, non–planar) dehydrobenzannulene complex **619** gives the highest energy absorption maxima at λ_{max} = 347 nm (ε = 20,300). The UV–vis spectra of complexes **615** and **617** both also show unassigned, high–energy absorption bands at approximately 305 and 320 nm, respectively.

The CD spectra for all cyclic *cis*–chiral complexes are shown in Figure 6.18. The curve for complex **617** shows a large bisignate band at 358 nm, presumably resulting from the MLCT absorption band of the acetylenic chromophore. A second, higher energy band is also observed at ca. 260 nm. Similar signals are observed in the CD spectrum of complex **615**, which shows two less–intense, higher–energy, bisignate bands at approximately 360 and 305 nm. The spectrum for **620** mirrors that of **615**, both in form and intensity, consistent with the enantiomeric relationship. This second, high–energy band is clearly associated with the unassigned transition observed in the UV-vis absorption spectrum. The remaining complexes (**612**, **614**, and **619**) all show only weak, high energy signals in the CD spectra, presumably due to electronic transitions of the chiral, chelating ligand attached to the metal centre. These observations imply that for effective chirality transfer to occur, the acetylenic chromophore attached to the metal must be large and rigid enough to interact with the chiral array of phenyl groups on the diphosphine ligand, but it must also be conformationally mobile enough to be biased by that interaction.

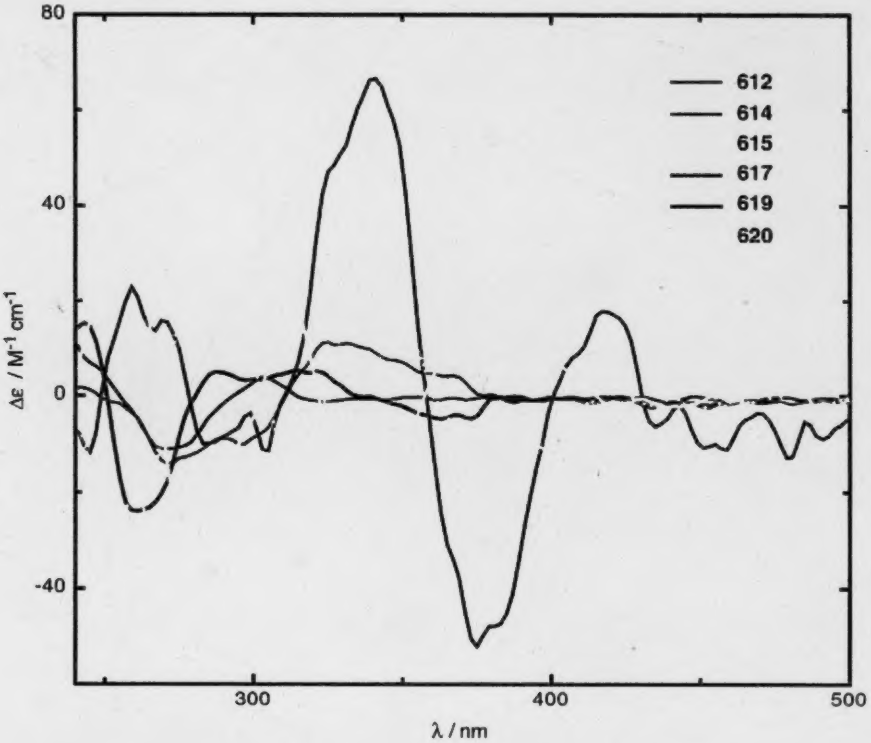

Figure 6.18 CD spectra for *cis*–chiral complexes in CH_2Cl_2.

6.3 Conclusions and Future Work

In this Chapter we have described an effective synthetic strategy for the transformation of *trans*–platinum acetylide complexes to their *cis*–bis(alkynyl) counterparts. By treating a *trans*–complex with a chelating diphosphine ligand, we have shown that *cis*–acetylide complexes can be accessed in good to excellent yields. This strategy is effective for the formation of simple, acyclic, complexes as well as large, macrocyclic assemblies. As an extension of this research, we have also discovered that it is possible to realize chiral analogues of these platinum acetylide complexes. Reaction of *trans*–platinum acetylide complexes with (*S,S*)–Chiraphos leads to the formation of *cis*–chiral acetylide complexes in good isolated yields. This transformation is equally effective for cyclic and acyclic species, as well as for pyridine-containing supramolecular building blocks. The solution–state characterization and solid–state properties of several complexes have been described. An analysis of the electronic properties of the *cis*–chiral derivatives was also provided, and the CD spectroscopic data clearly demonstrates the ability of the Chiraphos ligand to efficiently transfer chirality to the conjugated molecular framework of platinum acetylide complexes.

As described in the introduction to this chapter, ligand exchange reactions were targeted because we expected to realize larger and more robust porous solids through cross–linking at the platinum acetylide centre(s) of conjugated platinacycles. Future work will focus on the development of a ligand system capable of bridging two platinum acetylide species. The use of tetrakis(diphenylphosphino)benzene **621**[20] (Figure 6.19) will allow us to take advantage of the predisposition toward chelation while achieving this ultimate goal. The bis–chelated species **622** is expected to be more robust and rigid than what could be achieved through the use of a simple, bidentate bridging ligand.

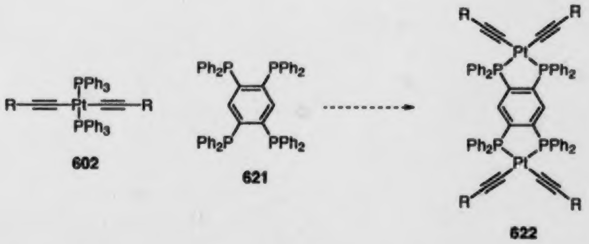

Figure 6.19 Proposed synthesis of cross–linked species **622**.

6.4 References and Notes

1. (a) Espinet, P.; Soulantica, K.; Charmant, J. P. H.; Orpen, A. G. *Chem. Commun.* **2000**, 915–916. (b) Campbell, K.; McDonald, R.; Ferguson, M. J.; Tykwinski, R. R. *J. Organomet. Chem.* **2003**, *683*, 379–387.

2. Fuhrmann, G.; Debaerdemaeker, T.; Bäuerle, P. *Chem. Commun.* **2003**, 948–949.

3. (a) Sonogashira, K.; Fujikura, Y.; Yatake, T.; Toyoshima, N.; Takahashi, S.; Hagihara, N. *J. Organomet. Chem.* **1978**, *145*, 101–108. (b) Sonogashira, K.; Yatake, T.; Tohda, Y.; Takahashi, S.; Hagihara, N. *J. Chem. Soc., Chem. Commun.* **1977**, 291–292.

4. For a more comprehensive review of metal–directed self–assembly reactions and applications, please see Chapter 3 and references therein.

5. (a) Mukherjee, P. S.; Das, N.; Kryschenko, Y. K.; Arif, A. M.; Stang, P. J. *J. Am. Chem. Soc.* **2004**, *126*, 2464–2473. (b) You, C.–C.; Würthner, F. *J. Am. Chem. Soc.* **2003**, *125*, 9716–9725. (c) Yamamoto, T.; Arif, A. M.; Stang, P. J. *J. Am. Chem. Soc.* **2003**, *125*, 12309–12317. (d) Forniés, J.; Gómez, J.; Lalinde, E.; Moreno, M. T. *Chem. Eur. J.* **2004**, *10*, 888–898. (e) Ferrer, M.; Rodríguez, L.; Rossell, O. *J. Organomet. Chem.* **2003**, *681*, 158–166.

6. (a) Mukherjee, P. S.; Das, N.; Stang, P. J. *J. Org. Chem.* **2004**, *69*, 3526–3529. (b) Su, C.–Y.; Cai, Y.–P.; Chen, C.–L.; Smith, M. D.; Kaim, W.; zur Loye, H.–C. *J. Am. Chem. Soc.* **2003**, *125*, 8595–8613. (c) Chand, D. K.; Fujita, M.; Biradha, K.; Sakamoto, S.; Yamaguchi, K. *Dalton Trans.* **2003**, 2750–2756. (d) Kumazawa, K.; Biradha, K.; Kusukawa, T.; Okano, T.; Fujita, M. *Angew. Chem. Int. Ed.* **2003**, *42*, 3909–3913. (e) Müller, I. M.; Spillmann, S.; Franck, H.; Pietschnig, R. *Chem. Eur.*

J. **2004**, *10*, 2207–2213. (f) Baldini, L.; Ballester, P.; Casnati, A.; Gomila, R.; Hunter, C. A.; Sansone, F.; Ungaro, R. *J. Am. Chem. Soc.* **2003**, *125*, 14181–14189.

7. (a) Le Bouder, T.; Maury, O.; Bondon, A.; Costuas, K.; Amouyal, E.; Ledoux, I.; Zyss, J.; Le Bozec, H. *J. Am. Chem. Soc.* **2003**, *125*, 12284–12299. (b) Rao, C. N. R.; Natarajan, S.; Vaidhyanathan, R. *Angew. Chem. Int. Ed.* **2004**, *43*, 1466–1496.
8. (a) Telfer, S. G.; Kuroda, R. *Coord. Chem. Rev.* **2003**, *242*, 33–46; (b) Mamula, O.; von Zelewsky, A. *Coord. Chem. Rev.* **2003**, *242*, 87–95.
9. (a) Lee, S. J.; Hu, A.; Lin W. *J. Am. Chem. Soc.* **2002**, *124*, 12948–12949; (b) Jiang, H.; Hu, A.; Lin, W. *Chem. Commun.* **2003**, 96–97.
10. (a) Lin, J.; Zhang, H.–C.; Pu, L. *Org. Lett.* **2002**, *4*, 3297–3300; (b) Lee, S. J.; Lin, W. *J. Am. Chem. Soc.* **2002**, *124*, 4554–4555.
11. Müller, C.; Whiteford, J. A.; Stang, P. J. *J. Am. Chem. Soc.* **1998**, *120*, 9827–9837.
12. Onitsuka, K.; Harada, Y.; Takei, F.; Takahashi, S. *Chem. Commun.* **1998**, 643–644.
13. For a more comprehensive review of metal σ–acetylide complexes, please see Chapter 4 and references therein.
14. Whiteford, J. A.; Lu, C. V.; Stang, P. J. *J. Am. Chem. Soc.* **1997**, *119*, 2524–2533.
15. For the synthesis of a related metallamacrocycle see Pak, J. J.; Darwish, O. S.; Weakley, T. J. R.; Haley, M. M. *J. Organomet. Chem.* **2003**, *683*, 430–434.
16. (a) Fryzuk, M. D.; Bosnich, B. *J. Am. Chem. Soc.* **1977**, *99*, 6262–6267; (b) Corey, E. J.; Bailar Jr., J. C. *J. Am. Chem. Soc.* **1959**, *81*, 2620–2629; (c) Brunkan, N. M.; White, P. S.; Gagné, M. R. *Angew. Chem. Int. Ed.* **1998**, *37*, 1579–1582.
17. Johansson, M. H.; Malmström, T.; Wendt, O. F. *Inorg. Chim. Acta* **2001**, *316*, 149–152.

18. Wicht, D. K.; Zhuravel, M. A.; Gregush, R. V.; Glueck, D. S.; Guzei, I. A.; Liabel–Sands, L. M.; Rheingold, A. L. *Organometallics* **1998**, *17*, 1412–1419.

19. (a) Faust, R.; Diederich, F.; Gramlich, V.; Seiler, P. *Chem. Eur. J.* **1995**, *1*, 111–117, and references therein. (b) Yam, V. W.–W. *Acc. Chem. Res.* **2002**, *35*, 555–563.

20. McFarlane, H. C. E.; McFarlane, W. *Polyhedron* **1988**, *7*, 1875–1879.

Chapter 7 Conclusions and Future Work

This thesis has provided a detailed description of many projects undertaken as part of my doctoral studies, ranging from target–oriented organic synthesis, to coordination chemistry, and solid–state NMR analysis. At the outset of my graduate work, we were primarily interested in the realization of shape–persistent, cross–conjugated macrocycles. We demonstrated that these macrocycles were synthetically accessible and we also provided a preliminary description of the effects of pendant substitution on the properties of the resultant macrocycles, including modifications to both their solubility and stability.

We then directed our efforts to the synthesis of macrocycles that incorporate pyridine functionality, suitable for coordination to transition metal centres. Macrocyclic species featuring both endo– and exotopic binding sites were realized, and the coordinative ability of these ligands via the pyridine(s) was established. We have discovered that these pyridine–containing macrocycles function as porous supramolecular building blocks, as demonstrated by the preparation of several supramolecular assemblies. The scope and limitations of these 'rigid' macrocyclic ligands were explored, and we have shown that, in some cases, these materials form highly ordered and porous solids.

These species were further elaborated to incorporate metal acetylide linkages for the dual purpose of expanding pore size and providing a second 'handle' to direct the association of the macrocyclic ligands. Our first attempt to cross–link the metal centres led us to the discovery of some interesting reactivity. We found that treatment of a *trans*–metal acetylide complex with a chelating diphosphine ligand leads to the formation of the *cis*–chelated analogue in excellent yield. This methodology was established through the preparation of several *trans*– and *cis*–acetylide complexes, and we later confirmed the applicability and economy of this synthetic strategy for the preparation of chiral metal acetylide complexes and chiral macrocycles.

A recent, collaborative project has focused on the study of the porous organic and metal–organic solids developed within our group through the use of hyperpolarized ^{129}Xe NMR spectroscopy. We have established that, despite our inability to perform X–ray crystallographic analysis on these solids upon desolvation, the crystalline solids nevertheless retain their porosity in the absence of associated solvent molecules. For nearly every system studied, ^{129}Xe NMR spectroscopy provided real insight into the porous nature of these systems, especially when used in conjunction with X–ray crystallographic data that was acquired in the presence of co–crystallized solvent.

There are numerous avenues available for future study. First, as described briefly in Chapters 2 and 3, we have on several occasions observed the formation of alkynyl iodides under oxidative homocoupling conditions. As alkynyl iodides are important synthetic intermediates, the optimization of this reaction may lead to the development of conditions that could provide alkynyl iodides **702** in a gentle, cost–effective manner (Scheme 7.1).

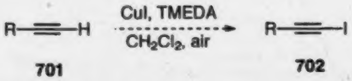

Scheme 7.1 Proposed synthesis of alkynyl iodides **702**.

Macrocycle **216c**, as described in Chapter 1, was targeted due the presence of endotopic binding sites, and we established via crystallographic analysis that these macrocyclic species stack in the solid–state such that channels are realized. It remains, however, to demonstrate the coordinative ability of this macrocyclic species. The insertion of a metal or metal complex into the centre of the macrocyclic cavity would potentially lead to the formation of a solid with an organized, linear array of metal ions (Figure 7.1). This is especially intriguing as it may allow for the formation of 'molecular wires' or ion channels.

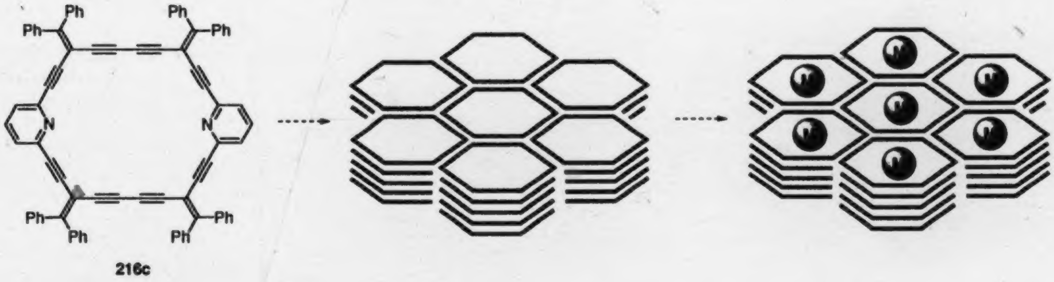

Figure 7.1 Installation of metal species in the channels of **216c**.

Macrocyclic species, such as **703**, featuring *both* endo– and exotopic binding sites are a natural extension of this project. A macrocyclic ligand whose assembly could be manipulated through coordination at the periphery of the macrocycle, while still possessing the means to interact with guest species within the macrocyclic core, would be an extremely desirable supramolecular building block.

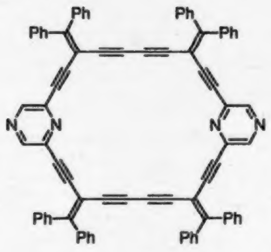
Ph
Ph
Ph
Ph
N
N
N
N
Ph
Ph
Ph
Ph

703

In addition to the preparation and assembly of new supramolecular building blocks, there are numerous questions that remain with regard to our ligand exchange methodology. First, it would be interesting to explore the effects of utilizing some other readily–available chiral diphosphine ligands, such as BINAP and DIOP, to establish the generality of this approach for the production of large, chiral assemblies (Scheme 7.2). These studies could also provide us with greater insight into the sources and magnitude of chiral induction.

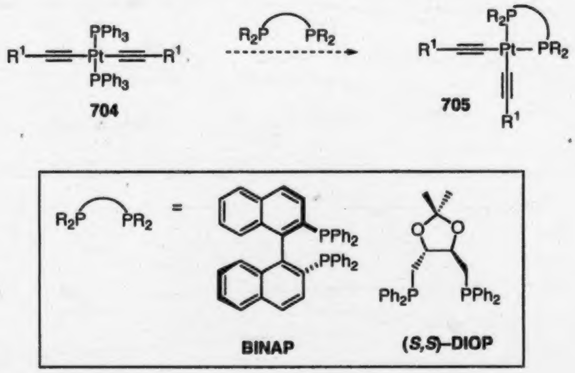
PPh3
R1
Pt
R1
PPh3
704
R2P
PR2
R2P
R1
Pt
PR2
705
R1
R2P
PR2
=
PPh2
PPh2
O
O
Ph2P
PPh2
BINAP
(S,S)–DIOP

Scheme 7.2 Preparation of *cis*–chiral acetylide complexes using alternate chiral diphosphines.

There is also a great deal of synthetic interest in the preparation of chiral oligomers or foldamers. Treatment of an oligomeric or polymeric species such as **706** with a chiral, chelating ligand, should provide access to helical structures (Figure 7.2).

Furthermore, in the presence of an *enantiopure* diphosphine ligand, the helical twist sense may be biased, leading to the formation of a *single* helical enantiomer.

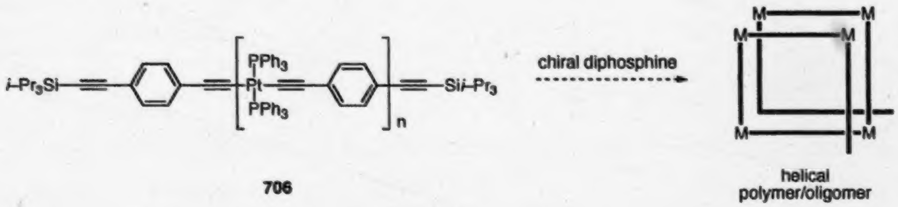
PPh3
Pt
PPh3
i-Pr3Si
Si-i-Pr3
n
706
chiral diphosphine
M
helical
polymer/oligomer

Figure 7.2 Formation of helical secondary structure through treatment of polymer/oligomer **706** with an enantiopure chelating phosphine ligand.

As described in Chapter 6, we are also keenly interested in the development of more robust porous solids. We may be able to take advantage of the propensity of diphosphine ligands to chelate and apply this phenomena to the preparation of even more highly ordered assemblies. For example, the treatment of platinacycle **403a** with tetrakis–diphenylphosphinobenzene **621** should lead to the desired cross–linking at the metal centre (Figure 7.3).

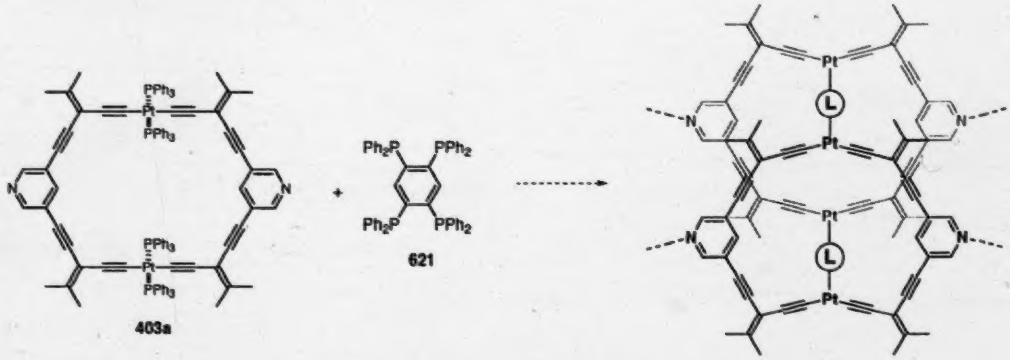
PPh3
Pt
PPh3
N
403a
+
Ph2P
PPh2
621
Pt
L
N

Figure 7.3 Illustration of cross–linking at the platinum acetylide centre.

Finally, several questions remain with respect to the application of ^{129}Xe NMR spectroscopy to the study of porous organic solids. Several additional experiments could be performed that may further support our interpretation of the spectroscopic results. For example, solid–state ^{31}P NMR studies of both solvated and desolvated platinacycles (for example, **402**, **403a** and **403b**), could provide us with a greater understanding of how well the solvated crystal packing diagrams correlate to the solid–state packing of the desolvated species. Additionally, cross–polarization experiments may allow us to more definitively locate the xenon gas within the crystal lattice, and thus further support our interpretations. A particularly intriguing avenue of research is the design of experiments that may help to establish the utility of these porous solids as materials for guest gas encapsulation. For example, quantitative experiments that would allow us to determine the volume of gas present within the solid, as well as gas exchange or competition experiments have been envisioned.

Chapter 8 Experimental Section

8.1 General Details

General Experimental Details.

Column chromatography: Aluminum oxide, neutral, Brockman 1, 150 mesh from *Aldrich Chemical Company, Inc.* (5% water) or silica gel–60 (230–400 mesh) from *General Intermediates of Canada* or *Silicycle*. Thin Layer Chromatography (TLC): Aluminum sheets coated with *aluminum oxide N/UV*$_{254}$ from *Macherey–Nagel* or plastic sheets coated with *silica gel G UV*$_{254}$ from *Macherey–Nagel*: visualization by UV light. Mp.: *Gallencamp* or *Fisher–Johns* apparatus; uncorrected. UV–vis spectra: *Varian Cary 400* at room temperature; λ_{max} in nm (ε in L M^{-1} cm^{-1}). Fluorescence spectra: *Photon Technology International* instrument at room temperature; solvent: dry, degassed CH_2Cl_2. CD spectra: *OLIS DSM 1000* spectrophotometer at room temperature; solvent: dry CH_2Cl_2. IR spectra: *Nic–Plan IR Microscope* (as solids or cast from CH_2Cl_2 as noted). ^{1}H–, ^{13}C–, ^{31}P–, ^{19}F–NMR: *Varian Gemini–300, –400,* or *–500,* and *Bruker–300* instruments at rt in CD_2Cl_2, $CDCl_3$, or C_6D_6; solvent peaks (5.32, 7.24, and 7.15 ppm for ^{1}H and 53.80, 77.00, and 128.0 ppm for ^{13}C, respectively) as reference; $CFCl_3$ as ^{19}F reference and H_3PO_4 as ^{31}P reference. EI MS (70 eV): *Kratos MS 50* instrument. ESI MS (*m/z*): *Micromass Zabspec oaTOF* or *PE Biosystems Mariner TOF* instruments; solvents as noted. MALDI MS (*m/z*): *PE Voyager Elite* instrument in reflectron mode with delayed extraction; matrices as noted; solvent: CH_2Cl_2. Elemental analyses were performed by the Microanalytical Service, Department of Chemistry, University of Alberta.

For IR data, useful functional groups and 3–4 of the strongest absorptions are reported, including but not limited to C–H, C=C and C≡C bond stretches.

For ^{1}H NMR data, coupling constants are expressed in Hertz (Hz) and are considered precise to within ±0.5 Hz. For simplicity, the coupling constants for the aryl protons of *para*–substituted phenyl groups have been reported as pseudo first–order even though they are second order spin systems.

Crystallographic data for unpublished compounds is available from the X–ray Crystallography Laboratory, Department of Chemistry, University of Alberta.

All solvent ratios reported are volume:volume, unless otherwise noted.

Measurements of the third order nonlinear optical second hyperpolarizabilities (γ) were acquired using differential optical Kerr effect (DOKE) detection, as previously reported.[1]

Continuous–flow, hyperpolarized ^{129}Xe NMR spectra were acquired on a *Chemagnetics CMX 200* wide–bore spectrometer operating at a frequency of 55.362366 MHz for ^{129}Xe. Hyperpolarized xenon (~7 % spin polarization) was generated using a home–build continuous–flow optical pumping system. A 60 W dual diode laser from *Coherent Inc.* equipped with a circular polarizer was used to excite the electron spin of rubidium gas. The gas mixture, consisting of 1% Xe (effective pressure 7 torr), 1% N_2, and 98% He, was passed through an O_2 and H_2O filter and bubbled through liquid rubidium and maintained at a temperature of 180 ± 10 °C. The gas flow was then passed through the optical cell (temperature 140 ± 10 °C) located in the fringe field of the magnet where the optical pumping spin–exchange occurred. The extent of polarization was monitored by directly observing the Rb absorption spectrum using an *Ocean Optics USB2000* fiber optics spectrometer. The gas then flowed into a modified *Chemagnetics* 5mm double resonance solenoid probe. The sample temperatures for all spectra were determined using the *Chemagnetics* temperature controller and calibrated using lead nitrate. The spectra were all referenced to the gas peak of ^{129}Xe in the gas mixture (0 ppm) prior to placing samples in the spectrometer. Bloch decay spectra were acquired using $\pi/2$ pulse widths of 2.5 μs.

2D EXSY ($\pi/2$-τ_1-$\pi/2$-τ_{mix}-$\pi/2$) experiments were conducted using a "Hypercomplex" pulse sequence employing mixing times of 1 to 100 msec. Each spectrum consisted of 64 points in the T_1 dimension and 2k points in the T_2 dimension. The spectra were zero–filled to 2k points in the T_1 dimension, processed with 100 Hz of line broadening, and symmetrized in order to overcome distortions caused by T_1 noise.

General Experimental Methods. Reagents were purchased reagent grade from commercial suppliers and used without further purification. THF was distilled from sodium/benzophenone ketyl, and hexanes and CH_2Cl_2 were distilled from CaH_2 immediately prior to use. Compounds **202a–c**,[2] **203**,[3] **208b**,[4] **211**,[5] **214**[6], **301**,[7], **307**,[8] **311**,[9] **319**,[10] *trans*–$PtCl_2(SEt_2)_2$[11], **510**,[12] **609b**[13], and 3–Bromo–5–(trimethylsilyl)ethynylpyridine[14] were prepared as previously reported. All Pd–catalyzed cross–coupling reactions and transmetallation reactions were performed in standard, dry glassware under an inert atmosphere of N_2. A positive pressure of N_2 was essential to the success of all Pd–catalyzed reactions. Degassing of solvents was accomplished by vigorously bubbling N_2 through the solutions for greater than 45 min. Anhydrous $MgSO_4$ was used as the drying agent after aqueous workup. Evaporation and concentration *in vacuo* was achieved at H_2O–aspirator pressure.

General Desilylation Procedure. The appropriate trimethyl–, triethyl–, or triisopropylsilyl–protected polyyne was dissolved in wet THF/MeOH (1:1, 25 mL, for deprotection using K_2CO_3 or NaOH) or wet THF (25 mL, for TBAF deprotection). K_2CO_3 (ca. 0.2 equiv.), NaOH (ca. 2.2 equiv.), or TBAF (ca. 2.2 equiv.) was added, and the resulting solution was stirred, in the presence of air at room temperature, until TLC analysis indicated complete conversion to the desilylated intermediate. Ether (25 mL) was added, and the resulting solution was washed with saturated NH_4Cl (2 × 25 mL) and dried. The solvent was reduced to ca. 1 mL and the deprotected polyyne was carried on, with no further purification.

General Palladium–Catalyzed Cross–Coupling Procedure. The respective terminal acetylene (ca. 0.4 mmol) was combined with the appropriate vinyl triflate or aryl halide species (one equivalent per terminal acetylene) and dissolved in dry THF or DMF (40 mL). Et_2NH (3 mL) was added and the resulting solution was degassed for at least 45 minutes. $Pd(PPh_3)_4$ or $PdCl_2(PPh_3)_2$ (ca. 0.05 equiv. per coupling event) was added and the reaction mixture was stirred at room temperature for 5 minutes. CuI (ca. 0.15 equiv. per coupling event) was added and the reaction mixture was stirred at the temperature indicated in the individual procedure. Reactions performed at elevated temperatures were sealed under N_2 for heating. When TLC analysis indicated full consumption of the starting polyyne, the reaction mixture was cooled to room temperature, ether (25 mL) was added, and the resulting solution was washed with saturated NH_4Cl (2 × 25 mL) and dried. Solvent removal followed by purification via chromatography and/or recrystallization yielded the desired product.

General Copper–Catalyzed Homocoupling Procedure. TMEDA (ca. 20 equiv.) was added to a vial containing CuI or CuCl (ca. 10 equiv.) in CH_2Cl_2 (10 mL). The resulting solution was stirred for 10 minutes and then slowly added (over 5 minutes) to a solution of the appropriate deprotected acetylene (ca. 0.1 mmol) in dry CH_2Cl_2 (250 mL). The reaction was stirred at the temperature indicated in the individual procedure, in the presence of air, until TLC analysis no longer indicated the presence of the deprotected polyyne. Ether (300 mL) was added, and the resulting solution was washed with saturated NH_4Cl (at least 6 × 75 mL), saturated $NaHCO_3$ (2 × 75 mL), brine (2 × 75 mL), and dried.

General Procedure for the Formation of Platinum–Acetylide Complexes. The appropriate terminal acetylene (ca. 0.3 mmol) was dissolved in dry Et_2NH (50 mL) and $PtCl_2(PPh_3)$ or $PtCl_2(PEt_3)_2$ (1 equiv.) was added. The resulting solution was degassed for at least 45 minutes and CuI (ca. 5 equiv.) was added. The reaction mixture was sealed under N_2 and heated at the temperature indicated in the individual procedure until TLC analysis indicated the consumption of all of the deprotected acetylene. After cooling to room temperature, ether (50 mL) and CH_2Cl_2 (50 mL) were added and the resulting solution was washed with water (2 × 75 mL), saturated NH_4Cl (4 × 75 mL), saturated $NaHCO_3$ (2 × 75 mL), brine (2 × 75 mL) and dried. Solvent removal *using no heat* and purification by recrystallization and/or chromatography gave the desired platinum acetylide complex. Macrocyclization reactions were performed at much higher dilution as indicated in the individual procedures.

8.2 Experimental Details for Chapter 2

3,5-Bis(3-adamantylidene-5-trimethylsilyl-1,4-pentadiynyl)benzene (204b).

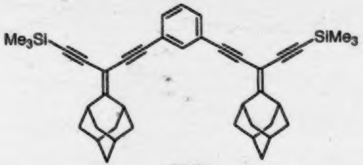

204b

3,5–Diethynylbenzene **203** (43 mg, 0.34 mmol) was cross–coupled with **202b** (0.25 g, 0.64 mmol) in dry, degassed DMF (20 mL) in the presence of $Pd(PPh_3)_4$ (46 mg, 0.040 mmol), CuI (20 mg, 0.010 mmol) and Et_2NH (2 mL) at rt for 1 h as described in the general procedure. Purification by column chromatography on silica (hexanes/CH_2Cl_2 2:1) afforded **204b** (189 mg, 91%) as a colourless solid. Mp 79–82 °C. R_f = 0.51 (hexanes/CH_2Cl_2 2:1). IR (CH_2Cl_2 cast) 2914, 2851, 2204, 2146, 1583, 1476 cm^{-1}; ^1H NMR (300 MHz, CD_2Cl_2) δ 7.58 – 7.57 (m, 1H), 7.45 – 7.42 (m, 2H), 7.36 – 7.31 (m, 1H), 3.35 (s br, 4H), 2.06 – 1.57 (m, 24 H), 0.26 (s, 18H); ^{13}C {^1H} NMR (75 MHz, APT, CD_2Cl_2) δ 172.2, 134.4, 131.2, 128.8, 124.1, 101.1, 96.0, 93.6, 90.1, 86.6, 39.7, 39.6, 37.1, 37.0, 36.9, 28.4, 0.1; ESI MS (MeOH/toluene 3:1, AgOTf added, $C_{42}H_{50}Si_2$) *m/z* (rel. intensity) 717.2 ([M + Ag]$^+$, 100); ESI HRMS calcd. for $C_{42}H_{50}Si_2Ag$ ([M + Ag]$^+$) 717.2502, found 717.2496. .

3,5-Bis(3-diphenylmethylene-5-triethylsilyl-1,4-pentadiynyl)benzene (204c).

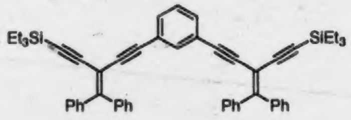

204c

3,5–Diethynylbenzene **203** (47 mg, 0.37 mmol) was cross–coupled with **202c**

(0.35 g, 0.75 mmol) in dry, degassed THF (40 mL) in the presence of $Pd(PPh_3)_4$ (30 mg, 0.026 mmol), CuI (10 mg, 0.053 mmol) and Et_2NH (3 mL) at 50 °C for 14 h as described in the general procedure. Purification by column chromatography on silica (hexanes/CH_2Cl_2 2:1) afforded **204c** (0.28 g, 98%) as a golden oil. R_f = 0.39 (hexanes/CH_2Cl_2 2:1). IR (CH_2Cl_2 cast) 3054, 2954, 2873, 2145, 1592, 1492 cm^{-1}; ^1H NMR (300 MHz, CD_2Cl_2) δ 7.51 – 7.45 (m, 8H), 7.39 – 7.33 (m, 12H), 7.20 – 7.18 (m, 4H), 0.96 (t, J = 7.8 Hz, 18H), 0.60 (q, J = 8.0 Hz, 12H); $^{13}C\{^1H\}$ NMR (125.3 MHz, APT, CD_2Cl_2) δ 157.6, 140.6, 140.4, 134.1, 131.6, 130.7, 130.6, 129.1, 129.0, 128.8, 128.1, 128.0, 123.7, 104.4, 102.1, 96.3, 90.9, 89.7, 7.6, 4.5; A ^{13}C – ^1H gHMQC experiment was also performed; EI HRMS calcd. for $C_{54}H_{54}Si_2$ (M^+) 758.3764, found 758.3789.

Compound 205b.

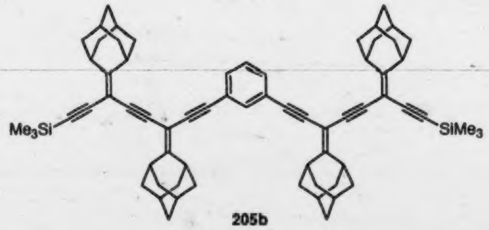

205b

Oligomer **204b** (33 mg, 0.055 mmol) was desilylated by treating with TBAF in wet THF for 30 min as described in the general procedure. Subsequent to aqueous workup, the deprotected polyyne was cross-coupled with **202b** (46 mg, 0.64 mmol) in dry, degassed DMF (10 mL) in the presence of $Pd(PPh_3)_4$ (6.5 mg, 0.0056 mmol), CuI (3.0 mg, 0.016 mmol) and Et_2NH (1.5 mL) at rt for 1 h as described in the general procedure. Purification by column chromatography on silica (hexanes/CH_2Cl_2 2:1) afforded **204b** (33 mg, 65%) as a colourless solid. ^{1}H NMR (300 MHz, CD_2Cl_2) δ 7.58 – 7.57 (m, 1H), 7.45 – 7.42 (m, 2H), 7.36 – 7.31 (m, 1H), 3.39 (s br, 2H), 3.31 (br s, 6H), 2.02 – 1.64 (m, 48 H), 0.25 (s, 18H); ESI MS (MeOH/toluene 3:1, AgOTf added, $C_{68}H_{78}Si_2$) *m/z* (re. intensity) 1057.5 ([M + Ag]$^+$, 100); ESI HRMS calcd. for $C_{68}H_{78}Si_2Ag$ ([M + Ag]$^+$) 1057.4693, found 1057.4701. Compound **205b** was carried on without full characterization.

Attempted synthesis of compound 206b.

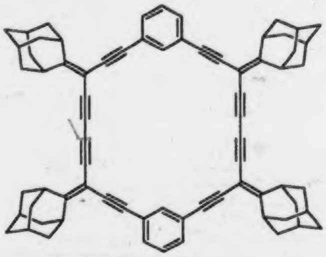

206b

Oligomer **204b** (27 mg, 0.044 mmol) was desilated by treating with TBAF in wet THF/MeOH for 30 min, as described in the general procedure. The resulting deprotected polyyne was treated with CuI (50 mg, 0.26 mmol), TMEDA (0.1 mL, 0.65 mmol) in dry CH_2Cl_2 (80 mL) in the presence of air for 3 days at rt. Workup and solvent reduction led to the precipitation of an insoluble off–white solid. ^{1}H NMR analysis of the crude solid was consistent with a mixture of products, which could not be separated due to insufficient solubility. Macrocycle **206b** was not isolated, nor was confirmation of its presence in the mixture acquired.

Attempted synthesis of compound 207b.

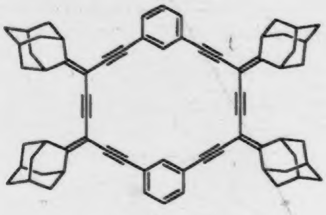

207b

Oligomer **205b** (33 mg, 0.035 mmol) was desilylated by treating with TBAF in wet THF/MeOH for 30 min as described in the general procedure. The resulting deprotected polyyne was dissolved in THF/Et_3N (50 mL, 1:1) and the resulting solution was degassed for 45 min. 1,3–diiodobenzene (9.0 mg, 0.027 mmol) was added, followed by $Pd(PPh_3)_4$ (5.0 mg, 0.0043 mmol) and CuI (<1 mg). The reaction mixture was stirred at rt for 4 days, and upon workup and solvent reduction an off–white precipitate was formed. ^1H NMR analysis of the crude solid was consistent with a mixture of products. ESI MS analysis of the crude mixture showed no evidence of the desired species, compound **207b**. As such, this synthetic sequence was abandoned.

Compound 206c.

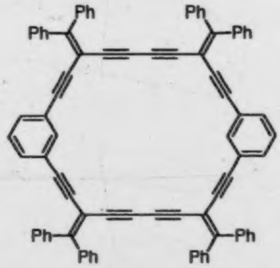

206c

Oligomer **204c** (0.11 g, 0.14 mmol) was desilylated by treating with TBAF for

30 min as described in the general procedure. The resulting deprotected polyyne was oxidatively coupled in the presence of CuI (0.40 g, 2.1 mmol), TMEDA (0.40 mL, 2.6 mmol) and air in dry CH_2Cl_2 (350 mL) for 14 h at rt. Following aqueous workup, the solvent was reduced by approximately 80%, and acetone (3 mL) was added resulting in the formation of a yellow precipitate. Isolation of the precipitate afforded **206c** (29 mg, 39%) as an orange–yellow solid that was not sufficiently soluble for meaningful ^{13}C NMR analysis. Mp 184 °C (dec.). IR (CH_2Cl_2 cast) 3053, (a *very* weak C≡C absorption is observed at ca. 2150), 1595, 1486 cm^{-1}; ^1H NMR (400 MHz, CD_2Cl_2) δ 7.60 (t, *J* = 1.5 Hz, 2H), 7.49 – 7.31 (m, 40H), 7.18 (t, *J* = 7.6 Hz, 2H), 7.01 (dd, *J* = 7.9, 1.6 Hz, 4H); ESI MS (NO_2Me, AgOTf added, $C_{84}H_{48}$) *m/z* (rel. intensity): 1937 ($[M + Ag^+ + 3AgOTf]^+$, 19), 1679 ($[M + Ag^+ + 2AgOTf]^+$, 53), 1421 ($[M + Ag^+ + AgOTf]^+$, 66), 1165 ($[M + Ag]^+$, 100).

1,4-Bis(3-diphenylmethylene-5-triethylsilyl-1,4-pentadiynyl)benzene (209a).

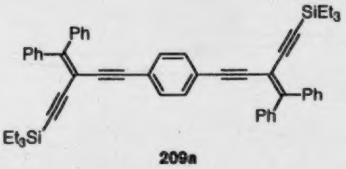

209a

1,4–Diethynylbenzene (40 mg, 0.32 mmol) was cross–coupled with **202c** (0.30 g, 0.64 mmol) in dry, degassed THF (40 mL), in the presence of Et_2NH (3 mL), $Pd(PPh_3)_4$ (30 mg, 0.030 mmol), and CuI (8 mg, 0.04 mmol) as described in the general procedure. The mixture was stirred at 50 °C for 14 h. Solvent removal and purification by column chromatography on silica gel (hexanes/CH_2Cl_2 6:1) afforded **209a** (225 mg, 92%) as a pale yellow solid. Mp 122–124 °C. R_f = 0.31 (hexanes/CH_2Cl_2 6:1). IR

(CH_2Cl_2 cast) 2954, 2910, 2873, 2147, 1504, 1486 cm^{-1}; ^1H NMR (400 MHz, CD_2Cl_2) δ 7.49 – 7.45 (m, 8H), 7.39 – 7.32 (m, 12H), 7.17 (s, 4H), 0.94 (t, J = 7.9 Hz, 18H), 0.59 (q, J = 7.9 Hz, 12H); ^{13}C {^1H} NMR (100 MHz, APT, CD_2Cl_2) δ 157.6, 140.7, 140.4, 131.6, 130.7, 129.1, 129.0, 128.1 (2×), 123.3, 104.4, 102.2, 96.3, 91.6, 91.2, 7.6, 4.5 (one coincident carbon not observed); ^{13}C – ^1H gHMQC and gHMBC experiments were also performed; ESI MS (3:1, MeOH:CH_2Cl_2, $C_{54}H_{54}Si_2$) *m/z* (rel. intensity) 759.4 ([M + H]$^+$, 100); ESI HRMS *m/z* calcd. for $C_{54}H_{55}Si_2$ ([M + H]$^+$) 759.3842, found 759.3824. Anal. Calcd. for $C_{54}H_{54}Si_2 \cdot 0.5H_2O$: C, 84.43; H, 7.22%. Found: C, 84.26; H, 7.17%.

Single crystals suitable for X–ray crystallographic analysis were grown by layering a solution of **209a** in acetone with methanol and allowing diffusion at 4 °C. X–ray crystallographic data for **209a**: $C_{54}H_{54}Si_2$ (formula weight 759.15) crystallized in the triclinic space group $P\bar{1}$ (No. 2) with a = 9.7544(10) Å, b = 10.0136(11) Å, c = 13.1411(14) Å; α = 68.1031(18)°, β = 70.458(2)°, γ = 75.7349(19)°; V = 1111.5(2) Å^3; Z = 1; ρ_{calcd} = 1.134 g cm^{-3}; μ (Mo Kα) = 0.115 mm^{-1}; T = –80 °C; $R_1(F)$ = 0.0442 (3587 reflections with $F_o^2 \geq 2\sigma(F_o^2)$), $wR_2(F^2)$ = 0.1128 for all 4473 unique data.

Compound 209b.

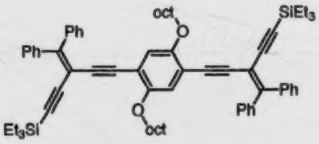

209b

1,4–Diethynyl–2,5–dioctyloxybenzene **208b** (22 mg, 0.057 mmol) was cross–coupled with **202c** (56 mg, 0.12 mmol) in dry, degassed THF (20 mL), in the presence of Et_2NH (2 mL), $Pd(PPh_3)_4$ (20 mg, 0.017 mmol), and CuI (5.0 mg, 0.026 mmol) as described in the general procedure. The mixture was stirred at 60 °C for 48 h. Solvent removal and purification by column chromatography on silica gel (hexanes/CH_2Cl_2 4:1) afforded **209b** (38 mg, 66%) as a pale yellow solid. Mp 76–78 °C. R_f = 0.36 (hexanes/CH_2Cl_2 2:1). IR (CH_2Cl_2 cast) 3054, 2954, 2200, 2145, 1598, 1498 cm^{-1}; ^1H NMR (300 MHz, $CDCl_3$) δ 7.51 – 7.45 (m, 8H), 7.33 – 7.28 (m, 12H), 6.55 (s, 2H), 3.80 (t, J = 6.9 Hz, 4H), 1.69 (p, J = 6.9 Hz, 4H) 1.38 – 1.25 (m, 20H), 0.94 – 0.85 (m, 6H), 0.92 (t, J = 7.9 Hz, 18H), 0.55 (q, J = 7.9 Hz, 12H); $^{13}C\ \{^1H\}$ NMR (100 MHz, $CDCl_3$) δ 156.2, 153.3, 140.4, 140.3, 130.5, 130.4, 128.3, 128.2, 127.6, 117.5, 114.1, 104.3, 102.5, 95.4, 94.2, 88.9, 69.7, 31.9, 29.3 (2×), 29.1, 25.9, 22.7, 14.1, 7.4, 4.2 (one coincident carbon not observed); ESI MS (MeOH/toluene, $C_{70}H_{86}O_2Si_2$) m/z (rel. intensity) 1038 ($[M + Na]^+$, 100).

Compound 210a.

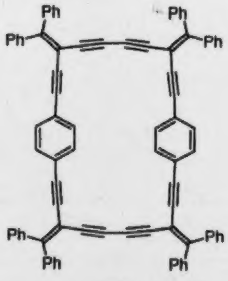

210a

Oligomer **209a** (42 mg, 0.055 mmol) was desilylated by treating with NaOH for 2 h as described in the general procedure. The resulting deprotected polyyne was oxidatively coupled in the presence of CuI (0.10 g, 0.53 mmol), TMEDA (0.20 mL, 1.3 mmol) and air in dry CH_2Cl_2 (180 mL) for 1 h at rt, followed by 14 h at 4 °C.

Following aqueous workup, the solvent was reduced by approximately 80% resulting in the formation of a yellow precipitate. Isolation of the precipitate afforded **210a** (5.0 mg, 17%) as an extremely insoluble yellow solid. Mp 260 °C (dec.). IR (μscope) 3055, 2182, 1950, 1532, 1487 cm^{-1}; ^{1}H NMR (300 MHz, CD_2Cl_2) δ 7.51 – 7.37 (m, 40H), 7.35 (s, 8H); ESI MS ($(MeO)_2CH_2/ClCH_2CH_2Cl$, AgOTf added, $C_{84}H_{48}$) *m/z* (rel. intensity) 1165 ([M + Ag]$^+$, 98).

Compound 210b.

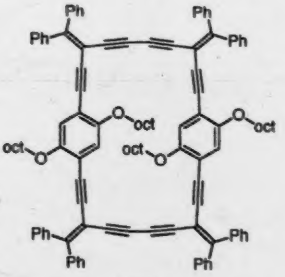

210b

Oligomer **209b** (30 mg, 0.029 mmol) was desilylated by treating with TBAF for 45 min as described in the general procedure. The resulting deprotected polyyne was oxidatively coupled as described in the general procedure in the presence of CuI (75 mg, 0.39 mmol), TMEDA (0.15 mL, 0.98 mmol) and air in dry CH_2Cl_2 (150 mL) for 14 h at rt. Aqueous workup and purification on an alumina column (hexanes/CH_2Cl_2 2:1) afforded **210b** (18 mg, 78%) as a yellow solid. Mp 178–181 °C. R_f = 0.32 (hexanes/CH_2Cl_2 2:1). IR (CH_2Cl_2 cast) 3056, 2924, 2197, 1598, 1496 cm^{-1}; ^{1}H NMR (400 MHz, $CDCl_3$) δ 7.52 –7.47 (m, 8H), 7.43 – 7.36 (m, 8H), 7.34 – 7.27 (m, 24H), 6.72 (s, 4H), 3.74 (t, *J* = 6.7 Hz, 8H), 1.64 – 1.62 (m, 8H), 1.25 – 1.19 (m, 40H), 0.83 (t, *J* = 6.6 Hz, 12H); ^{13}C {^{1}H} NMR (125.7 MHz, $CDCl_3$) δ 155.1, 154.1, 139.9, 139.8, 130.7, 130.5, 129.0, 128.9, 127.9, 127.7, 116.9, 114.3, 101.9, 94.2, 90.3, 83.3, 77.9, 70.2, 32.0, 29.5, 29.4, 29.3, 26.0, 22.8, 14.2; ESI MS (NO_2Me, $C_{116}H_{112}O_4$) *m/z* (rel. intensity) 1593 ([M + Na]$^+$, 42); the base peak could not be identified.

Compound 212.

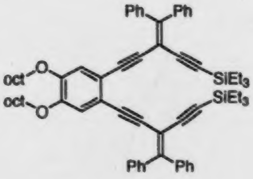

212

1,2–Diethynyl–4,5–dioctyloxybenzene **211** (65 mg, 0.17 mmol) was cross–coupled with **202c** (0.18 g, 0.39 mmol) in dry, degassed THF (80 mL), in the presence of Et_2NH (4 mL), $Pd(PPh_3)_4$ (60 mg, 0.052 mmol), and CuI (15 mg, 0.079 mmol) as described in the general procedure. The mixture was stirred at 40 °C for 14 h. Solvent removal and purification by column chromatography on silica gel (hexanes/CH_2Cl_2 2:1) afforded **212** (60 mg, 35%) as a yellowish oil. R_f = 0.15 (hexanes/CH_2Cl_2 2:1). IR (CH_2Cl_2 cast) 3054, 2954, 2143, 1593, 1507 cm^{-1}; ^{1}H NMR (400 MHz, $CDCl_3$) δ 7.50 – 7.44 (m, 8H), 7.33 – 7.23 (m, 12H), 6.66 (s, 2H), 3.87 (t, *J* = 6.7 Hz, 4H), 1.77 (p, *J* = 6.8 Hz, 4H) 1.46 – 1.21 (m, 20H), 0.97 – 0.84 (m, 6H), 0.89 (t, *J* = 8.1 Hz, 18H), 0.52 (q, *J* = 7.9 Hz, 12H); ^{13}C {^{1}H} NMR (100.6 MHz, $CDCl_3$) δ 156.3, 149.0, 140.6, 140.1, 130.7, 130.5, 128.5, 128.3, 127.7, 127.6, 118.3, 116.5, 104.8, 102.4, 95.6, 90.7, 90.4, 69.2, 31.9, 29.4, 29.3, 29.1, 26.0, 22.7, 14.1, 7.4, 4.3; ESI MS (MeOH/toluene, $C_{70}H_{86}O_2NaSi_2$) *m/z* (rel. intensity) 1037.6 ([M + Na]$^+$, 42); the base peak could not be identified; ESI HRMS calcd. for $C_{70}H_{86}O_2NaSi_2$ ([M + Na]$^+$) 1037.6064, found

1037.6056.

Compound 213.

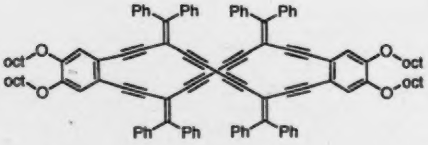

213

Oligomer **212** (30 mg, 0.089 mmol) was desilylated by treating with TBAF for 2 h as described in the general procedure. The resulting deprotected polyyne was oxidatively coupled in the presence of CuCl (0.30 g, 3.0 mmol), TMEDA (0.3 mL, 2.0 mmol) and air in dry CH_2Cl_2 (250 mL) for 48 h at rt as described in the general procedure. Aqueous workup and purification on an alumina column (hexanes/CH_2Cl_2 3:1) afforded **213** (30 mg, 43%) as an amber oil. R_f = 0.25 (hexanes/CH_2Cl_2 2:1). IR (CH_2Cl_2 cast) 2955, 2924, 1594, 1465 cm^{-1}; ^1H NMR (300 MHz, $CDCl_3$) δ 7.59 –7.49 (m, 8H), 7.42 – 7.30 (m, 32H), 6.60 (s, 4H), 3.89 (t, *J* = 6.7 Hz, 8H), 1.77 (p, *J* = 6.7 Hz, 8H), 1.35 – 1.22 (m, 40H), 0.92 – 0.81 (m, 12H); ^{13}C {^1H} NMR (100 MHz, $CDCl_3$) δ 149.3, 147.4, 140.0, 139.3, 130.7, 130.0, 129.0, 128.9, 128.1, 127.7, 118.8, 116.6, 109.8, 103.8, 94.4, 92.5, 88.5, 69.1, 31.8, 29.3 (2×), 29.0, 26.0, 22.7, 14.1; MALDI–TOF MS (dithranol as matrix, $C_{116}H_{112}O_4$) *m/z* (rel. intensity) 1568.8 ($[M^+]$, 13), 784.5 ($[M - C_{58}H_{56}O_2]^+$, 100).

2,6-Bis(3-propylidene-5-trimethylsilyl-1,4-pentadiynyl)pyridine 215a.

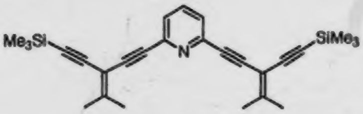

215a

2,6–Diethynyl pyridine **214** (47 mg, 0.37 mmol) was cross–coupled with vinyl triflate **202a** (0.22 g, 0.73 mmol) in dry, degassed THF (40 mL) in the presence of Et$_2$NH (3 mL), Pd(PPh$_3$)$_4$ (30 mg, 0.026 mmol), and CuI (15 mg, 0.079 mmol) for 3 h at room temperature as described in the general procedure. Flash chromatography on silica (hexanes/CH$_2$Cl$_2$ 2:1) yielded **3a** (128 mg, 81%) as a colourless solid. Mp 90–94 °C. $R_f = 0.26$ (hexanes/CH$_2$Cl$_2$ 2:1). IR (μscope) 2961, 2903, 2847, 2204, 2154, 1569, 1557 cm^{-1}; ^{1}H NMR (300 MHz, CD$_2$Cl$_2$) δ 7.6 (app–dd, $J = 7.5$, 8.2 Hz, 1H), 7.36 (app–d, $J = 7.8$ Hz, 2H), 2.13 (s, 6H), 2.10 (s, 6H), 0.22 (s, 18H); ^{13}C {^{1}H} NMR (100 MHz, CD$_2$Cl$_2$) δ 159.1, 144.0, 136.7, 126.3, 101.1 (2×), 97.2, 90.6, 86.3, 23.2, 23.1, 0.0; ESI MS (MeOH/toluene, C$_{27}$H$_{33}$NSi$_2$) *m/z* (rel. intensity) 428.2 ([M + H]$^+$, 100); ESI HRMS *m/z* calcd. for C$_{27}$H$_{34}$NSi$_2$, ([M + H]$^+$) 428.2224, found 428.2227.

Single crystals suitable for X–ray crystallographic analysis were grown by slow evaporation from a solution of **215a** in hexanes at 4 °C. X–ray crystallographic data for **215a**: C$_{27}$H$_{33}$NSi$_2$ (formula weight 427.72) crystallized in the monoclinic space group $P2_1/c$ (No. 14) with $a = 12.1954(12)$ Å, $b = 11.0839(11)$ Å, $c = 20.1834(18)$ Å; $\beta = 95.0252(17)°$; $V = 2717.8(4)$ Å^3; $Z = 4$; $\rho_{\text{calcd}} = 1.045$ g cm^{-3}; μ (Mo Kα) = 0.143 mm^{-1}; $T = -80$ °C; $R_1(F) = 0.0603$ (2598 reflections with $F_o^2 \geq 2\sigma(F_o^2)$), $wR_2(F^2) = 0.1341$ for all 5582 unique data. CCDC no. 218984.

2,6-Bis(3-diphenylmethylene-5-triethylsily-1,4-pentadiynyl)pyridine (215c).

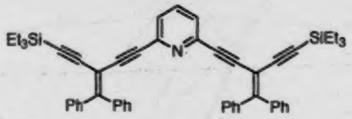

215c

2,6–Diethynyl pyridine **214** (47 mg, 0.37 mmol) was cross–coupled with vinyl triflate **202c** (0.35 g, 0.75 mmol) as described in the general procedure in dry, degassed THF (40 mL) in the presence of Et_2NH (3 mL), $Pd(PPh_3)_4$ (35 mg, 0.030 mmol), and CuI (15 mg, 0.079 mmol) at room temperature for 14 h. Flash chromatography on alumina (hexanes/CH_2Cl_2 2:1) yielded **215c** (0.14 g, 49%) as a pale orange solid. Mp 126–128 °C. R_f = 0.61 (hexanes/CH_2Cl_2 2:1, alumina). IR (CH_2Cl_2 cast) 3055, 2955, 2910, 2874, 2203, 2145, 1557 cm^{-1}; ^1H NMR (400 MHz, CD_2Cl_2) δ 7.51 – 7.47 (m, 9H), 7.40 – 7.34 (m, 12H), 7.05 (app–d, J = 7.8 Hz, 2H), 0.95 (t, J = 7.9 Hz, 18H), 0.60 (q, J = 7.9 Hz, 12H); ^{13}C {^1H} NMR (100 MHz, CD_2Cl_2) δ 159.3, 143.8, 140.5, 140.3, 136.4, 130.7 (2×), 129.2, (2×), 128.2, 128.1, 126.8, 103.8, 101.7, 96.7, 90.5, 88.8, 7.6, 4.5; ESI MS (MeOH/toluene, $C_{53}H_{53}NSi_2$) m/z (rel. intensity) 760.4 ($[M + H]^+$, 100); ESI HRMS m/z calcd. for $C_{53}H_{54}NSi_2$, ($[M + H]^+$) 760.3795, found 760.3794.

Compound 216c.

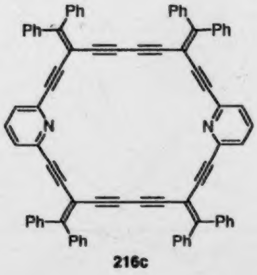

216c

Oligomer **215c** (91 mg, 0.12 mmol) was desilylated by treating with NaOH in wet THF/MeOH (25 mL, 1:1) for 3 hours as described in the general procedure. The resulting deprotected tetrayne was oxidatively homocoupled in the presence of CuCl (250 mg, 2.53 mmol), TMEDA (0.3 mL, 2.0 mmol), and air in CH_2Cl_2 (250 mL) for 3 days as described in the general procedure. Subsequent to work–up, the solvent volume was then reduced to ca. 5 mL and 5 mL of acetone was added. This led to the precipitation and subsequent isolation of macrocycle **216c** (39 mg, 62%) as a bright yellow–orange solid, which was insufficiently soluble for meaningful ^{13}C NMR analysis. Mp 255 °C (dec.). IR (CH_2Cl_2 cast) 3081, 3050, 2214, 1628, 1575, 1559 cm^{-1}; ^1H NMR (400 MHz, CD_2Cl_2) δ 7.49 – 7.32 (m, 42H), 6.91 (app–d, J = 7.9 Hz, 4H); ESI MS (MeOH/toluene, $C_{82}H_{46}N_2$) m/z (rel. intensity) 1081.4 ($[M + Na]^+$, 14), 1059.4 ($[M + H]^+$, 100).

Single crystals suitable for X–ray crystallographic analysis were grown by dissolving **216c** in boiling $CH_2Cl_2/ClCH_2CH_2Cl$ (at 100 °C) and allowing slow evaporation from the resulting solution at room temperature. X–ray crystallographic data for **216c**: $C_{82}H_{46}N_2 \bullet 2(\text{solvent})^*$ (formula weight 1229.06) crystallized in the monoclinic space group $P2_1/n$ (an alternate setting of $P2_1/c$ [No. 14]) with a = 9.7664(9) Å, b = 16.6488(15) Å, c = 20.6911(18) Å; β = 101.1778(19)°; V = 3300.5(5) Å^3; Z = 2; ρ_{calcd} = 1.237 g cm^{-3}; μ (Mo Kα) = 0.227 mm^{-1}; T = –80 °C; $R_1(F)$ = 0.0790 (3035 reflections with $F_o^2 \geq 2\sigma(F_o^2)$), $wR_2(F^2)$ = 0.1734 for all 6749 unique data. CCDC no. 218985.

[*] The co–crystallized solvent molecules were disordered and, as a result, could not be refined. It was not possible to crystallographically distinguish between CH_2Cl_2 and $ClCH_2CH_2Cl$.

2,6-Bis(3-propylidene-5-iodo-1,4-pentadiynyl)pyridine (217a).

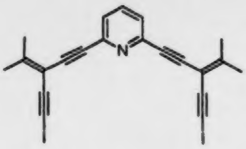

217a

Oligomer **215a** (41 mg, 0.096 mmol) was desilylated by treating with TBAF for 30 min as described in the general procedure. The resulting deprotected polyyne was oxidatively coupled in the presence of CuI (15 mg, 0.079 mmol), TMEDA (0.20 mL, 1.3 mmol) and air in dry CH_2Cl_2 (200 mL) for 14 h at rt. Following aqueous workup and purification via flash chromatography on silica (hexanes/CH_2Cl_2 1:1), oligomer **217a** (17 mg, 33%) was achieved as a tan solid. The melting point was not acquired due to the fact that iodoalkynes are often lachrymators, and, occasionally, explosive upon heating. R_f = 0.27 (hexanes/CH_2Cl_2 1:1). IR (μscope) 3058, 2917, 2213, 2197, 1572, 1552 cm^{-1}; ^1H NMR (300 MHz, CD_2Cl_2) δ 7.63 (app–dd, J = 7.5 Hz, J = 8.2 Hz, 1H), 7.37 (d, J = 7.7 Hz, 2H), 2.15 (two overlapping singlets, 2 × 3H), 2.12 (s, 3H), 2.11 (s, 3H); ^{13}C {^1H} NMR (125.3 MHz, APT, CD_2Cl_2) δ 160.0, 143.9, 136.7, 126.4, 101.4, 90.9, 90.5, 86.1, 23.0 (2×), 8.6; ESI MS (NO_2Me, $C_{21}H_{15}I_2N$) m/z (rel. intensity) 535.9 ($[M + H]^+$, 100).

Single crystals suitable for X–ray crystallographic analysis were grown by layering a solution of **217a** in CH_2Cl_2 with hexanes and allowing diffusion/evaporation at 4 °C. X–ray crystallographic data for **217a**: $C_{21}H_{15}I_2N$ (formula weight 535.14) crystallized in the monoclinic space group $P2_1/c$ (No. 14) with a = 7.9185(5) Å, b = 29.6593(18) Å, c = 9.0763(6) Å; β = 112.2162(11)°; V = 1973.4(2) Å^3; Z = 4; ρ_{calcd} =

1.801 g cm^{-3}; μ (Mo Kα) = 3.189 mm^{-1}; T = –80 °C; $R_1(F)$ = 0.0285 (3573 reflections with $F_o^2 \geq 2\sigma(F_o^2)$), $wR_2(F^2)$ = 0.0764 for all 4022 unique data.

2,6-Bis(3-diphenylmethylene-5-iodo-1,4-pentadiynyl)pyridine (217c).

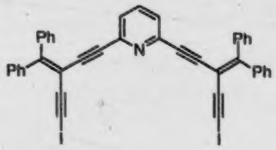

217c

Oligomer **215c** (30 mg, 0.039 mmol) was desilylated by treating with TBAF for 30 min as described in the general procedure. The resulting deprotected polyyne was treated with oxidative coupling conditions: CuI (50 mg, 0.26 mmol), TMEDA (0.10 mL, 0.65 mmol) and air in dry CH_2Cl_2 (125 mL) for 14 h at rt. Following aqueous workup, ESI MS analysis was performed on the crude reaction mixture: ESI MS (NO_2Me, $C_{41}H_{23}I_2N$) *m/z* (rel. intensity) 1059.4 ([**216c** + H]$^+$, 8), 784.5 ([M + H]$^+$, 100).

8.3 Experimental Details for Chapter 3

3,5-Bis(3-propylidene-5-trimethylsilyl-1,4-pentadiynyl)pyridine (302a).

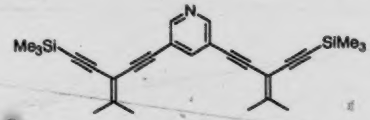

302a

Diethynyl pyridine **301** (0.13 g, 1.0 mmol) was cross–coupled with vinyl triflate **202a** (0.63 g, 2.1 mmol) in dry, degassed THF (80 mL) in the presence of $Pd(PPh_3)_4$ (50 mg, 0.040 mmol), CuI (25 mg, 0.13 mmol) and Et_2NH (4 mL) at rt for 30 min as described in the general procedure. Flash chromatography on alumina (hexanes/CH_2Cl_2

2:1) yielded **302a** (0.36 g, 79%) as a colourless solid. Mp 71–72 °C. R_f = 0.40 (hexanes/CH_2Cl_2 2:1). UV–vis (CH_2Cl_2) 297 (30700) nm; IR (μscope) 2959, 2904, 2210, 2151, 1577 cm^{-1}; ^1H NMR (300 MHz, $CDCl_3$) δ 8.54 (br s, 2H), 7.78 (br s, 1H), 2.08 (s, 12H), 0.21 (s, 18H); ^{13}C {^1H} NMR (75.5 MHz, APT, CD_2Cl_2) δ 158.3, 150.9, 140.3, 120.4, 101.2, 101.2, 97.1, 90.2, 87.5, 23.1, 23.0, 0.0; ESI MS (MeOH/toluene, $C_{27}H_{34}NSi_2$) *m/z* (rel. intensity) 428.2 ($[M + H]^+$, 100); ESI HRMS calcd. for $C_{27}H_{34}NSi_2$ ($[M + H]^+$) 428.2230, found 428.2226.

3,5-Bis(3-adamantylidene-5-trimethylsilyl-1,4-pentadiynyl)pyridine (302b).

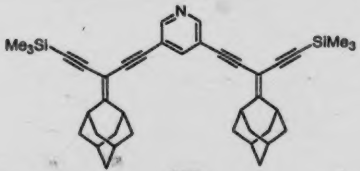

302b

Compound **301** (35 mg, 0.28 mmol) was cross–coupled with **202b** (0.19 g, 0.47 mmol) in dry, degassed THF (20 mL) in the presence of $Pd(PPh_3)_4$ (25 mg, 0.020 mmol), CuI (12 mg, 0.060 mmol) and Et_2NH (2 mL) at rt for 1 h as described in the general procedure. Purification by column chromatography on alumina (hexanes/CH_2Cl_2 1:1) afforded **302b** (113 mg, 67%) as an off–white solid. Mp 181–183 °C. R_f = 0.65 (hexanes/CH_2Cl_2 1:1). UV–vis (CH_2Cl_2) 250 (35600), 305 (32900) nm; IR (μscope) 3037, 2850, 2203, 2152, 1448 cm^{-1}; ^1H NMR (300 MHz, CD_2Cl_2) δ 8.53 (d, *J* = 2.1 Hz, 2H), 7.78 (t, *J* = 2.0, 1H), 3.30 (s br, 4H), 2.02 – 1.80 (m, 24 H), 0.22 (s, 18H); ^{13}C {^1H} NMR (75 MHz, APT, CD_2Cl_2) δ 173.3, 150.7, 140.3, 120.5, 100.7, 96.4, 93.4, 89.8, 87.0, 39.7, 39.6, 37.2, 37.1, 37.0, 28.4, 0.1; ESI MS (MeOH/toluene

3:1, $C_{41}H_{49}NSi_2$) m/z (rel. intensity) 612.3 ($[M + H]^+$, 100); ESI HRMS calcd. for $C_{41}H_{50}NSi_2$ ($[M + H]^+$) 612.3482, found 612.3482.

Single crystals of **302b** suitable for X–ray crystallographic analysis were grown by slow evaporation of a CH_2Cl_2/acetone solution at 4 °C. X–Ray crystallographic data for **302b**: $C_{41}H_{49}NSi_2$ (formula weight 611.99) crystallized in the triclinic space group $P\bar{1}$ (No. 2) with a = 11.8898(8) Å, b = 12.6017(9) Å, c = 12.7275(9) Å; α = 83.4069(15)°, β = 73.8638(14)°, γ = 82.6286(14)°; V = 1810.4(2) Å^3; Z = 2; ρ_{calcd} = 1.123 g cm^{-3}, μ(Mo Kα) = 0.126 mm^{-1}, T = –80 °C, $R_1(F)$ = 0.0573 (4812 reflections with $F_o^2 \geq 2\sigma(F_o^2)$), and $wR_2(F^2)$ = 0.1509 for all 7255 data.

3,5-Bis(3-diphenylmethylene-5-triethylsilyl-1,4-pentadiynyl)pyridine (302c).

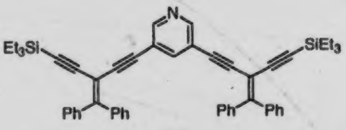

302c

Compound **301** (70 mg, 0.55 mmol) was cross–coupled with vinyl triflate **202c** (0.50 g, 1.1 mmol) in dry, degassed THF (65 mL) in the presence of $Pd(PPh_3)_4$ (35 mg, 0.030 mmol), CuI (20 mg, 0.10 mmol) and Et_2NH (1.5 mL) for 24 h at 55 °C, as described in the general procedure. Subsequent to work–up, flash chromatography on alumina (hexanes/CH_2Cl_2 2:1) yielded **302c** (254 mg, 61%) as a colourless solid. Mp 118–121 °C. R_f = 0.40 (hexanes/CH_2Cl_2 2:1). UV–vis (CH_2Cl_2) 259 (48800), 348 (41700) nm; IR (μscope) 3081, 2910, 2205, 2151, 1536 cm^{-1}; ^{1}H NMR (300 MHz, CD_2Cl_2) δ 8.30 (d, J = 2.0 Hz, 2H), 7.33 – 7.51 (m, 21H), 0.95 (t, J = 7.8 Hz, 18H), 0.60 (q, J = 7.8 Hz, 12H); ^{13}C {^{1}H} NMR (75.5 MHz, APT, CD_2Cl_2) δ 158.6, 151.0, 140.6, 140.2, 140.0, 130.7, 130.6, 129.3, 129.2, 128.2, 128.1 (2×), 104.0, 101.8, 96.7, 92.8, 87.7, 7.6, 4.5; ESI MS (MeOH/toluene, $C_{53}H_{53}NSi_2$) *m/z* (rel. intensity) 760.4 ([M + H]$^+$, 100); ESI HRMS calcd. for $C_{53}H_{54}NSi_2$, ([M + H]$^+$) 760.3795, found 760.3792. Anal. Calcd. for $C_{53}H_{53}NSi_2$: C, 83.74, H, 7.03, N, 1.84. Found: C, 83.56, H, 7.21, N, 1.84.

Single crystals of **302c** suitable for X–ray crystallographic analysis were grown by slow evaporation of an acetone solution at 4 °C. X–Ray crystallographic data for **302c**: $C_{53}H_{53}NSi_2$ (formula weight 760.14) crystallized in the monoclinic space group *C2/c* (No. 15) with a = 20.402(2) Å, b = 11.2543(11) Å, c = 19.6404(19) Å; β = 91.444(2)°; V = 4508.1(8) Å^3; Z = 4; ρ_{calcd} = 1.120 g cm^{-3}; μ(Mo Kα) = 0.114 mm^{-1}; T = –80 °C; $R_1(F)$ = 0.0487 (3128 reflections with $F_o^2 \geq 2\sigma(F_o^2)$), and $wR_2(F^2)$ = 0.1231 for all 4612 data.

Compound 303b.

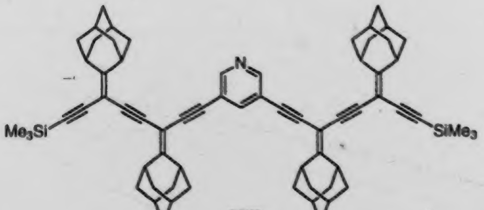

303b

Compound **302b** (0.16 g, 0.26 mmol) was desilylated by treating with TBAF in wet THF for 30 min as described in the general procedure. Subsequent to aqueous workup, the deprotected polyyne was cross–coupled with **202b** (0.20 g, 0.50 mmol) in dry, degassed THF (40 mL) in the presence of $Pd(PPh_3)_4$ (18 mg, 0.030 mmol), CuI (18 mg, 0.090 mmol) and Et_2NH (4 mL) at rt for 1 h as described in the general procedure.

Purification by column chromatography on alumina (hexanes/CH_2Cl_2 2:1) afforded **303b** (161 mg, 66%) as an off–white solid. Mp (dec.) 110 °C. R_f = 0.25 (hexanes/CH_2Cl_2 2:1). UV–vis (CH_2Cl_2) 292 (53600) nm; IR (*μ*scope) 2911, 2850, 2210, 2146, 1575, 1467 cm^{-1}; ^1H NMR (300 MHz, C_6D_6) δ 8.55 (d, *J* = 2.0 Hz, 2H), 7.27 (t, *J* = 2.0 Hz, 1H), 3.63 (br s, 6H), 3.47 (br s, 2H), 2.79 – 1.57 (m, 48 H), 0.19 (s, 18H); ^{13}C {^1H} NMR (75 MHz, APT, CD_2Cl_2) δ 171.6, 170.9, 150.7, 140.3, 120.6, 101.3, 96.0, 93.9, 93.3, 89.9, 87.7, 87.1, 86.9, 39.7, 39.6 (2×), 37.2, 37.1, 37.0, 36.9, 36.8, 28.5, 28.4, 0.1 (2 coincident carbons not observed); ESI MS (MeOH/toluene 3:1, $C_{67}H_{77}NSi_2$) *m/z* (rel. intensity) 952.6 ([M + H]$^+$, 100); ESI HRMS calcd. for $C_{67}H_{78}NSi_2$ ([M + H]$^+$) 952.5673, found 952.5676.

Compound 303c.

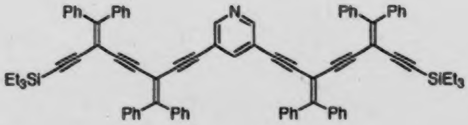

303c

Compound **302c** (75 mg, 0.10 mmol) was dissolved in THF (25 mL) and desilylated by treating with TBAF for 30 min. as described in the general procedure. The deprotected polyyne was cross–coupled with vinyl triflate **202c** (90 mg, 0.19 mmol) in dry, degassed THF (20 mL) in the presence of Et_2NH (2 mL), $Pd(PPh_3)_4$ (20 mg, 0.02 mmol), and CuI (10 mg, 0.05 mmol) for 14 h at 60 °C as describe in the general procedure. Purification by column chromatography on alumina (hexanes/CH_2Cl_2 1:1) afforded **303c** (85 mg, 75%) as a bright yellow solid. Mp 160–163 °C. R_f = 0.40 (hexanes/CH_2Cl_2 1:1). UV–vis (CH_2Cl_2) 343 (53,400), 373 (50,300) nm; IR (μscope) 3080, 3051, 3028, 2954, 2910, 2144, 1599 cm^{-1}; ^{1}H NMR (300 MHz, CD_2Cl_2) δ 8.26 (d, J = 2.0 Hz, 2H), 7.44 – 7.23 (m, 41H), 0.88 (t, J = 7.8 Hz, 18H), 0.54 (q, J = 7.9 Hz, 12H); ^{13}C {^{1}H} NMR (125 MHz, C_6D_6) δ 157.8, 157.0, 151.1, 140.8 (2×), 140.5, 140.3, 139.8, 130.8 (3×), 130.7 (5×), 129.0 (3×), 128.6, 120.2, 104.8, 102.8, 102.2, 95.6, 92.7, 92.0, 90.7, 88.2, 7.7, 4.6; ESI MS (NO_2Me, $C_{85}H_{73}NSi_2$) *m/z* (rel. intensity) 1164.3 ([M + H]$^+$, 100); ESI HRMS *m/z* calcd. for $C_{85}H_{74}NSi_2$ ([M + H]$^+$) 1164.5354, found 1164.5364. Anal. Calcd. for $C_{85}H_{73}NSi_2$•$0.5CH_2Cl_2$•$0.5C_6H_{14}$: C, 85.02; H, 6.53; N, 1.12. Found: C, 85.32; H, 6.29; N, 1.17.

Single crystals of **303c** suitable for X–ray crystallographic analysis were grown by slow diffusion of MeOH into an ether solution at 4 °C. X–Ray crystallographic data for **303c**: $C_{85}H_{73}NSi_2$ (formula weight 1164.62) crystallized in the triclinic space group $P\bar{1}$ (No. 2) with a = 9.5464(11) Å, b = 16.7693(18) Å, c = 22.222(2) Å; α = 80.877(2)°, β = 84.299(2)°, γ = 77.507(2)°; V = 3421.4(7) Å^3; Z = 2; ρ_{calcd} = 1.130 g cm^{-3}; μ(Mo Kα) = 0.097 mm^{-1}; T = –80 °C; $R_1(F)$ = 0.0606 (3156 reflections with $F_o^2 \geq 2\sigma(F_o^2)$), and $wR_2(F^2)$ = 0.1936 for all 13803 data.

Compound 304b.

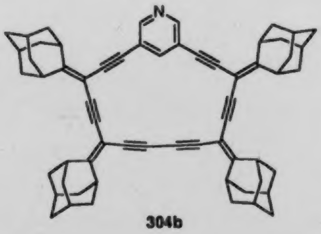

304b

Compound **303b** (0.13 g, 0.14 mmol) was desilylated by treating with TBAF in wet THF for 30 min as described in the general procedure. Subsequent to aqueous workup, the deprotected polyyne was oxidatively homocoupled using CuI (0.60 g, 3.0 mmol) and TMEDA (9.6 mL, 62 mmol) in dry CH_2Cl_2 (350 mL) in the presence of air at rt for 45 min as described in the general procedure. Purification by column chromatography on alumina (hexanes/CH_2Cl_2 2:1) afforded **304b** (85 mg, 75%) as a yellow solid. Mp (dec.) 205 °C. $R_f = 0.30$ (hexanes/CH_2Cl_2 2:1). IR (μscope) 2912, 2851, 2210, 1575, 1467 cm^{-1}; ^1H NMR (300 MHz, CD_2Cl_2) δ 8.5 (d, $J = 2.2$ Hz, 2H), 7.97 (t, $J = 2.2$ Hz, 1H), 3.36 (br s, 2H), 3.29 (br s, 2H), 3.20 (br s, 4H), 2.09 – 1.86 (m, 48 H); $^{13}C\ \{^1H\}$ NMR (75 MHz, CD_2Cl_2,) δ 171.5, 168.9, 148.9, 143.2, 120.7, 93.9, 93.7, 91.1, 88.9, 87.9, 87.6, 78.9, 75.7, 39.8, 39.6, 37.4 (2×), 37.3, 37.1 (2×), 28.5 (4 coincident carbons not observed); ESI MS (MeOH/toluene 3:1, $C_{61}H_{59}N$) *m/z* (rel. intensity) 806.5 ($[M + H]^+$, 100); ESI HRMS calcd. for $C_{61}H_{60}N$ ($[M + H]^+$) 806.4726, found 806.4731.

Compound 304c

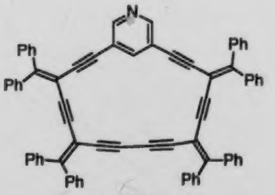

304c

Compound **303c** (26 mg, 0.022 mmol) was desilylated by treating with TBAF in wet THF for 30 min as described in the general procedure. Subsequent to aqueous workup, the deprotected polyyne was oxidatively homocoupled using CuI (75 mg, 0.39 mmol) and TMEDA (0.12 mL, 0.78 mmol) in dry CH_2Cl_2 (100 mL) in the presence of air at rt for 1 h as described in the general procedure. Solvent removal and purification by column chromatography on alumina (hexanes/CH_2Cl_2 1:1) afforded **304c** (11 mg, 53%) as a bright yellow solid. Mp 104 °C (dec.). $R_f = 0.32$ (hexanes/CH_2Cl_2 1:1). IR (μscope) 3052, 3030, 2954, 2925, 2869, 2205, 1577 cm^{-1}; ^1H NMR (300 MHz, CD_2Cl_2) δ 8.21 (d, $J = 2.0$ Hz, 2H), 7.90 (t, $J = 2.0$ Hz, 1H), 7.44 – 7.07 (m, 40H); $^{13}C\ \{^1H\}$ NMR (125 MHz, CD_2Cl_2) δ 159.2, 155.4, 149.8, 142.8, 140.4, 140.2, 139.7, 139.6, 130.8, 130.7, 130.4, 130.3, 129.8, 129.6, 129.5, 129.4, 128.2, 128.1, 120.2, 101.5, 101.0, 93.5, 92.0, 91.0, 88.2, 82.0, 76.0 (two coincident peaks not observed); ESI MS (NO_2Me, $C_{73}H_{43}N$) *m/z* (rel. intensity) 934.4 ($[M + H]^+$, 100); ESI HRMS *m/z* calcd. for $C_{73}H_{44}N$ ($[M + H]^+$) 934.3474, found 934.3475. Anal. Calcd. for $C_{73}H_{43}N \cdot 0.5CH_2Cl_2 \cdot 0.5C_6H_{14}$: C, 90.11; H, 5.04; N, 1.37. Found: C, 90.44; H, 4.80; N, 1.37.

Single crystals of **304c** suitable for X–ray crystallographic analysis were grown by slow evaporation of a CH_2Cl_2/acetone solution at 4 °C. X–Ray crystallographic data for **304c**: $C_{73}H_{43}N \cdot 0.5CH_2Cl_2$ (formula weight 976.55) crystallized in the triclinic space group $P\bar{1}$ (No. 2) with $a = 10.4978(8)$ Å, $b = 17.2773(14)$ Å, $c = 17.4207(14)$ Å; $\alpha = 116.6701(14)°$, $\beta = 95.7338(16)°$, $\gamma = 91.9950(18)°$; $V = 2798.1$ (4) Å^3; $Z = 2$; $\rho_{calcd} = 1.159$ g cm^{-3}; μ (Mo Kα) = 0.112 mm^{-1}; $T = -80$ °C; $R_1(F) = 0.0866$ (5429 reflections with $F_o^2 \geq 2\sigma(F_o^2)$), $wR_2(F^2) = 0.2980$ for all 11265 unique data. CCDC no. 209101.

Compound 305a.

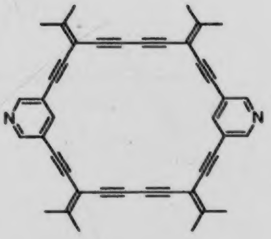

305a not isolated

Oligomer **302a** (0.15 g, 0.36 mmol) was desilylated by treating with methanolic K_2CO_3 for 1 h as described in the general procedure. The deprotected polyyne was then oxidatively homocoupled in the presence of CuI (0.52 g, 2.7 mmol), TMEDA (1.0 mL, 6.6 mmol) and air in dry CH_2Cl_2 (350 mL) for 90 min at rt. Subsequent to aqueous workup, the solvent was removed under reduced pressure to yield an off–white solid. Macrocycle **305a** was not isolated due to the extremely limited solubility of this crude reaction mixture.

Compound 305b.

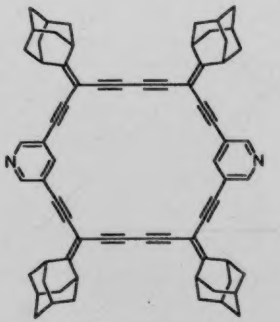

305b not isolated

Oligomer **302b** (30 mg, 0.049 mmol) was desilylated by treating with TBAF for 30 min as described in the general procedure. The deprotected polyyne was then oxidatively coupled in the presence of CuCl (50 mg, 0.51 mmol), DBU (0.50 mL) and O_2 in pyridine (75 mL). The mixture was stirred for 14 h at rt. Ether was added and the resulting solution was washed with satd NH_4Cl (4 × 50 mL) and dried. Removal of the solvent yielded the crude macrocycle **305b** that could not be further purified.

Compound 305c.

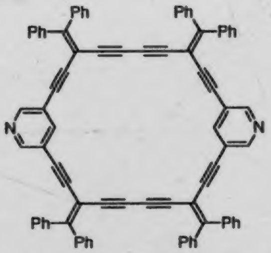

305c

Compound **302c** (82 mg, 0.11 mmol) was desilylated by treating with TBAF for 30 min as described in the general procedure. The resulting deprotected polyyne was oxidatively coupled in the presence of CuI (0.18 g, 0.92 mmol), TMEDA (0.35 mL, 2.3 mmol) and air in dry CH_2Cl_2 (220 mL) for 3 h at rt followed by 12 h at 4 °C. Following aqueous workup, the solvent was reduced by approximately 80%, resulting in the formation of a bright yellow precipitate. Isolation of the precipitate afforded **305c** (29 mg, 51%) as a bright yellow solid that was not sufficiently soluble for meaningful ^{13}C NMR analysis. Mp 172 °C (dec.). UV–vis (CH_2Cl_2) 260 (72600), 362 (88900), 401 (sh, 43400) nm; IR (μscope) 3052, 2210, 1583, 1513 cm^{-1}; ^1H NMR (300 MHz, CD_2Cl_2) δ 8.13 (d, J = 1.9 Hz, 4H),), 7.83 (t, J = 1.9 Hz, 2H), 7.31 – 7.48 (m, 40H); ESI MS (MeOH/toluene, $C_{82}H_{46}N_2$) m/z (rel. intensity) 1059.4 ($[M + H]^+$, 43); ESI HRMS calcd. for $C_{82}H_{47}N_2$ ($[M + H]^+$) 1059.3734, found 1059.3738.

3,5-Bis(3-adamantylidene-5-iodo-1,4-pentadiynyl)pyridine (306).

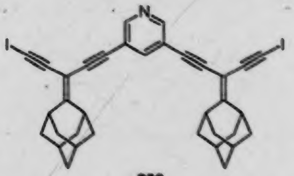

306

Compound **302b** (0.10 g, 0.16 mmol) was desilylated by treating with methanolic K_2CO_3 for 1 h as described in the general procedure. Subsequent to aqueous workup, the deprotected polyyne was treated with CuI (0.20 g, 1.1 mmol) and TMEDA (0.40 mL, 2.6 mmol) in dry CH_2Cl_2 (350 mL) in the presence of air. The reaction mixture was stirred at rt for 2 h, ether was added, and the resulting solution was washed with satd NH_4Cl (6 × 75 mL), dried and the solvent removed *in vacuo*. Purification by column chromatography on silica gel (neat CH_2Cl_2) yielded **306** (49 mg, 42%) as an off–white solid. $R_f = 0.35$ (CH_2Cl_2). IR (μscope) 2921, 2851, 2205, 1703, 1575 cm^{-1}; ^1H NMR (300 MHz, CD_2Cl_2) δ 8.53 (d, $J = 2.1$ Hz, 2H), 7.78 (t, $J = 2.1$ Hz, 1H), 3.28 (br s, 4H), 1.80 – 2.03 (m, 24H); ^{13}C {^1H} NMR (125 MHz, APT, CD_2Cl_2) δ 174.2, 150.6, 140.2, 120.3, 93.6, 89.9, 89.5, 87.3, 39.8, 39.7, 37.1, 37.0, 28.4, 7.8 (one coincident sp^3 peak not observed); ESI MS (NO_2Me, $C_{35}H_{31}NI_2$) *m/z* (rel. intensity) 720.1 ($[M + H]^+$, 100); ESI HRMS calcd. for $C_{35}H_{32}NI_2$ ($[M + H]^+$) 720.0624, found 720.0635.

Compound 308b.

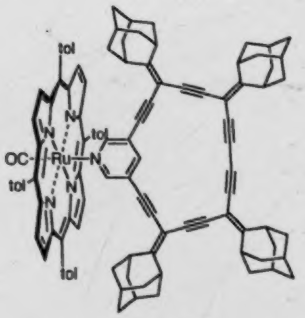

308b

Ruthenium porphyrin **307** (20 mg, 0.025 mmol) was added to a CH_2Cl_2 (2 mL) solution of macrocycle **304b** (17 mg, 0.021 mmol). Flash chromatography on alumina (hexanes/CH_2Cl_2 2:1) yielded assembly **308b** (27 mg, 80%) as a bright red solid. Mp 196 °C (dec.). R_f = 0.33 (hexanes/CH_2Cl_2 2:1). IR (μscope) 3021, 2915, 2852, 2210, 1965, 1721, 1574, 1528 cm^{-1}; ^1H NMR (300 MHz, CD_2Cl_2) δ 8.65 (s, 8H), 8.06 (d, J = 6.8 Hz, 4H), 7.98 (d, J = 7.08 Hz, 4H), 7.53 (br pseudo–t, J = 5.13 Hz, 8H), 6.30 (br s, 1H), 3.03 (br s, 2H), 2.95 (br s, 4H), 2.83 (br s, 2H), 2.68 (s, 12H), 2.14 – 1.64 (m, 48H), 1.26 (br s, 2H); ^{13}C {^1H} NMR (125.7 MHz, APT, $CDCl_3$) δ 181.2 (C≡O), 171.5, 169.3, 144.1, 143.5, 141.4, 140.0, 137.3, 134.7, 134.1, 132.1, 127.6 (2×), 122.0, 118.5, 93.3, 93.2, 90.8, 88.1, 87.4, 85.4, 78.5, 75.4, 39.8, 39.7, 39.5, 39.5, 37.3 (2×), 37.2 (2×), 37.0, 28.5, 28.4 (2 coincident carbons not observed); ^{13}C – ^1H HETCOR (125.7 MHz, CD_2Cl_2) relevant correlations: δ 143.5 ↔ 1.26, 141.4 ↔ 6.30, 132.1 ↔ 8.65; ESI MS (NO_2Me, $C_{110}H_{95}N_5ORu$) m/z (rel. intensity) 1605 ($[M + H]^+$, 47), 807 ($[M - \mathbf{307} + H]^+$, 100).

Compound 308c.

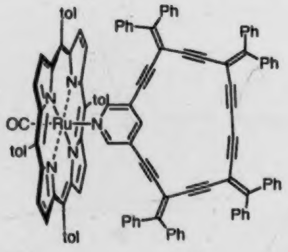

308c

A CD_2Cl_2 (0.50 mL) solution containing ruthenium porphyrin **307** (20 mg, 0.025 mmol) was added dropwise to a CD_2Cl_2 NMR solution of macrocycle **304c** (8 mg, 0.0096 mmol) until ^1H NMR spectroscopic analysis indicated full conversion to **308c**. Solvent reduction and drying yielded assembly **308b** (15 mg, 100%, based on **304c**) as a purple–red solid. Mp shrinks at 138 °C; melts at 210 °C. IR (μscope) 3022, 2923, 2867, 2198, 1951, 1574, 1529 cm^{-1}; ^1H NMR (300 MHz, CD_2Cl_2) δ 8.61 (s, 8H), 8.07 (dd, *J* = 7.6 Hz, 1.6 Hz, 4H), 7.79 (dd, *J* = 7.6 Hz, 1.6 Hz, 4H), 7.55 (d, *J* = 7.9 Hz, 4H), 7.47 (d, *J* = 7.3 Hz, 4H), 7.36 – 7.00 (m, 40H), 6.37 (t, *J* = 1.9 Hz, 1H), 2.68 (s, 12H), 1.19 (d, *J* = 1.9 Hz, 2H); ^{13}C NMR (125.7 MHz, CD_2Cl_2) δ 158.7, 155.7, 144.1, 144.0, 141.7, 140.0, 139.9, 139.7 (3×), 137.3, 134.6, 134.5, 132.2, 130.5, 130.4, 130.3 (2×), 129.9. 129.7, 129.5, 129.4, 128.5, 128.2, 128.1, 127.7, 127.5, 122.0, 118.3, 100.7, 100.5, 92.9, 91.5, 90.3, 85.8, 81.7, 75.7, 21.6 (one coincident carbon not observed; C≡O not observed); ^{13}C – ^1H gHMQC (500 MHz, CD_2Cl_2) relevant correlations: δ 144.1 ↔ 1.19, 132.2 ↔ 8.61; signal to noise ratio was not sufficient to observe correlation to proton at δ 6.37; ^{13}C – ^1H gHMBC (500 MHz, CD_2Cl_2) relevant correlations: δ 141.7, 85.8 ↔ 6.37; ESI MS (CH_3CN/toluene, $C_{122}H_{79}N_5ORu$) *m/z* (rel. intensity) 1733.5 ($[M + H]^+$, 17), 798 ($[\mathbf{307}]^+$, 100).

Compound 309a.

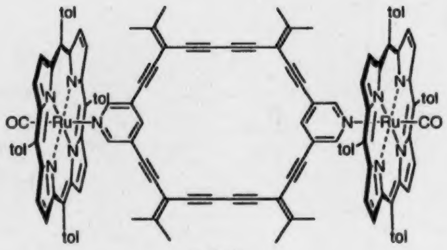

309a

The crude product mixture containing macrocycle **305a** (0.16 g) was added to a solution of ruthenium porphyrin **307** (0.20 g, 0.25 mmol, 2 equivalents based on **302a**) in CH_2Cl_2 (2 mL). Flash chromatography on alumina (hexanes/CH_2Cl_2 1:1) yielded **309a** (0.15 g, 39% overall from **302a**) as a burgundy solid. Mp 132 °C (dec.). UV–vis (CH_2Cl_2) 295 (130900), 414 (519400), 534 (42800); IR (μscope) 3126, 2866, 2210, 1916, 1806, 1575 cm^{-1}; ^{1}H NMR (300 MHz, CD_2Cl_2) δ 8.64 (s, 16H), 8.11 (dd, *J* = 7.8, 1.9 Hz, 8H), 7.90 (dd, *J* = 7.8, 1.9 Hz, 8H), 7.57 (d, *J* = 7.8 Hz, 8H), 7.46 (d, *J* = 7.8 Hz, 8H), 6.04 (t, *J* = 1.7 Hz, 2H), 2.70 (s, 24H), 2.00 (s, 12H), 1.84 (s, 12H), 1.30 (d, *J* = 1.9 Hz, 4H); ^{13}C NMR (125.3 MHz, CD_2Cl_2) δ 181.1 (C≡O), 161.0, 145.1, 144.0, 139.8, 137.8, 137.4, 134.4 (2×), 132.1, 127.6, 127.3, 122.0, 118.1, 99.7, 88.8, 85.5, 78.1, 75.7, 23.5, 23.2, 21.5; ^{13}C – ^{1}H gHMQC (500 MHz, CD_2Cl_2) relevant correlations: δ 145.1 ↔ 1.30, 137.8 ↔ 6.04, 132.1 ↔ 8.64; ESI MS (NO_2Me, $C_{140}H_{102}N_{10}O_2Ru_2$) *m/z* (rel. intensity) 2160 ([M + H]$^+$, 3), 1361 ([M – **307**]$^+$, 21), 798 ([**307**]$^+$, 100), 563 ([**305a** + H]$^+$, 92).

Single crystals of **309a** suitable for X–ray crystallographic analysis were grown by slow evaporation of a crude CH_2Cl_2 solution containing excess porphyrin **307** at 4 °C. X–Ray crystal data for **309a**: $C_{191}H_{144}N_{14}O_4Ru_3$ (formula weight 3002.41) crystallized in the triclinic space group $P\bar{1}$ (No. 2) with a = 16.1421(11) Å, b = 17.1025(11) Å, c = 17.5359(12) Å; α = 90.3641(14)°, β = 100.8011(13)°, γ = 114.5012(14)°; V = 4308.0(5) Å^3; $Z = 1$; ρ_{calcd} = 1.157 g cm^{-1}; μ(Mo Kα) = 0.316 mm^{-1}; T = –80 °C; $R_1(F)$ = 0.0887 (10363 reflections with $F_o^2 \geq 2\sigma(F_o^2)$), $wR_2(F^2)$ = 0.2941 for all 17506 unique data. CCDC nos. 165685 and 179948.

Compound 309c.

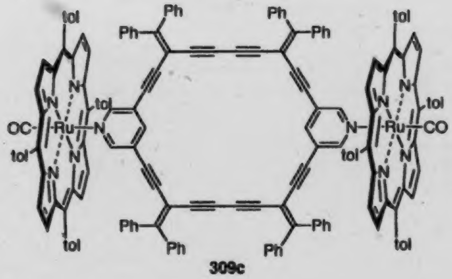

309c

Macrocycle **305c** (10 mg, 0.0090 mmol) was added to a solution of ruthenium porphyrin **307** (15 mg, 0.019 mmol) in CH_2Cl_2 (2 mL) and the product crystallized upon concentration to give **309c** (15 mg, 60%) as a bright red solid. Mp 266 °C (dec.). UV–vis (CH_2Cl_2) 363 (101200), 413 (493200), 533 (36000), 568 (9200) nm; IR (μscope) 3021, 1949, 1529, 1512, 1493 cm^{-1}; ^{1}H NMR (300 MHz, CD_2Cl_2) δ 8.58 (s, 16H), 8.05 (d, J = 7.7 Hz, 8H), 7.76 (d, J = 7.7 Hz, 8H), 7.53 (d, J = 7.7 Hz, 8H), 7.02 – 7.43 (m, 48H), 6.08 (br s, 2H), 2.65 (s, 24H), 1.12 (br s, 4H); ^{13}C {^{1}H} NMR (125.3 MHz, APT, CD_2Cl_2) δ 160.4, 145.3, 143.9, 139.8, 139.6, 139.0, 137.3, 134.5, 134.4, 132.1, 130.5, 130.1, 129.7, 128.3, 128.2, 127.6, 127.5, 117.6, 99.2, 90.5, 85.4, 81.3, 76.4, 21.5 (C≡O peak not observed, two sp^2 CH not observed); ^{13}C –^{1}H gHMQC (500 MHz, CD_2Cl_2) relevant correlations: δ 145.3 ↔ 1.12, 139.8 ↔ 6.08, 132.1 ↔ 8.58; ESI MS

(NO_2Me) *m/z* (rel. intensity) 1856 ([M + H – **307**]$^+$, 4), 1059 ([**305c** + H]$^+$, 34), 770 ([**307** – CO]$^+$, 100); MALDI MS (dithranol as matrix, $C_{180}H_{118}N_{10}O_2Ru_2$) 1829 ([M + H – **307** – CO]$^+$).

Single crystals of **309c** were grown by slow evaporation from a CH_2Cl_2 solution in the presence of *n*–hexadecane. X–ray crystal data for **309c**: $C_{180}H_{118}N_{10}O_2Ru_2 \bullet C_{16}H_{34}$ (formula weight 2881.42) crystallized in the triclinic space group $P\bar{1}$ (No. 2) with a = 13.9983(16) Å, b = 17.099(2) Å, c = 22.220(3) Å; α = 100.949(2)°, β = 96.942(2)°, γ = 113.311(2)°; V = 4680.6 (9) Å^3; Z = 1; ρ_{calcd} = 1.022 g cm^{-3}; μ(Mo Kα) = 0.211 mm^{-1}, T = –80 °C; $R_1(F)$ = 0.1079 (8613 reflections with $F_o^2 \geq 2\sigma(F_o^2)$), and $wR_2(F^2)$ = 0.3587 for all 18770 data. CCDC no. 179949.

Attempted synthesis of compound 310.

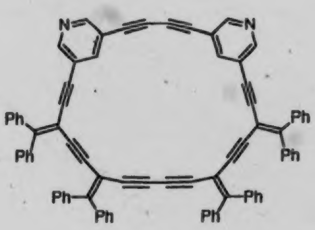

310

Oligomer **318** (7.0 mg, 0.0051 mmol) was desilylated by treating with TBAF in wet THF for 1 h as described in the general procedure. The resulting deprotected polyyne was dissolved in dry CH_2Cl_2 (40 mL) and treated with CuCl (20 mg, 0.20 mmol) in the presence of TMEDA (0.30 mL, 2.0 mmol) and air, as described in the general procedure. After stirring at rt for 3h, TLC analysis indicated the disappearance of all of the oligomeric precursor. After workup and solvent removal a yellow precipitate was formed. MALDI–TOF MS analysis (retinoic acid as matrix) of the crude reaction mixture showed a peak at *m/z* 1060.3 (100%) confirming the presence of **310**. Several higher mass peaks were also observed at *m/z* 2119.4 (33%), 3179.3 (41%), 4238.7 (32%), 5315.1 (27%), and 6360.7 (20%), consistent with oligomeric byproducts. Macrocycle **310** was not isolated in sufficient purity for characterization.

Compound 312.

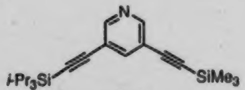

312

3–Bromo–5–(trimethylsilyl)ethynylpyridine (0.38 g, 1.5 mmol) was cross–coupled with TIPS–acetylene (0.42 mL, 0.35 g, 1.9 mmol) in the presence of $PdCl_2(PPh_3)_2$ (0.15 g, 0.21 mmol) and CuI (0.030 g, 0.16 mmol) in dry, degassed THF/Et_3N (80 mL, 1:1) for 14 h at 45 °C as described in the general procedure. Following aqueous workup and solvent reduction, purification on an alumina column (hexanes) led to the isolation of pure **312** (0.53 g, 100%) as a colourless oil. $R_f = 0.08$ (hexanes). IR (CH_2Cl_2 cast) 2943, 2157, 1581, 1463 cm^{-1}; ^{1}H NMR (400 MHz, CD_2Cl_2) δ 8.57 (d, $J = 2.0$ Hz, 1H), 8.55 (d, $J = 2.0$ Hz, 1H), 7.89 (t, $J = 2.0$ Hz, 1H), 1.14 – 1.13 (m, 21H), 0.26 (s, 9H); ^{13}C {^{1}H} NMR (100.6 MHz, CD_2Cl_2) δ 151.8, 151.5, 141.6, 120.4, 120.1, 102.9, 100.9, 99.2, 96.0, 18.7, 11.6, –0.2; EI MS *m/z* (rel. intensity) 355.2 ((M^+), 19), 312.2 ($[M - C_3H_7]^+$, 100); EI HRMS calcd. for $C_{21}H_{33}NSi_2$ (M^+) 355.2152, found 355.2150.

Compound 313.

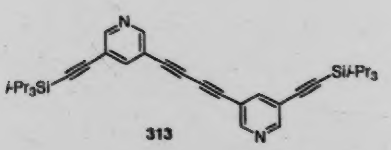

313

Compound **312** (0.30 g, 0.85 mmol) was desilylated by treating with K_2CO_3 in wet THF/MeOH for 1 h as described in the general procedure. The resulting monodeprotected polyyne was oxidatively coupled in the presence of CuCl (0.30 g, 3.2 mmol), TMEDA (0.30 mL, 2.0 mmol) and air in dry CH_2Cl_2 (100 mL) for 1.5 h at rt. Following aqueous workup and solvent reduction, purification on an alumina column (hexanes/CH_2Cl_2 2:1) led to the isolation of pure **313** (0.18 g, 75%) as a colourless solid. Mp 46–48 °C. R_f = 0.32 (hexanes/CH_2Cl_2 2:1). IR (CH_2Cl_2 cast) 2943, 2157, 1579, 1463 cm^{-1}; ^{1}H NMR (400 MHz, CD_2Cl_2) δ 8.65 (pseudo–d, J = 2.0 Hz, 4H), 7.89 (t, J = 2.0 Hz, 2H), 1.17 – 1.13 (m, 42H); ^{13}C {^{1}H} NMR (100.6 MHz, CD_2Cl_2) δ 152.6, 152.0, 142.2, 120.7, 118.5, 102.5, 96.8, 78.9, 76.9, 18.7, 11.6; EI MS *m/z* (rel. intensity) 564.3 ((M$^+$), 20), 521.3 ([M – C_3H_7]$^+$, 100); EI HRMS calcd. for $C_{36}H_{48}N_2Si_2$ (M$^+$) 564.3356, found 564.3364.

Single crystals of **313** were grown by slow evaporation of an acetone solution at 0 °C. X–ray crystallographic data for **313**: $C_{36}H_{48}N_2Si_2$ (formula weight 564.94) crystallized in the triclinic space group *P*I (No. 2) with a = 8.1724(10) Å, b = 14.6539(19) Å, c = 15.925(2) Å; α = 109.945(2)°, β = 94.527(2)°, γ = 96.898(2)°; V = 1765.0(4) Å^3; Z = 2; ρ_{calcd} = 1.063 g cm^{-3}; μ(Mo Kα) = 0.125 mm^{-1}; T = –80 °C; $R_1(F)$ = 0.0553 (4652 reflections with $F_o^2 \geq 2\sigma(F_o^2)$), and $wR_2(F^2)$ = 0.3587 for all 7094 data.

Compound 314.

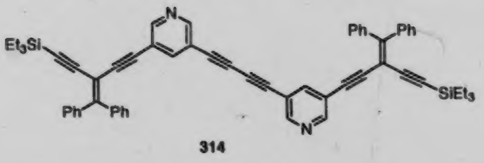

314

Compound **313** (67 mg, 0.12 mmol) was desilylated by treating with TBAF in wet THF as described in the general procedure. The resulting deprotected tetrayne was cross–coupled with vinyl triflate **202c** (0.11 g, 0.24 mmol) in dry, degassed THF (20 mL) in the presence of Pd(PPh_3)$_4$ (18 mg, 0.015 mmol), CuI (4.0 mg, 0.015 mmol) and Et_2NH (2.0 mL). The reaction flask was sealed under N_2 and stirred for 14 h at 45 °C. After workup, evaporation of the solvent and flash chromatography on alumina (hexanes/CH_2Cl_2, 1:1) yielded **314** (35 mg, 33%) as a yellow–brown oily solid. Mp 104–106 °C. R_f = 0.32 (hexanes/CH_2Cl_2 1:1). IR (neat film) 3054, 2954, 2203, 2143, 1578, 1493 cm^{-1}; ^{1}H NMR (300 MHz, CD_2Cl_2) δ 8.61 (d, J = 2.1 Hz, 2H), 8.41 (d, J = 2.0 Hz, 2H), 7.67 (t, J = 2.1 Hz, 2H), 7.52 –7.34 (m, 20H), 0.95 (t, J = 8.1 Hz, 18H), 0.60 (q, J = 7.9 Hz, 12H); ^{13}C NMR (100.6 MHz, CD_2Cl_2) δ 158.9, 152.0 (2×), 141.3, 140.5, 140.1, 130.7, 130.6, 129.3 (2×), 128.2, 128.1, 120.4, 118.6, 103.9, 101.6, 96.9, 93.3, 87.2, 79.0, 76.9, 7.6, 4.5; ESI MS (MeOH/toluene, $C_{62}H_{56}N_2Si_2$) m/z (rel. intensity) 885 ([M + H]$^+$, 100); ESI HRMS calcd. for $C_{62}H_{57}N_2Si_2$, ([M + H]$^+$) 885.4060, found 885.4069.

Attempted synthesis of Compound 315.

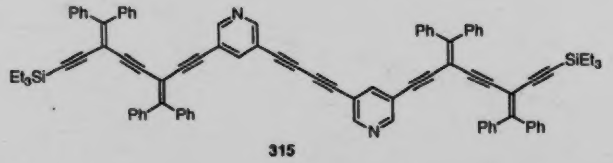

315

Compound **314** (35 mg, 0.040 mmol) was desilylated by treating with TBAF in wet THF as described in the general procedure. The resulting terminal acetylene was cross–coupled with vinyl triflate **202c** (40 mg, 0.096 mmol) in dry, degassed THF (20 mL) in the presence of $Pd(PPh_3)_4$ (20 mg, 0.017 mmol), CuI (4.0 mg, 0.015 mmol) and Et_2NH (2.0 mL). The reaction flask was sealed under N_2 and stirred for 14 h at 45 °C. TLC analysis indicated a mixture of products and, subsequent to an aqueous workup, an alumina column (hexanes/CH_2Cl_2 2:1) was performed in an attempt to isolate **315**. ^1H NMR analysis indicated that **315** was present but impure (~80% pure, 43% yield). Due the low yields of this and prior reactions in the sequence, this synthetic strategy was abandoned.

Compound 316.

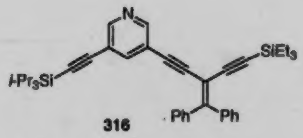

316

Compound **312** (0.13 g, 0.35 mmol) was desilylated by treating with K_2CO_3 in wet THF/MeOH for 1 h as described in the general procedure. The resulting monodeprotected polyyne was cross–coupled with vinyl triflate **202c** (0.17 g, 0.36

mmol) in dry, degassed THF (40 mL) in the presence of $Pd(PPh_3)_4$ (40 mg, 0.034 mmol), CuI (4.0 mg, 0.021 mmol) and Et_2NH (3.0 mL). The reaction flask was stirred under N_2 for 14 h at rt. After workup, evaporation of the solvent and flash chromatography on alumina (hexanes/CH_2Cl_2, 1:1) yielded **316** (0.21 g, 99%) as a brown oil. $R_f = 0.78$ (hexanes/CH_2Cl_2 1:1). IR (CH_2Cl_2 cast) 3055, 2955, 2155, 1581, 1493 cm^{-1}; ^1H NMR (400 MHz, CD_2Cl_2) δ 8.55 (d, J = 2.0 Hz, 1H), 8.36 (d, J = 2.0 Hz, 1H), 7.60 (t, J = 2.1 Hz, 1H), 7.52 –7.50 (m, 2H), 7.46 – 7.40 (m, 2H), 7.40 – 7.34 (m, 6H), 1.17 –1.16 (m, 21H), 0.97 (t, J = 8.1 Hz, 9H), 0.62 (q, J = 7.9 Hz, 6H); ^{13}C {^1H} NMR (100.6 MHz, CD_2Cl_2) δ 158.6, 151.5, 150.9, 141.0, 140.6, 140.1, 130.6 (2×), 129.2, 128.2, 128.1, 120.4, 120.0, 104.0, 103.0, 101.8, 96.7, 96.0, 92.9, 87.7, 18.8, 11.6, 7.5, 4.5 (one coincident carbon not observed); EI MS m/z (rel. intensity) 599.3 ((M^+), 100), 556.3 ($[M - C_3H_7]^+$, 36); EI HRMS calcd. for $C_{40}H_{49}NSi_2$, (M^+) 599.3403, found 599.3403.

Compound 317.

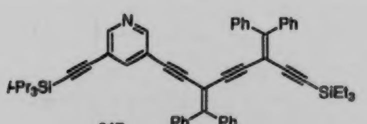

317

Compound **316** (60 mg, 0.10 mmol) was selectively deprotected by treating with NaOH in wet THF/MeOH for 3 h as described in the general procedure. The resulting monodeprotected polyyne was cross–coupled with vinyl triflate **202c** (60 mg, 0.16 mmol) in dry, degassed THF (35 mL) in the presence of $Pd(PPh_3)_4$ (30 mg, 0.026 mmol), CuI (10 mg, 0.053 mmol) and Et_2NH (3.0 mL). The reaction flask was stirred under N_2 for 14 h at rt. After workup, evaporation of the solvent and flash chromatography on alumina (hexanes/CH_2Cl_2 2:1) yielded **317** (39 mg, 49%) as a yellow oil. R_f = 0.32 (hexanes/CH_2Cl_2 2:1). IR (CH_2Cl_2 cast) 3054, 2954, 2147, 1581, 1493 cm^{-1}; ^{1}H NMR (400 MHz, CD_2Cl_2) δ 8.54 (d, J = 2.0 Hz, 1H), 8.28 (d, J = 2.1 Hz, 1H), 7.53 (t, J = 2.1 Hz, 1H), 7.45 – 7.26 (m, 20H), 1.17 – 1.15 (m, 21H), 0.90 (t, J = 7.9 Hz, 9H), 0.58 (q, J = 7.5 Hz, 6H); ^{13}C {^{1}H} NMR (100.6 MHz, CD_2Cl_2) δ 157.8, 157.3, 151.5, 151.0, 141.1, 140.7, 140.5, 140.4, 140.0, 130.7 (2×), 130.6, 130.5, 129.4, 129.2, 129.1, 129.0, 128.2 (3×), 128.0, 120.4, 120.0, 130.9, 103.0, 102.1, 101.6, 96.0 (2×), 92.3, 91.6, 90.1, 87.6, 18.8, 11.6, 7.6, 4.5; ESI MS (MeOH/toluene, $C_{56}H_{60}NSi_2$) m/z (rel. intensity) 802 ([M + H]$^+$, 100); ESI HRMS calcd. for $C_{56}H_{60}NSi_2$, ([M + H]$^+$) 802.4264, found 802.4267.

Compound 318.

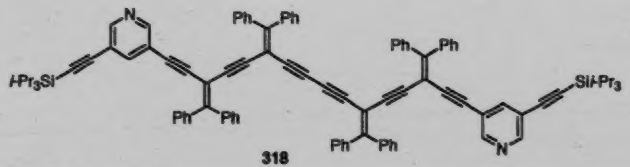

318

Compound **317** (39 mg, 0.049 mmol) was selectively deprotected by treating with NaOH in wet THF/MeOH for 8 h as described in the general procedure. The resulting monodeprotected polyyne was oxidatively homocoupled as described in the general procedure using CuCl (0.10 g, 1.0 mmol) and TMEDA (0.20 mL, 1.3 mmol) in dry CH_2Cl_2 in the presence of air. After stirring at rt for 14 h, flash chromatography on alumina (hexanes/CH_2Cl_2, 1:1), subsequent to an aqueous workup, yielded **318** (17 mg, 51%) as a yellow solid. Mp 162 °C. R_f = 0.26 (hexanes/CH_2Cl_2 1:1). IR (CH_2Cl_2 cast)

3058, 2924, 2372, 2345, 2322, 1582 cm^{-1}; ^{1}H NMR (400 MHz, CD_2Cl_2) δ 8.54 (d, *J* = 2.0 Hz, 2H), 8.28 (d, *J* = 2.0 Hz, 2H), 7.53 (t, *J* = 2.0 Hz, 2H), 7.45 – 7.24 (m, 40H), 1.15 (br s, 42H); ^{13}C {^{1}H} NMR (125.2 MHz, APT, CD_2Cl_2) δ 159.3, 158.1, 151.5, 150.9, 141.1, 140.5, 140.1 (2×), 139.8, 130.8, 130.7, 130.6, 130.5, 129.7, 129.6, 129.3, 128.4, 128.3 (2×), 128.2, 120.4, 120.0, 103.0, 101.3, 101.1, 96.1, 92.1, 91.2, 90.4, 87.9, 81.4, 77.0, 18.8, 11.7 (one coincident carbon not observed); ESI MS (MeOH/toluene, $C_{100}H_{88}N_2Si_2$) *m/z* (rel. intensity) 1412.7 ([M + K]$^+$, 7); 1396.7 ([M + Na]$^+$, 10); 1374.7 ([M + H]$^+$, 100).

Compound 320.

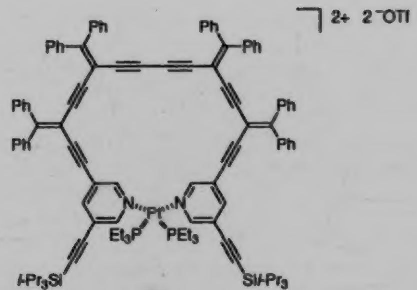

320

Oligomer **318** (10 mg, 0.0073 mmol) was dissolved in CD_2Cl_2 and placed in an NMR tube. *Cis*–$Pt(OTf)_2(PEt_3)_2$ (5.0 mg, 0.0069 mmol) dissolved in CD_2Cl_2 was slowly added to the NMR tube until ^{1}H NMR spectroscopic analysis indicated full conversion of **318** to **320**. Solvent removal and drying allowed for the isolation of pure **320** (15 mg, 100%) as a yellow solid. Mp 155 °C (dec.). IR (CH_2Cl_2 cast) 3056, 2942, 2208, 1579, 1492 cm^{-1}; ^{1}H NMR (300 MHz, CD_2Cl_2) δ 9.17 (br s, 2H), 8.67 (br s, 2H), 7.38 – 7.20 (m, 42H), 1.88 – 1.78 (br m, 12H), 1.30 – 1.17 (m, 18H) 1.16 – 1.14 (m, 42H); ^{13}C {^{1}H} NMR (100.6 MHz, APT, CD_2Cl_2) δ 161.3, 159.4, 150.2, 148.5, 147.0, 139.6, 138.9, 138.7 (2×), 130.5, 130.2, 130.1, 130.0, 129.9, 129.7, 129.4, 129.2, 128.1, 127.8, 127.7, 127.5, 124.7, 124.1, 120.4 (q, *J* = 320 Hz, *C*F$_3$), 101.9, 99.1, 99.0, 98.1, 97.4, 88.7, 87.7, 83.5, 81.5, 75.7, 18.2, 15.2 – 14.9 (m), 10.7, 7.9; ^{31}P {^{1}H} NMR (161.9 MHz, CD_2Cl_2) δ –3.94 (pseudo–t, $^1J_{P-Pt}$ = 3206 Hz); ESI MS (NO_2Me, $C_{114}H_{118}F_6N_2O_6P_2PtSi_2S_2$) *m/z* (rel. intensity) 1954 ([M – ($^-$OTf)]$^+$, 7); 902 ([M – 2($^-$OTf)]$^{2+}$, 100).

8.4 Experimental Details for Chapter 4

Compound 402.

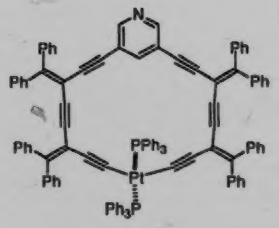

402

Oligomer **303c** (30 mg, 0.026 mmol) was desilylated by treating with TBAF in wet THF and stirring at rt for 30 min, as described in the general procedure. The deprotected polyyne was dissolved in Et_2NH (40 mL) and *trans*–$PtCl_2(PPh_3)_2$ (20 mg, 0.025 mmol) was added. The solution was degassed for ca. 1 h and then a catalytic amount of CuI (5 mg, 0.016 mmol) was added. The sealed reaction vessel was stirred at 40 °C for 14 h, cooled to rt, ether (100 mL) added, and the organic solution washed with H_2O (2 × 50 mL), sat'd NH_4Cl (5 × 50 mL) and dried ($MgSO_4$). Solvent removal and purification by column chromatography on silica gel (hexanes/CH_2Cl_2 1:3) afforded platinaycle **402** (30 mg, 70%) as a bright yellow solid. Mp 248 °C. R_f = 0.37 (hexanes/CH_2Cl_2 1:3). IR (CH_2Cl_2 cast) 3052, 2085, 1574, 1482, 1435 cm^{-1}; ^{1}H

NMR (400 MHz, CD_2Cl_2) δ 7.93 (d, $J = 2.0$ Hz, 2H), 7.78 – 7.72 (m, 12H), 7.66 (t, $J = 2.0$ Hz, 1H), 7.48 – 6.86 (m, 58H); $^{13}C\ \{^1H\}$ NMR (125 MHz, CD_2Cl_2) δ 154.4, 151.6, 144.7, 141.5, 141.3, 141.2, 139.7, 138.4, 135.1 (pseudo–t, $J_{C\text{-}P} = 6.2$ Hz), 131.5 (pseudo–t, $J_{C\text{-}P} = 29$ Hz), 130.9, 130.5, 130.3, 130.2, 129.2, 129.0, 128.3 (pseudo–t, $J_{C\text{-}P} = 5.2$ Hz), 128.2, 127.9, 127.8, 127.3, 127.2, 120.5, 119.9 (t, $^2J_{C\text{-}P} = 15$ Hz), 113.7, 106.9, 102.7, 97.0, 93.9, 89.3, 87.8, (two coincident peaks not observed); $^{31}P\ \{^1H\}$ NMR (162 MHz, CD_2Cl_2) δ 20.0 ($^1J_{P\text{-}Pt} = 2610$ Hz). ESI MS (MeOH/toluene/CH_2Cl_2 9:3:1, $C_{109}H_{73}NP_2P$) *m/z* (rel. intensity) 1676.4 ($[M + Na]^+$, 100), 1654.4 ($[M + H]^+$, 82). Anal. Calcd for $C_{109}H_{73}NP_2Pt{\bullet}0.5CH_2Cl_2{\bullet}0.5C_6H_{14}$: C, 77.69; H, 4.69; N, 0.81. Found: C, 77.80; H, 4.63; N, 0.83.

Single crystals of **402** suitable for X–ray crystallographic analysis were grown by slow evaporation of a CH_2Cl_2/acetone solution at 4 °C. X–ray crystallographic data for **402**: $C_{109}H_{73}NP_2Pt{\bullet}0.5CH_2Cl_2{\bullet}$acetone (formula weight 1754.25) crystallized in the triclinic group $P\bar{1}$ (No. 2) with $a = 14.6025(13)$ Å, $b = 17.2169(15)$ Å, $c = 20.0200(17)$ Å; $\alpha = 107.5427(17)^\circ$, $\beta = 109.1503(16)^\circ$, $\gamma = 94.3186(16)^\circ$; $V = 4448.0\ (7)$ Å^3; $Z = 2$; $\rho_{calcd} = 1.310$ g cm^{-3}; μ (Mo Kα) = 1.695 mm^{-1}; $T = -80$ °C; $R_1(F) = 0.0571$ (13339 reflections with $F_o^2 \geq 2\sigma(F_o^2)$), $wR_2(F^2) = 0.1520$ for all 18125 unique data. CCDC no. 209102.

Compound 403a.

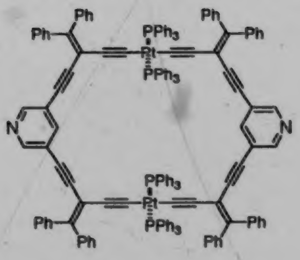

403a

Oligomer **302c** (62 mg, 0.082 mmol) was deprotected by treating with NaOH in THF/MeOH for 4 h as described in the general procedure. The resulting deprotected alkyne was added, with no further purification, to a degassed solution of $(PPh_3)_2PtCl_2$ (65 mg, 0.082 mmol) in Et_2NH (150 mL). A catalytic amount of CuI (5 mg, 0.03 mmol) was added and the mixture was stirred at 50 °C for 14 h. Ether/CH_2Cl_2 (150 mL, 1:1 v/v) were added, and the resulting solution was washed with water (2 × 50 mL), sat'd NH_4Cl (4 × 50 mL) and dried ($MgSO_4$). Solvent removal (using *no* heat) followed by precipitation from CH_2Cl_2/acetone afforded platinacycle **403a** (45 mg, 45%) as a bright yellow solid. Mp 166 °C (dec.). $R_f = 0.08$ (hexanes/CH_2Cl_2 1:1, alumina). IR (CH_2Cl_2 cast) 3050, 2201, 2083, 1581, 1481 cm^{-1}; ^1H NMR (400 MHz, CD_2Cl_2) δ 7.77 (d, J = 2.0 Hz, 4H), 7.65 – 7.59 (m, 24H), 7.42 – 7.37 (m, 12H), 7.35 (t, J = 2.0 Hz, 2H), 7.31 – 6.82 (m, 64H); $^{13}C\{^1H\}$NMR (125 MHz, CD_2Cl_2) δ 150.3, 149.1, 142.3, 140.6, 139.1, 135.4 (pseudo–t, $J_{C\text{-}P}$ = 6.2 Hz), 131.2 (pseudo–t, $J_{C\text{-}P}$ = 29 Hz), 130.9, 130.8, 130.4, 128.2 (pseudo–t, $J_{C\text{-}P}$ = 6.6 Hz), 127.8 (2×), 127.5, 127.2, 120.7, 118.9 (signal too weak to observe P or Pt coupling), 111.2 (signal too weak to observe P or Pt coupling), 105.9, 95.7, 85.5; $^{31}P\{^1H\}$ NMR (162 MHz, CD_2Cl_2) δ 18.0 (coupling to Pt not observed due to poor signal/noise); ESI MS ($NO_2Me/ClCH_2CH_2Cl$, $C_{154}H_{106}N_2P_4Pt_2$) m/z (rel.

intensity) 2498.7 ($[M + H]^+$, 100).

Single crystals of **403a** suitable for X–ray crystallographic analysis were grown by slow evaporation/diffusion of a $CH_2Cl_2/ClCH_2CH_2Cl$/acetone solution at 4 °C. X–ray crystallographic data for **403a**: $C_{154}H_{106}N_2P_4Pt_2 \cdot 2.5ClCH_2CH_2Cl$ (formula weight 2745.85) crystallized in the triclinic group $P\bar{1}$ (No. 2) with a = 12.8940(5) Å, b = 14.4595(6) Å, c = 19.9990(9) Å; α = 104.9381(8)°, β = 97.9082(8)°, γ = 99.8794(8)°; V = 3483.9(3) Å^3; Z = 1; ρ_{calcd} = 1.309 g cm^{-3}; μ (Mo Kα) = 2.198 mm^{-1}; T = –80 °C; $R_1(F)$ = 0.0517 (12208 reflections with $F_o^2 \geq 2\sigma(F_o^2)$), $wR_2(F^2)$ = 0.1589 for all 13938 unique data.

Compound 403b.

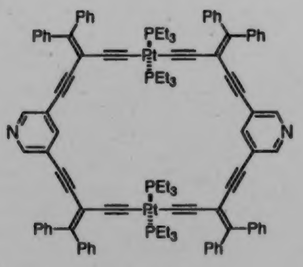

403b

Oligomer **302c** (50 mg, 0.066 mmol) was deprotected by treating with NaOH in THF/MeOH for 4 h as described in the general procedure. The resulting deprotected alkyne was added, with no further purification, to a degassed solution of $(PEt_3)_2PtCl_2$ (33 mg, 0.066 mmol) in Et_2NH (120 mL). A catalytic amount of CuI (5 mg, 0.03 mmol) was added and the mixture was stirred at 40 °C for 14 h. Ether/CH_2Cl_2 (150 mL, 1:1 v/v) were added, and the resulting solution was washed with water (2 × 50 mL), sat'd

NH_4Cl (4 × 50 mL) and dried ($MgSO_4$). Solvent removal (using *no* heat) followed by purification using a gradient ($CH_2Cl_2 \rightarrow$ acetone) silica gel column afforded platinacycle **403b** (45 mg, 71%) as a pale yellow solid. Mp 280 °C (dec.). $R_f = 0.06$ (CH_2Cl_2). IR (CH_2Cl_2 cast) 3051, 2927, 2147, 2081, 1580, 1491 cm^{-1}; ^1H NMR (400 MHz, CD_2Cl_2) δ 8.00 (d, $J = 2.0$ Hz, 4H), 7.51 – 7.26 (m, 42H), 1.88 – 1.83 (br m, 24H), 1.10 – 1.00 (pseudo–pentet, $J = 8.1$ Hz, 36H); ^{13}C {^1H} NMR (100.6 MHz, CD_2Cl_2) δ 151.1, 150.9, 142.0, 137.8, 130.6, 130.5, 128.0 (3×), 127.7, 120.7, 116.0 (t, $^1J_{C-P} = 15$ Hz), 107.3, 106.1, 95.4, 85.5, 16.7 (pseudo–t, $J_{C-P} = 17$ Hz), 8.7 (one coincident carbon not observed); ^{31}P {^1H} NMR (162 MHz, CD_2Cl_2) δ 13.9 ($^1J_{P-Pt} = 2344$ Hz); ESI MS ($NO_2Me/ClCH_2CH_2Cl$, $C_{106}H_{106}N_2P_4Pt_2$) *m/z* (rel. intensity) 1923 ($[M + H]^+$, 100).

Single crystals of **403b** suitable for X–ray crystallographic analysis were grown by slow evaporation of a CH_2Cl_2/acetone solution at 4 °C. X–ray crystallographic data for **403b**: $C_{106}H_{106}N_2P_4Pt_2 \bullet CH_2Cl_2$ (formula weight 2006.91) crystallized in the monoclinic group *Ia* (an alternate setting of *Cc* [No. 9])) with $a = 29.555(2)$ Å, $b = 13.1084(11)$ Å, $c = 26.278(2)$ Å; $\beta = 105.498(8)^\circ$; $V = 9810.3(14)$ Å^3; $Z = 4$; $\rho_{calcd} = 1.359$ g cm^{-3}; μ (Mo Kα) = 3.015 mm^{-1}; $T = -80$ °C; $R_1(F) = 0.0531$ (15052 reflections with $F_o^2 \geq 2\sigma(F_o^2)$), $wR_2(F^2) = 0.1249$ for all 18646 unique data.

Compound 404.

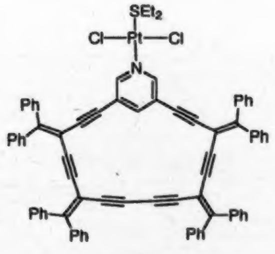

404

Macrocyclic ligand **304c** (20 mg, 0.021 mmol) was dissolved in CH_2Cl_2 (20 mL) and *trans*–$PtCl_2(SEt_2)_2$ (7.8 mg, 0.018 mmol) was added. The reaction mixture was stirred at rt overnight. Solvent removal and purification by column chromatography on silica gel (neat CH_2Cl_2) afforded complex **404** (9.0 mg, 40%) as an orange solid. Mp 238 °C (dec.). R_f = 0.93 (neat CH_2Cl_2). IR (CH_2Cl_2 cast) 3080, 3052, 2967, 2928, 2211, 1958, 1584, 1486 cm^{-1}; ^1H NMR (400 MHz, CD_2Cl_2) δ 8.46 (d, J = 1.8 Hz, 2H), 7.99 (t, J = 1.8 Hz, 1H), 7.46 – 7.05 (m, 40H), 3.05 – 2.90 (br m, 2H), 2.73 – 2.58 (br m, 2H), 1.47 (t, J = 7.4 Hz, 6H); ^{13}C {^1H} NMR (125 MHz, CD_2Cl_2) δ 159.4, 156.7, 151.7, 144.8, 140.2 (2×), 139.8, 139.4, 130.8, 130.7, 130.5, 130.4, 129.9, 129.8, 129.7, 129.5, 128.3, 128.2 (2×), 122.3, 101.0, 100.9, 95.6, 91.6, 91.3, 86.0, 82.0, 76.0, 31.1, 12.6 (one coincident peak not observed); ESI MS (NO_2Me, AgOTf added, $C_{77}H_{53}Cl_2NPtS$) *m/z* (rel. intensity) 2688 ($[2M + Ag]^+$, 41), 1042 ([**304c** + Ag]$^+$, 51), 934 ([**304c** + H]$^+$, 49). Anal. Calcd for $C_{77}H_{53}Cl_2NPtS{\bullet}H_2O$: C, 70.69; H, 4.24; N, 1.07. Found: C, 70.49; H, 3.97; N, 1.05.

Single crystals of complex **404** were grown by slow evaporation of a $CHCl_3$ solution at room temperature. X–ray crystallographic data for complex **404**: $C_{77}H_{53}Cl_2NPtS{\bullet}1/3CHCl_3$ (formula weight 1330.03) crystallized in the monoclinic group $P2_1/n$ (an alternate setting of $P2_1/c$ [No. 14]) with a = 19.9238(15) Å, b = 17.3126(13) Å, c = 20.0804(15) Å; β = 106.9222(13)°; V = 6626.5(9) Å^3; Z = 4; ρ_{calcd} = 1.333 g cm^{-3}; μ (Mo Kα) = 2.312 mm^{-1}; T = –80 °C; $R_1(F)$ = 0.0802 (9989 reflections with $F_o^2 \geq 2\sigma(F_o^2)$), $wR_2(F^2)$ = 0.2327 for all 13527 unique data. CCDC no. 209103.

Compound 405.

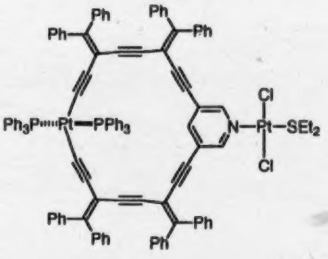

405

Platinacycle **402** (36 mg, 0.022 mmol) was dissolved in CH_2Cl_2 (25 mL) and an excess of *trans*–$PtCl_2(SEt_2)_2$ (81 mg, 0.18 mmol) was added. The reaction mixture was stirred at rt for 2 days. Solvent removal and purification by column chromatography on silica gel (neat CH_2Cl_2) afforded complex **405** (27 mg, 62%) as an orange solid. Mp 196 °C (dec.). R_f = 0.59 (hexanes/CH_2Cl_2 1:3). IR (CH_2Cl_2 cast) 3052, 2926, 2205, 2084, 1576, 1482, 1435 cm^{-1}; ^{1}H NMR (400 MHz, CD_2Cl_2) δ 8.16 (d, J = 1.8 Hz, 2H), 7.77 – 7.70 (m, 12H), 7.61 (t, J = 1.8 Hz, 1H), 7.54 – 6.86 (m, 58H), 3.13 – 2.98 (br m, 2H), 2.75 – 2.56 (br m, 2H), 1.57 (t, J = 7.4 Hz, 6H); ^{13}C {^{1}H} NMR (100 MHz, CD_2Cl_2) δ 155.6, 153.4, 144.8 (pseudo–t, J_{C-P} = 1.6 Hz), 141.4, 141.1, 140.9, 139.8, 139.4, 135.1 (pseudo–t, J_{C-P} = 6.2 Hz), 131.3 (pseudo–t, J_{C-P} = 29 Hz), 130.8, 130.6, 130.5, 130.3, 130.2, 129.5, 129.4, 128.5, 128.3 (pseudo–t, J_{C-P} = 5.4 Hz), 128.2, 127.9 (2×), 127.3, 127.2, 122.5, 120.0 (t, $^2J_{C-P}$ = 15 Hz), 113.6 (t, $^3J_{C-P}$ = 2.5 Hz), 106.7 (t,

$^4J_{C\text{-}P}$ = 2.0 Hz), 102.1, 97.5, 96.0, 88.9, 85.6, 31.2, 12.7; ^{31}P {^{1}H} NMR (162 MHz, CD_2Cl_2) δ 20.0 ($^1J_{P\text{-}Pt}$ = 2604 Hz); ESI MS ($CH_2(OMe)_2$, AgOTf added, $C_{113}H_{83}Cl_2NP_2Pt_2S$) *m/z* (rel. intensity) 2116 ($[M + Ag]^+$, 100). Anal. Calcd for $C_{113}H_{83}Cl_2NP_2Pt_2S{\bullet}CH_2Cl_2$: C, 65.36; H, 4.09; N, 0.67. Found: C, 65.17; H, 3.95; N, 0.68.

Single crystals of **405** were grown by slow evaporation of a CH_2Cl_2/acetone solution at rt. X–ray crystallographic data for complex **405**: $C_{113}H_{83}Cl_2NP_2Pt_2S{\bullet}3CH_2Cl_2$ (formula weight 2264.66) crystallized in the triclinic group $P\bar{1}$ (No. 2) with a = 15.0241(11) Å, b = 18.4070(13) Å, c = 20.9726(15) Å; α = 64.8410(10)°, β = 88.1120(10)°, γ = 72.132(2)°; V = 4964.4(6) Å^3; Z = 2; ρ_{calcd} = 1.515g cm^{-3}; μ (Mo Kα) = 3.134 mm^{-1}; T = –80 °C; $R_1(F)$ = 0.0382 (15112 reflections with $F_o^2 \geq 2\sigma(F_o^2)$), $wR_2(F^2)$ = 0.0950 for all 19877 unique data. CCDC no. 209104.

Compound 406.

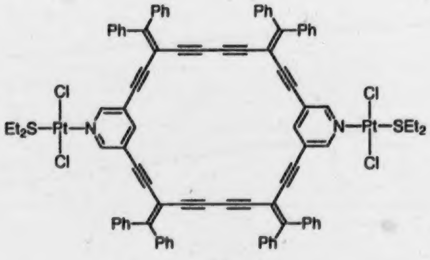

406

Macrocyclic ligand **305c** (32 mg, 0.030 mmol) was dissolved in CH_2Cl_2 (20 mL) and *trans*–$PtCl_2(SEt_2)_2$ (54 mg, 0.12 mmol) was added. The reaction mixture was stirred at room temperature for four days. Solvent removal and purification by column chromatography on silica gel (CH_2Cl_2) afforded complex **406** (26 mg, 49%) as a bright yellow solid. Mp 65 °C (dec.). R_f = 0.73 (neat CH_2Cl_2). IR (μscope) 3083, 2957, 2923, 2854, 2210, 1585 cm^{-1}; ^1H NMR (300 MHz, CD_2Cl_2) δ 8.43 (d, J = 1.8 Hz, 4H), 7.90 (t, J = 1.7 Hz, 2H), 7.50 – 7.33 (m, 40H), 3.12 – 2.92 (br m, 4H), 2.74 – 2.56 (br m, 4H), 1.52 (t, J = 7.4 Hz, 12H); ^{13}C {^1H} NMR (125.7 MHz, CD_2Cl_2) δ 162.4, 153.1, 141.2, 139.8, 139.5, 130.7 (2×), 130.2, 130.0, 128.5, 128.3, 122.0, 99.9, 93.6, 86.1, 81.3, 77.1, 30.1, 12.7; ESI MS (NO_2Me, AgOTf added, $C_{90}H_{66}Cl_4N_2Pt_2S_2$) m/z (rel. intensity) 1879 ($[M + Ag]^+$, 100), 992 ($[M + 2Ag]^{+2}$, 77).

8.5 Experimental Details for Chapter 5

Compound 508.

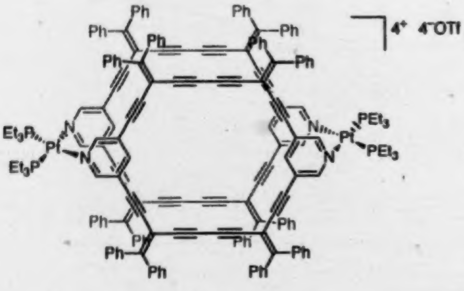

508

Cis-$(TfO)_2Pt(PEt_3)_2$ **319** (8 mg, 0.01 mmol) and macrocycle **305c** (6 mg, 0.006 mmol) were each dissolved in 10 mL of dry CH_2Cl_2. The solution containing the ligand was slowly added to the metal solution and the reaction was stirred at room temperature, under a positive pressure of N_2, for 18 h. A second equivalent of macrocycle **305c** (6 mg, 0.006 mmol) was dissolved in dry CH_2Cl_2 (10 mL) and added to the reaction. The mixture was stirred for a further 18 h and the majority of the solvent was then allowed to evaporate, yielding bright orange crystals, assembly **508** (17 mg, 84% yield). Mp 245 °C (dec.). IR (μscope) 3503, 3058, 2970, 2932, 2215, 1583, 1520

cm^{-1}; ^1H NMR (300 MHz, CD_2Cl_2) δ 8.42 (m, 8H), 7.95 (t, J = 1.7 Hz, 4H), 7.46 – 7.26 (m, 80H), 1.90 – 1.72 (m, 24H), 1.22 – 1.11 (m, 36H); $^{13}C\{^1H\}$ NMR (125.3 MHz, CD_2Cl_2) δ 163.6, 150.2, 145.1, 139.7, 139.1, 131.1, 130.7, 130.3, 130.1, 128.4, 128.3, 125.1, 99.2, 96.2, 84.1, 81.1, 77.5, 15.9 –15.5 (m), 3.3 (CF_3 not observed); $^{31}P\{^1H\}$ NMR (162 MHz, CD_2Cl_2) –1.3 ppm; ^{19}F NMR (400 MHz, CD_2Cl_2) –78.2 ppm; ESI MS (CH_2Cl_2/NO_2Me, $C_{192}H_{152}F_{12}N_4O_{12}P_4Pt_2S_4$) *m/z* (rel. intensity) 1059 ([**305c** + H]$^+$, 9), 745 ([M – 4($^-$OTf)]$^{+4}$, 24), 492 ([**319** –2 ($^-$OTf) + NO_2Me]$^+$, 78), 429 ([**319** – 2($^-$OTf)]$^+$, 100).

Single crystals of **508** were grown by slow evaporation of a $CH_2Cl_2/ClCH_2CH_2Cl$ solution at room temperature. X–ray crystallographic data for complex **508**: $C_{192}H_{152}F_{12}N_4O_{12}P_4Pt_2S_4 \bullet 8ClCH_2CH_2Cl$ (formula weight 4369.09) crystallized in the triclinic group $P\bar{1}$ (No. 2) with a = 13.252(2) Å, b = 20.821(3) Å, c = 21.983(3) Å; α = 102.407(3)°, β = 102.973(3)°, γ = 95.742(3)°; V = 5701.9(15) Å^3; Z = 1; ρ_{calcd} = 1.272 g cm^{-3}; μ (Mo Kα) = 1.540 mm^{-1}; T = –80 °C; $R_1(F)$ = 0.1216 (15230 reflections with $F_o^2 \geq 2\sigma(F_o^2)$), $wR_2(F^2)$ = 0.3645 for all 23153 unique data. CCDC no. 205116.

Attempted synthesis of compound 511.

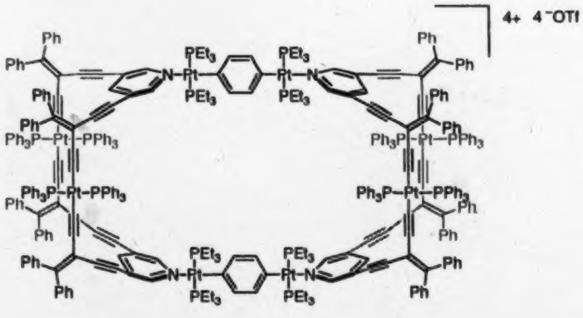

511

Platinacycle **403a** (10 mg, 0.0040 mmol) was dissolved in CD_2Cl_2 (ca. 0.5 mL) and was slowly added, over a period of 2 days, to an NMR tube containing a CD_2Cl_2 solution of **510** (5.5 mg, 0.0044 mmol). Solvent removal led to the formation of an orange solid (15 mg), which was only tentatively identified as **511**, due to inconclusive MS analysis. IR (CH_2Cl_2 cast) 3054, 2964, 2203, 2086, 1580, 1482 cm^{-1}; ^1H NMR (400 MHz, CD_2Cl_2) δ 7.67 – 7.62 (m, 52H), 7.45 – 7.41 (m, 32H), 7.34 – 7.27 (m, 72H), 7.17 – 7.13 (m, 16H), 7.09 – 7.04 (m, 16H), 6.98 – 6.94 (m, 16H), 6.91 – 6.88 (m, 16H), 1.33 – 1.24 (m, 48H), 1.12 – 1.02 (m, 72H); ^{13}C NMR (125 MHz, CD_2Cl_2) δ 152.0, 150.6, 142.2, 139.8, 136.7 (br), 135.4 (pseudo–t, $J_{C\text{-}P}$ = 6.3 Hz), 131.2 (pseudo–t, $J_{C\text{-}P}$ = 29 Hz), 131.0, 130.8, 130.3, 128.3 (pseudo–t, $J_{C\text{-}P}$ = 5.1 Hz), 127.9, 127.4, 125.0, 121.5 (q, $^1J_{C\text{-}F}$ = 321 Hz, CF_3), 104.7, 99.8, 82.3, 13.0 –12.7 (m), 8.1 (6 carbon resonances not observed); ^{31}P {^1H} (162 MHz, CD_2Cl_2) δ 18.0 (pseudo–t, $^1J_{P\text{-}Pt}$ = 2614 Hz), 14.4 (pseudo–t, $^1J_{P\text{-}Pt}$ = 2707 Hz); ESI MS (CH_2Cl_2/NO_2Me) *m/z* (rel. intensity) 3472.8 ([**403a** + **510** – 2($^-$OTf) + ($^-$Cl)]$^+$, 27), 2968.4 ([**403a** + 2(**510**) – 2($^-$OTf)]$^{2+}$, 48), 1718.9 ([**403a** + **510** – 2($^-$OTf)]$^{2+}$, 37), 973.3 ([**510** – 2($^-$OTf) + ($^-$Cl)]$^+$, 100).

8.6 Experimental Details for Chapter 6

Trans–$(Ph_3P)_2Pt(C{\equiv}CSi\textit{i}\text{–}Pr_3)_2$ (602a).

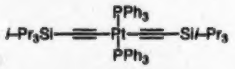

$$i\text{-}Pr_3Si{-}C{\equiv}C{-}\overset{PPh_3}{\underset{PPh_3}{Pt}}{-}C{\equiv}C{-}Si\,i\text{-}Pr_3$$

602a

An excess of triisopropylsilylacetylene (112 mg, 0.615 mmol) was added to a degassed solution of $PtCl_2(PPh_3)_2$ (114 mg, 0.144 mmol) in Et_2NH (50 mL). A catalytic amount of CuI (5 mg, 0.03 mmol) was added and the mixture was stirred at rt for 12 h and then heated to 50 °C for 4 h. Ether/CH_2Cl_2 (100 mL, 1:1 v/v) were added, and the resulting solution was washed with water (2 × 50 mL), sat'd NH_4Cl (4 × 50 mL) and dried ($MgSO_4$). Solvent removal and subsequent precipitation from concentrated CH_2Cl_2 afforded **602a** (121 mg, 78%) as an off–white solid. Mp 205 °C (dec.). $R_f = 0.68$ (hexanes/CH_2Cl_2 2:1, alumina). IR (μscope) 3079, 3052, 2939, 2887, 2859, 2031, 1573, 1481 cm^{-1}; ^1H NMR (400 MHz, CD_2Cl_2) δ 7.85 – 7.80 (m, 12H), 7.38 – 7.31 (m, 18H), 0.57 (d, J = 7.3 Hz, 36H), 0.37 (septet, J = 7.3 Hz, 6H); ^{13}C $\{^1H\}$ NMR (100 MHz, APT, CD_2Cl_2) δ 135.4 (pseudo–t, $J_{C\text{-}P}$ = 6.3 Hz), 132.7 (pseudo–t, $J_{C\text{-}P}$ = 29 Hz), 130.3, 128.9 (t, $^1J_{C\text{-}P}$ = 15 Hz), 128.1 (pseudo–t, $J_{C\text{-}P}$ = 5.3 Hz), 112.5, 18.8, 12.0; ^{31}P $\{^1H\}$ NMR (162 MHz, CD_2Cl_2) δ 21.2 (pseudo–t, $^1J_{P\text{-}Pt}$ = 2719 Hz); ESI MS ($NO_2Me/ClCH_2CH_2Cl$, $C_{58}H_{72}P_2PtSi_2$) m/z (rel. intensity) 1082 ($[M + H]^+$, 14), 900 ($[M - CCSi(i\text{–}Pr)_3 + H]^+$, 100); ESI HRMS m/z calcd. for $C_{58}H_{73}Si_2P_2Pt$ ($[M + H]^+$) 1082.4374, found 1082.4373. Anal. Calcd. for $C_{58}H_{72}P_2PtSi_2$: C, 64.36, H, 6.70. Found: C, 64.05, H, 6.64.

Single crystals of **602a** suitable for X–ray crystallography were grown by slow evaporation from a CD_2Cl_2 solution at room temperature. X–Ray crystallographic data for **602a**: $C_{58}H_{72}P_2PtSi_2$ (formula weight 1082.37) crystallized in the triclinic space group $P\bar{1}$ (No. 2) with a = 9.0547(6) Å, b = 11.6651(8) Å, c = 14.2860(10) Å; α = 67.069(1)°, β = 87.606(1)°, γ = 75.287(1)°; V = 1341.36(16) Å^3; Z = 1; ρ_{calcd} = 1.340 g cm^{-3}; μ(Mo Kα) = 2.755 mm^{-1}; T = –80 °C; $R_1(F)$ = 0.0308 (5376 reflections with $F_o^2 \geq 2\sigma(F_o^2)$), and $wR_2(F^2)$ = 0.0804 for all 5385 data. CCDC no. 210797.

Trans–**$(Ph_3P)_2Pt(C≡C$-*p*–CN–$C_6H_4)$ (602b).**

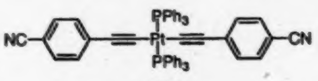

602b

Trimethylsilylethynylbenzonitrile (60 mg, 0.30 mmol) was deprotected by treating with NaOH in THF/MeOH (20 mL) for 1 h as described in the general procedure. The resulting deprotected alkyne was added, with no further purification, to a degassed solution of $PtCl_2(PPh_3)_2$ (120 mg, 0.152 mmol) in Et_2NH (50 mL). A catalytic amount of CuI (5 mg, 0.03 mmol) was added and the mixture was stirred at 50 °C for 14 h. Ether/CH_2Cl_2 (100 mL, 1:1 v/v) were added, and the resulting solution was washed with water (2 × 50 mL), sat'd NH_4Cl (4 × 50 mL) and dried ($MgSO_4$). Solvent removal and subsequent precipitation from concentrated CH_2Cl_2 afforded **602b** (90 mg, 62%) as an off–white solid. Mp 228 °C (dec.). R_f = 0.25 (CH_2Cl_2, silica). IR (CH_2Cl_2 cast) 3053, 2223, 2105, 1595, 1495 cm^{-1}; ^{1}H NMR (400 MHz, CD_2Cl_2) δ 7.80 – 7.75 (m, 12H), 7.47 – 7.38 (m, 18H), 7.19 (d, J = 8.6 Hz, 4H), 6.31 (d, J = 8.6 Hz, 4H); ^{13}C

$\{^1H\}$ NMR (100 MHz, APT, CD_2Cl_2) δ 135.1 (pseudo–t, $J_{C\text{-}P} = 6.0$ Hz), 133.2 (t, $^4J_{C\text{-}P} = 1.3$ Hz), 131.3, 131.2 (t, $^5J_{C\text{-}P} = 1.3$ Hz), 131.1 (pseudo–t, $J_{C\text{-}P} = 29$ Hz), 130.9 (pseudo–t, $J_{C\text{-}P} = 1.0$ Hz), 128.3 (pseudo–t, $J_{C\text{-}P} = 5.4$ Hz), 119.6, 119.3 (t, $^2J_{C\text{-}P} = 15$ Hz), 112.8 (t, $^3J_{C\text{-}P} = 2.3$ Hz), 107.8; $^{31}P\ \{^1H\}$ NMR (162 MHz, CD_2Cl_2) δ 19.8 (pseudo–t, $^1J_{P\text{-}Pt} =$ 2601 Hz); ESI MS ($NO_2Me/ClCH_2CH_2Cl$, $C_{54}H_{38}N_2P_2Pt$) *m/z* (rel. intensity) 1004 ([M + H^+ + MeOH]$^+$, 100); ESI HRMS *m/z* calcd. for $C_{55}H_{43}N_2OP_2Pt$ ([M + H^+ + MeOH]$^+$) 1004.2494, found 1004.2499. Anal. Calcd. for $C_{54}H_{38}N_2P_2Pt{\bullet}CH_2Cl_2$: C, 62.51, H, 3.81, N, 2.65. Found: C, 63.28, H, 3.64, N, 2.62.

Single crystals of **602b** for X–ray crystallography were grown by layering a CH_2Cl_2 solution with hexanes and allowing slow diffusion at 4 °C. X–Ray crystallographic data for **602b**: $C_{54}H_{38}N_2P_2Pt{\bullet}2CH_2Cl_2$ (formula weight 1141.75) crystallized in the monoclinic space group $P2_1/c$ (No. 14) with $a = 13.3751(7)$ Å, $b = 11.1464(6)$ Å, $c = 16.6531(9)$ Å; $\beta = 94.9834(10)°$; $V = 2473.3(2)$ Å^3; $Z = 2$; $\rho_{\text{calcd}} = 1.533$ g cm^{-3}; μ(Mo Kα) = 3.157 mm^{-1}; $T = -80$ °C; $R_1(F) = 0.0329$ (4258 reflections with $F_o^2 \geq 2\sigma(F_o^2)$), and $wR_2(F^2) = 0.0947$ for all 5050 data. CCDC no. 210798.

***Trans*–(Ph$_3$P)$_2$Pt(C≡Cpyr–*meta*–(C≡CSi*i*–Pr$_3$))$_2$ (602c).**

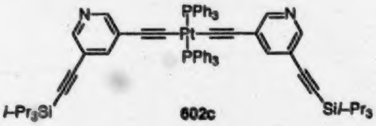

602c

3–(Trimethylsilylethynyl)–5–(triisopropylsilylethynyl)pyridine (28 mg, 0.079 mmol) was mono–deprotected by dissolving in THF/MeOH (20 mL) and treating with

K_2CO_3 (10 mg). After stirring at rt for 2h, ether (15 mL) was added and the resulting solution was washed with sat'd NH_4Cl (2 × 15 mL), dried over $MgSO_4$ and the solvent was removed. The resulting deprotected alkyne was added, with no further purification, to a degassed solution of $PtCl_2(PPh_3)_2$ (31 mg, 0.039 mmol) in Et_2NH (40 mL). A catalytic amount of CuI (3 mg, 0.02 mmol) was added and the mixture was stirred at 50 °C for 14 h. Ether/CH_2Cl_2 (100 mL, 1:1 v/v) were added, and the resulting solution was washed with water (2 × 50 mL), sat'd NH_4Cl (4 × 50 mL) and dried ($MgSO_4$). Solvent removal and purification via column chromatography (neat CH_2Cl_2, alumina) afforded **602c** (38 mg, 76%) as an off–white solid. Mp 190 °C (dec.). R_f = 0.78 (neat CH_2Cl_2, alumina). IR (CH_2Cl_2 cast) 3056, 2942, 2864, 2155, 2106, 1573, 1463 cm^{-1}; ^1H NMR (400 MHz, CD_2Cl_2) δ 8.17 (br d, J = 1.5 Hz, 2H), 7.82 – 7.77 (m, 12H), 7.47 – 7.40 (m, 20H), 6.50 (t, J = 2.0 Hz, 2H), 1.13 (s, 42H); $^{13}C\{^1H\}$ NMR (100 MHz, APT, CD_2Cl_2) δ 150.8, 148.2, 140.6, 135.3 (pseudo–t, J_{C-P} = 6.0 Hz), 131.4 (pseudo–t, J_{C-P} = 29 Hz), 131.0, 128.4 (pseudo–t, J_{C-P} = 5.3 Hz), 124.5, 119.3, 117.1 (t, $^2J_{C-P}$ = 15 Hz), 109.0, 104.1, 93.9, 18.8, 11.7; $^{31}P\{^1H\}$ NMR (162 MHz, CD_2Cl_2) δ 19.9 (pseudo–t, $^1J_{P-Pt}$ = 2607 Hz); ESI MS ($NO_2Me/ClCH_2CH_2Cl$, $C_{72}H_{78}N_2P_2PtSi_2$) *m/z* (rel. intensity) 1285.5 ($[M + H]^+$, 100).

Single crystals of **602c** suitable for X–ray crystallographic analysis were grown by layering a CH_2Cl_2 solution with hexanes and allowing slow diffusion at 4 °C. X–ray crystallographic data for **602c**: $C_{72}H_{78}N_2P_2PtSi_2$ (formula weight 1284.57) crystallized in the triclinic space group $P\bar{1}$ (No. 2) with a = 11.5751(12) Å, b = 16.4187(17) Å, c = 17.9730(19) Å; α = 79.1095(18)°, β = 72.4028(17)°, γ = 86.4749(17)°; V = 3197.2(6) $Å^3$; Z = 2; ρ_{calcd} = 1.334 g cm^{-3}; μ(Mo Kα) = 2.324 mm^{-1}; T = –80 °C; $R_1(F)$ = 0.0410

(10087 reflections with $F_o^2 \geq 2\sigma(F_o^2)$), and $wR_2(F^2) = 0.0900$ for all 13055 data.

Compound 607.

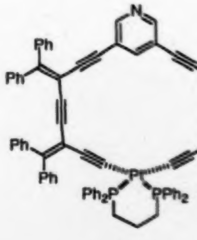

607

Bis(diphenylphosphino)propane (2.2 mg, 0.0054 mmol) was added to a solution of platinacycle **402** (18 mg, 0.011 mmol) in CH_2Cl_2 (2 mL) and the mixture was stirred at rt for 14 h. Solvent removal followed by plugging through silica gel (hexanes/CH_2Cl_2 1:3 → acetone) afforded an orange solid. Mass spectral analysis suggested the presence of **607**: ESI MS (NO_2Me, AgOTf added) *m/z* (rel. intensity) 3191 ($[2M + Ag]^+$, 6), 1649 ($[M + Ag]^+$, 100). This complex was neither isolated nor characterized.

Compound 608.

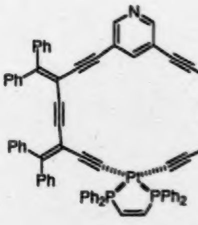

608

Cis–1,2–bis(diphenylphosphino)ethylene (6 mg, 0.02 mmol) was added to a solution of platinacycle **402** (25 mg, 0.015 mmol) in CH_2Cl_2 (2 mL) and the mixture was stirred at rt for 14 h. Solvent removal followed by purification via column

chromatography (hexanes/CH_2Cl_2 1:2, alumina) afforded **608** (20 mg, 87%) as a bright yellow solid. Mp 201 °C (dec.). $R_f = 0.38$ (hexanes/CH_2Cl_2 1:2). IR (CH_2Cl_2 cast) 3053, 2157, 2093, 1658, 1597, 1486 cm^{-1}; ^1H NMR (400 MHz, CD_2Cl_2) δ 8.12 (d, $J = 2.0$ Hz, 2H), 8.08 (t, $J = 2.0$ Hz, 1H), 7.85 – 7.78 (m, 8H), 7.50 – 7.00 (m, 54H); ^{13}C {^1H} NMR (125 MHz, APT, CD_2Cl_2) δ 153.8, 149.7, 148.7, 146.9 (pseudo–dd, $^1J_{C\text{-}P} = 48$ Hz, $^2J_{C\text{-}P} = 26$ Hz), 143.1, 142.1, 141.2, 140.9, 140.1, 133.9 – 133.7 (m), 131.6, 130.9 (2×), 130.8, 130.4, 130.0 (pseudo–t, $J_{C\text{-}P} = 58$ Hz), 129.3 – 129.2 (m), 129.0, 128.9, 128.1 (2×), 127.9 (2×), 127.8, 127.6, 120.3, 112.1 (pseudo–dd, $^2J_{C\text{-}P} = 118$ Hz (*trans*), $^2J_{C\text{-}P} = 12$ Hz (*cis*)), 110.5 (pseudo–d, $^3J_{C\text{-}P} = 27$ Hz), 105.8, 102.9, 94.9, 93.9, 88.3, 88.2; ^{31}P {^1H} NMR (162 MHz, CD_2Cl_2) δ 51.7 (pseudo–t, $^1J_{P\text{-}Pt} = 2267$ Hz); ESI MS (NO_2Me/$ClCH_2CH_2Cl$, $C_{99}H_{65}NP_2P$) *m/z* (rel. intensity) 1548 ($[M + Na]^+$, 100), 1525 ($[M + H]^+$, 64). Anal. Calcd. for $C_{99}H_{65}NP_2Pt$: C, 77.94, H, 4.29, N, 0.92. Found: C, 77.75, H, 4.22, N, 0.95.

Single crystals of **608** suitable for X–ray crystallographic analysis were grown from a boiling 1,2–dichloroethane solution upon cooling. X–Ray crystallographic data for **608**: $C_{99}H_{65}NP_2Pt \cdot 2ClCH_2CH_2Cl \cdot H_2O$ (formula weight 1741.47) crystallized in the triclinic space group $P\bar{1}$ (No. 2) with $a = 10.1674(4)$ Å, $b = 15.3820(6)$ Å, $c = 27.2200(12)$ Å; $\alpha = 97.089(1)°$, $\beta = 98.465(1)°$, $\gamma = 99.225(1)°$; $V = 4108.8(3)$ Å^3; $Z = 2$; $\rho_{\text{calcd}} = 1.408$ g cm^{-3}; μ(Mo Kα) = 1.928 mm^{-1}; $T = -80$ °C; $R_1(F) = 0.0342$ (14840 reflections with $F_o^2 \geq 2\sigma(F_o^2)$), and $wR_2(F^2) = 0.0896$ for all 16535 data. CCDC no. 210801.

Cis–(dppee)Pt(C≡CSi*i*–Pr$_3$)$_2$ (610a).

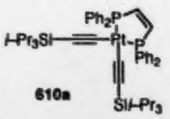

610a

Cis–1,2–Bis(diphenylphosphino)ethylene (18 mg, 0.045 mmol) was added to a solution of **602a** (50 mg, 0.046 mmol) in CH_2Cl_2 (5 mL) and the mixture was stirred at rt for 14 h. Solvent removal followed by purification via column chromatography (hexanes/CH_2Cl_2 2:1, alumina) afforded **610a** (42 mg, 95%) as a colourless solid. Mp 250 °C (dec.). R_f = 0.68 (hexanes/CH_2Cl_2 2:1). IR (CH_2Cl_2 cast) 2938, 2888, 2860, 2057, 1462, 1436 cm^{-1}; ^{1}H NMR (400 MHz, CD_2Cl_2) δ 7.89 – 7.83 (m, 8H), 7.50 – 7.31 (m, 14H), 0.98 – 0.93 (m, 42H); ^{13}C {^{1}H} NMR (100 MHz, CD_2Cl_2) δ 146.9 (pseudo–dd, $^1J_{C-P}$ = 48, $^2J_{C-P}$ = 26 Hz), 134.1 – 133.9 (m), 131.5, 130.3 (pseudo–dt, $^1J_{C-P}$ = 57, $^2J_{C-Pt}$ = 24 Hz), 129.2 – 129.1 (m), 125.0 (dd, $^2J_{C-P}$ = 137 Hz (*trans*), $^2J_{C-P}$ = 15 Hz (*cis*), 111.3 – 108.4 (pseudo–dt, $^3J_{C-P}$ = 30 Hz, $^2J_{C-Pt}$ = 273 Hz), 19.1, 12.3; ^{31}P {^{1}H} NMR (162 MHz, CD_2Cl_2) δ 52.0 (pseudo–t, $^1J_{P-Pt}$ = 2208 Hz); ESI MS ($NO_2Me/ClCH_2CH_2Cl$, $C_{48}H_{64}P_2PtSi_2$) *m/z* (rel. intensity) 976 ([M + Na]$^+$, 100), 955 ([M + H]$^+$, 37); ESI HRMS *m/z* calcd. for $C_{48}H_{64}NaP_2PtSi_2$ ([M + Na]$^+$) 976.3562, found 976.3560. Anal. Calcd. for $C_{48}H_{64}P_2PtSi_2 \cdot 0.5H_2O$: C, 59.85, H, 6.80. Found: C, 59.83, H, 6.61.

Single crystals of **610a** suitable for X–ray crystallography were grown by layering a CH_2Cl_2 solution with hexanes and allowing slow diffusion at 4 °C. X–Ray crystallographic data for **610a**: $C_{48}H_{64}P_2PtSi_2$ (formula weight 954.20) crystallized in the orthorhombic space group *Pbca* (No. 61) with a = 25.3967(10) Å, b = 24.6617(10) Å, c = 30.4032(13) Å; V = 19042.3(13) Å^3; Z = 16; ρ_{calcd} = 1.331 g cm^{-3}; μ(Mo Kα) =

3.095 mm^{-1}; T = –80 °C; $R_1(F)$ = 0.0366 (13174 reflections with $F_o^2 \geq 2\sigma(F_o^2)$), and $wR_2(F^2)$ = 0.0979 for all 19465 data. CCDC no. 210799.

Cis–(dppee)Pt(C≡C–p–CN–C_6H_4)$_2$ (610b).

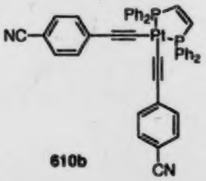

610b

Cis–1,2–Bis(diphenylphosphino)ethylene (10 mg, 0.025 mmol) was added to a solution of **602b** (25 mg, 0.026 mmol) in CH_2Cl_2 (2 mL) and the mixture was stirred at rt for 14 h. Solvent removal followed by purification via column chromatography (CH_2Cl_2, alumina) afforded **610b** (20 mg, 91%) as a light brown solid. Mp 164 °C (dec.). R_f = 0.70 (CH_2Cl_2). IR (CH_2Cl_2 cast) 3054, 2223, 2112, 1597, 1495, 1483 cm^{-1}; ^{1}H NMR (400 MHz, CD_2Cl_2) δ 7.81 – 7.74 (m, 8H), 7.58 – 7.35 (m, 18H), 7.22 (d, J = 8.6 Hz, 4H); ^{13}C {^{1}H} NMR (100 MHz, CD_2Cl_2) δ 146.7 (pseudo–dd, $^1J_{C\text{-}P}$ = 48 Hz, $^2J_{C\text{-}P}$ = 25 Hz), 133.6 – 133.3 (m), 132.6 (pseudo–t, $J_{C\text{-}Pt}$ = 270 Hz), 131.9, 131.8, 131.5 (pseudo–t, $J_{C\text{-}P}$ = 5 Hz), 129.9 – 129.1 (m, two coincident carbons), 119.4 112.3 (pseudo–dd, $^2J_{C\text{-}P}$ = 146 Hz (*trans*), $^2J_{C\text{-}P}$ = 15 Hz (*cis*)), 110.7 (pseudo–dt, $^3J_{C\text{-}P}$ = 31 Hz, $^2J_{C\text{-}Pt}$ = 308 Hz), 108.6; ^{31}P {^{1}H} NMR (162 MHz, CD_2Cl_2) δ 53.93 (pseudo–t, $^1J_{P\text{-}Pt}$ = 2276 Hz); ESI MS ($NO_2Me/ClCH_2CH_2Cl$, $C_{44}H_{30}N_2P_2Pt$) *m/z* (rel. intensity) 1710 ([2M + Na]$^+$, 61), 866 ([M + Na]$^+$, 30); ESI HRMS *m/z* calcd. for $C_{44}H_{31}N_2P_2Pt$ ([M + H]$^+$) 844.1610, found 844.1613. Anal. Calcd. for $C_{44}H_{30}N_2P_2Pt{\bullet}CH_2Cl_2$: C, 58.20, H, 3.47, N, 3.01. Found: C, 58.13, H, 3.20, N, 2.96.

Single crystals for X–ray crystallography were grown by layering a CH_2Cl_2 solution with hexanes and allowing slow diffusion at 4 °C. X–Ray crystallographic data for **610b**: $C_{44}H_{30}N_2P_2Pt{\bullet}CH_2Cl_2$ (formula weight 928.66) crystallized in the monoclinic space group $P2_1/c$ (No. 14) with a = 17.0043(8) Å, b = 14.1145(7) Å, c = 17.0083(8) Å; β = 103.8327(10)°; V = 3963.7(3) Å^3; Z = 4; ρ_{calcd} = 1.556 g cm^{-3}; μ(Mo Kα) = 3.790 mm^{-1}; T = –80 °C; $R_1(F)$ = 0.0280 (6584 reflections with $F_o^2 \geq 2\sigma(F_o^2)$), and $wR_2(F^2)$ = 0.0659 for all 8102 data. CCDC no. 210800.

***Cis*–(dppee)Pt(C≡Cpyr–*meta*–(C≡CSi*i*–Pr$_3$))$_2$ (610c).**

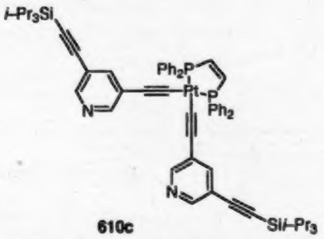

610c

Cis–1,2–Bis(diphenylphosphino)ethylene (8 mg, 0.02 mmol) was added to a solution of **602c** (25 mg, 0.019 mmol) in CH_2Cl_2 (2 mL) and the mixture was stirred at rt for 2 h. Solvent removal followed by purification via gradient column chromatography (CH_2Cl_2 to CH_2Cl_2/acetone 5:1, alumina) afforded **610c** (14 mg, 64%) as a pale blue transparent solid. Mp 93 °C. R_f = 0.20 (neat CH_2Cl_2, alumina). IR (CH_2Cl_2 cast) 2942, 2890, 2864, 2156, 2113, 1574, 1462 cm^{-1}; ^{1}H NMR (400 MHz, CD_2Cl_2) δ 8.35 (br s, 2H), 8.26 (br s, 2H), 7.82 – 7.76 (m, 8H), 7.59 – 7.34 (m, 16H) 1.13 – 1.12 (m, 42 H); ^{13}C NMR (100 MHz, CD_2Cl_2) δ 151.1, 148.8, 146.8 (pseudo–dd, $^1J_{C\text{-}P}$ = 48 Hz, $^2J_{C\text{-}P}$ = 26 Hz), 140.6, 133.8 – 133.5 (m), 132.0, 130.0 – 129.2 (m, two coincident carbons), 124.1 119.8, 103.9, 94.5, 18.4, 11.7 (two carbons not observed); ^{31}P {^{1}H}

NMR (162 MHz, CD_2Cl_2) δ 53.9 (pseudo–t, $^1J_{P\text{–}Pt}$ = 2277 Hz); ESI MS ($NO_2Me/ClCH_2CH_2Cl$, $C_{62}H_{70}N_2P_2PtSi_2$) *m/z* (rel. intensity) 1179 ($[M + Na]^+$, 70), 1157 ($[M + H]^+$, 100).

Compound 611.

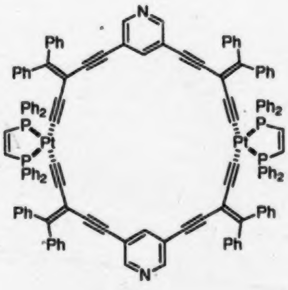

611

Cis–1,2–Bis(diphenylphosphino)ethylene (5 mg, 0.01 mmol) was added to a solution of **403a** (16 mg, 0.0064 mmol) in CH_2Cl_2 (5 mL) and the mixture was stirred at rt for 14 h. Solvent reduction followed by addition of ether (2 mL) and subsequent filtration (2×) afforded **611** (10 mg, 71%) as a pale yellow solid. Mp 160 °C (dec.). IR (CH_2Cl_2 cast) 3050, 2090, 1575, 1483 cm^{-1}; ^1H NMR (400 MHz, CD_2Cl_2) δ 7.95 (d, *J* = 2.0 Hz, 4H), 7.62 – 7.57 (m, 16H), 7.49 – 7.45 (m, 8H), 7.37 – 7.18 (m, 48H), 7.05 (pseudo–t, *J* = 2.1 Hz, 2H), 6.88 – 6.84 (m, 4H), 6.65 – 6.61 (m, 8H); $^{13}C\ \{^1H\}$ NMR (100 MHz, CD_2Cl_2) δ 151.6, 150.1, 141.9, 141.2, 139.6, 133.7 – 133.6 (m), 131.5, 130.8, 130.5, 129.7 (pseudo–t, $J_{C\text{–}P}$ = 57 Hz), 129.1 – 129.0 (m), 127.9, 127.7, 127.4 (two coincident carbons), 119.9, 95.6, 85.8 (4 carbons not observed); $^{31}P\ \{^1H\}$ NMR (162 MHz, CD_2Cl_2) δ 53.6 (pseudo–t, $^1J_{P\text{–}Pt}$ = 2292 Hz); ESI MS ($NO_2Me/ClCH_2CH_2Cl$) *m/z* (rel. intensity) 2265 ($[M + Na]^+$, 75), 2243 ($[M + H]^+$, 100).

Compound 612.

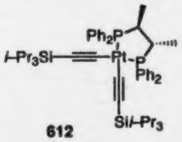

612

(2*S*,3*S*)-(–)-Bis(diphenylphosphino)butane (7.9 mg, 0.019 mmol) was added to a solution of **602a** (20 mg, 0.018 mmol) in CD_2Cl_2 (1 mL). The mixture was stirred at rt for 14 h. Solvent removal followed by purification on a silica gel column (hexanes/CH_2Cl_2 1:1) afforded **612** (16 mg, 89%) as a colourless solid. Mp 218 °C (dec.). R_f = 0.18 (hexanes/CH_2Cl_2 1:1). IR (CH_2Cl_2 cast) 3054, 2937, 2859, 2048, 1461 cm^{-1}; ^1H NMR (400 MHz, CD_2Cl_2) δ 8.07 – 8.02 (m, 4H), 7.84 – 7.79 (m, 4H), 7.50 – 7.36 (m, 12H), 2.48 – 2.47 (br m, 2H), 0.89 – 0.76 (m, 48H); ^{13}C {^1H, ^{31}P} NMR (100 MHz, CD_2Cl_2) δ 136.5 (pseudo–t, $^3J_{C-Pt}$ = 20 Hz), 134.1 (pseudo–t, $^3J_{C-Pt}$ = 17 Hz), 131.5, 131.1, 129.6 (pseudo–t, $^2J_{C-Pt}$ = 21 Hz), 128.9, 128.5, 128.4, 128.3 (pseudo–t, $^2J_{C-Pt}$ = 22 Hz), 108.6 (pseudo–t, $^1J_{C-Pt}$ = 240 Hz), 39.9 (pseudo–t, $^2J_{C-Pt}$ = 40 Hz), 19.1, 19.0, 16.1 (pseudo–t, $^3J_{C-Pt}$ = 15 Hz), 12.2; ^{31}P {^1H} NMR (162 MHz, CD_2Cl_2) δ 46.4 (pseudo–t, $^1J_{P-Pt}$ = 2194 Hz); ESI MS (CH_3NO_2, $C_{50}H_{70}P_2PtSi_2$) *m/z* (rel. intensity) 1091.3 ([M + CH_2Cl_2 + Na]$^+$, 100), 1007.4 ([M + Na]$^+$, 5), 985.4 ([M + H]$^+$, 8); ESI HRMS *m/z* calcd. for $C_{50}H_{71}Si_2P_2Pt$ ([M + H]$^+$) 984.4217, found 984.4217.

Single crystals of **612** suitable for X–ray crystallographic analysis were grown by slow evaporation from a CH_2Cl_2/hexanes solution at 4 °C. Crystallographic data for **612**: $C_{50}H_{70}P_2PtSi_2 \bullet CH_2Cl_2$ (formula weight 1069.20) crystallized in the orthorhombic space group $P2_12_12_1$ (No. 19) with a = 14.1414(6) Å; b = 14.6660(6) Å; c = 25.5887(11) Å; V = 5307.0(4) Å^3; Z = 4; ρ_{calcd} = 1.338 g cm^{-3}; μ(Mo Kα) = 2.881 mm^{-1}; T = –80 °C;

$R_1(F)$ = 0.0208 (10217 reflections $F_o^2 \geq 2\sigma(F_o^2)$) and $wR_2(F^2)$ = 0.0457 for all 10797 unique data. CCDC no. 243209.

Compound 613

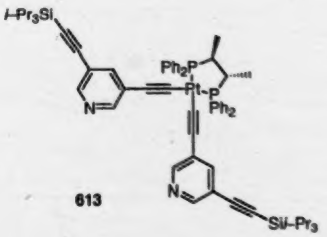

613

(2*S*,3*S*)-(–)-Bis(diphenylphosphino)butane (5.0 mg, 0.012 mmol) was added to a solution of **602c** (15 mg, 0.011 mmol) in CD_2Cl_2 (1 mL). The mixture was stirred at rt for 15 min. Solvent removal followed by purification via gradient column chromatography (CH_2Cl_2 to CH_2Cl_2/acetone 5:1, silica) afforded **613** (14 mg, 99%) as a pale tan solid. Mp 148 °C. IR (CH_2Cl_2 cast) 3054, 2942, 2864, 2155, 2112, 1574, 1462 cm^{-1}; ^1H NMR (300 MHz, CD_2Cl_2) δ 8.30 (br s, 2H), 8.08 (br s, 2H), 7.86 – 7.76 (m, 8H), 7.59 – 7.46 (m, 12H), 7.31 (pseudo–t, J = 2.0 Hz, 2H), 2.42 – 2.38 (br m, 2H), 1.13 (br s, 42H), 1.11 – 1.04 (m, 6H); ^{13}C {^1H} NMR (100 MHz, CD_2Cl_2) δ 151.1, 148.6, 140.7, 136.8 (pseudo–t, $J_{C\text{-}P}$ = 5.9 Hz), 133.2 (pseudo–t, $J_{C\text{-}P}$ = 4.4 Hz), 132.3, 131.4, 129.1 (pseudo–t, $J_{C\text{-}P}$ = 5.2 Hz), 128.8 (pseudo–t, $J_{C\text{-}P}$ = 5.5 Hz), 128.4 (dd, $^1J_{C\text{-}P}$ = 60 Hz, $^3J_{C\text{-}P}$ = 2.8 Hz), 127.2 (dd, $^1J_{C\text{-}P}$ = 56 Hz, $^3J_{C\text{-}P}$ = 4.2 Hz), 124.3 (br), 119.7 (br), 114.2 (dd, $^2J_{C\text{-}P}$ = 142 Hz (*trans*), $^2J_{C\text{-}P}$ = 15 Hz (*cis*), 106.0 (pseudo–d, $^3J_{C\text{-}P}$ = 35 Hz), 104.1, 94.2, 38.2 – 37.7 (m), 18.8, 14.9 –14.7 (m), 11.6; ^{31}P {^1H} NMR (162 MHz, CD_2Cl_2) δ 43.5 (pseudo–t, $^1J_{P\text{-}Pt}$ = 2230 Hz); ESI MS ($ClCH_2CH_2Cl$, $C_{64}H_{76}N_2P_2PtSi_2$) *m/z* (rel. intensity) 1187.5 ([M + H]$^+$, 100); ESI HRMS *m/z* calcd. for $C_{64}H_{77}N_2P_2PtSi_2$

([M + H]$^+$) 1185.4727, found 1185.4722.

Compound 614.

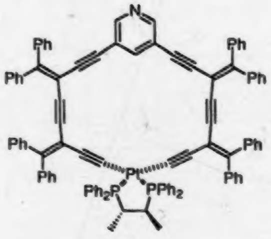

614

(2*S*,3*S*)-(–)-Bis(diphenylphosphino)butane (4.0 mg, 0.0094 mmol) was added to a solution of **402** (16 mg, 0.0097 mmol) in CD_2Cl_2 (1 mL). The mixture was stirred at rt for 4 days. Solvent removal followed by purification on a gradient silica gel column (hexanes/CH_2Cl_2 1:3 → neat CH_2Cl_2 followed by flushing with acetone) afforded **614** (11 mg, 73%) as a yellow solid. Mp 162 °C (dec.). IR (CH_2Cl_2 cast) 3051, 2969, 2094, 1492 cm^{-1}; ^{1}H NMR (300 MHz, CD_2Cl_2) δ 8.15 (d, *J* = 2.0 Hz, 2H), 8.07 (t, *J* = 2.0 Hz, 1H), 7.84 – 7.77 (m, 8H), 7.49 – 6.97 (m, 52H), 2.36 (br m, 2H), 0.95 – 0.89 (m, 6H); ^{13}C {^{1}H} NMR (100 MHz, CD_2Cl_2) δ 153.5, 149.7, 148.1, 143.2, 142.2, 141.2, 140.9, 140.1, 136.5 – 136.4 (m), 133.6 – 133.5 (m), 131.8, 131.1, 130.8 (2×), 130.4, 129.0, 128.9, 128.9 – 128.8 (m) 128.8 – 128.7 (m), 128.1, 128.0, 127.8, 127.7, 127.6, 127.5, 120.4, 116.1 (pseudo–dd, $^2J_{C-P}$ = 145 Hz (*trans*), $^2J_{C-P}$ = 16 Hz (*cis*)), 109.1 – 108.8 (m), 106.1, 102.9, 95.0, 94.0, 88.3, 88.2, 38.6 – 38.1 (m), 15.3 – 15.2 (m) (three coincident carbons not observed); ^{31}P {^{1}H} NMR (162 MHz, CD_2Cl_2) δ 43.6 (pseudo–t, $^1J_{P-Pt}$ = 2228 Hz); ESI MS (CH_2Cl_2/NO_2Me, $C_{107}H_{71}NP_2Pt$) *m/z* (rel. intensity) 1594.4 ([M + K]$^+$, 25), 1578.5 ([M + Na]$^+$, 100), 1556.5 ([M + H]$^+$, 79).

Single crystals of **614** suitable for X–ray crystallographic analysis were grown by slow evaporation/diffusion of a $CH_2Cl_2/ClCH_2CH_2Cl/Et_2O$ solution at 4 °C. Crystallographic data for **614**: $C_{107}H_{71}NP_2Pt\bullet 1.75(ClCH_2CH_2Cl)H_2O$ (formula weight 1746.80) crystallized in the triclinic space group $P\bar{1}$ (No. 1) with $a = 10.2491(6)$ Å, $b = 15.5943(10)$ Å, $c = 27.6134(17)$ Å; $\alpha = 77.4626(12)°$, $\beta = 84.5413(13)°$, $\gamma = 79.1701(11)°$; $V = 4224.6(4)$ Å^3; $Z = 2$; $\rho_{calcd} = 1.373$ g cm^{-3}; μ(Mo Kα) = 1.860 mm^{-1}; $T = -80$ °C; $R_1(F) = 0.0622$ (20815 reflections $F_o^2 \geq 2\sigma(F_o^2)$) and $wR_2(F^2) = 0.1389$ for all 28700 unique data. CCDC no. 243208.

Compound 615

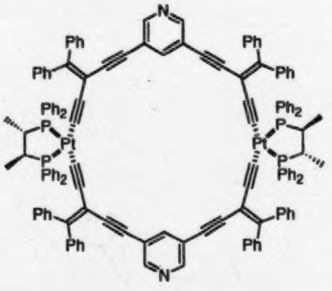

615

(2*S*,3*S*)-(–)-Bis(diphenylphosphino)butane (6.0 mg, 0.014 mmol) was added to a solution of **403a** (18 mg, 0.0072 mmol) in CH_2Cl_2 (5 mL). The mixture was stirred at rt for 5 days. The mixture was applied to a silica gel column and flushed using CH_2Cl_2. The product was then eluted off the column using CH_2Cl_2/acetone 1:1 affording **615** (16 mg, 96%) as a bright yellow solid. Mp 172 °C (dec.). IR (CH_2Cl_2 cast) 3051, 2158, 2094, 1580, 1436 cm^{-1}; ^1H NMR (400 MHz, CD_2Cl_2) δ 7.85 (d, *J* = 2.1 Hz, 4H), 7.80 – 7.75 (m, 8H), 7.59 – 7.21 (m, 60H), 6.88 (t, *J* = 2.1 Hz, 2H), 6.87 – 6.82 (m, 4H), 6.65

– 6.61 (m, 8H), 2.26 (br m, 4H), 0.90 – 0.86 (m, 12H); $^{13}C\{^1H\}$ NMR (100 MHz, CD_2Cl_2) δ 151.0, 150.2, 142.2, 141.1, 139.8, 136.7 – 136.6 (m), 133.4 – 133.3 (m), 132.2, 131.0, 130.9, 130.6, 128.9 – 128.7 (m, 2 overlapping m for *ipso* carbons), 127.9 (2×), 127.5, 127.3, 120.2, 105.9, 95.7, 86.0 (2 alkynyl carbons not observed due to poor signal to noise), 37.7 – 37.4 (m), 14.9 – 14.8 (m) (two coincident carbons not observed); $^{31}P\{^1H\}$ NMR (162 MHz, CD_2Cl_2) δ 43.4 (pseudo–t, $^1J_{P\text{-}Pt}$ = 2247 Hz); ESI MS (CH_2Cl_2/NO_2Me, AgOTf added, $C_{138}H_{102}N_2P_4Pt_2$) *m/z* (rel. intensity) 2409.6 ([M + Ag]$^+$, 100), 2324 ([M + Na]$^+$, 50), 2302.6 ([M + H]$^+$, 93).

Compound 616.

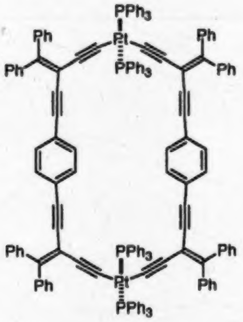

616

Oligomer **209a** (58 mg, 0.076 mmol) was deprotected by treating with NaOH in wet THF/MeOH for 4h at rt as described in the general procedure. The resulting deprotected alkyne was added, with no further purification, to a degassed solution of $PtCl_2(PPh_3)_2$ (61 mg, 0.077 mmol) in Et_2NH (225 mL). A catalytic amount of CuI (8 mg, 0.04 mmol) was added and the mixture was stirred at 50 °C for 14 h. 150 mL of ether/CH_2Cl_2 were added, and the resulting solution was washed with water (2 × 50 mL), sat'd NH_4Cl (6 × 100 mL) and dried ($MgSO_4$). Solvent removal (using *no* heat) and subsequent purification by gradient column chromatography on silica gel (hexanes/CH_2Cl_2 2:1 → neat CH_2Cl_2) afforded **616** (61 mg, 64%) as a bright yellow solid. Mp 232 °C (dec.). $R_f = 0.08$ (hexanes/CH_2Cl_2 1:1). IR (CH_2Cl_2 cast) 3052, 2083, 1482 cm^{-1}; ^1H NMR (400 MHz, CD_2Cl_2) δ 7.77 – 7.72 (m, 24H), 7.36 – 6.97 (m, 84H); ^{13}C {^1H} NMR (100 MHz, CD_2Cl_2) δ 145.6, 142.0, 140.9, 135.3 (pseudo–t, $J_{C-P} = 6.1$ Hz), 131.4 (pseudo–t, $J_{C-P} = 29$ Hz), 131.3, 130.8, 130.6, 130.4, 128.2 (pseudo–t, $J_{C-P} =$ 5.4 Hz), 127.6, 127.5, 127.3 (2×), 123.6, 94.6, 90.0 (two alkynyl and one vinylidene carbon resonances are not observed due to poor signal/noise resulting from extreme insolubility of compound **616**); ^{31}P {^1H} NMR (162 MHz, CD_2Cl_2) δ 18.6 (pseudo–t, $^1J_{P-Pt} = 2626$ Hz); ESI MS (THF, AgOTf added, $C_{156}H_{108}P_4Pt_2$) *m/z* (rel. intensity) 3118 ($[M + Ag + 2(AgOTf)]^+$, 70), 2860 ($[M + Ag + AgOTf]^+$, 85), 2605 ($[M + Ag]^+$, 9), 1613 ($[M + 2Ag + 2(AgOTf)]^{2+}$, 100). Anal. Calcd. For $C_{156}H_{108}P_4Pt_2 \cdot 2H_2O$: C, 73.98; H, 4.46%. Found: C, 73.74; H, 4.55%.

Single crystals of **616** suitable for X–ray crystallographic analysis were grown by dissolving in boiling $CH_2Cl_2/ClCH_2CH_2Cl$ and allowing slow evaporation at room temperature. Crystallographic data for **616**: $C_{156}H_{108}P_4Pt_2 \cdot 5ClCH_2CH_2Cl$ (formula weight 2991.24) crystallized in the triclinic space group $P\bar{1}$ (No. 2) with $a =$ 11.6210(10) Å, $b = 13.8619(12)$ Å, $c = 23.046(2)$ Å; $\alpha = 73.4487(16)°$, $\beta = 80.464(2)°$, $\gamma = 85.7774(18)°$; $V = 3508.1(5)$ Å^3; $Z = 1$; $\rho_{calcd} = 1.416$ g cm^{-3}; μ(Mo Kα) = 2.281 mm^{-1}; $T = -80$ °C; $R_1(F) = 0.0649$ (10006 reflections $F_o^2 \geq 2\sigma(F_o^2)$) and $wR_2(F^2) =$ 0.1599 for all 14018 unique data.

Compound 617.

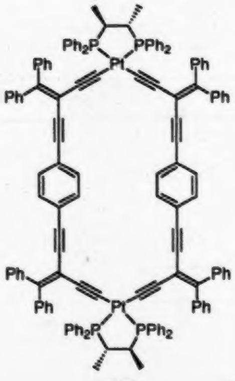

617

(2*S*,3*S*)-(–)-Bis(diphenylphosphino)butane (3.5 mg, 0.0082 mmol) was added to a solution of **616** (10 mg, 0.0040 mmol) in CD_2Cl_2 (1 mL). The mixture was stirred at rt for 3 days. Solvent removal followed by purification on a gradient silica gel column (hexanes/CH_2Cl_2 1:3 → CH_2Cl_2/acetone 3:1) afforded **617** (6 mg, 65%) as a bright yellow solid. Mp 168 °C (dec.); IR (µscope) 3053, 2959, 2927, 2155, 2090, 1434 cm^{-1}; ^1H NMR (400 MHz, CD_2Cl_2) δ 7.78 – 7.73 (m, 8H), 7.64 – 7.60 (m, 4H), 7.51 – 7.48 (m, 8H), 7.45 – 7.41 (m, 4H), 7.37 – 7.20 (m, 44H), 6.85 – 6.81 (m, 4H), 6.63 – 6.59 (m, 16H), 2.16 (br m, 4H), 0.89 – 0.87 (m, 12H); $^{31}P\ \{^1H\}$ NMR (162 MHz, CD_2Cl_2) δ 42.2 (pseudo–t, $^1J_{P-Pt}$ = 2239 Hz); ESI MS (THF, AgOTf added, $C_{140}H_{104}P_4Pt_2$) *m/z* (rel. intensity) 2408 ($[M + Ag]^+$, 23), 2301 ($[M]^+$, 11), 1258 ($[M + 2Ag]^{2+}$, 100).

Compound 619.

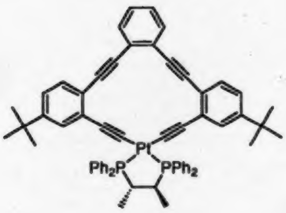

619

(2*S*,3*S*)-(–)-Bis(diphenylphosphino)butane (5.0 mg, 0.012 mmol) was added to a solution of **618** (13 mg, 0.011 mmol) in CD_2Cl_2 (1 mL). The mixture was stirred at rt for 3 days. Solvent removal followed by purification on a gradient alumina column (hexanes/CH_2Cl_2 1:1→CH_2Cl_2/acetone 4:1) afforded **619** (10 mg, 83%) as a colourless solid. Mp 190 °C (dec.). IR (CH_2Cl_2 cast) 3054, 2961, 2103, 1594, 1498 cm^{-1}; ^{1}H NMR (400 MHz, CD_2Cl_2) δ 7.97 – 7.82 (m, 8H), 7.45 – 7.41 (m, 2H), 7.40 –7.29 (m, 12H), 7.05 – 7.03 (m, 6H), 6.35 (br dd, *J* = 5.8, 3.4 Hz, 2H), 2.49 (br m, 2H), 1.21 (s, 18H), 0.99 – 0.92 (m, 6H); ^{13}C {^{1}H, ^{31}P} NMR (100 MHz, CD_2Cl_2) δ 150.7, 136.5, 133.6, 132.9, 131.9, 131.5, 131.1, 130.8, 128.9, 128.5, 127.8, 125.8, 122.3, 121.8, 110.7 (pseudo–t, $^1J_{\text{C-Pt}}$ = 304 Hz), 94.1, 91.8, 38.6, 34.8, 31.3, 15.6 (one alkynyl carbon is not observed due to poor signal/noise; 3 coincident carbons are not observed); ^{31}P {^{1}H} NMR (162 MHz, CD_2Cl_2) δ 45.1 (pseudo–t, $^1J_{\text{P-Pt}}$ = 2226 Hz); ESI MS (THF, AgOTf added, $C_{62}H_{56}P_2Pt$) *m/z* (rel. intensity) 1165.3 ([M + Ag]$^+$, 100).

Compound 620.

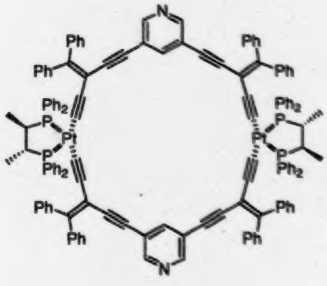

620

(2*R*,3*R*)-(–)-Bis(diphenylphosphino)butane (7.0 mg, 0.016 mmol) was added to a solution of **403a** (20 mg, 0.0080 mmol) in CH_2Cl_2 (10 mL). The mixture was stirred at rt for 4 days. The mixture was applied to a silica gel column and flushed using CH_2Cl_2. The product was then eluted off the column using CH_2Cl_2/acetone 1:1 affording **620** (17 mg, 92%) as a bright yellow solid. Mp 170 °C (dec.). IR (CH_2Cl_2 cast) 3051, 2090, 1485, 1436 cm^{-1}; ^1H NMR (400 MHz, CD_2Cl_2) δ 7.85 (d, J = 2.08 Hz, 4H), 7.80 – 7.75 (m, 8H), 7.57 – 7.21 (m, 60H), 6.87 (t, J = 2.05 Hz), 6.86 – 6.82 (m, 4H), 6.65 – 6.61 (m, 8H), 2.27 (br m, 4H), 0.90 – 0.87 (m, 12H); ^{13}C {^1H, ^{31}P} NMR (100 MHz, CD_2Cl_2) δ 151.0, 150.2, 142.2, 141.1, 139.8, 136.7, 133.3, 132.2, 131.0, 130.9, 130.6, 128.9, 128.8, 128.5, 127.9 (2×), 127.8, 127.5, 127.3, 120.1, 114.6, 107.4, 105.9, 95.7, 86.0, 37.6, 14.8; ^{31}P {^1H} NMR (162 MHz, CD_2Cl_2) δ 43.4 (pseudo–t, $^1J_{P\text{-}Pt}$ = 2246 Hz); ESI MS (CH_2Cl_2/NO_2Me, AgOTf added, $C_{138}H_{102}N_2P_4Pt_2$) *m/z* (rel. intensity) 2409.6 ($[M + Ag]^+$, 100).

8.7 References and Notes

1. Slepkov, A. D.; Hegmann, F. A.; Zhao, Y. M.; Tykwinski, R. R.; Kamada, K. *J. Chem. Phys.* **2002**, *116*, 3834–3840.
2. Stang, P. J.; Fisk, T. E. *Synthesis* **1979**, 438–440.
3. Neenan, T. X.; Whitesides, G. M. *J. Org. Chem.* **1988**, *53*, 2489–2496.
4. Weder, C.; Wrighton, M. S. *Macromolecules* **1996**, *29*, 5157–5165.
5. Zhou, Q.; Carroll, P. J.; Swager, T. M. *J. Org. Chem.* **1994**, *59*, 1294–1301.
6. Bunten, K. A.; Kakkar, A. K. *Macromolecules* **1996**, *29*, 2885–2893.
7. Ng, S. C.; Novak, I.; You, X.; Huang, W. *J. Phys. Chem. A* **1998**, *102*, 904–908.
8. Collman, J. P.; Barnes, C. E.; Brothers, P. J.; Collins, T. J.; Ozawa, T.; Gallucci, J. C.; Ibers, J. A. *J. Am. Chem. Soc.* **1984**, *106*, 5151–5163.
9. Tominaga, M.; Kato, M.; Okano, T.; Sakamoto, S.; Yamaguchi, K.; Fujita, M. *Chem. Lett.* **2003**, *32*, 1012–1013.
10. Stang, P. J.; Cao, D. H.; Saito, S.; Arif, A. M.; *J. Am. Chem. Soc.* **1995**, *117*, 6273–6283.
11. Cox, E. G.; Saenger, H.; Wardlaw, W. *J. Chem. Soc.* **1934**, 182–186.
12. Manna, J.; Kuehl, C. J.; Whiteford, J. A.; Stang, P. J.; Muddiman, D. C.; Hofstadler, S. A.; Smith, R. D. *J. Am. Chem. Soc.* **1997**, *119*, 11611–11619.
13. Hirsch, K. A.; Wilson, S. R.; Moore, J. S. *J. Am. Chem. Soc.* **1997**, *119*, 10401–10412.
14. Tominaga, M.; Kato, M.; Okano, T.; Sakamoto, S.; Yamaguchi, K.; Fujita, M. *Chem. Lett.* **2003**, *32*, 1012–1013.

Appendix A – Selected Spectra

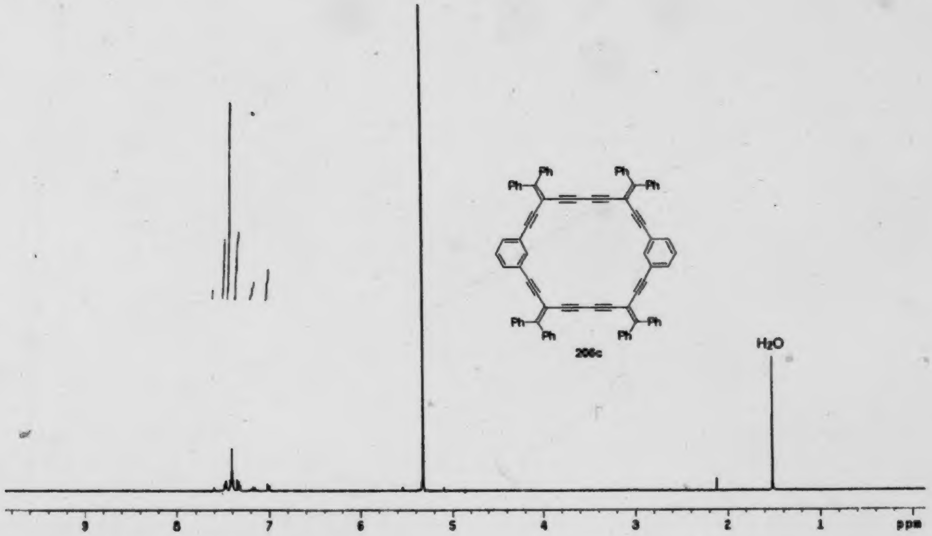

Figure A1 ^{1}H NMR spectrum of **206c**.

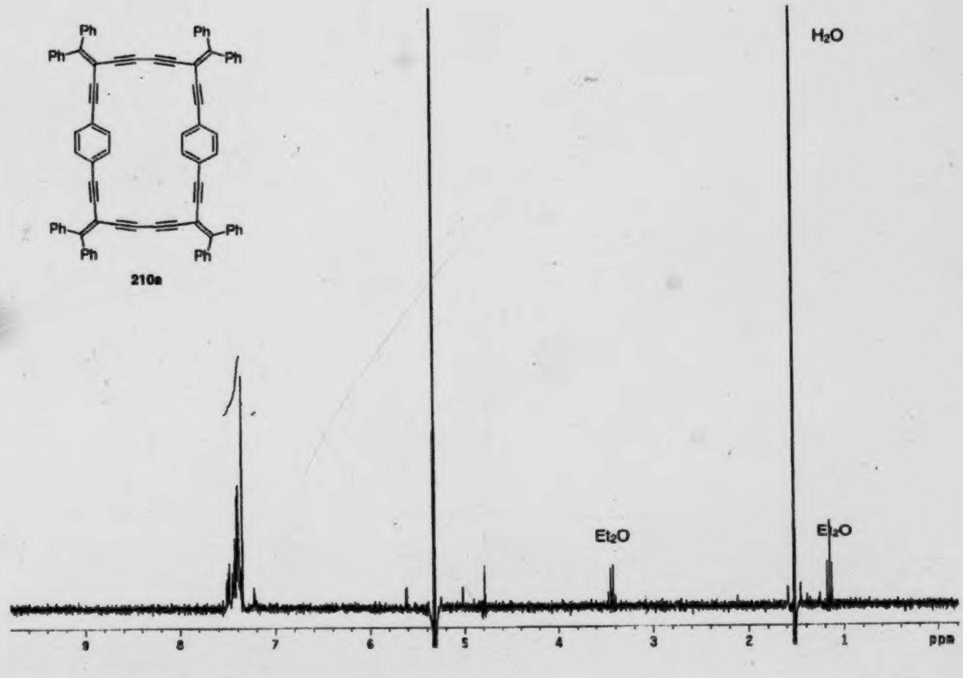

Figure A2 ^{1}H NMR spectrum of **210a**.

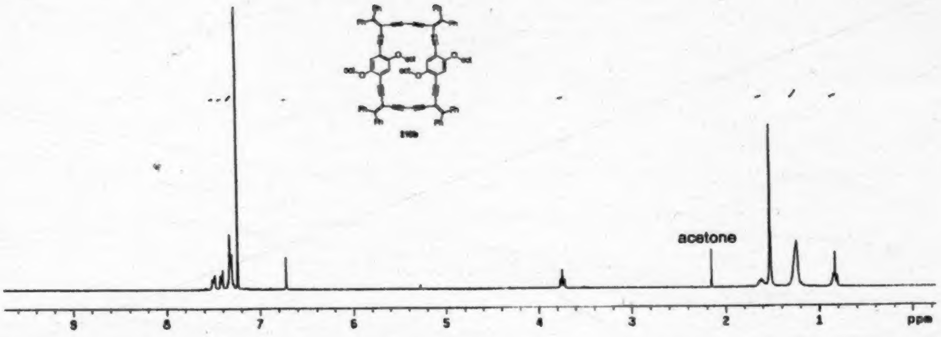

Figure A3 ^{1}H NMR spectrum of **210b**.

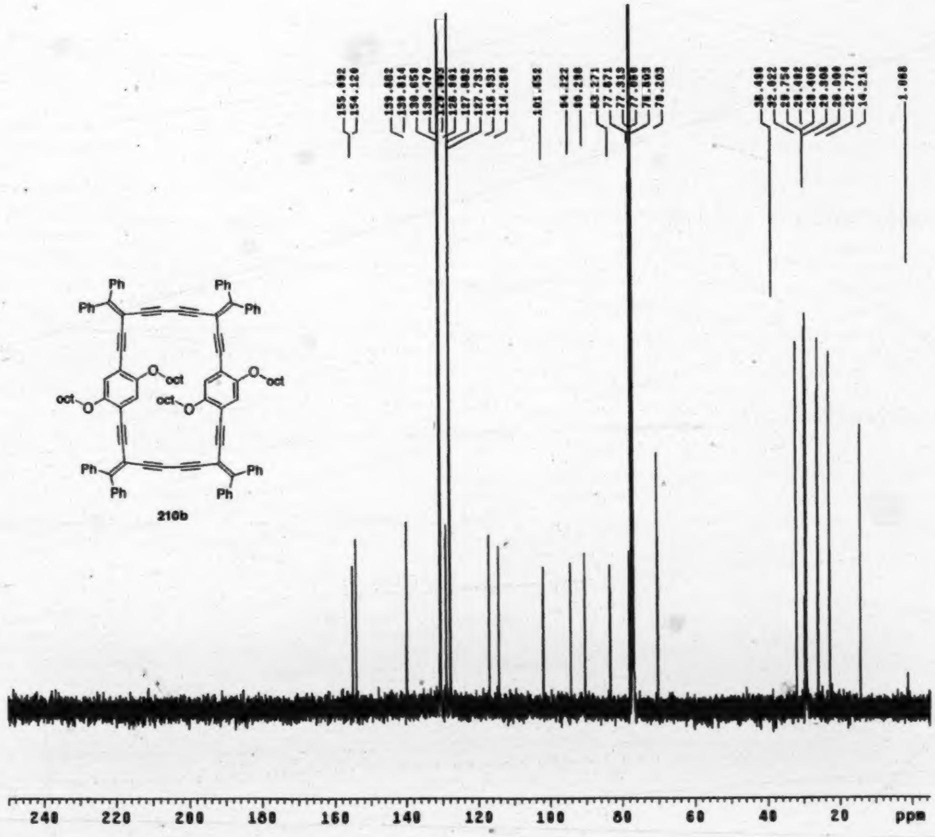

Figure A4 ^{13}C NMR spectrum of **210b**.

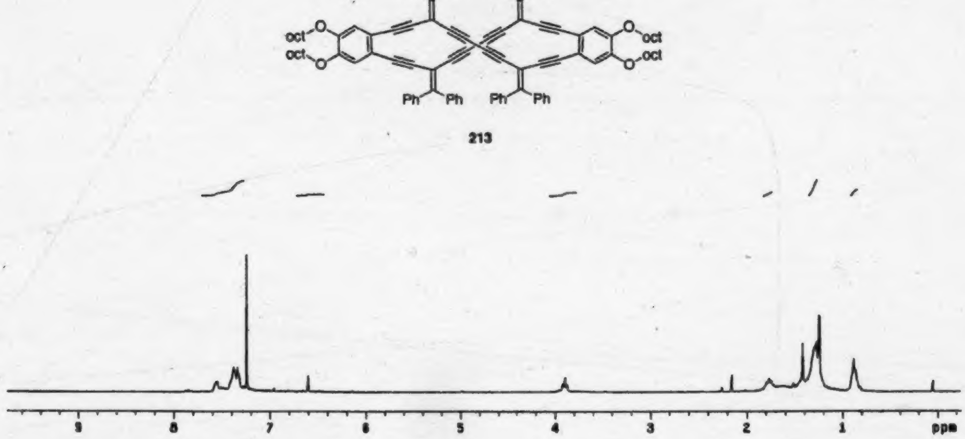

Figure A5 ^{1}H NMR spectrum of 213.

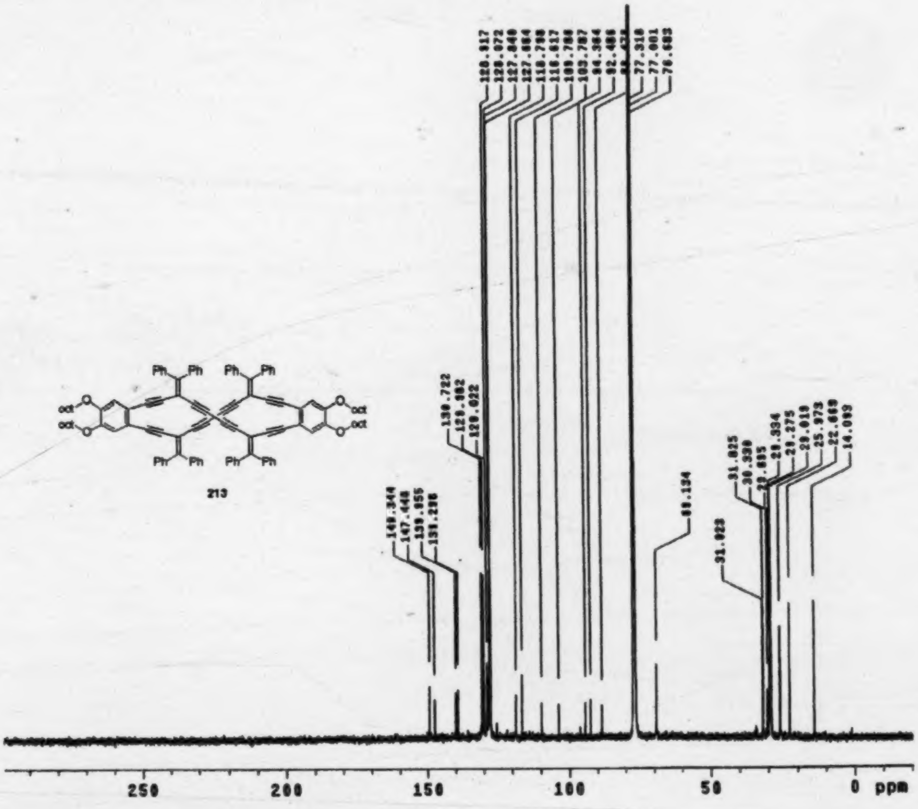

Figure A6 ^{13}C NMR spectrum of 213.

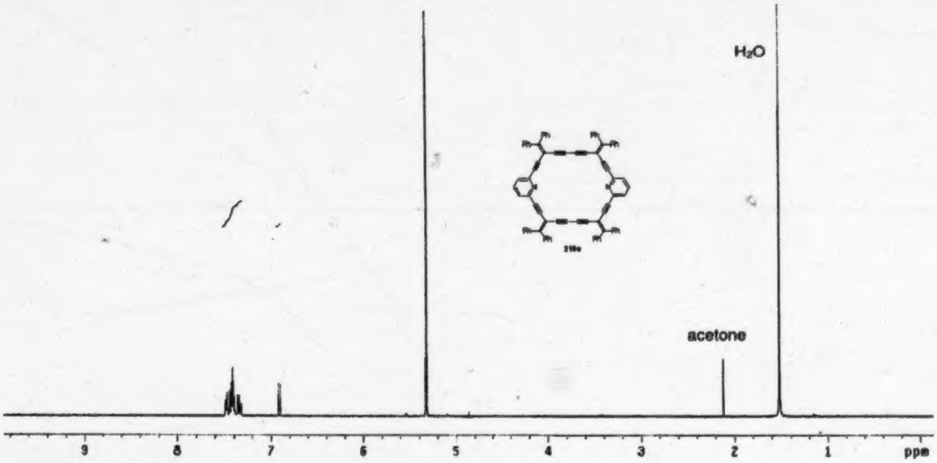

Figure A7 ^{1}H NMR spectrum of **216c**.

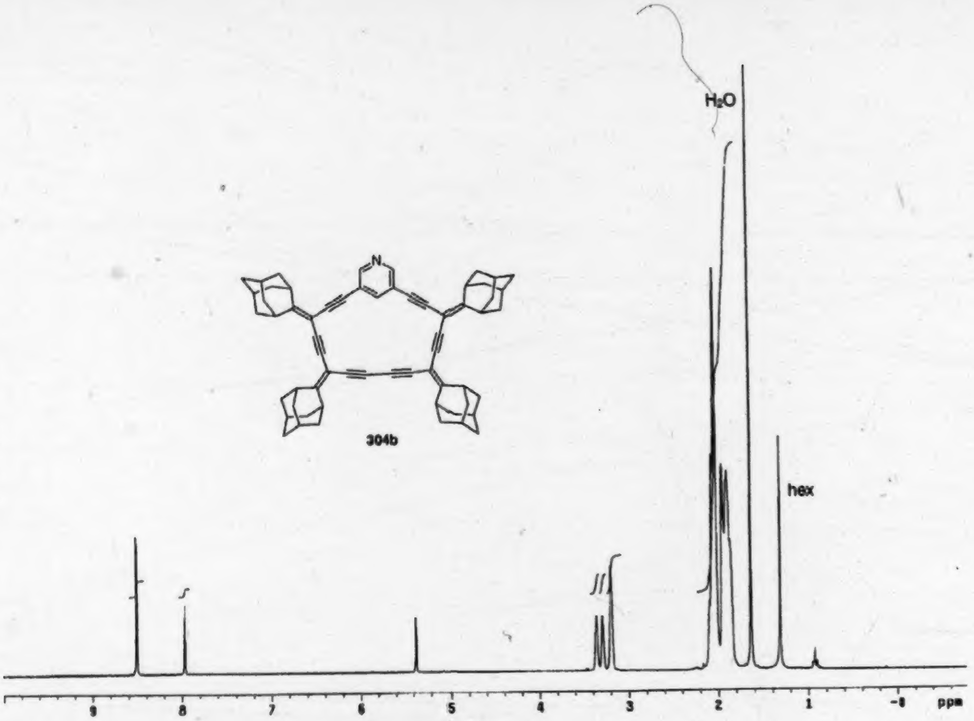

Figure A8 ^1H NMR spectrum of **304b**.

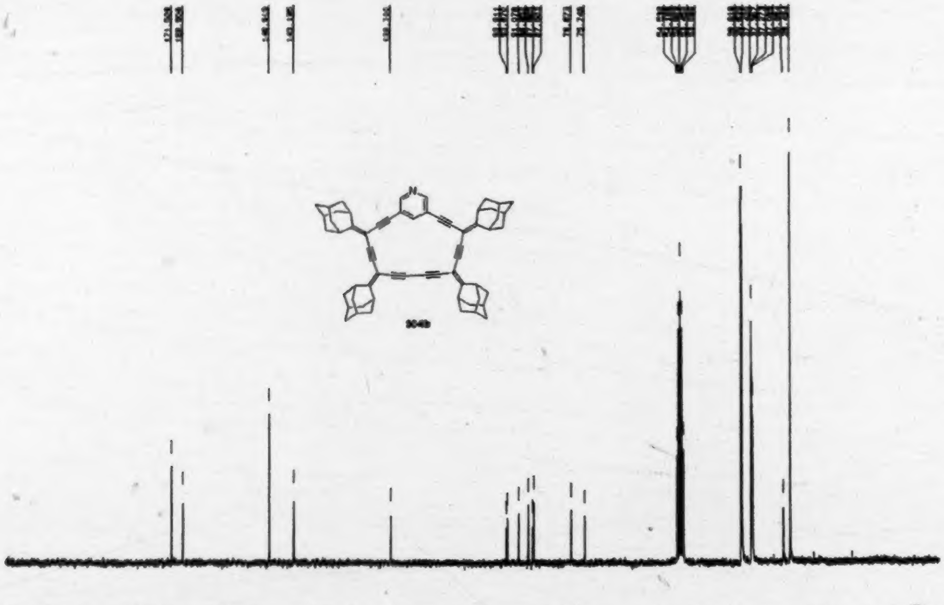

Figure A9 ^{13}C NMR spectrum of **304b**.

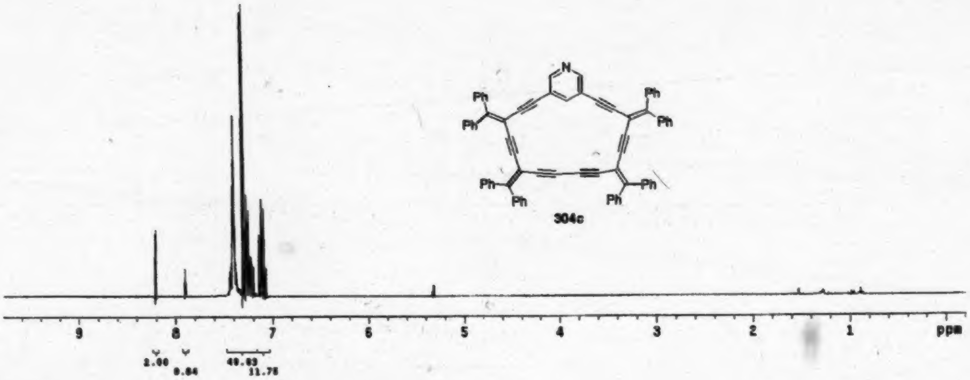

Figure A10 ^{1}H NMR spectrum of **304c**.

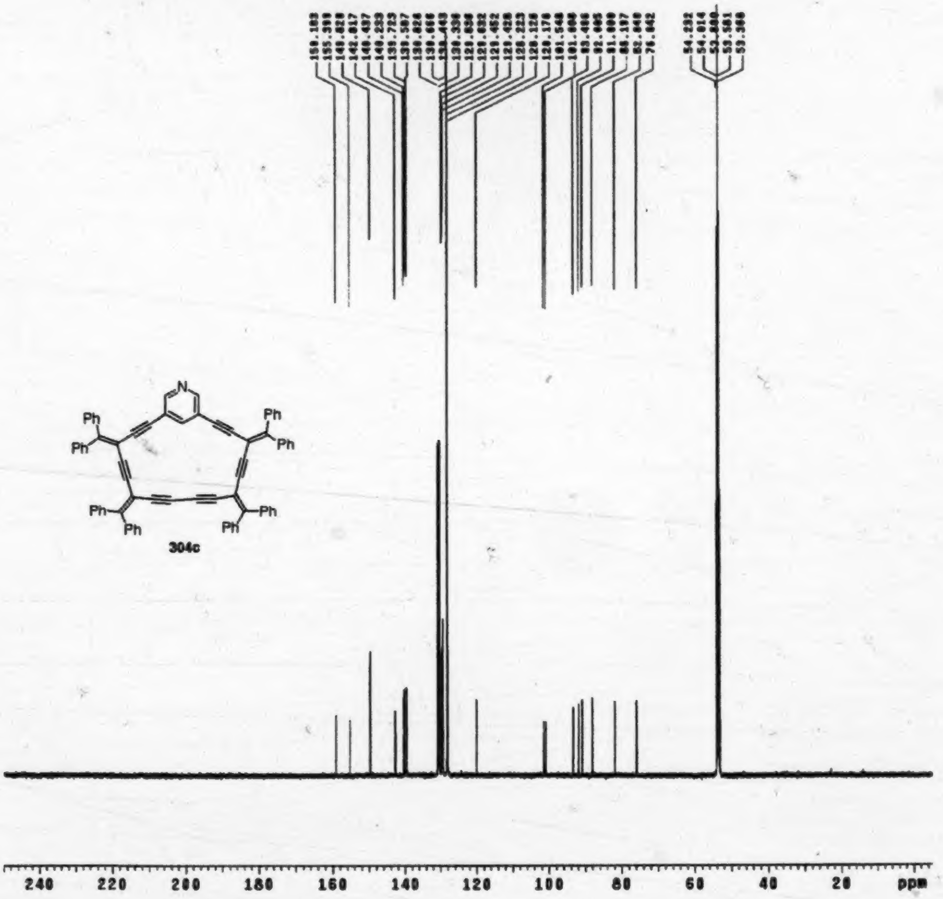

Figure A11 ^{13}C NMR spectrum of **304c**.

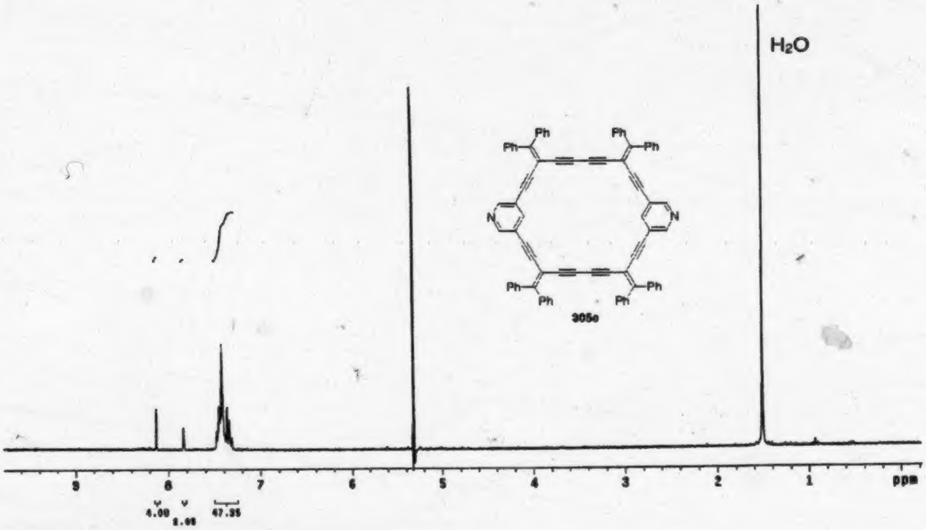

Figure A12 ^{1}H NMR spectrum of **305c**.

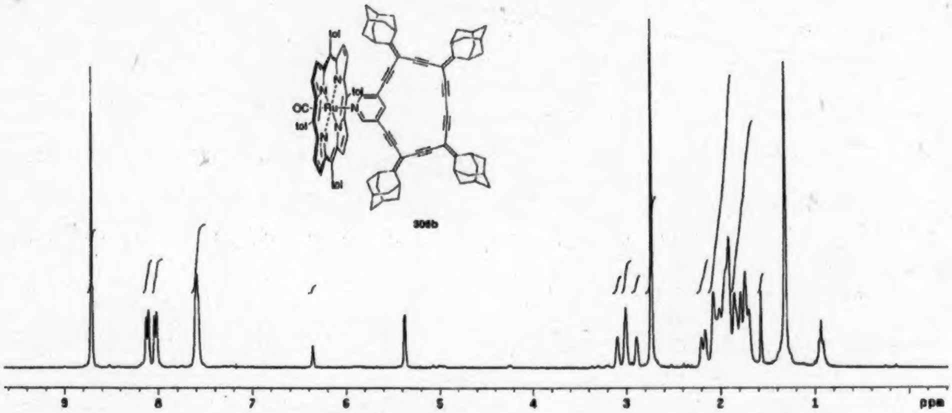

Figure A13 ^{1}H NMR spectrum of **308b**.

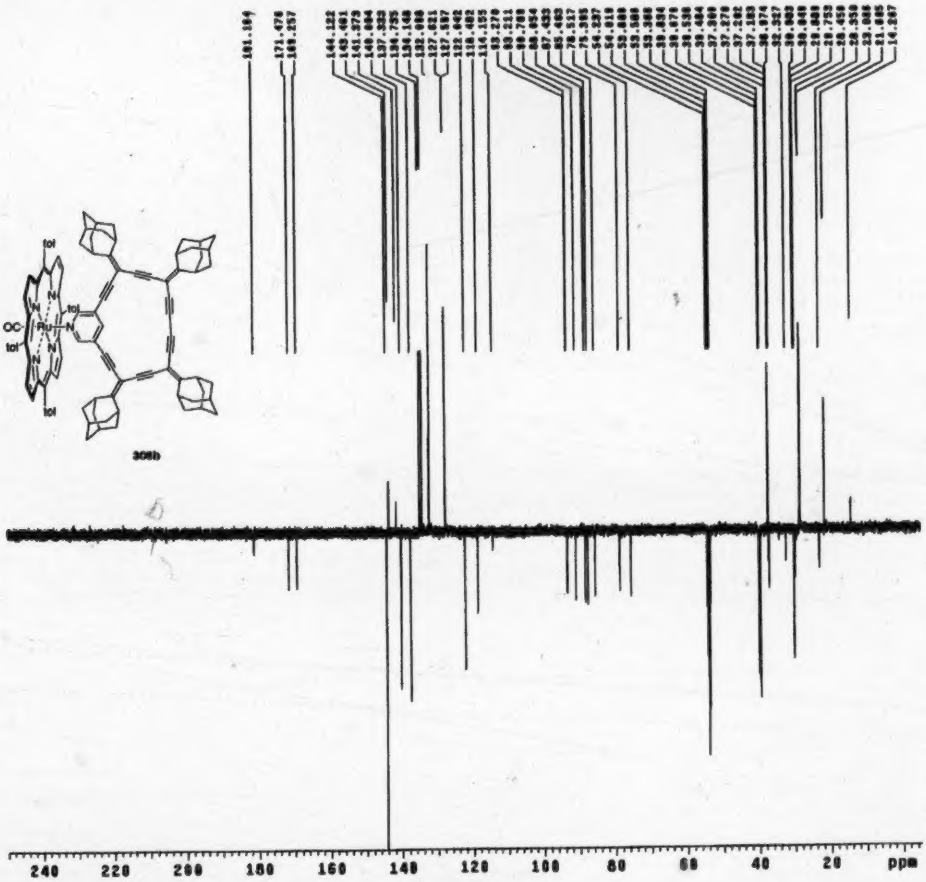

Figure A14 ^{13}C (APT) NMR spectrum of **308b**.

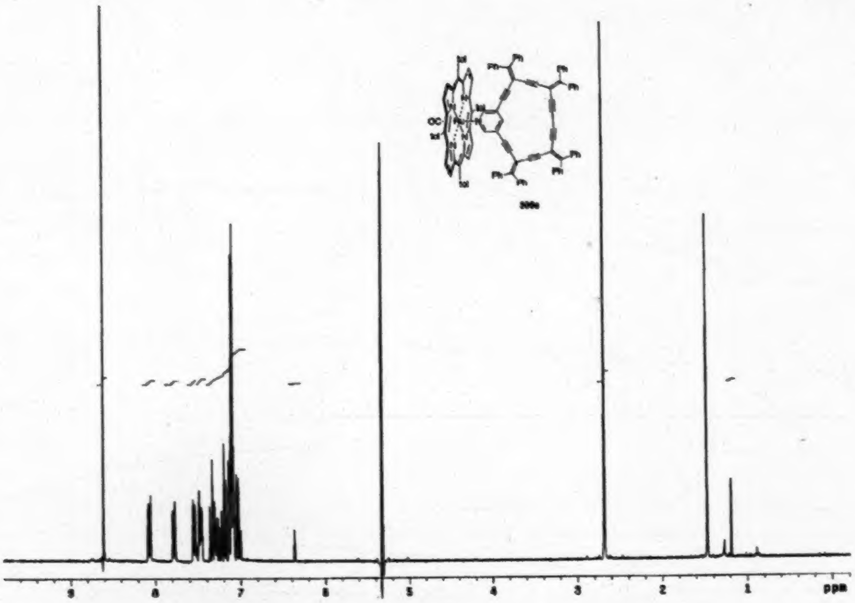

Figure A15 ^{1}H NMR spectrum of **308c**.

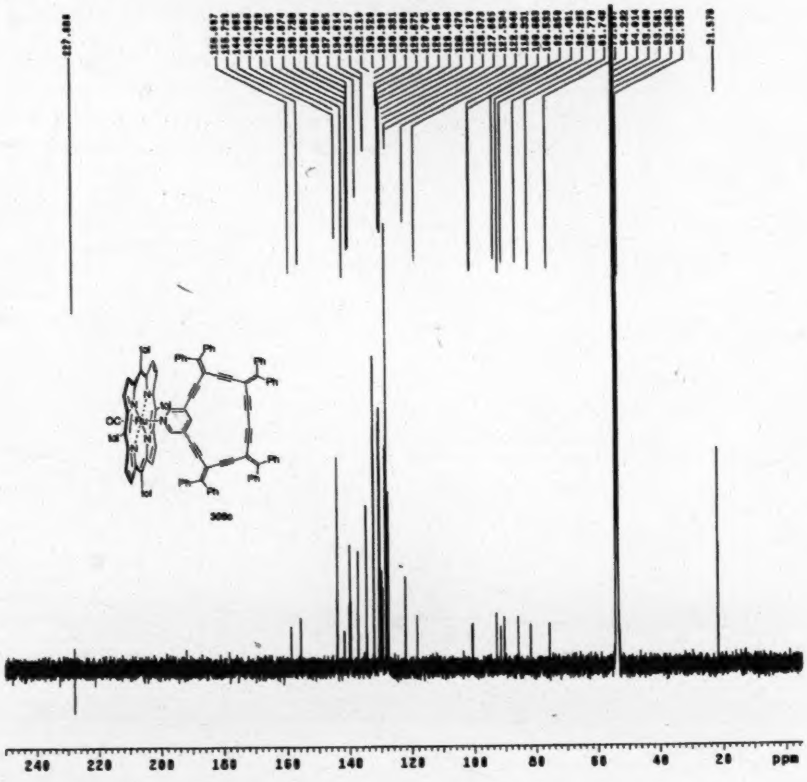

Figure A16 ^{13}C NMR spectrum of **308c**.

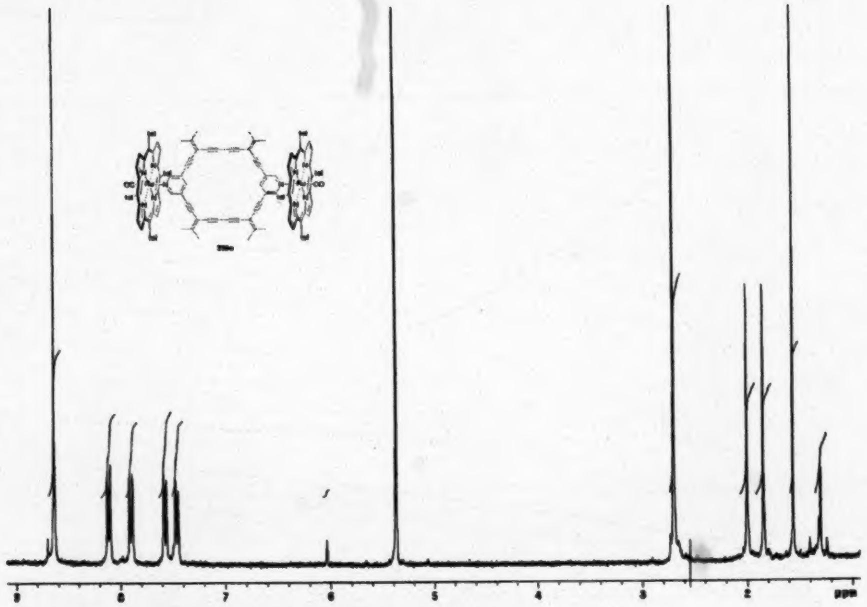

Figure A17 ^{1}H NMR spectrum of **309a**.

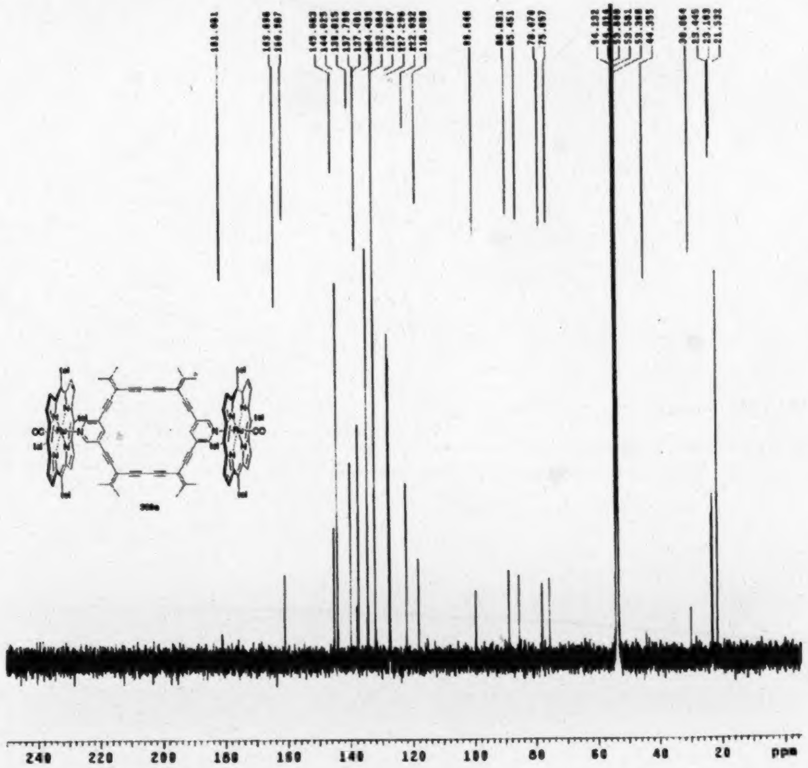

Figure A18 ^{13}C NMR spectrum of **309a**.

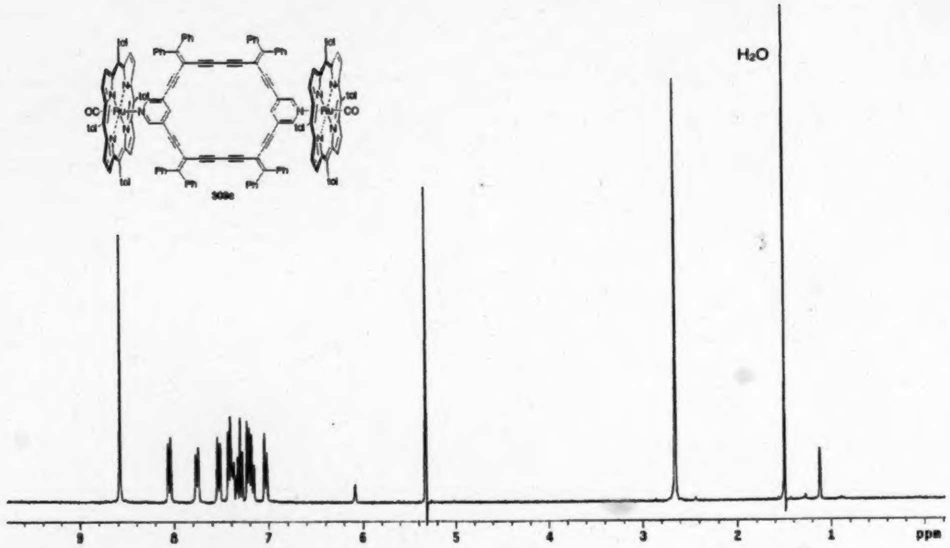

Figure A19 ^{1}H NMR spectrum of **309c**.

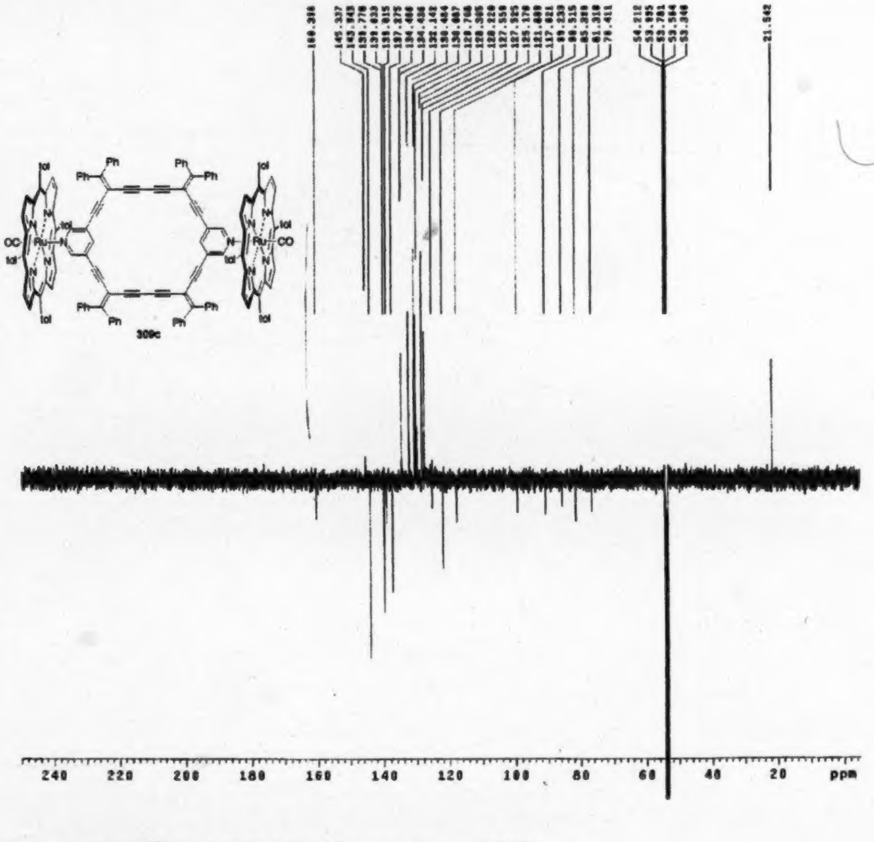

Figure A20 ^{13}C (APT) NMR spectrum of **309c**.

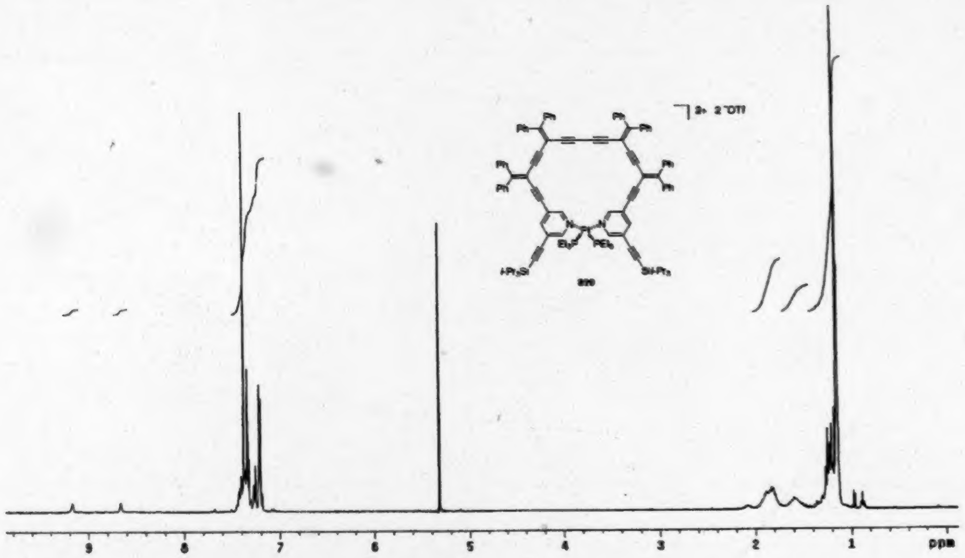

Figure A21 ^{1}H NMR spectrum of **320**.

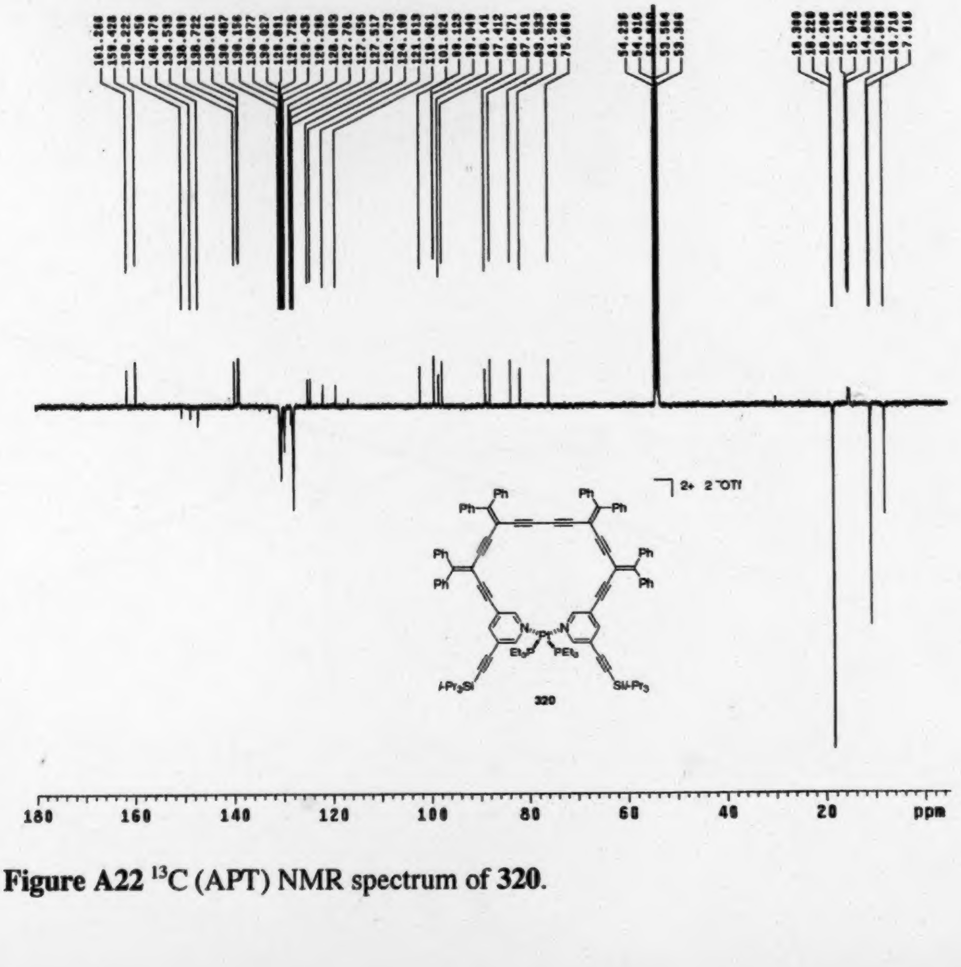

Figure A22 ^{13}C (APT) NMR spectrum of **320**.

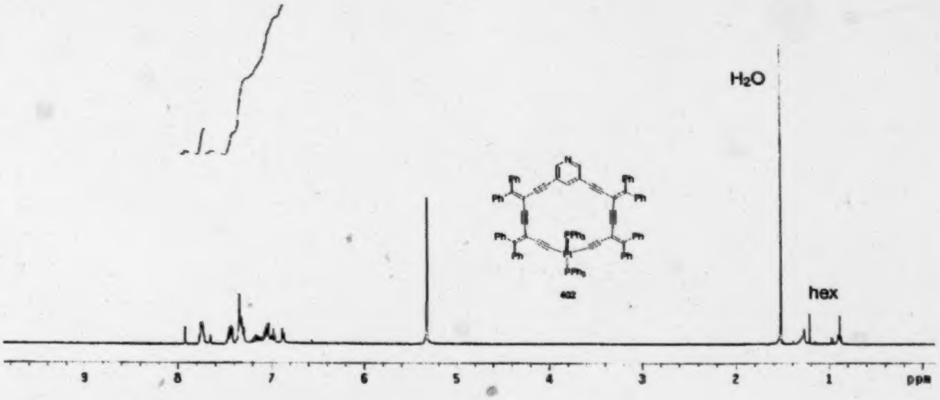

Figure A23 ^{1}H NMR spectrum of **402**.

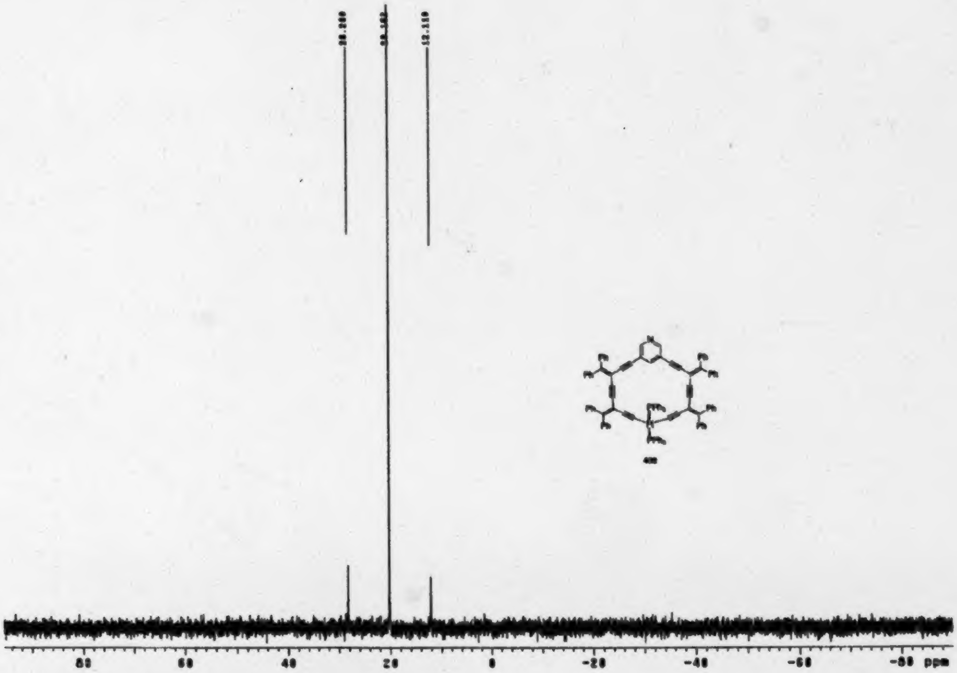

Figure A24 ^{31}P NMR spectrum of **402**.

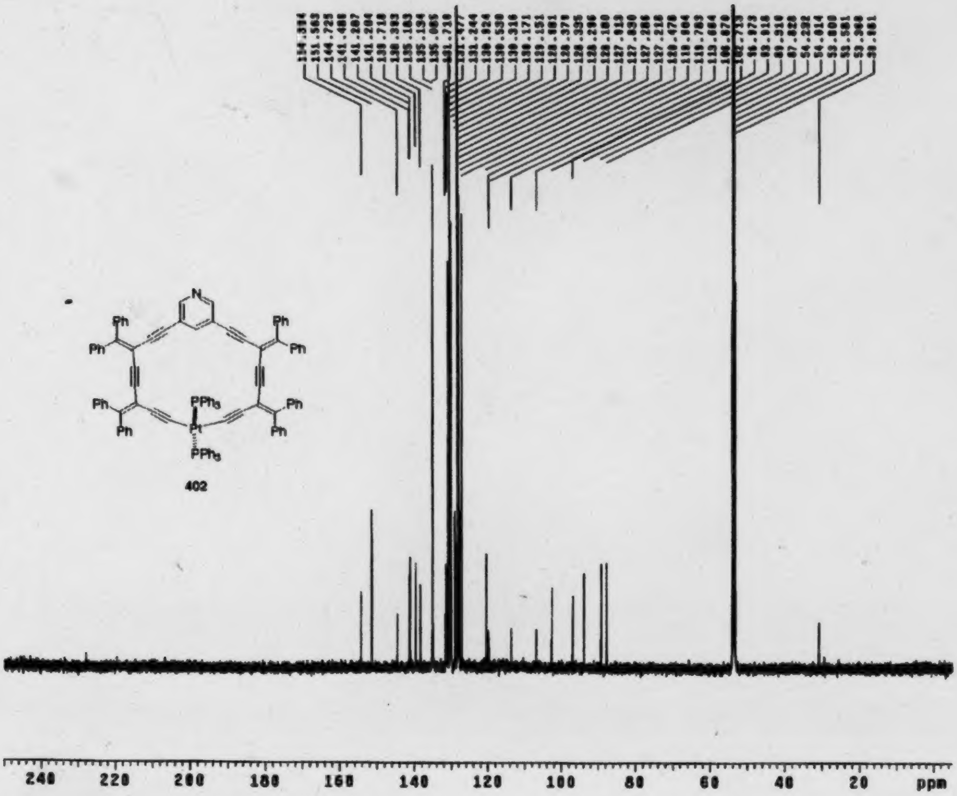

Figure A25 ^{13}C NMR spectrum of **402**.

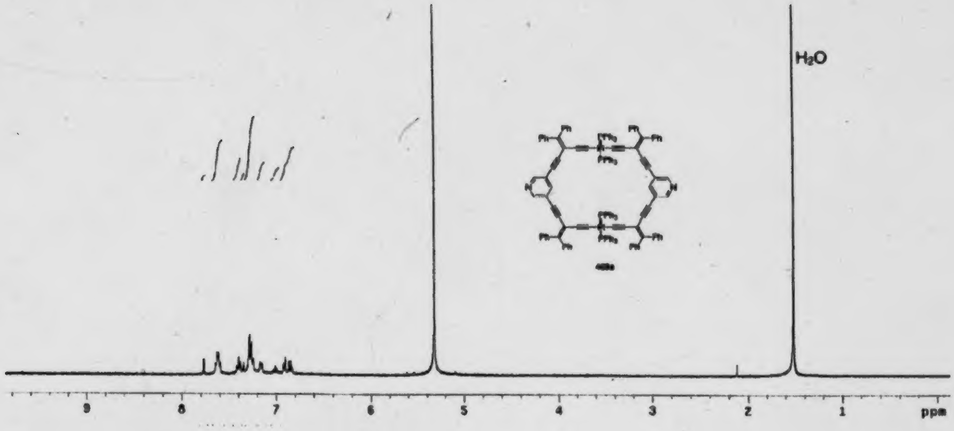

Figure A26 ^{1}H NMR spectrum of **403a**.

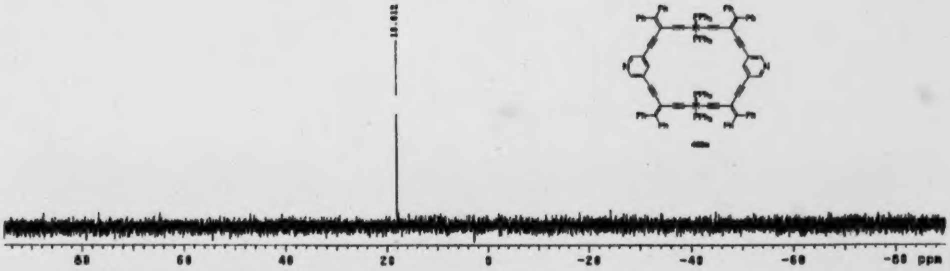

Figure A27 ^{31}P NMR spectrum of **403a**.

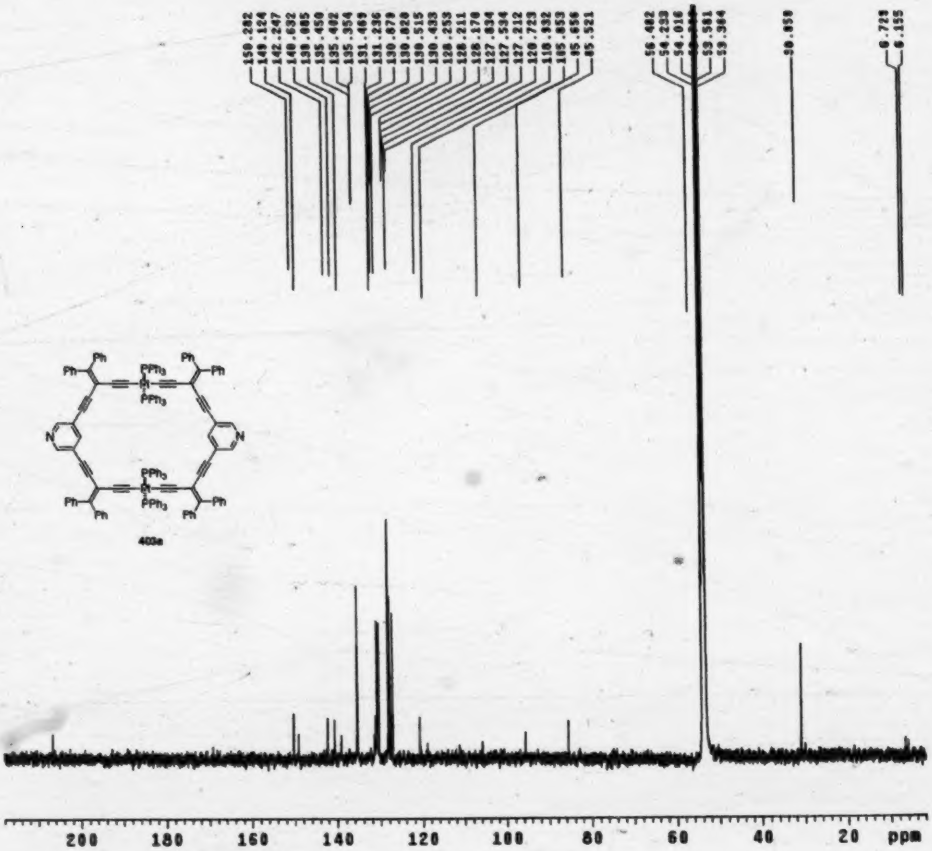

Figure A28 ^{13}C NMR spectrum of **403a**.

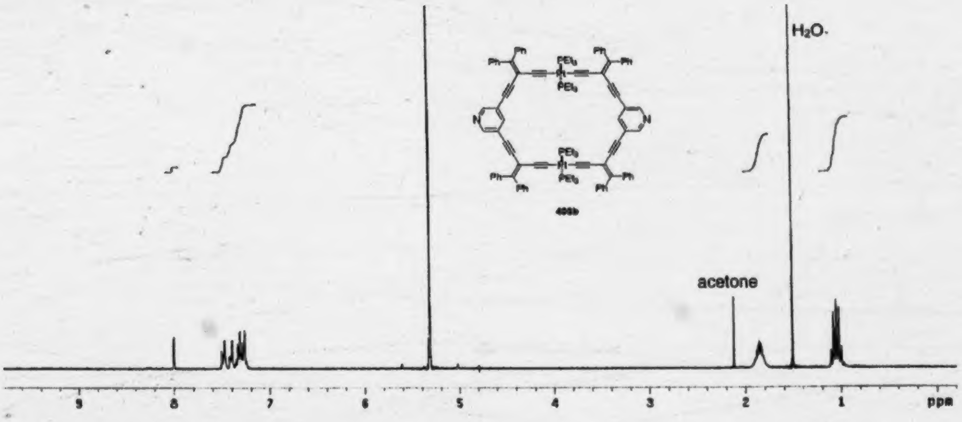

Figure A29 ^{1}H NMR spectrum of **403b**.

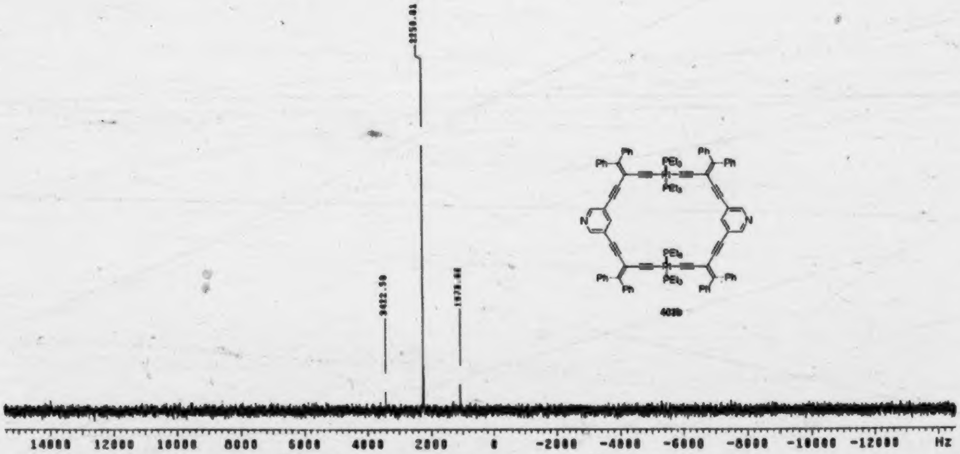

Figure A30 ^{31}P NMR spectrum of **403b**.

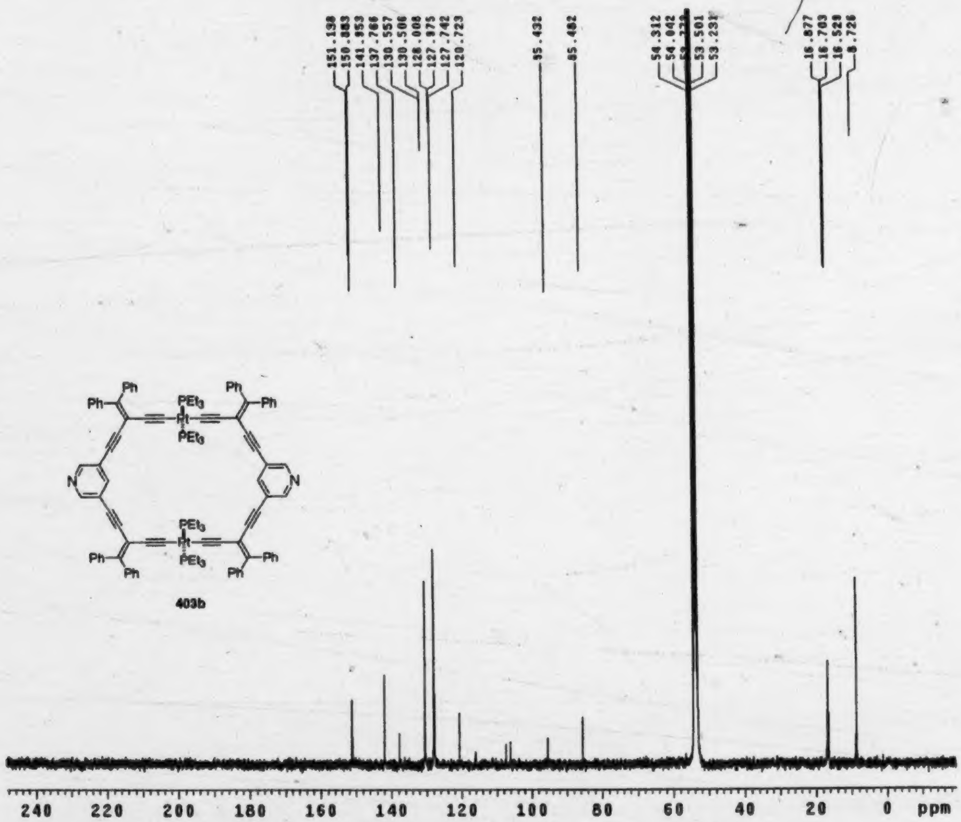

Figure A31 ^{13}C NMR spectrum of **403b**.

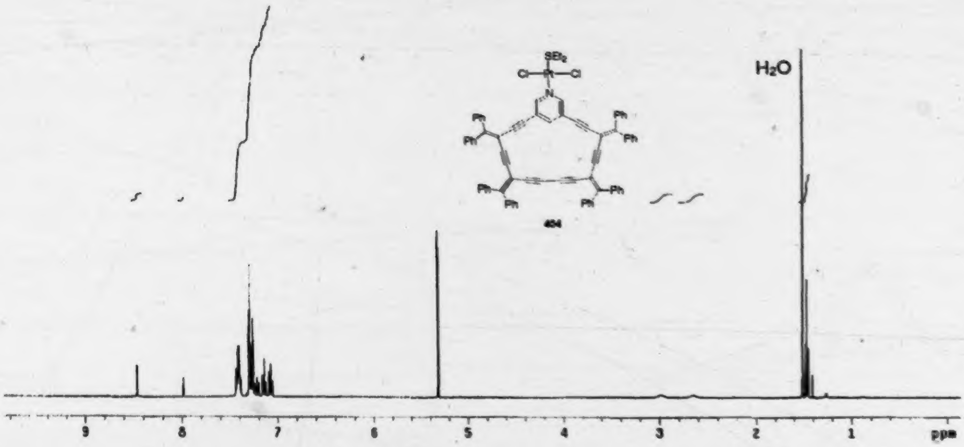

Figure A32 ^{1}H NMR spectrum of **404**.

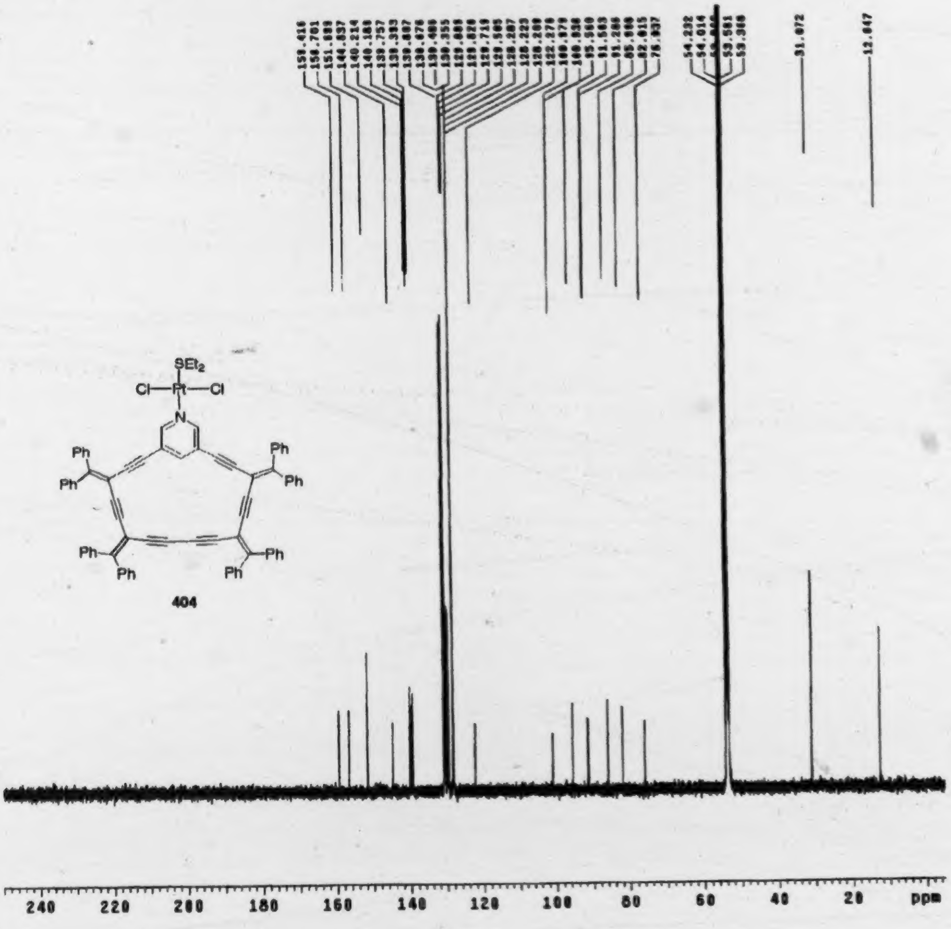

Figure A33 ^{13}C NMR spectrum of **404**.

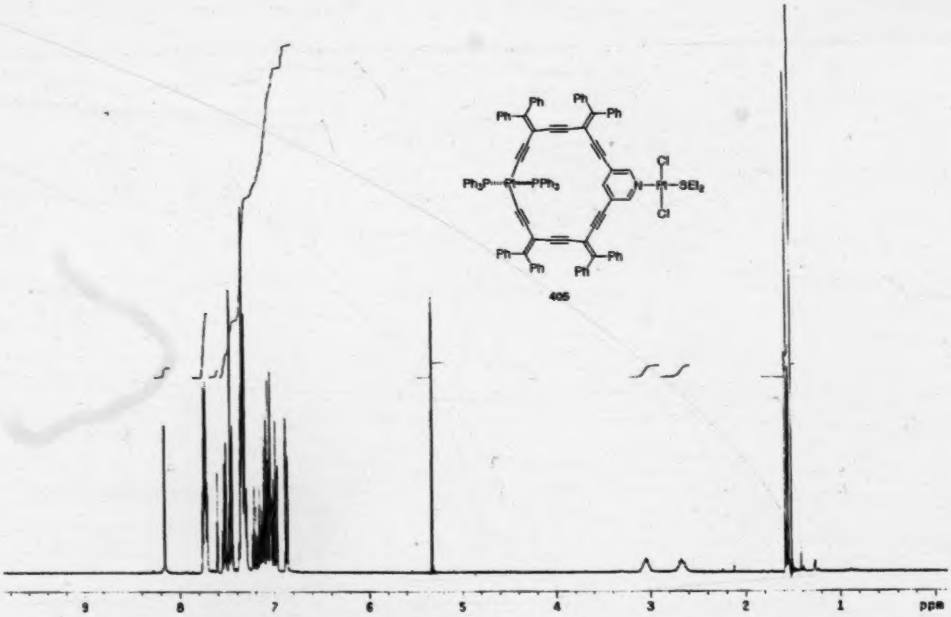

Figure A34 ^{1}H NMR spectrum of **405**.

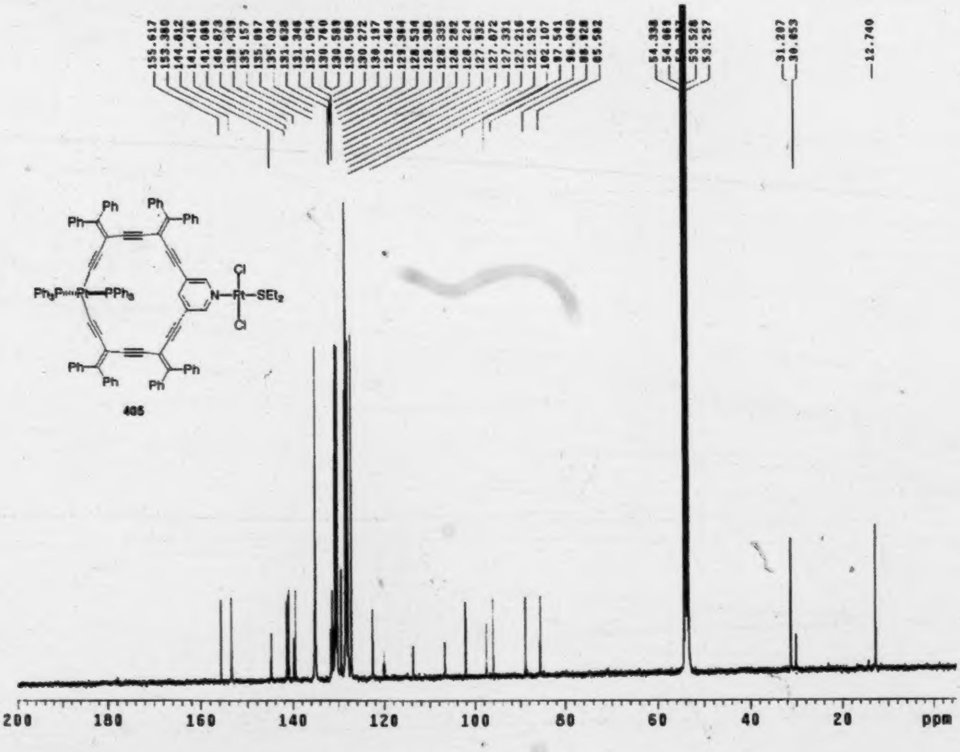

Figure A35 ^{13}C NMR spectrum of **405**.

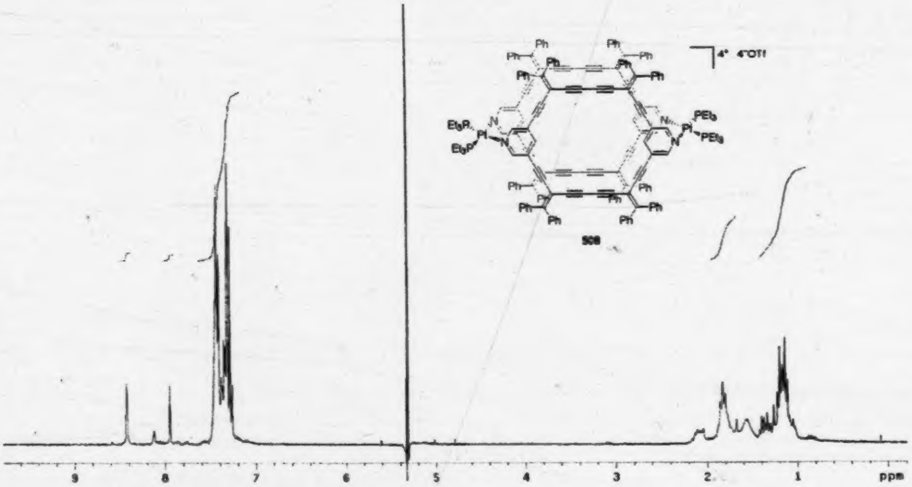

Figure A36 ^{1}H NMR spectrum of **508**.

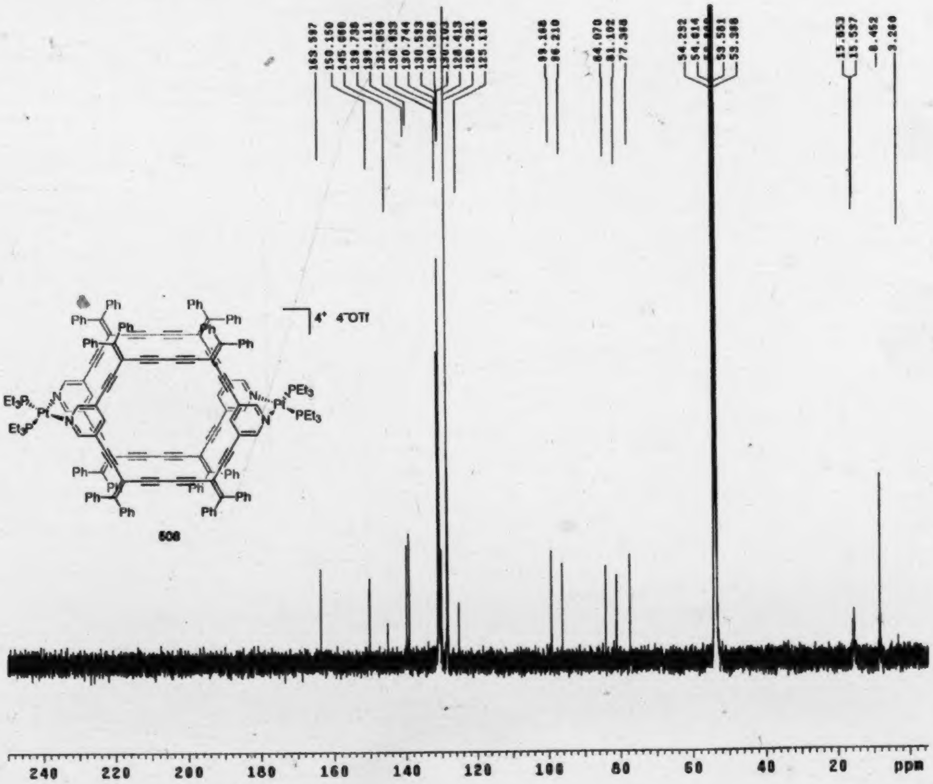

Figure A37 ^{13}C NMR spectrum of **508**.

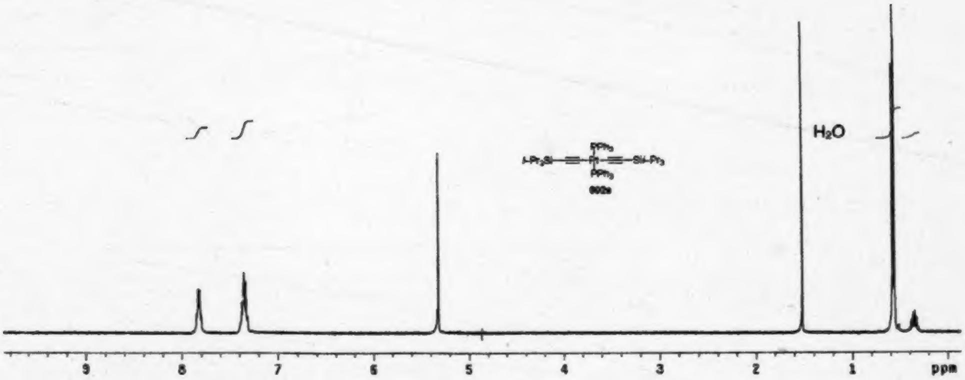

Figure A38 ^{1}H NMR spectrum of **602a**.

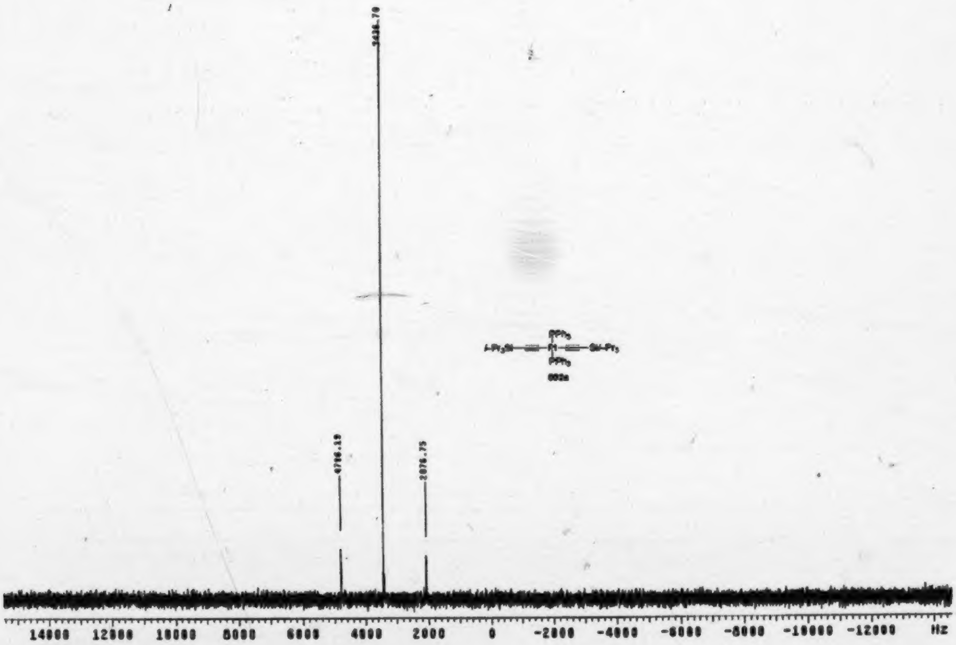

Figure A39 ^{31}P NMR spectrum of **602a**.

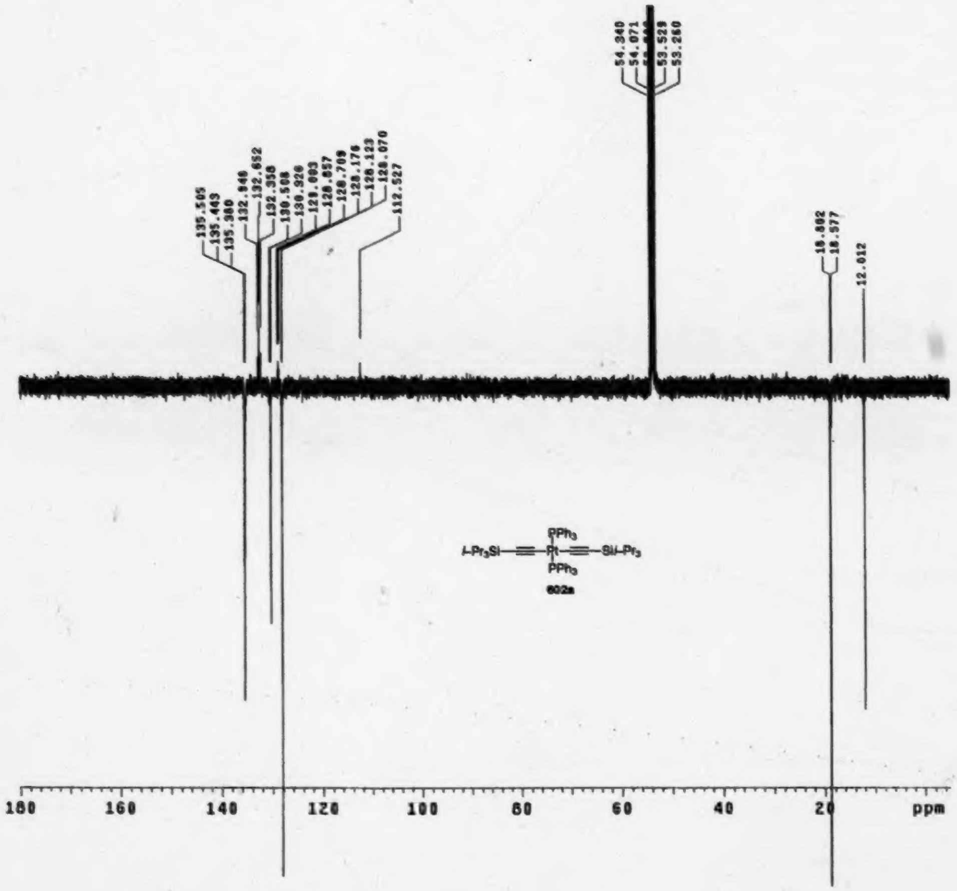

Figure A40 ^{13}C (APT) NMR spectrum of **602a**.

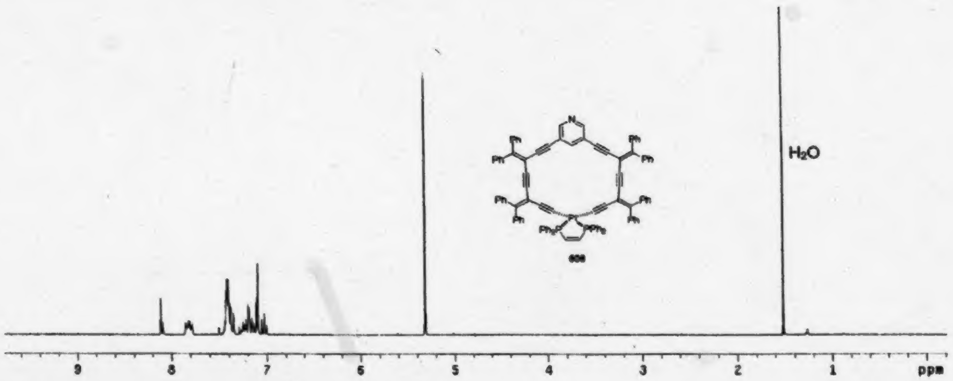

Figure A41 ^{1}H NMR spectrum of **608**.

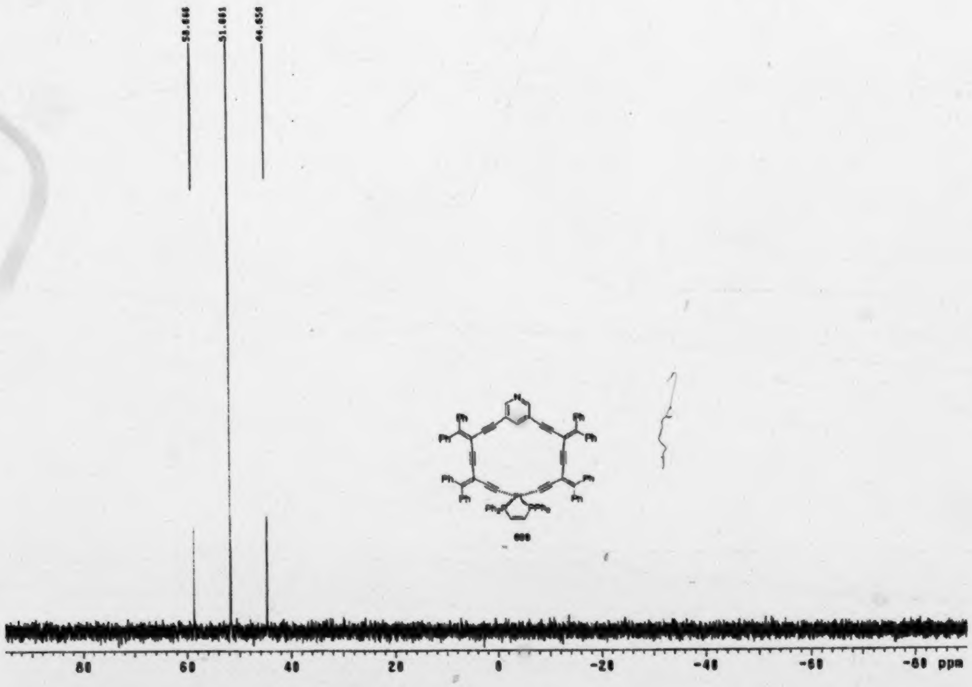

Figure A42 ^{31}P NMR spectrum of **608**.

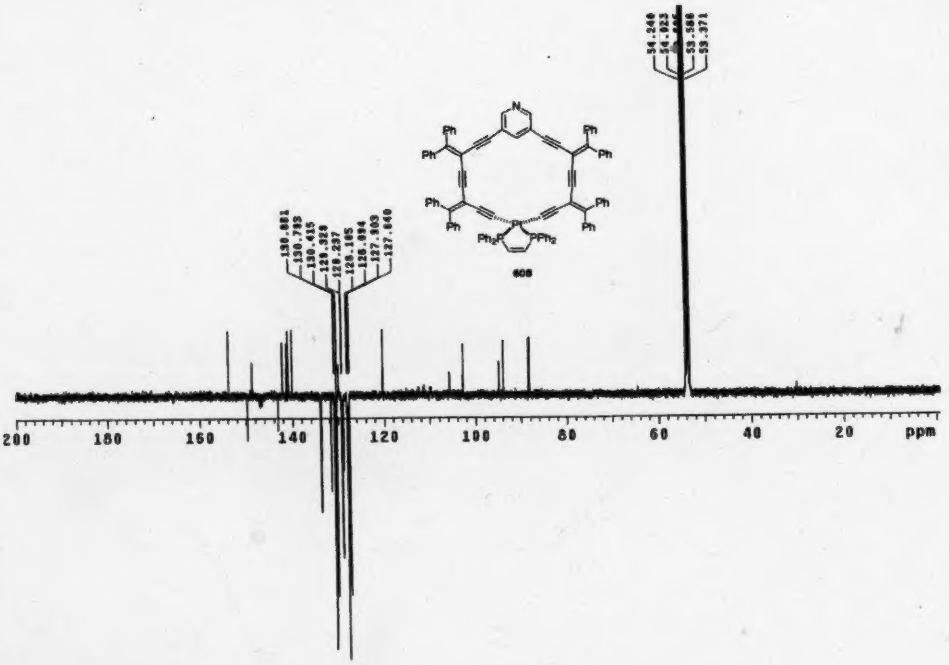

Figure A43 ^{13}C (APT) NMR spectrum of **608**.

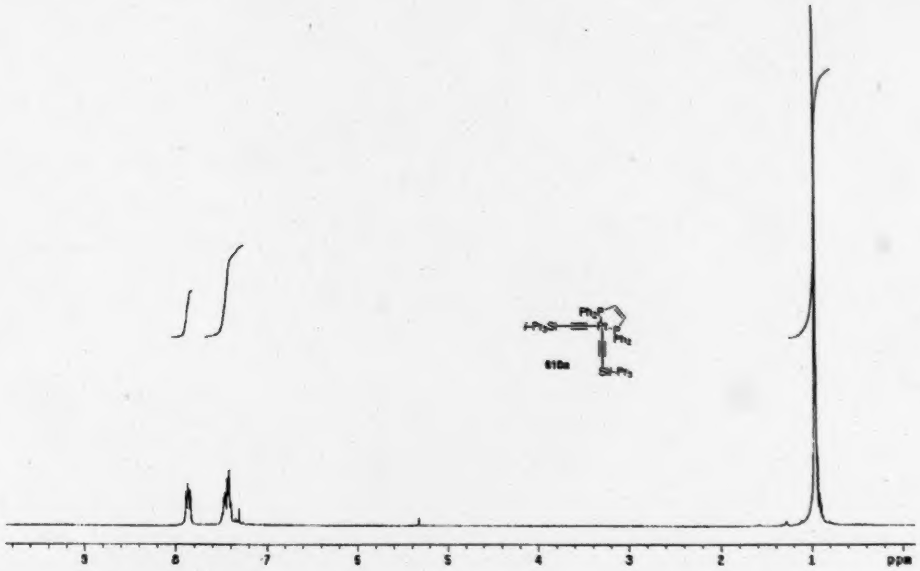

Figure A44 ^{1}H NMR spectrum of **610a**.

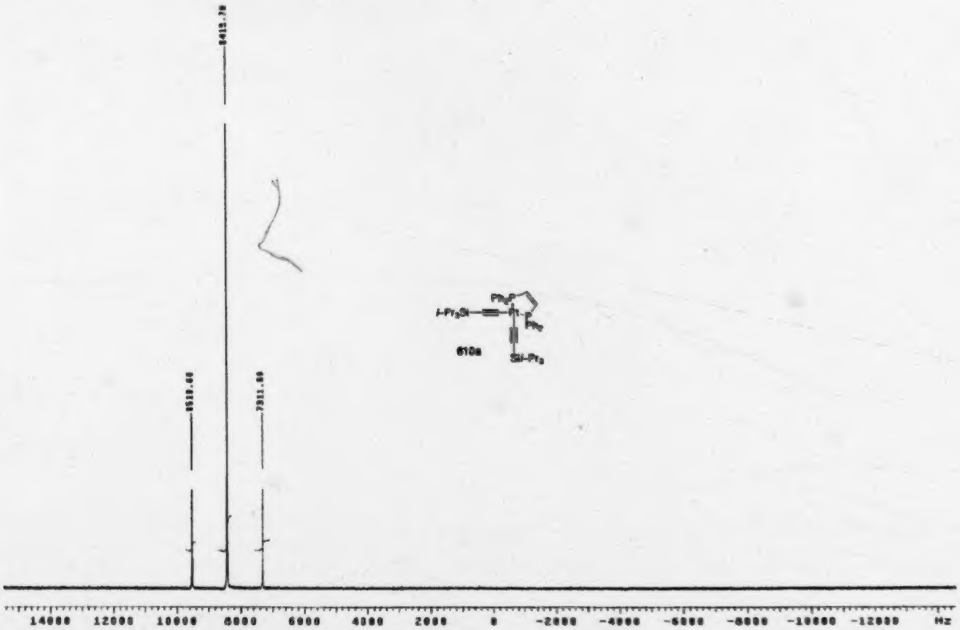

Figure A45 ^{31}P NMR spectrum of **610a**.

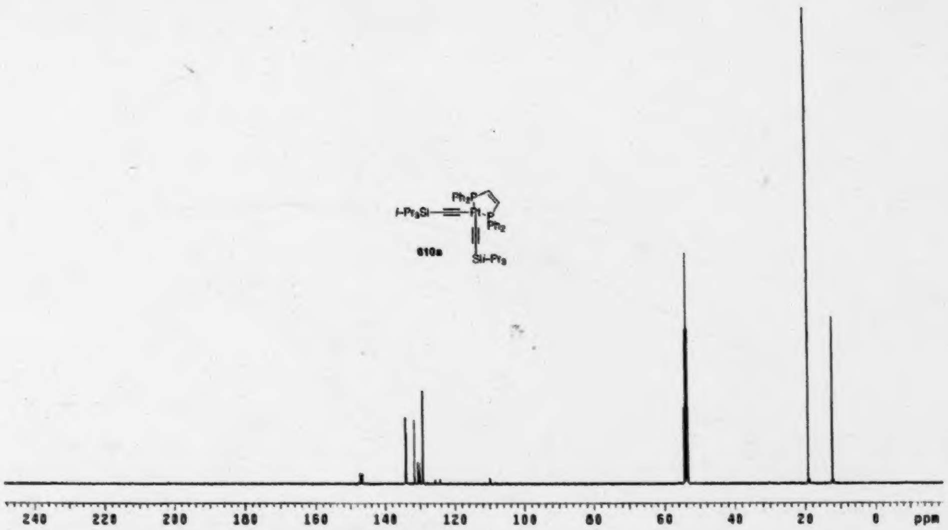

Figure A46 ^{13}C NMR spectrum of **610a**.

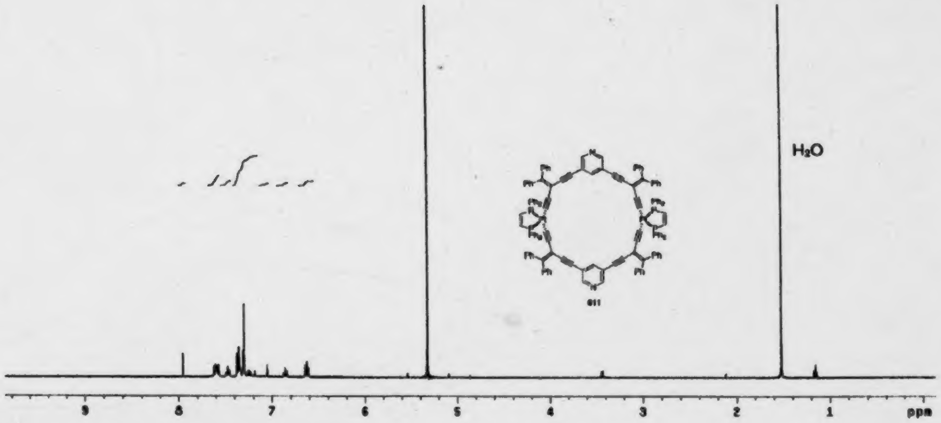

Figure A47 ^{1}H NMR spectrum of **611**.

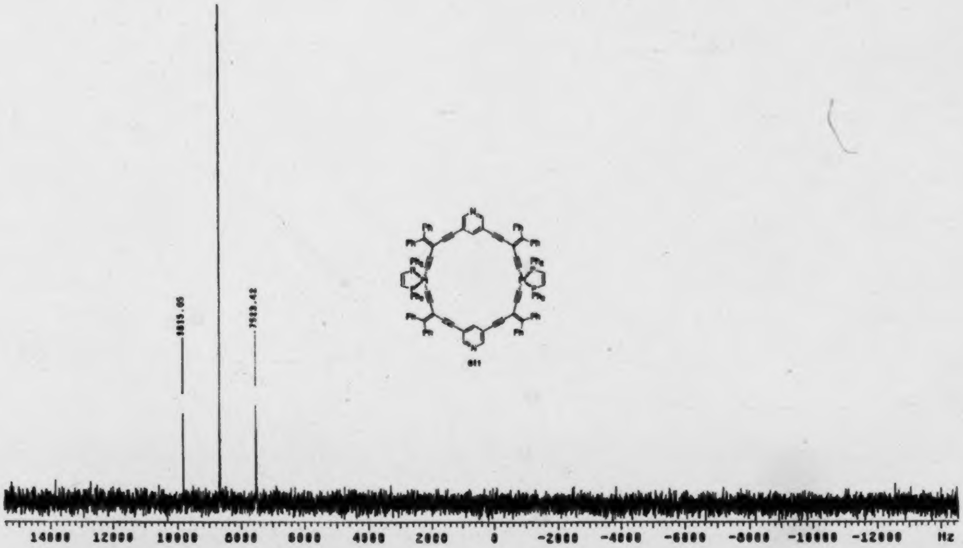

Figure A48 ^{31}P NMR spectrum of **611**.

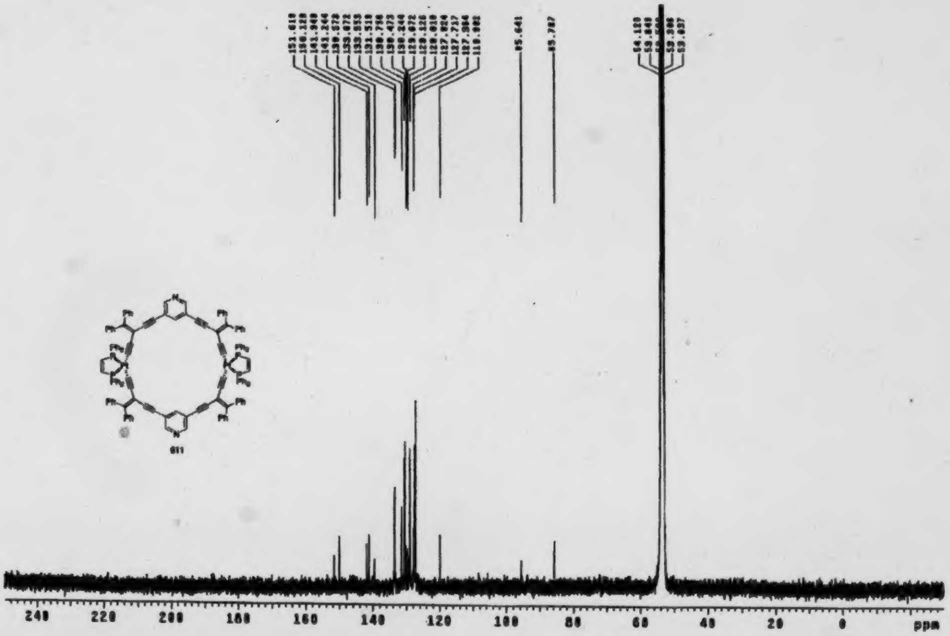

Figure A49 ^{13}C NMR spectrum of **611**.

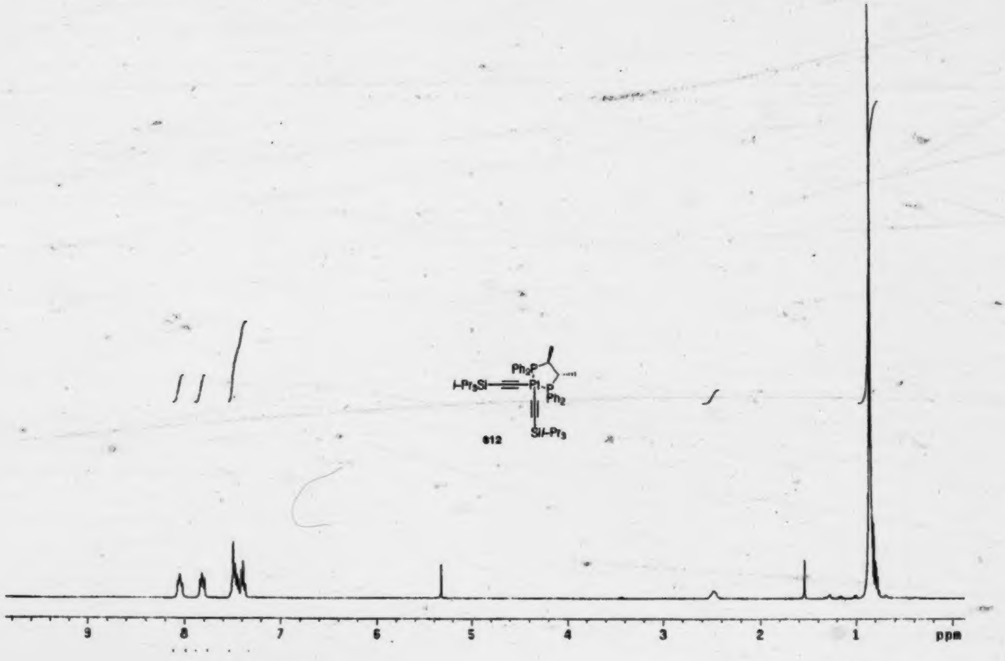

Figure A50 ^{1}H NMR spectrum of **612**.

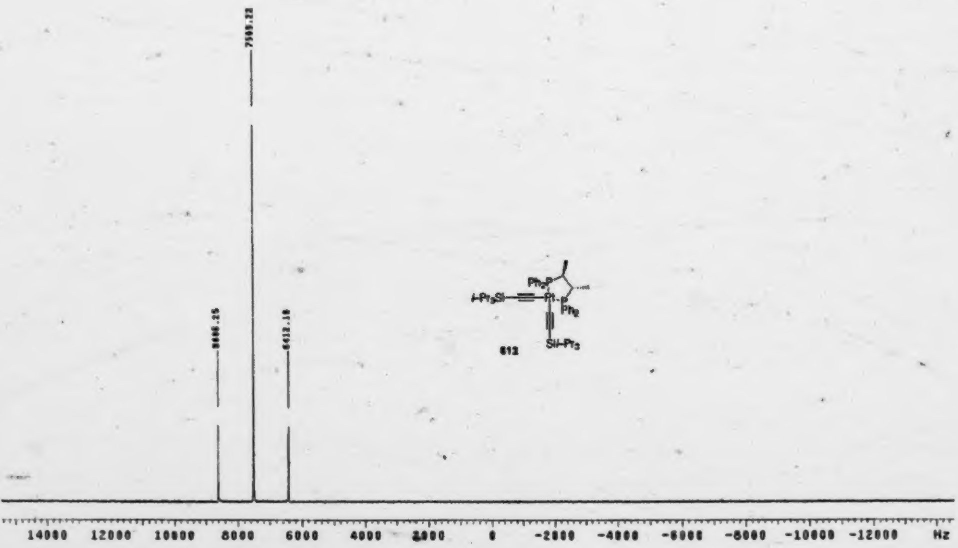

Figure A51 ^{31}P NMR spectrum of **612**.

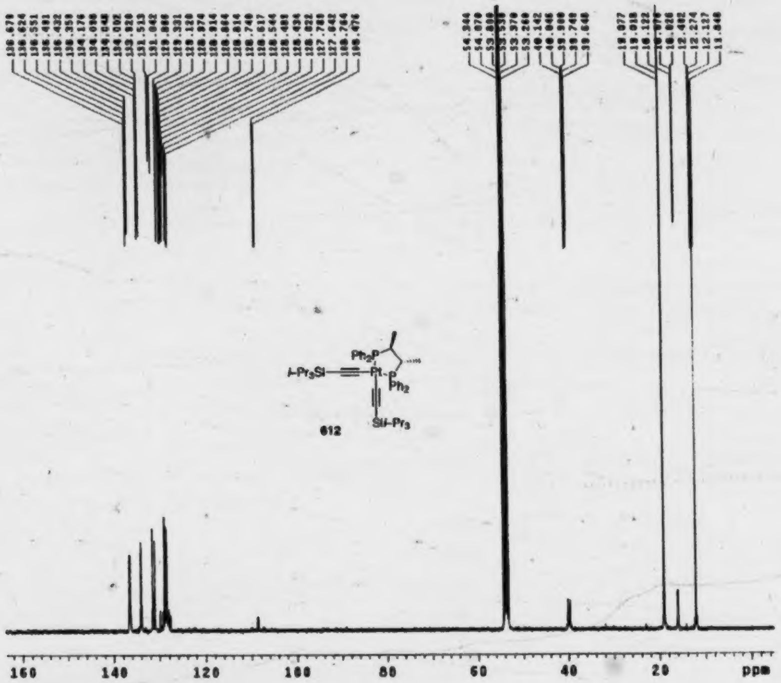

Figure A52 ^{13}C NMR spectrum of **612**.

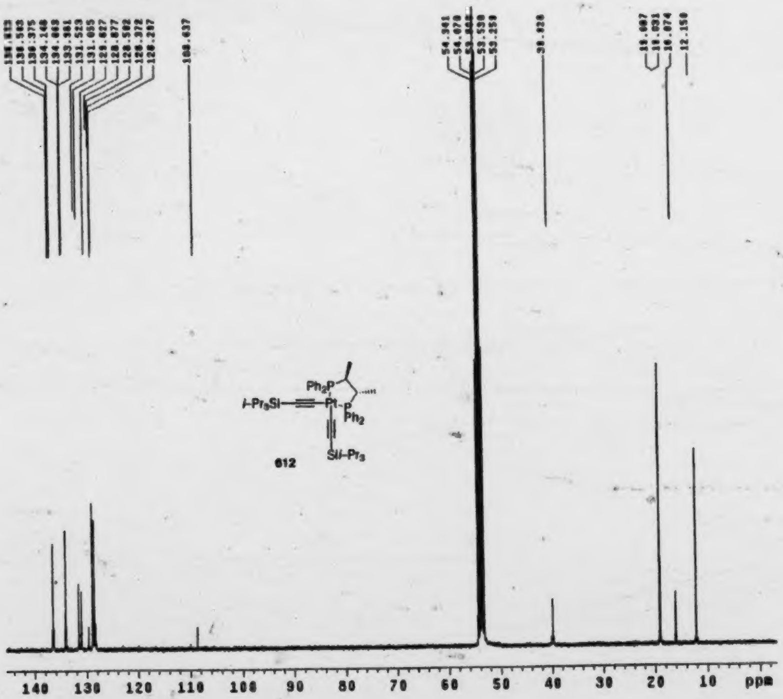

Figure A53 ^{13}C{^{31}P} NMR spectrum of **612**.

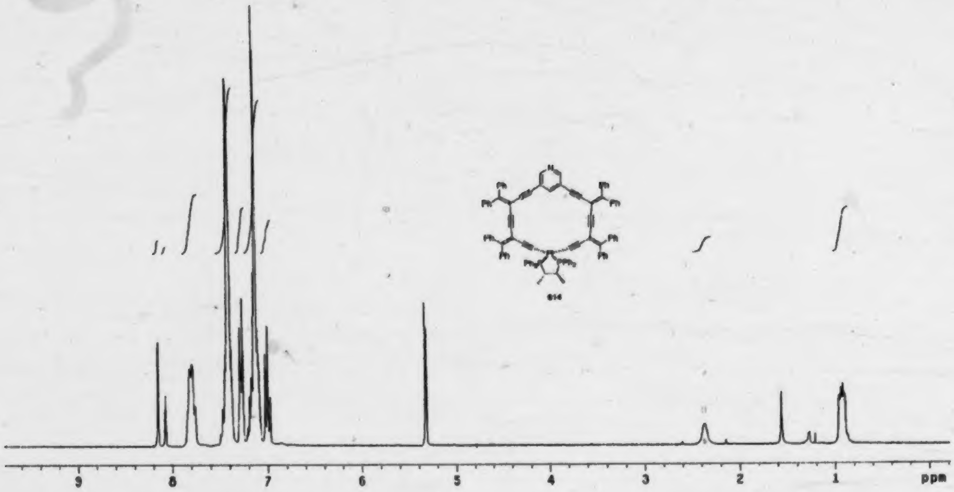

Figure A54 ^{1}H NMR spectrum of **614**.

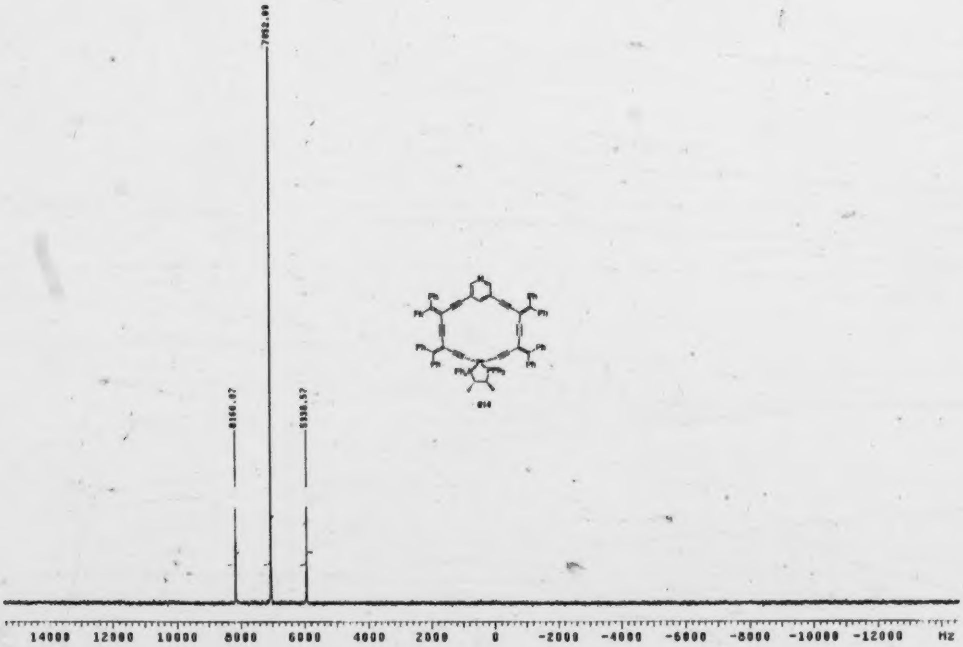

Figure A55 ^{31}P NMR spectrum of **614**.

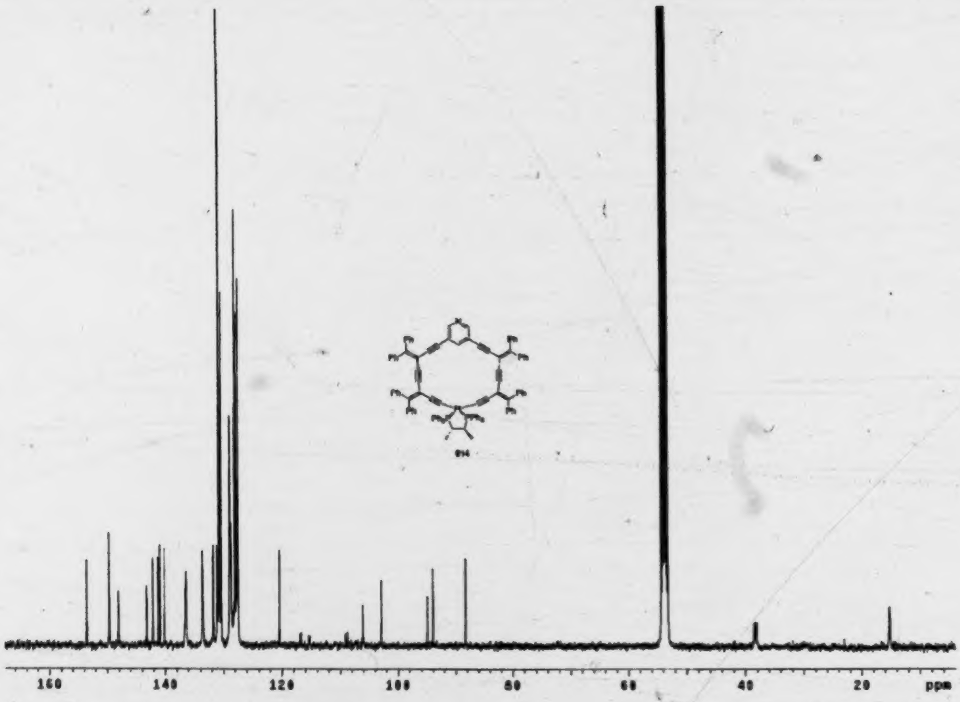

Figure A56 ^{13}C NMR spectrum of **614**.

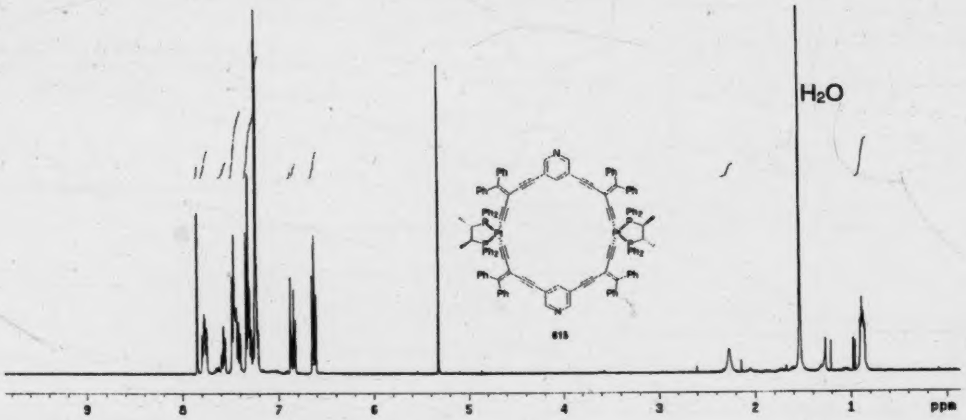

Figure A57 ^1H NMR spectrum of **615**.

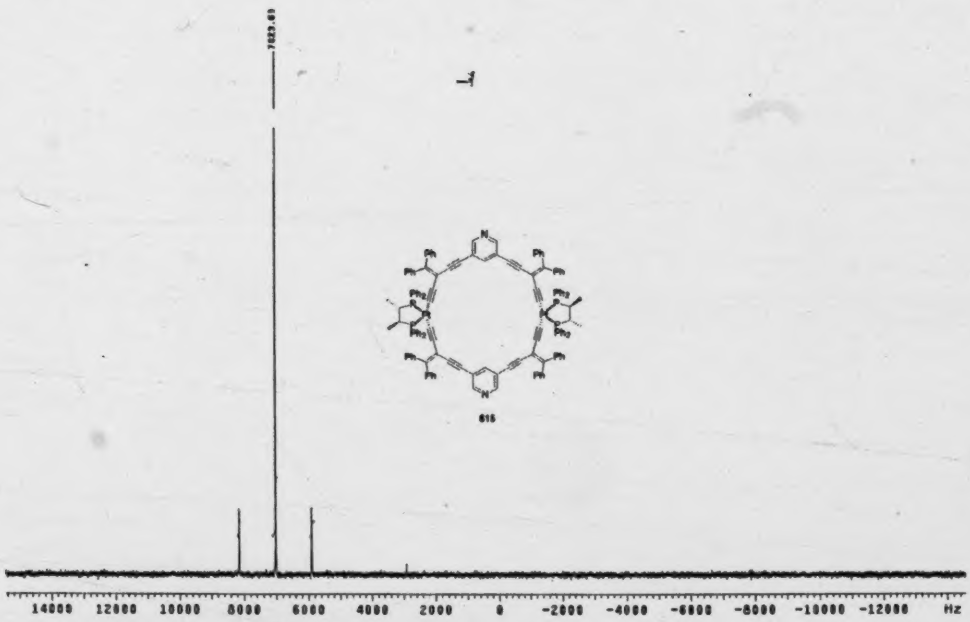

Figure A58 ^{31}P NMR spectrum of **615**.

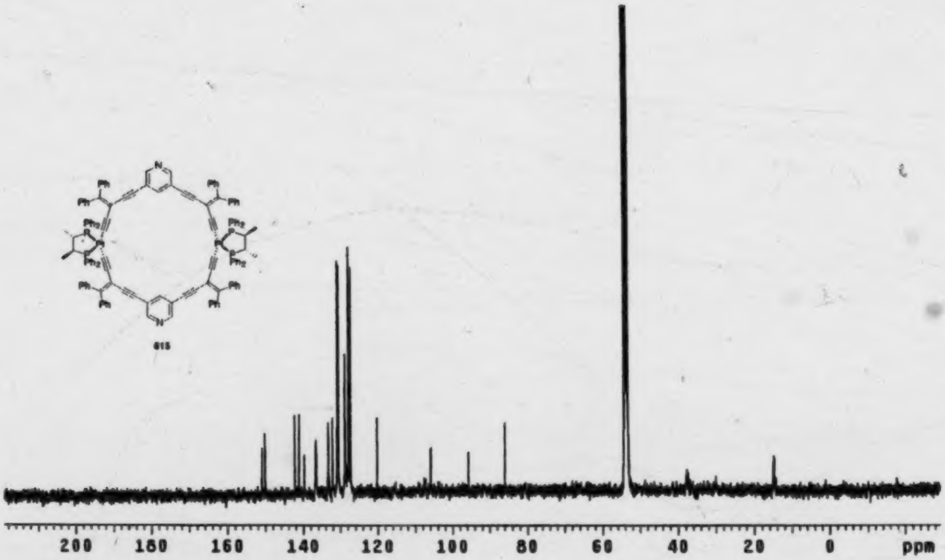

Figure A59 ^{13}C NMR spectrum of **615**.

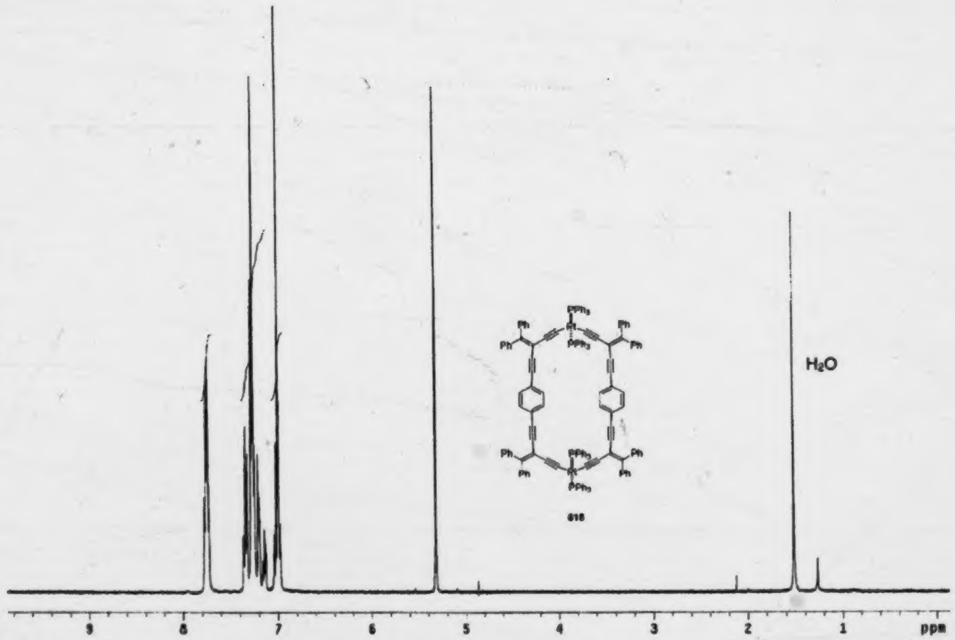

Figure A60 ^{1}H NMR spectrum of **616**.

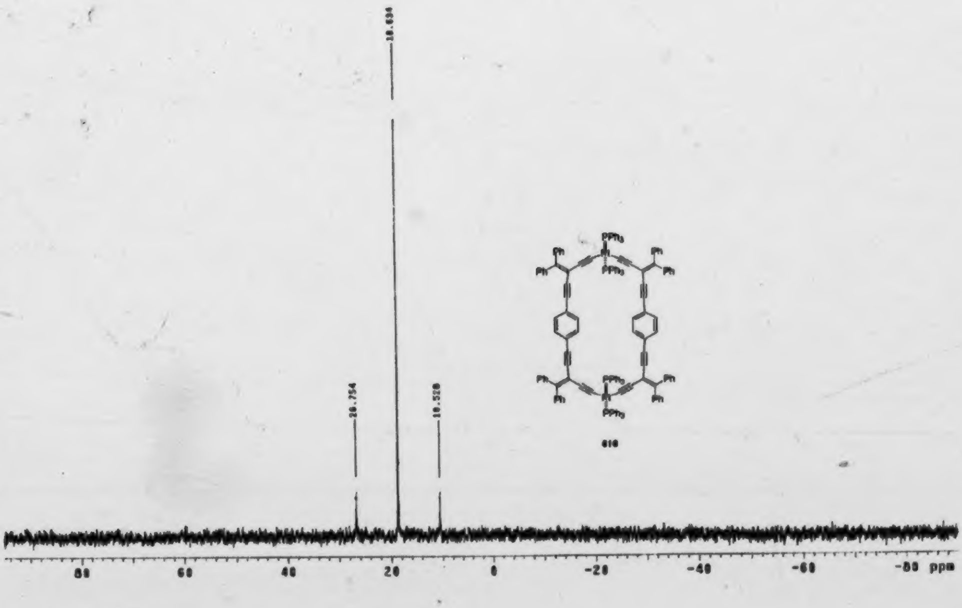

Figure A61 ^{31}P NMR spectrum of **616**.

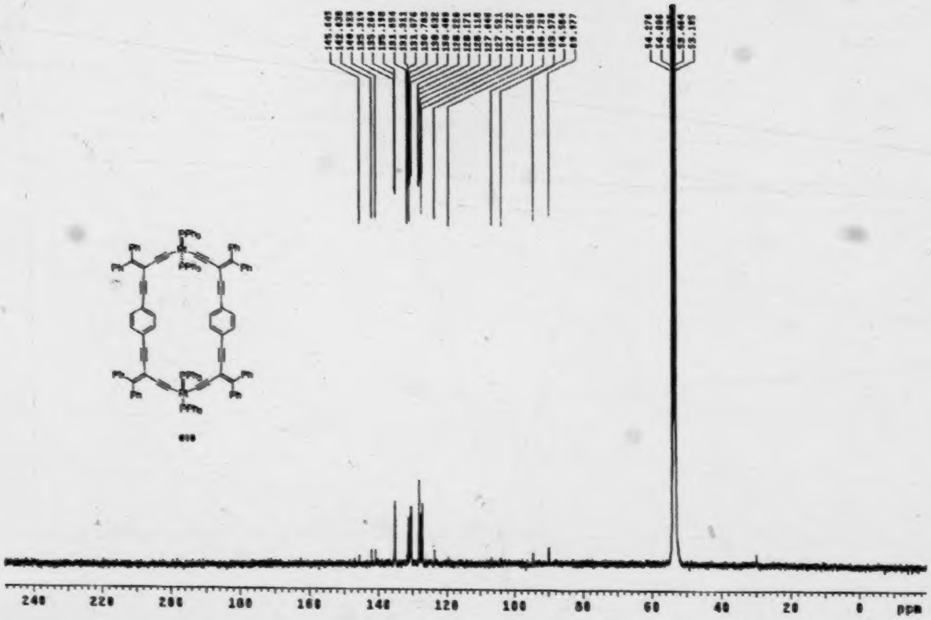

Figure A62 ^{13}C NMR spectrum of **616**.

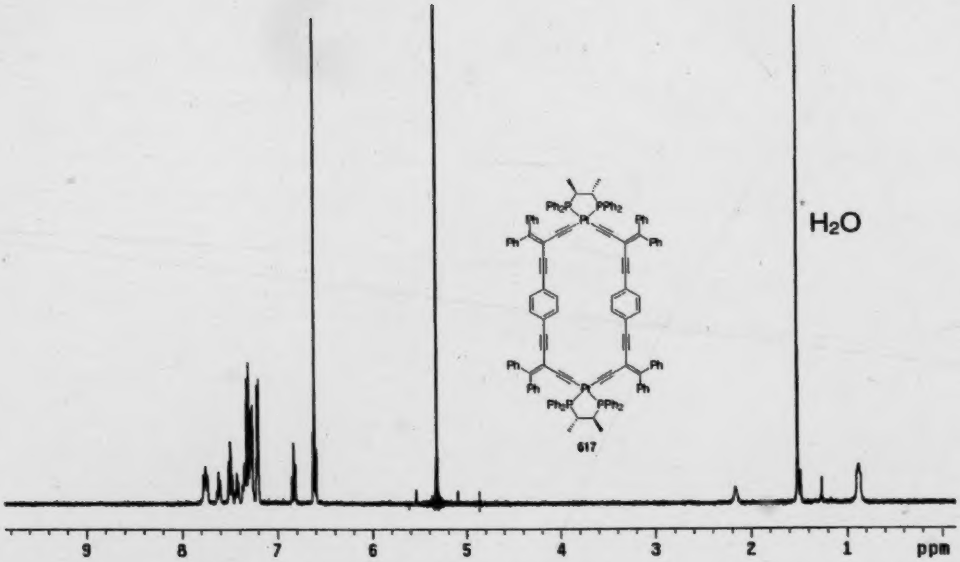

Figure A63 ^{1}H NMR spectrum of **617**.

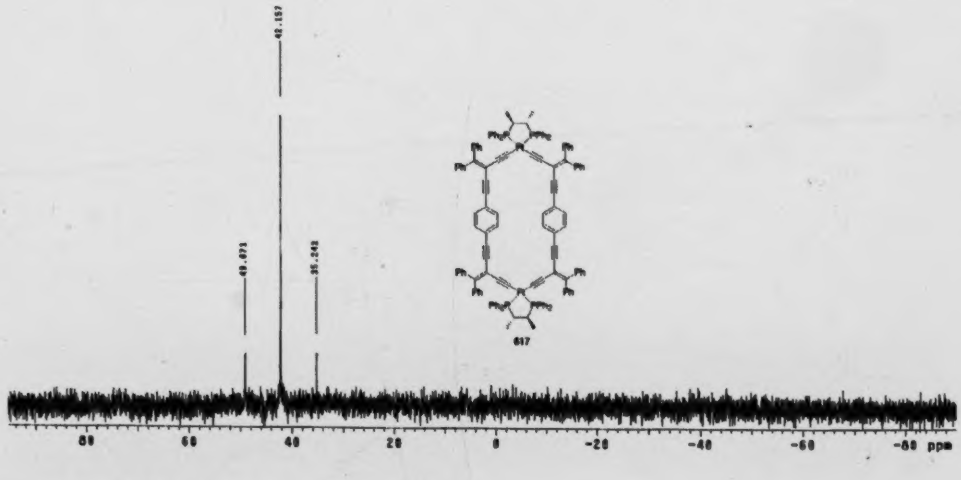

Figure A64 ^{31}P NMR spectrum of **617**.

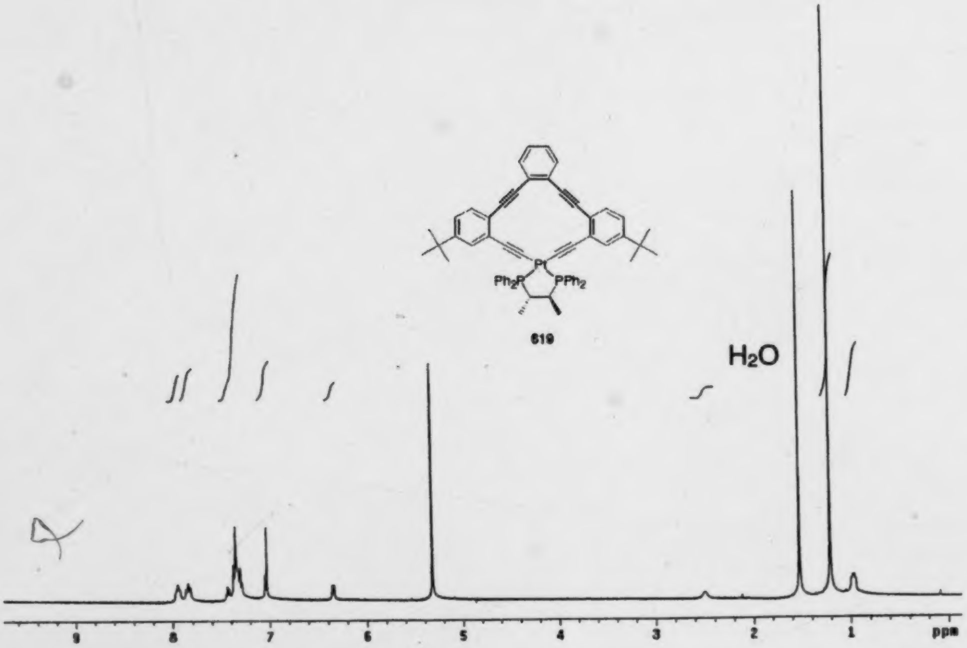

Figure A65 ^{1}H NMR spectrum of **619**.

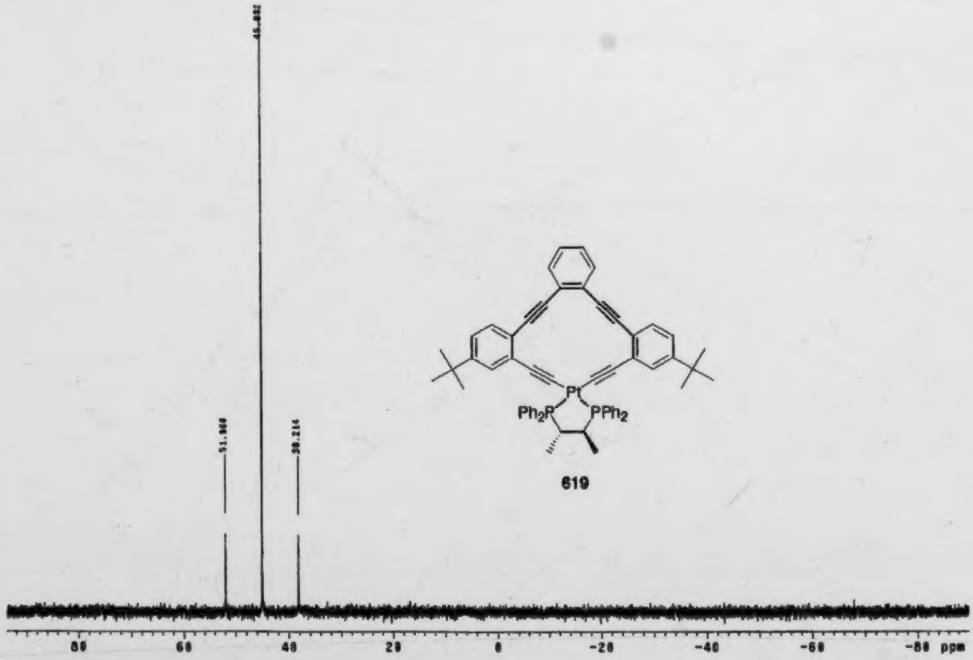

Figure A66 ^{31}P NMR spectrum of **619**.

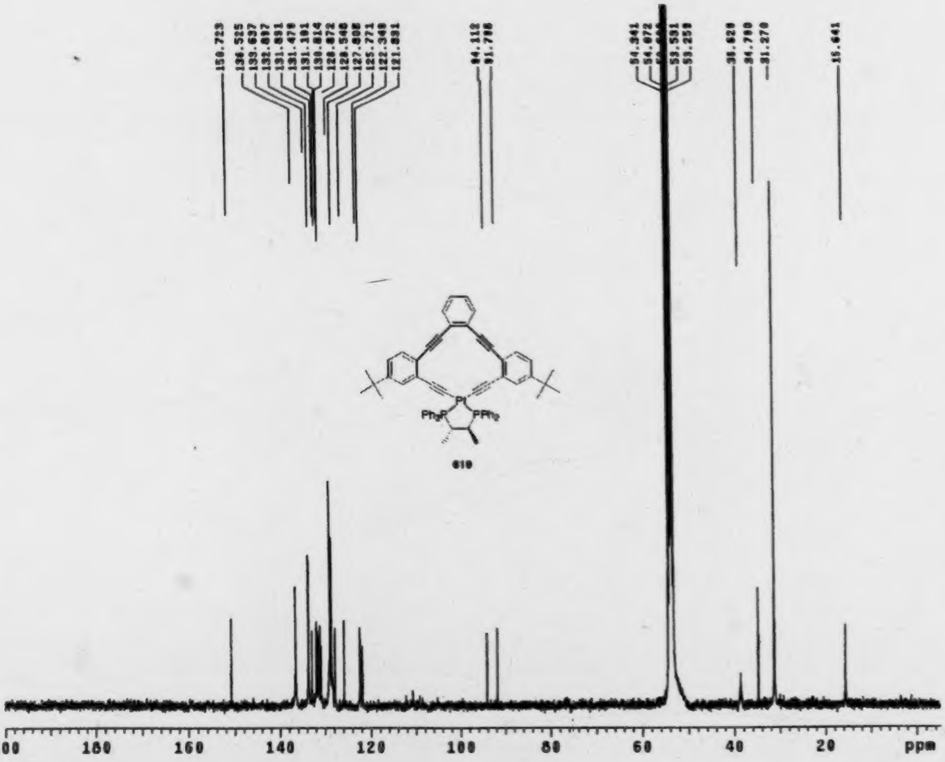

Figure A67 ^{13}C NMR spectrum of **619**.

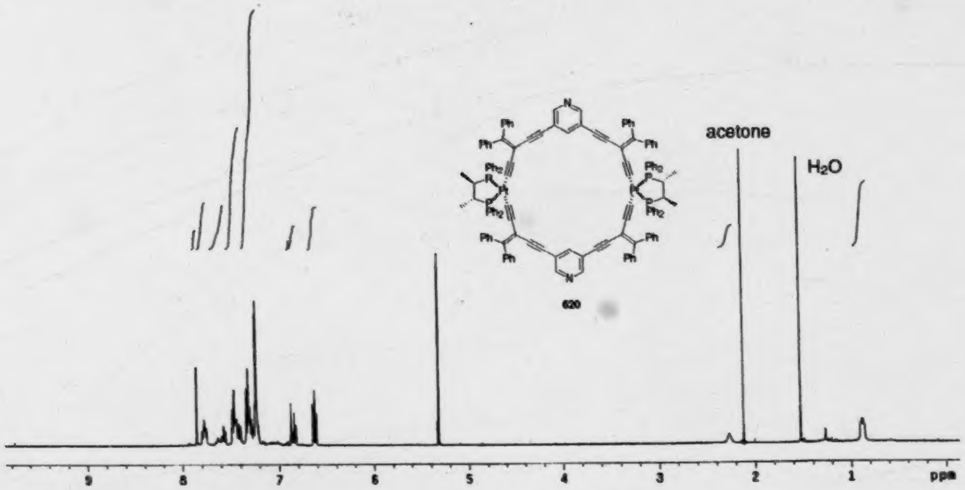

Figure A68 ^{1}H NMR spectrum of **620**.

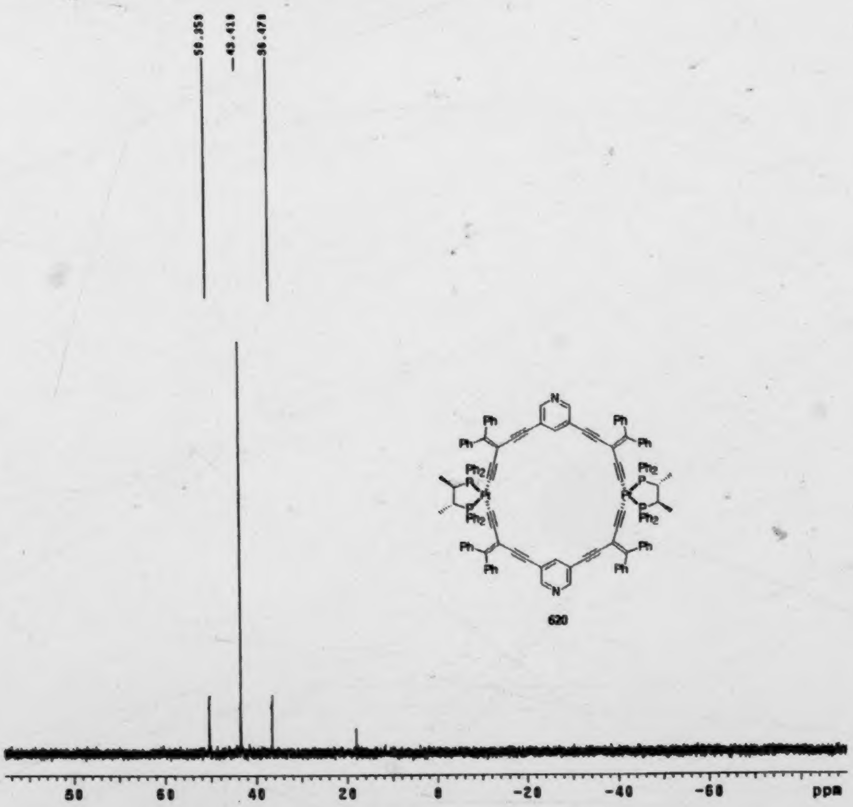

Figure A69 ^{31}P NMR spectrum of **620**.

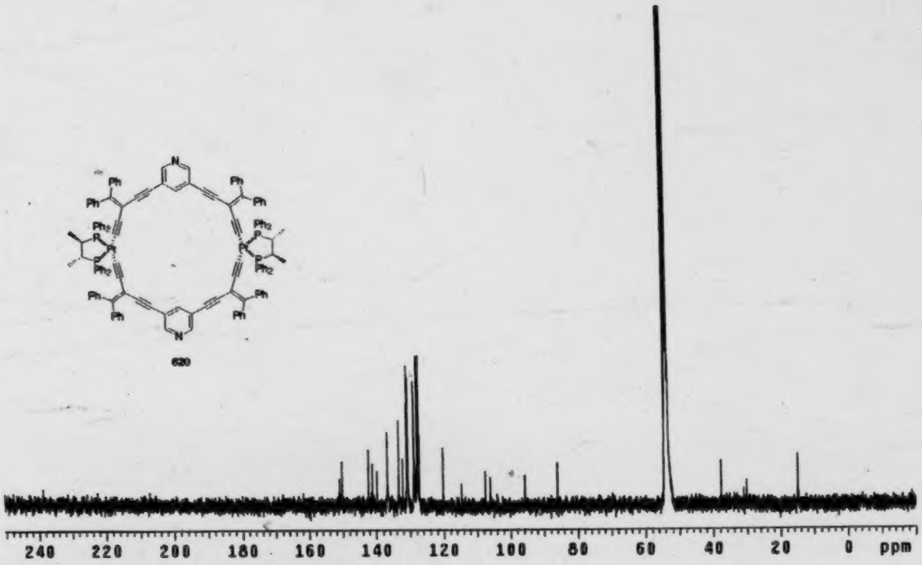

Figure A70 ^{13}C NMR spectrum of **620**.